Low-noise THz Niobium SIS Mixers

Thesis by

Mei Bin

In Partial Fulfillment of the Requirements

for the Degree of

Doctor of Philosophy

California Institute of Technology

Pasadena, California

1997

(Submitted October 3, 1996)

Acknowledgements

Foremost, I am indebted to my advisor Tom Phillips for his support and patience. He is always willing to answer my questions. The Thanksgiving dinners and graduation parties at his submillimeter ranch have become part of my joyful memories.

I would like to express my deep gratitude to Jonas Zmuidzinas for his guidance throughout my stay in the submillimeter group at Caltech. Without his insight and encouragement, I would have never been able to complete the work.

Mike Gaidis deserves much of the credit for his contribution to the FTS system and the device design and testing. Thomas Büttgenbach got me started on the FTS system and SIS detectors, and answered many naive questions patiently. I would like to thank both of them.

Many thanks to Ning Wang for being a good friend, who provided a lot of advice and shared many feelings. Her laughter brightened many cloudy days.

Thanks also go to John Calstrom for his encouragement; Jacob Kooi for many helpful discussions; Henry LeDuc for his hard and beautiful work in SIS junction fabrication; Dave Woody for his input on the FTS system alignment, and IF chain calibration; Paul Stockman and Geoff Blake for providing the infrared laser; Walt Schaal and Dave Vail for the prompt construction of the FTS purging box, and Walt for being always helpful when it got to mechanical design; Pat Schaffer for his always in-stock spare parts, and sometimes entertaining exclamations cross the hallway; Dave Miller for his friendly chat, for lending me his dewar, and for the beam pattern map; Richard Borup for teaching me how to use machine tools; Susan McCurdy and Dheera Sharma for being very nice and caring; Bruce Perger for being a short period officemate yet a good friend whom I have missed. I also want to thank Todd Hunter, Jocelyn Keene, Gene Serabyn, Darek Lis, Rob Schoelkopf, Keith Matthews, Taco, John Ward, Dominic Benford, Man Chan, and Andre Clapp for their generous help when I needed them.

My husband, Yong Cheng, has been a true companion through highs and lows. His love, encouragement, critics, and humor are great resources that keep me going. My parents, brothers, and parents-in-law have been also very supportive of me. Their boundless love is a key to the success of my work. My daughter, Meini, has brought true joy to life for the past two years. I thank all of them from the bottom of my heart.

Abstract

This thesis describes the development of low-noise heterodyne receivers at THz frequencies for submillimeter astronomy using Nb-based superconductor-insulator-superconductor (SIS) tunneling junctions. The mixers utilize a quasi-optical configuration which consists of a planar twin-slot antenna and antisymmetrically-fed two-junctions on an antireflection-coated silicon hyperhemispherical lens. On-chip integrated tuning circuits, in the form of microstrip lines, are used to obtain maximum coupling efficiency in the designed frequency band. To reduce the rf losses in the integrated tuning circuits above the superconducting Nb gap frequency ($\sim$ 700 GHz), normal-metal Al is used to replace Nb as the tuning circuits.

To account the rf losses in the microstrip lines, we calculated the surface impedance of the Al films using the nonlocal anomalous skin effect for finite thickness films. Nb films were calculated using the Mattis-Bardeen theory in the extreme anomalous limit. Our calculations show that the losses of the Al and Nb microstrip lines are about equal at 830 GHz. For Al-wiring and Nb-wiring mixers both optimized at 1050 GHz, the RF coupling efficiency of Al-wiring mixer is higher than that of Nb-wiring one by almost 50%. We have designed both Nb-wiring and Al-wiring mixers below and above the gap frequency.

A Fourier transform spectrometer (FTS) has been constructed especially for the study of the frequency response of SIS receivers. This FTS features large aperture size (10 inch) and high frequency resolution (114 MHz). The FTS spectra, obtained using the SIS receivers as direct detectors on the FTS, agree quite well with our theoretical simulations. We have also, for the first time, measured the FTS heterodyne response of an SIS mixer at sufficiently high resolution to resolve the LO and the sidebands.

Heterodyne measurements of our SIS receivers with Nb-wiring or Al-wiring have yielded results which are among the best reported to date for broadband heterodyne receivers. The Nb-wiring mixers, covering 400 – 850 GHz band with four sep-

arate fixed-tuned mixers, have uncorrected DSB receiver noise temperature around $5h\nu/k_B$ to 700 GHz, and better than 540 K at 808 GHz. An Al-wiring mixer designed for 1050 GHz band has an uncorrected DSB receiver noise temperature 840 K at 1042 GHz and 2.5 K bath temperature. Mixer performance analysis shows that Nb junctions can work well up to twice the gap frequency and the major cause of loss above the gap frequency is the rf losses in the microstrip tuning structures. Further advances in THz SIS mixers may be possible using circuits fabricated with higher-gap superconductors such as NbN. However, this will require high-quality films with low RF surface resistance at THz frequencies.

Contents

List of Figures

List of Tables

Chapter 1 Introduction

Superconductor-insulator-superconductor (SIS) receivers are the most sensitive receivers for millimeter and submillimeter astronomy. This thesis represents a specific attempt to construct SIS receivers at a frequency of 1 THz. In this chapter, submillimeter astronomy is briefly described to justify the need for sensitive heterodyne receivers. The principle of heterodyne detection is then presented along with some practical considerations. This is followed by a brief review of current SIS receivers and an overview of the thesis.

1.1 Submillimeter astronomy

The submillimeter wavelength band, ranging from 1 mm (300 GHz) to 0.1 mm (3 THz), is one of the least explored spectral regions in astronomy today. This band is critical for astronomy since it provides important spectral and spatial information for studying many astrophysical topics, such as the cosmic background, very distant newly formed galaxies, and star formation within gas clouds in our own galaxy (Phillips and Keene, 1992). There are several aspects which make the submillimeter band important. First, the temperature of the dense interstellar gas ranges from 10 K to 200 K, with thermal emission corresponding to the frequency region ($h\nu \approx k_B T$) from about 200 GHz to 4 THz. Secondly, many interesting molecular species which are important for understanding cosmo-chemistry have a wealth of transitions in this band. Fig. 1.1 shows a composite spectrum from 325 GHz to 360 GHz towards the Orion molecular cloud. In addition to molecules, some atomic species which are important coolants for the interstellar medium (ISM), such as neutral or singly ionized carbon, have transitions in the submillimeter band. Thirdly, for extragalactic sources at cosmological distances, the emissions at far-infrared wavelengths, including the

powerful $\lambda = 158$ nm C^+ fine structure line, can be redshifted to the submillimeter band.

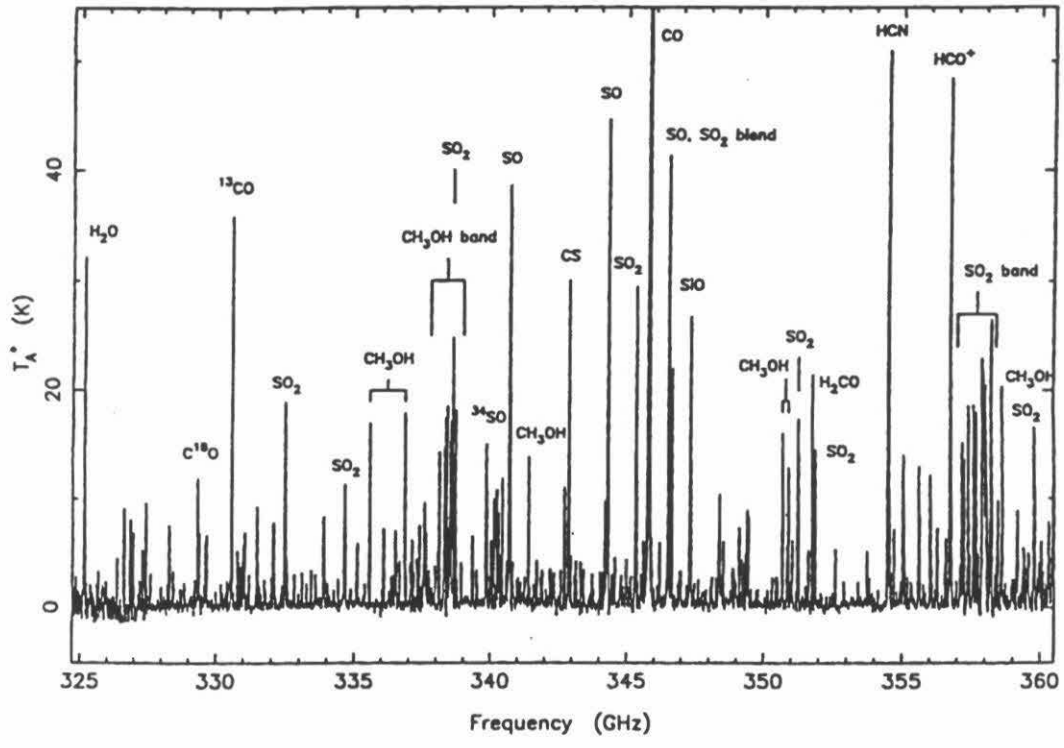

Figure 1.1: Submillimeter spectrum from 325 to 360 GHz towards the Orion molecular cloud taken at Caltech Submillimeter Observatory (Groesbeck 1994). The spectrum is a composite of over 100 individual spectra showing the diversity of chemical species in molecular clouds.

The challenge in fully exploring the submillimeter band is of a technical nature. Due to the relatively weak sources in the submillimeter band, large aperture radio telescopes with high surface accuracy must be constructed in order to have high sensitivity and good angular resolution. In addition, these large telescopes have to be placed at sites where the earth's atmosphere is sufficiently transparent. Since water is mostly responsible for the absorption in the submillimeter band, high altitude sites are required. In 1987, the first ground-based submillimeter telescope with an aperture

of 10.4 m, the Caltech Submillimeter Observatory (CSO), went into operation on Mauna Kea, Hawaii, at an altitude of 4200 m. The James Clerk Maxwell Telescope (JCMT) with an aperture of 15 m followed shortly after, at the same site. On a clear night on Mauna Kea, the atmosphere has several windows in the submillimeter band, allowing astronomy observations in the 230, 490, 650 and 850 GHz bands, as shown in Fig. 1.2. Today there are several dedicated millimeter and submillimeter observatories operating around the world, e.g., the 30 m telescope of the Institut de Radioastrnomie Millimétrique (IRAM) at an altitude of 2560 m, the 15 meter Swedish-European Southern Observatory (ESO) telescope (SEST) located at 2300 m, *etc.* (more examples are to be found in Carlstrom and Zmuidzinas' review paper, 1996). To increase angular resolution beyond $\sim 10''$, interferometry is needed. A six element submillimeter-wave array (SMA) of 6 m telescopes to operate from 2 mm to 350 μm is being built near the summit of Mauna Kea. The Millimeter Array (MMA) to consist of forty 8 m telescopes and to be built by the U.S. NRAO, and the Large Millimeter and Submillimeter Array (LMSA) of fifty 10 m telescopes by Japan are both in the planning stage. Both MMA and LMSA will be located on very high sites: $\sim$ 4000 to 5000 m sites either on Mauna Kea or on high plateaus in Chile. From 1974 to 1995, The Kuiper Airborne Observatory (KAO), with an aperture of 0.9 m, allowed observations at an altitude of up to 13.7 km with little atmosphere degradation in large windows in the submillimeter band (see Fig. 1.2). An upgraded air-borne observatory with an aperture of 2.5 m, the Stratospheric Observatory for Infrared Astronomy (SOFIA), will begin construction in 1997. To avoid the atmosphere absorption, the ideal observatories are space-borne. Several space-borne missions are now under construction or in planning. NASA will launch a 0.55 m aperture satellite (SWAS) in 1996 as a limited exploratory survey of only five lines. ESA is building a 3 m aperture satellite, the Far Infra-Red and Submillimeter Space Telescope (FIRST), to be launched in the year 2006. It is clear that there is a very large international investment in the field.

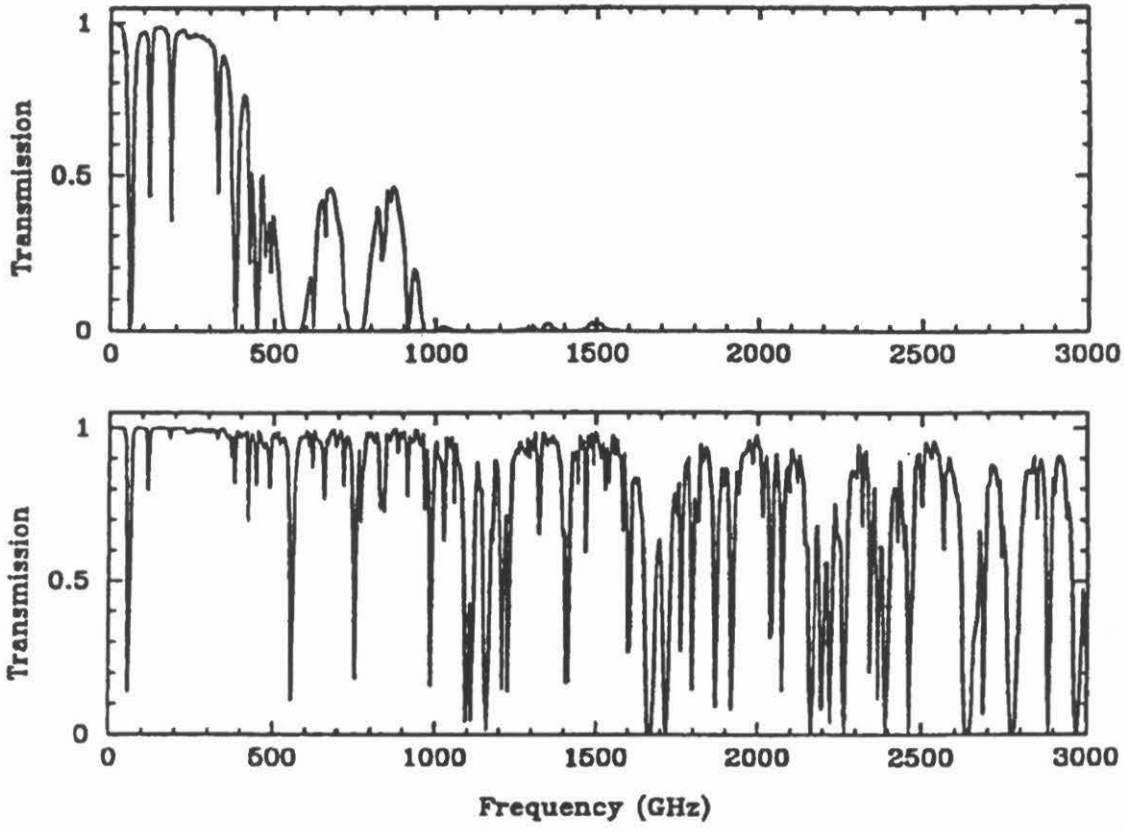

Figure 1.2: Atmospheric transmissions at Mauna Kea (4200 m) with a precipitable water vapor of 1 mm (top) and from an air-borne observing site like KAO (13.7 km) (bottom).

A second challenge is to develop sensitive detectors. Since the submillimeter band lies between the microwave and the infrared, technologies used in those two fields can be borrowed and adapted. Bolometers are available by adapting techniques from infrared astronomy. Since they have high sensitivity but do not easily provide high frequency resolution, they are suitable for observing broadband continuum emission, such as thermal radiation from dust. For spectroscopic investigations such as those of Fig. 1.1, very high resolution ($\Delta\nu/\nu \sim 10^{-6}$) is required, so the heterodyne detection technique used in radio astronomy must be pushed up into submillimeter band. The most sensitive heterodyne receivers in the low submillimeter band are made of superconductor-insulator-superconductor (SIS) detectors, whose noise can be quan-

tum limited. The past decade has seen great progress in building SIS receivers. Quasi-optical coupling has been developed; the use of on-chip integrated tuning circuits has become standard practice; technologies for fabrication of SIS detectors is more mature. Now SIS receivers routinely provide astronomers state-of-the-art detectors for observations in the 200 - 850 GHz range. Section 1.3 will present a brief review of the development of SIS receivers.

When new air-borne and space-borne telescopes are equipped with sensitive SIS receivers, more exciting astronomical discoveries can be expected. The heterodyne spectroscopic part of FIRST will include several SIS detectors to cover 500 - 1200 GHz in five bands. The continued development of SIS receivers is clearly critical.

1.2 Heterodyne receiver principles

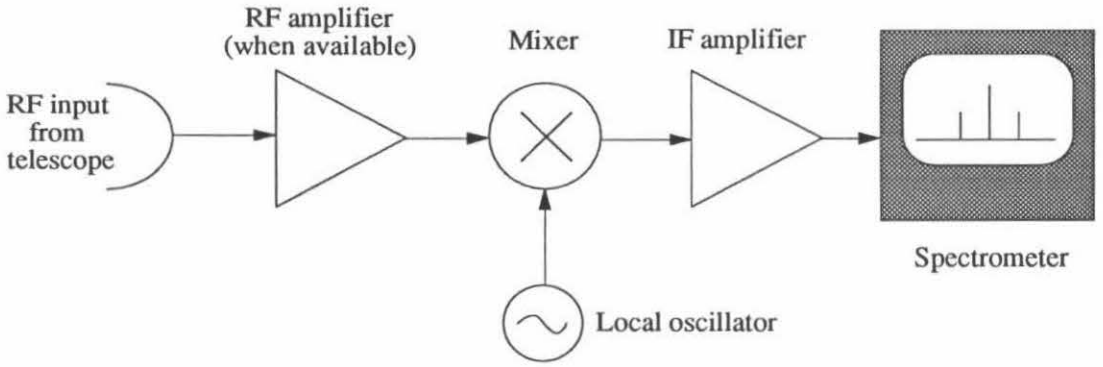

Figure 1.3: A schematic layout of a heterodyne receiver. The mixer down-converts the high frequency signal by combining it with the local oscillator. The difference frequency is filtered out and amplified by an IF amplifier and then spectrally analysed. When the signal frequency is higher than about 50 GHz, the amplifier before the mixer is not sufficiently low noise to be useful.

In radio astronomy and many other fields, the radiation received by an antenna is often too high in frequency and too weak in signal strength to be handled by the following electronics. A heterodyne receiver is then used to down-convert the signal from radio frequency (RF) to a much lower intermediate frequency (IF) where current

technologies are available for amplification and for analysing the signal. Heterodyne detection preserves the amplitude and phase information of the signal. Fig. 1.3 shows a general layout of a heterodyne receiver. The heart is a non-linear device called the mixer, which performs the down-conversion by mixing the signal with a strong coherent source known as the local oscillator (LO). The difference signal is then filtered out and fed to an IF amplifier and later to the analysis instrument, which is usually some form of a spectrometer. For signal frequencies above about 50 GHz, a sufficiently low noise amplifier in front of the mixer is not available. In that case, the mixer is then the first element to process the weak signal. This makes the mixer the most critical component of the receiver.

The electronic device most commonly used in a mixer is a diode which therefore has a non-linear current-voltage characteristic. The non-linear devices can be Schottky diodes or SIS tunnel junctions. If the non-linear device is supplied with a bias voltage V_0 and a small time-varying voltage $V(t)$, the current through the device can be expanded by Taylor series:

$$\begin{aligned} I(t) = I(V_0 + V(t)) &= I(V_0) + \frac{dI(V_0)}{dV}V(t) + \frac{d^2I(V_0)}{2dV^2}V^2(t) + ... \\ &\equiv I(V_0) + K_1V(t) + K_2V^2(t) + ... \end{aligned} \tag{1.1}$$

In the case when the time-varying voltage is the combination of the LO with amplitude A and frequency ω_{LO}, and the signal with amplitude B and frequency ω_{SIG},

$$V(t) = A\sin(\omega_{\mathrm{LO}}t) + B\sin(\omega_{\mathrm{SIG}}t), \tag{1.2}$$

the current becomes

$$
\begin{aligned}
I(t) = {} & I(V_0) + K_1[A\sin(\omega_{\mathrm{LO}}t) + B\sin(\omega_{\mathrm{SIG}}t)] && \text{(original signal)} \\
& + K_2\Big(\frac{A^2}{2} + \frac{B^2}{2}\Big) && \text{(rectified signal)} \\
& - K_2\Big(\frac{A^2}{2}\cos(2\omega_{\mathrm{LO}}t) + \frac{B^2}{2}\cos(2\omega_{\mathrm{SIG}}t)\Big) && \text{(first harmonic)} \\
& + K_2AB\cos[(\omega_{\mathrm{LO}} - \omega_{\mathrm{SIG}})t] && \text{(difference frequency)} \\
& - K_2AB\cos[(\omega_{\mathrm{LO}} + \omega_{\mathrm{SIG}})t] && \text{(sum frequency)} \\
& + \ldots
\end{aligned}
\tag{1.3}
$$

The current contains the original signal, the rectified signal, harmonics of the local oscillator and signal, and the sum and difference of the local oscillator and signal frequency. Of course for a linear device, the Taylor expansion coefficient $K_2 = 0$ and no frequency conversion will occur. The receiver down-converts not only a single frequency, but a frequency band determined by the IF bandwidth. This IF bandwidth is often referred to as the instantaneous bandwidth of the receiver.

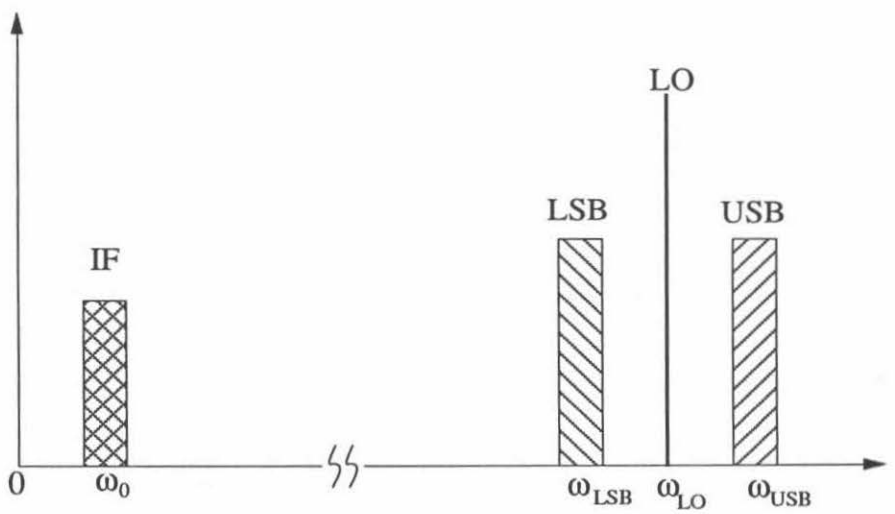

Figure 1.4: Down-conversion process of a heterodyne receiver from the upper and lower sideband into the intermediate frequency band.

In general the current spectrum in the mixer contains frequencies $\omega = |m\omega_{\rm LO} \pm n\omega_{\rm SIG}|$, m, n being integers. The IF filter and amplifier only pick out the frequency component $\omega = \omega_0$. In other words, signals incident on the mixer at sideband frequencies $|\omega_{\rm m}|$ are converted with some efficiency to power at the output IF frequency ω_0. The sideband frequencies are

$$\omega_{\rm m} = m\omega_{\rm LO} + \omega_0, \qquad \text{for all integers } m. \tag{1.4}$$

The signal at frequency ω_1 is called the upper sideband (USB) or signal band, while the signal with frequency $|\omega_{-1}|$ is called the lower sideband (LSB) or image band. A schematic down-conversion process is given in Fig. 1.4, showing the relations among LO, USB, LSB and IF. Since the IF frequency ω_0 is much smaller than the LO frequency $\omega_{\rm LO}$, it is often assumed that $-\omega_{-\rm m} \approx \omega_{\rm m}$. Many mixers respond equally well to signals in USB and LSB. A receiver that allows both sidebands to be mixed equally well into the IF band is called a double sideband (DSB) receiver, whereas a receiver that employs some means to block one sideband before the mixer or has a much greater response to one sideband is a single sideband (SSB) receiver.

The difference frequency signal depends on K_2, which is a measure of the nonlinearity of the IV characteristic. This implies that we should have as strong a nonlinearity as possible to maximize the conversion gain. It is desirable that a mixer has a linear gain, *i.e.*, the output IF power is proportional to the input signal power. For our simple model here, we can have linear gain if the LO amplitude is held constant and K_2 does not change, and if the signal is sufficiently weak that higher order terms in the Taylor expansion do not contribute significantly.

An important figure of merit of all receivers is the noise added to the signal by the receiver. In radio astronomy the signal strength (power, or more accurately, spectral density) is typically quoted in radiation temperature, and so it is convenient to quote the noise power as a noise temperature $T_{\rm N}$. If the signal has an equivalent temperature

$T_{\rm in}$, the signal-to-noise ratio of the receiver is given by the famous Dicke equation

$$\frac{S}{N} = \frac{T_{\rm in}}{T_{\rm N}}\sqrt{B\Delta t}\ , \tag{1.5}$$

where B is the bandwidth received by the IF detector and Δt is the integration time. The noise temperature can be thought of as the detectable power in a 1 Hz bandwidth over 1 second integration time when the signal-to-noise ratio is one. Since the integration time required to detect a weak signal at a particular signal-to-noise ratio decreases as the square of the noise temperature, it is easy to see the need for low noise receivers in radio astronomy, when telescope time can be very limited and sources are generally weak.

The receiver noise is often calibrated by the so-called *Y-factor* method. This method involves measuring the receiver output for two blackbody sources at the receiver input with known temperatures. These two inputs are called the hot load and cold load, with temperatures $T_{\rm hot}$ and $T_{\rm cold}$. The power P, per unit bandwidth, received by an antenna whose beam is filled with radiation from a blackbody at temperature T is

$$P = \frac{h\nu}{e^{h\nu/k_{\rm B}T} - 1}\ . \tag{1.6}$$

This is just the power in a single mode of a blackbody radiation field. If $k_{\rm B}T \gg h\nu$, the thermal radiation is in the Rayleigh-Jeans limit, and the power is approximated by

$$P = k_{\rm B}T\ ; \tag{1.7}$$

here $k_{\rm B}$ is the Boltzmann constant. The output power in the IF band is the sum of power from the blackbody input and from the receiver's own noise contribution. This noise is often quoted in noise temperature $T_{\rm rec}$, referenced to the input of the receiver. If the receiver has a gain G and bandwidth B, the IF output power can be written

in the form

$$P^{\mathrm{IF}} = Gk_{\mathrm{B}}(T_{\mathrm{rec}} + T)B \ . \tag{1.8}$$

Taking two measurements, with T_{hot} and T_{cold} as inputs, yields the Y factor

$$Y = \frac{P^{\mathrm{IF}}_{\mathrm{hot}}}{P^{\mathrm{IF}}_{\mathrm{cold}}} = \frac{T_{\mathrm{rec}} + T_{\mathrm{hot}}}{T_{\mathrm{rec}} + T_{\mathrm{cold}}} \ . \tag{1.9}$$

The receiver's noise temperature can then be calculated as

$$T_{\mathrm{rec}} = \frac{T_{\mathrm{hot}} - YT_{\mathrm{cold}}}{Y - 1} \ . \tag{1.10}$$

All receiver noise temperatures quoted in this thesis were performed using this Y-factor technique with a hot load at room temperature (295 K) and a cold load at liquid nitrogen temperature (77 K). A few words should be said about the usage of (1.7) - (1.10), which are based on the Rayleigh-Jeans (RJ) approximation. At THz frequencies and room-to-cryogenic load temperatures, obvious deviations occur between the RJ approximation and the Planck formula. For instance, at 1 THz, the power radiated from a 295 K blackbody is 92% of that calculated by the RJ approximation; while the power from a 77 K blackbody is only 72% of that obtained from the RJ limit. The strict noise temperature should therefore be calculated from the Planck formula, as below:

$$T_{\mathrm{N}} = \frac{P(T_{\mathrm{hot}}, \nu) - YP(T_{\mathrm{cold}}, \nu)}{Y - 1} \ , \tag{1.11}$$

where $P(T, \nu)$ is given by (1.6). This calculation is frequency-dependent and often inconvenient to carry out during an experiment. The difference between the two noise temperatures calculated by the RJ limit and the Planck formula is illustrated in Fig. 1.5 for various frequencies. The horizontal axis is the noise temperature calculated using the RJ limit (1.10), and the vertical axis gives the difference between the two noise temperatures and should be added to the RJ limit value to obtain

the Planck noise temperature. Since the correction is less than 10% of the noise temperature achieved to date (see section 1.4), we will neglect this effect at the moment.

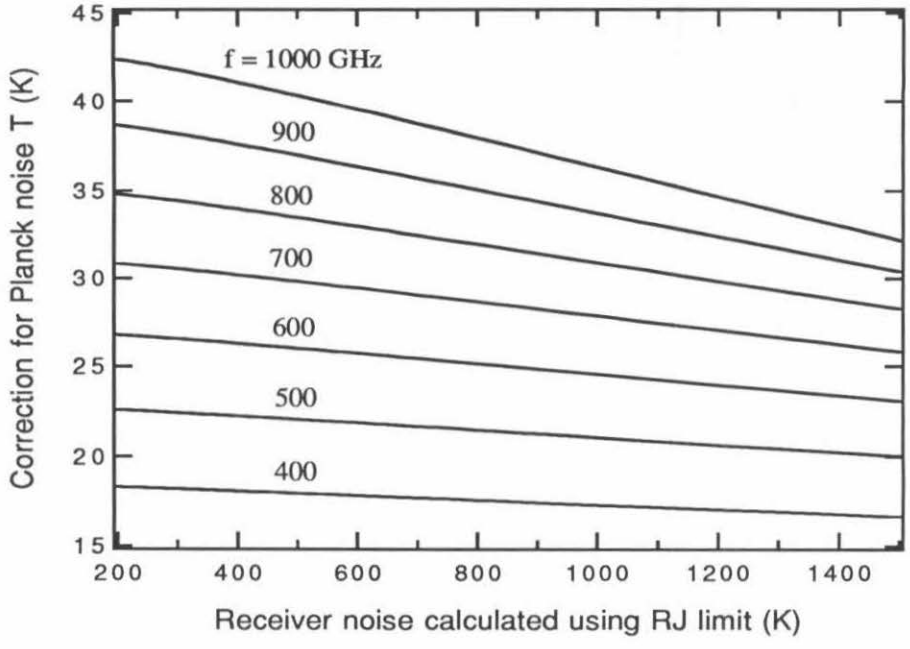

Figure 1.5: Difference between the receiver noise temperatures calculated by Rayleigh-Jeans limit and the Planck's formula. x-axis gives the noise temperature by Rayleigh-Jeans limit and the y-axis value is added to obtain the Planck noise temperature.

For a receiver system with several stages of amplifiers, it is interesting to investigate each stage's contribution to the total receiver noise. Fig. 1.6 shows a chain of components in the signal path, each with a gain G_i, and a noise T_i referred to its input. The whole system noise and gain are

$$\begin{aligned} T_{\text{sys}} &= T_1 + \frac{T_2}{G_1} + \frac{T_3}{G_1 G_2} + \ldots \\ G_{\text{sys}} &= G_1 \times G_2 \times G_3 \times \ldots \end{aligned} \tag{1.12}$$

Note that these formulas assume that the input of each successive stage is impedance matched to the output of the previous stage. This shows that the first stage is the

most important stage if all the stages have a gain larger than unity. For receivers that have no amplifier before the mixer, the mixer's noise contribution is thus most important. Additionally, the gain of a mixer, often termed as conversion efficiency, is usually less than unity. This makes the IF amplifier following the mixer also critical, since its noise contribution to the receiver is magnified by the conversion loss of the mixer. The first IF amplifier usually has a large enough gain that the subsequent system components do not greatly affect the system noise temperature.

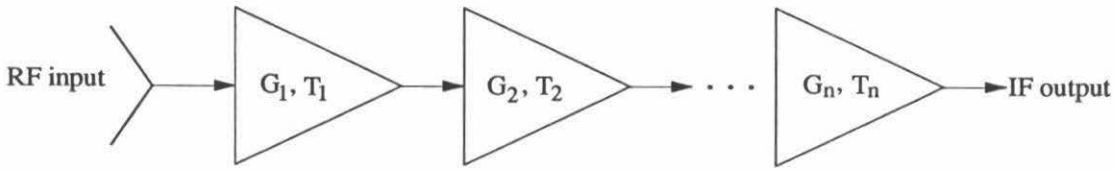

Figure 1.6: A chain of components of a receiver system, each component having its one gain G_i and noise temperature T_i.

The goal in mixer design is to make it as sensitive to the signal as possible. However, there are fundamental and practical limitations which affect the mixer noise we can achieve. The Heisenberg uncertainty principle places a bound on the measurement accuracy of any attempt to simultaneously measure the phase and amplitude of electromagnetic field. Since a mixer preserves phase and amplitude of the signal, there is a lowest noise temperature imposed by quantum mechanics. General linear and phase-preserving amplifier theories, such as Caves' (Caves 1982), predict this quantum-limited noise temperature to be $T_{\rm Q} = h\nu/k_{\rm B}$ for a single sideband mixer.

In practice it is hard to obtain quantum-limited performance. The mixing element itself is typically a tunneling device, such as an SIS or Schottky diode, which introduces shot noise due to the leakage current of the diode. Any lossy element with a gain less than unity in the path of the signal to the mixer, such as an infrared blocking filter or a beam-shaping lens or a transmission line, will introduce thermal noise. If the transmission (or gain) of such an element is G, the noise temperature referred to the input of the element in the Rayleigh-Jeans limit will be $T_{\rm amb}(1-G)/G$, where

T_{amb} is the physical or ambient temperature of the element. Any signal mismatch at the RF input will cause signal to be reflected and thus a higher conversion loss, also degrading the noise performance.

1.3 A brief review of SIS receivers

In 1979, Tucker established mixer theories for superconducting tunnel diodes, including SIS detectors (Tucker 1979). His theory suggested that SIS mixers could achieve nearly perfect sensitivity as heterodyne detectors, only limited by the quantum noise as pointed out by Wengler and Woody (Wengler & Woody 1987). Unlike devices which fit the classical mixer theory (Torrey & Whitmer 1948), SIS's are capable of power gain on downconversion. The first experimental work in 1979 on SIS receivers (Dolan *et al.* 1979; Richards *et al.* 1979; Rudner & Claeson 1979) showed very low noise at frequencies of 115 GHz, 36 GHz and 10 GHz. The work at 115 GHz verified the quantum nature of the detection process. It did not take long before the predictions of Tucker were experimentally verified (Feldman 1983; McGrath *et al.* 1981; Phillips & Dolan 1982). In the last one and half decade, major technology progress has been achieved and SIS mixers have replaced GaAs Schottky-diode mixers at nearly all major millimeter and submillimeter radio observatories. Several recent review papers on SIS receivers (Blundell & Tong 1992; Carlstrom & Zmuidzinas 1996; Wengler 1992) have been published.

There are several important issues in making practical and sensitive SIS receivers. First the technology must be available to fabricate good quality SIS junctions. In the early days, SIS junctions were made of lead-alloys. These junctions had the drawback of the chemical and crystallographic instabilities of the lead-alloy, which made them difficult to handle and store. A big improvement in quality was achieved with the introduction of Nb/Al-oxide/Nb junction fabrication technique (Gurvitch *et al.* 1983). The Nb junctions are very stable in terms of thermal recycling and atmospheric storage. Now Nb-based junctions are the work-horse for all SIS receivers in the submillimeter band up to frequencies of 1 THz (the critical temperature of Nb

is 9.2 K, corresponding to a Nb energy gap frequency of $\sim$ 700 GHz). NbN junctions have been under continuous development in the hope of achieving mixers working at even higher frequencies (the critical temperature of NbN is about 16 K, corresponding to a gap frequency of $\sim$ 1200 GHz). However, high quality NbN junctions are not yet readily available (Kohjiro *et al.* 1993; Wang *et al.* 1994).

The type of feed antennas to couple the radiation onto the junction is a major issue for SIS receivers. Waveguide coupling is the traditional radio scheme which has been used exclusively for SIS receivers below 500 GHz and has been extended, with difficulty, for receivers working at frequencies as high as 850 GHz (de Lange *et al.* 1994a; Kooi *et al.* 1995a). The advantages of waveguide coupling include well-defined beam patterns and high coupling efficiency to the primary antenna. It also provides adjustable tuning to the mixers. But waveguides are difficult and expensive to manufacture and the skin-effect losses become large for high frequency applications. The alternative to waveguide coupling is quasi-optical coupling. A micro-antenna is integrated on chip with the SIS junctions, and dielectric lenses are used to help shape the beam in a quasi-optical receiver. One of the first quasi-optical receivers developed (Wengler *et al.* 1985) utilized an integrated bow-tie antenna on a quartz substrate and a quartz hyperhemispherical lens. In the following ten years, efforts have been made to achieve better antenna beam patterns and higher coupling efficiencies (Büttgenbach *et al.* 1993; Filipovic *et al.* 1993a; Zmuidzinas & LeDuc 1992; Zmuidzinas *et al.* 1995). Several planar antenna structures, like spiral, log-periodic, twin-slot, and double-dipoles, have been tried on quartz or silicon substrates. Quasi-optical mixers are easy to fabricate and assemble, and have the advantage of natural adaptation to imaging arrays. The disadvantage is that they lack the adjustable tuners. But with the progress in broadband on-chip integrated tuning circuits, this is not a serious problem anymore.

The integrated tuning circuit serves two purposes. First it tunes out the geometrical capacitance of the junction, which shorts out the high frequency signal if left untuned. Secondly, it can behave as a transformer which matches the impedance of the junction to that of the planar antenna or the waveguide probe. The tuning

circuit is usually made of microstrip transmission lines. The width and length of the microstrip line can be chosen properly so that part of it looks like an inductor in parallel or series with the junction capacitance, and part of it looks like sections of quarter-wavelength transformer. The first work of applying integrated tuning circuits on SIS receivers was done more than ten years ago (D'addario 1984; Räisänen *et al.* 1985). Now integrated tuning circuits have been widely adopted by both waveguide and quasi-optical SIS receiver builders.

The microstrip line tuning circuit is conveniently made of the same superconductor that makes the junction and also all the electrodes. For a superconductor, there is a frequency threshold $f_{\rm gap}$ below which the signal losses in the microstrip are negligible and above which the losses increase significantly. This frequency corresponds to the superconductor pair binding energy (or gap energy) Δ, $f_{\rm gap} = 2\Delta/h$. When the incoming photon has energy high enough to break the Cooper-pair in the superconductor, the photon will essentially only "see" normal electrons and thus the superconductor will behave like a normal metal to the incoming radiation. Skin effect RF losses hence come in as a result. In the case of a Nb junction, $f_{\rm gap} \approx 700$ GHz. For Nb SIS receivers working above 700 GHz, the losses contributed by the integrated tuning circuit can be significant and worth study. Since normal-metal Nb is not a good conductor, it has been speculated that by replacing Nb with other good normal-metals (e.g., Al, Ag, Al or Cu) for the tuning circuit and electrodes, better receiver performance would be achieved (Bin *et al.* 1996; de Lange *et al.* 1994a). This is studied in this thesis.

SIS receivers have been pushed to work towards higher and higher frequencies. By 1992, low-noise waveguide or quasi-optical SIS mixers had been developed to about 500 GHz as summarized in the review paper by Blundell and Tong (Blundell & Tong 1992). Since then work has been focused on the 650 and 850 GHz atmospheric windows, and on the 1 THz band for future air-borne and space-borne missions. Recent progress in waveguide mixers has been made by several submillimeter astronomy groups, at Caltech (Kooi *et al.* 1994a; Kooi *et al.* 1996), Harvard-Smithsonian (Tong *et al.* 1995a), JPL (Febvre *et al.* 1994), University of Cologne (Honingh *et al.* 1995),

and University of Groningen (de Lange *et al.* 1994b; van de Stadt *et al.* 1996). Meanwhile, quasi-optical receivers have also been developed to the same frequency range and achieved noise temperatures equivalent to the best waveguide receivers above 500 GHz. Several groups around the world have been involved, e.g., the Max Planck Institute for Extraterrestrial Physics in Germany (Rothermel *et al.* 1994; Schuster *et al.* 1993), Russian Academy of Science (Belitsky *et al.* 1995b), University of Groningen in Holland (Shitov *et al.* 1996; Skalare *et al.* 1993), and Caltech (Bin *et al.* 1996; Gaidis *et al.* 1996a; Zmuidzinas *et al.* 1994; Zmuidzinas *et al.* 1995). Fig. 1.7 shows the noise temperatures of SIS receivers in the world reported to the end of 1995. It is adapted from figure 2 in Carlstrom and Zmuidzinas' review paper (Carlstrom & Zmuidzinas 1996). The ratio of double-sideband receiver noise temperature to frequency $T_{\rm rec}/\nu$ is plotted. We can see that the receiver noise temperatures are getting lower than or close to five times the quantum limit below $\sim$ 600 GHz. However, the noise temperatures increase sharply around the gap frequency at 700 GHz, due to the RF losses in the tuning circuits. Note that the data points represented by "Ga" and "Bi" in the plot are part of this thesis work.

A question needs to be answered for SIS mixers working above the superconducting gap frequency: what is the upper frequency limit and what will be the mixer performance vs. frequency? There is a fundamental upper frequency limit to efficient mixer performance, which is two times the superconducting gap frequency ($2f_{\rm gap} = 4\Delta/h$). The reason for this can be seen from the semiconductor model (see chapter 2). With the junction biased below the gap voltage, absorption of a small energy photon will result in an extra electron in the tunnel current, and this photon is thus detected. But when the photon energy is sufficiently high ($> 2f_{\rm gap}$), not only can it cause an electron to join in the tunnel current, but also an electron to tunnel backwards across the junction, producing current of the opposite sign. On average, there will be more electrons tunneling forward than backward, so there will still be a net tunnel current. However, the responsivity does drop to a fraction of what it was before this backward tunneling became possible, resulting in a sharp drop off in the mixer performance. The mixer performance between $f_{\rm gap}$ and $2f_{\rm gap}$ also degrades compared to the per-

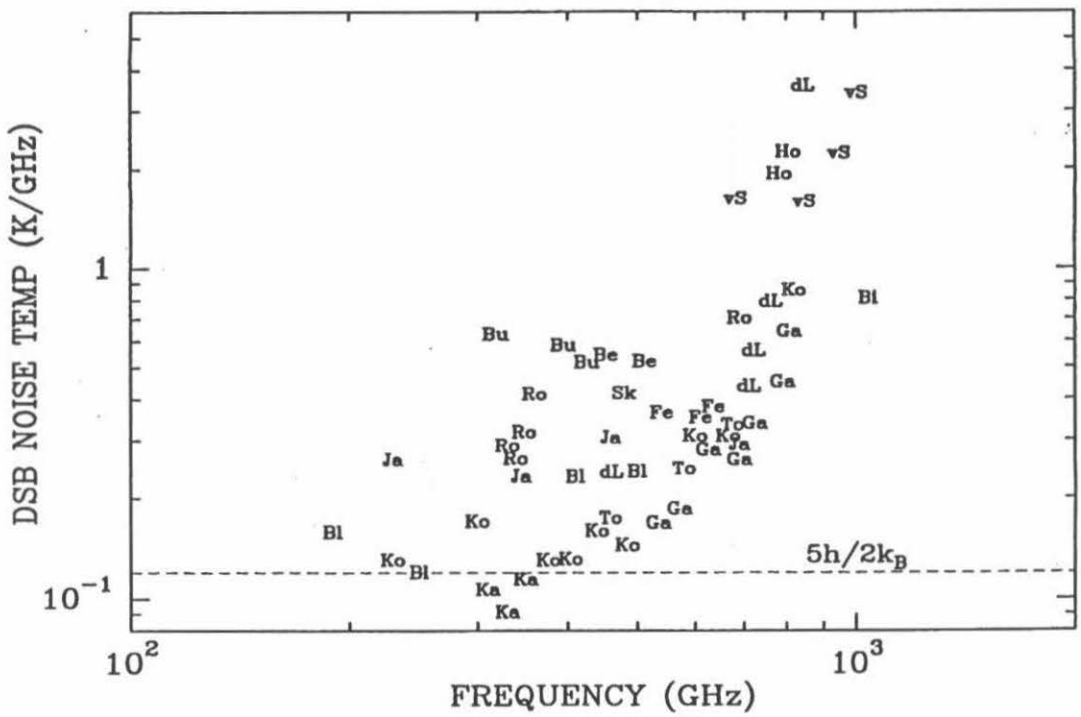

Figure 1.7: SIS receiver noise temperatures reported up to the end of 1995 (adapted from figure 2 of Carlstrom and Zmuidzinas (Carlstrom & Zmuidzinas 1996)). The ratio of double-sideband receiver noise temperature to frequency $T_{\rm rec}/\nu$ is plotted. The dashed line represents a single-sideband noise temperature of $5h\nu/k_{\rm B}$, *i.e.*, 5 times the quantum limit. All data are uncorrected for optical losses. The sharp increase in noise temperature above 700 GHz is mainly caused by the RF losses in the integrated tuning circuits. QO represents quasi-optical SIS and WG represents waveguide SIS. The data are from: Be (Belitsky *et al.* 1995b) (QO); Bi (Bin *et al.* 1996) (QO, Al-wiring); Bl (Blundell *et al.* 1995a; Blundell *et al.* 1995b) (WG); Bu (Büttgenbach *et al.* 1992) (QO); dL (de Lange *et al.* 1994a; de Lange *et al.* 1994b) (WG); Fe (Febvre *et al.* 1994) (WG); Ga (Gaidis *et al.* 1995a; Gaidis *et al.* 1995b) (QO); Ho (Honingh *et al.* 1995) (WG); Ja (Jacobs *et al.* 1994) (WG); Ka (Karpov *et al.* 1995) (WG); Ko (Kooi *et al.* 1994a; Kooi *et al.* 1994b; Kooi *et al.* 1995a; Kooi *et al.* 1996) (WG); Ro (Rothermel *et al.* 1994) (QO); Sk (Skalare *et al.* 1993) (QO); To (Tong *et al.* 1995a; Tong *et al.* 1995b) (WG); vS (van de Stadt *et al.* 1995a; van de Stadt *et al.* 1995b) (WG, Al-wiring). Note this thesis work contributed to the data points presented by Ga and Bi.

formance below the gap frequency. This is the result of electron tunneling assisted by the simultaneous absorption of two photons. Like the absorption of a photon with energy higher than 4Δ, the absorption of two photons with energy higher than 2Δ can result in electron tunneling in either direction across the junction. Since the single photon process is much more important than the two photon process, the degradation in performance is not nearly as severe as the sudden fall off in the performance above $2f_{\rm gap}$. Theoretical modeling and simulation by Danchi and Sutton (Danchi & Sutton 1986) suggested that the mixer noise increased proportionally to the frequency from $f_{\rm gap}$ to $2f_{\rm gap}$, and as the cube of the frequency above $2f_{\rm gap}$. Though we know that SIS junctions work well above the gap frequency, no experimental data have been available to reveal the mixer performance vs. frequency.

1.4 Thesis overview

This thesis describes the development of Nb-based SIS receivers above gap frequency up to the 1 THz regime. The main topic addressed by this research is the receiver performance as a function of frequency. There are two issues: first the mixing performance of the SIS junction as function of frequency, and second the tuning circuit performance as a function of frequency. As stated in the last section, tuning circuits are critical for SIS receivers. We have investigated superconducting and normal-metal microstrip line properties for the purpose of effective tuning circuit design. The anomalous skin effect phenomenon was studied for normal-metal microstrip lines at high frequency and low temperature.

To experimentally characterize the frequency performance of a mixer, we can measure the frequency response obtained with a Fourier transform spectrometer (FTS) when using the SIS receiver as a direct detector. We have constructed a laboratory FTS, especially designed for the testing of SIS receivers at submillimeter band. This FTS has large throughput and high frequency resolution and has become a powerful tool in checking design ideas and pre-sorting mixer elements.

We use the quasi-optical coupling scheme, which is intrinsically broadband and thus advantageous in studying the frequency response of SIS mixers. Mixers with niobium junctions and tuning circuits were designed for frequencies from 450 GHz to 750 GHz. In addition, mixers with niobium junctions and normal-metal Al tuning circuits were designed for frequencies above the niobium gap. We investigated both the direct and heterodyne properties of these mixers. Our designs were successful: the all-Nb receivers obtained very low-noise performance and our 1 THz Nb-based mixers with normal-metal Al tunings achieved an uncorrected, double-sideband receiver noise temperature of 840 K at 1042 GHz. This is about four times better than the semiconductor Schottky diode receivers that were previously used at the same frequency (Bin *et al.* 1996). Our low-noise THz receivers should be valuable for air-borne and space missions like SOFIA and FIRST.

The thesis is organized following the above line of the work. Chapter 2 presents the theories of SIS mixer, including the semiconductor model and Tucker's quantum theory. Chapter 3 describes quasi-optical SIS receiver systems, in particular the twin-slot antenna, double junction configuration used for our work. Chapter 4 discusses the method we use in SIS mixer design. Various integrated tuning circuits are reviewed and models for calculating microstrip line properties are given. The surface impedance of superconductor and normal-metals are investigated, which is an important issue in terms of loss. A design and optimization program was created for mixer analysis and design, and an example of its use for the twin-slot double junction mixer design is given. Chapter 5 describes in detail the Fourier transform spectrometer we constructed for studying the frequency performance of SIS receivers. Direct and heterodyne tests on the FTS are discussed and their relationship is explored. Chapter 6 and 7 give a detailed description on the design of SIS mixers with superconducting Nb or normal-metal Al tuning structures. The FTS spectrum and heterodyne results are provided for several devices working at different frequency bands, from below the gap up to 1 THz. The receiver performance is analyzed with respect to optical and

RF losses and IF mismatch, and is then compared with SIS quantum theory. Finally, a summary and outlook is presented in chapter 8.

Chapter 2 Theories of SIS Mixers

A superconductor-insulator-superconductor (SIS) tunnel junction is a sandwich of two superconductors separated by a very thin layer of insulator. Two types of charge carriers can tunnel through the insulation barrier: the Cooper pairs, and the quasiparticles. Both carrier currents present a non-linear characteristic and can be used for mixing. Mixers using Cooper pairs as current carriers are called Josephson effect mixers (Schoelkopf 1995), while those utilizing quasiparticle tunneling are known as SIS mixers. SIS mixers are the state-of-the-art heterodyne technology for millimeter and submillimeter detection. A quantum theory for SIS mixers was laid out by Tucker (Tucker 1979). Unlike classical mixers, SIS mixers are predicted to be capable of conversion gain rather than loss and quantum-limited noise. Tucker's theory has proved very successful in predicting and explaining SIS mixer behavior. A complete review on this theory was given by Tucker and Feldman (Tucker & Feldman 1985).

In this chapter we will cover some theoretical basics that are helpful in understanding SIS mixers. First some relevant superconductor phenomena are briefly mentioned. Then a semiconductor picture is presented to explain the dc and photon-assisted tunneling of quasiparticles in SIS detectors. Finally, Tucker's quantum heterodyne theory is described.

2.1 Superconductivity

Superconductivity is a phenomenon of electronic quantum state of metal. When the temperature of a certain kind of metal or alloy is lower than a critical temperature T_c, two hallmark features occur. One is the vanishing of the dc electrical resistance and the other is the expelling of magnetic field from the interior of a bulk superconductor. A microscopic theory which can explain nearly every feature of low-T_c superconduc-

tivity was first presented by Bardeen, Cooper and Schriefer in 1957. This theory is known as BCS theory.

In normal metals, electrons can be treated approximately as a free Fermi gas. In the ground state, all energy levels below Fermi energy are occupied and above levels are empty. There is no gap between the valence band and the conduction band, and the energy required to excite an electron can be arbitrarily small. The occupation probability of a state is described by Fermi distribution

$$f(\varepsilon) = \frac{1}{e^{\varepsilon/k_B T} + 1} , \tag{2.1}$$

where $\varepsilon = E - \mu$ is the electron energy relative to the Fermi level μ.

In 1956 Cooper presented the idea that Fermi sea of electrons is unstable against the formation of at least one bound electron pair and a very weak attraction can bind pairs of electrons into a bound state. Attraction between two electrons with equal but opposite momenta and spins occurs when the motion of ion cores (represented as phonons) is taken into account. When the temperature is low enough, the attractive force overrides the Coulumb repulsive force. Electrons are then bound into pairs (called Cooper pairs), and condense until equilibrium is reached. Since Cooper pairs are bosons (zero spin), at T=0 K they all occupy the same minimum energy pair state, called the BCS ground state. The superconductor state can be described by a single many-particle condensate wavefunction $\Psi(\vec{r})$ which maintains phase coherence over macroscopic distances.

The excited state of a superconductor occurs when one Cooper pair is removed from the Bose condensate. There are no stable pair states above the BCS ground state, so the minimum energy needed to remove a pair from the ground state is that required to break it. Each electron has a binding energy Δ with respect to the pair. The minimum energy for excitation above the ground state is thus 2Δ, which is referred to as the superconducting energy gap. A Cooper pair can be described as two electrons in a state $(\vec{k}\uparrow, -\vec{k}\downarrow)$, where $\vec{k}$ represents momentum and $\uparrow$ represents spin. An excitation of state k is defined as $\vec{k}\uparrow$ occupied, and $-\vec{k}\downarrow$ empty. In analogy

to semiconductor theory, we can see this as a creation of an electron-like particle and a hole-like particle. Unlike in semiconductors, here both electron-like and hole-like particles have electric charge of $-e$. These excited particles are called quasiparticles. Quasiparticles act in most ways like electrons, but they have finite lifetimes and will decay back into pair states.

Using quantum field theory, it can be shown that quasiparticles are elementary excitation states of a superconductor with energy E relative to Fermi level (Tinkham 1975)

$$E = \sqrt{\varepsilon^2 + \Delta^2} \,, \tag{2.2}$$

where ε is the single-particle energy relative to Fermi level.

We can see that Δ plays the role of an energy gap or minimum excitation energy. Even at the Fermi surface where $\varepsilon = 0$, $E = \Delta > 0$.

Density of states

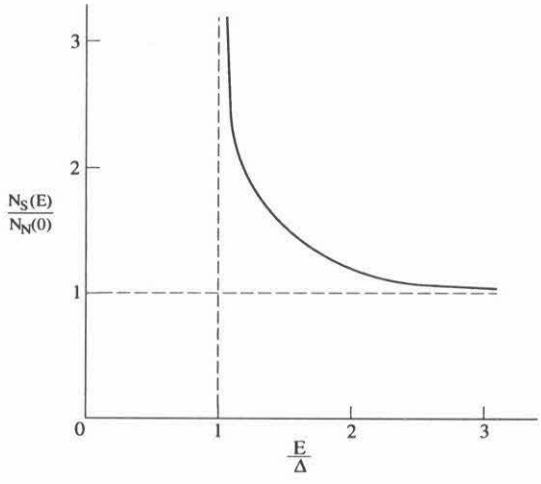

Figure 2.1: Density of states $N_S(E)$ of a superconductor at 0 K. $N_N(0)$ is the density of states of normal conductor electrons at Fermi level.

The density of states $N_S(E)$ for quasiparticles can be found in the following way. We assume that the states' number does not change in the transition from a normal

metal to a superconductor (Tinkham 1975), *i.e.*,

$$N_{\rm S}(E)dE = N_{\rm N}(\varepsilon)d\varepsilon \ . \tag{2.3}$$

Therefore, we can obtain the quasiparticle density of states:

$$N_{\rm S}(E) = N_{\rm N}(\varepsilon)\frac{d\varepsilon}{dE} \ . \tag{2.4}$$

Because we are largely interested in energy ε only a few millielectron volts from Fermi energy, we can take $N_{\rm N}(\varepsilon) = N_{\rm N}(0)$. Using (2.2), the above equation leads to

$$N_{\rm S}(E) = N_{\rm N}(0)\frac{d\varepsilon}{dE} = \begin{cases} N_{\rm N}(0)\frac{E}{\sqrt{E^2-\Delta^2}} \ , & (E > \Delta) \\ 0. & (E < \Delta) \end{cases} \tag{2.5}$$

There are no quasiparticle states allowed for $E < \Delta$, *i.e.*, in the gap. It's worth noting that a divergent state density occurs just above $E = \Delta$, as indicated in Fig. 2.1. This divergence is responsible for the highly non-linear SIS IV curve as we shall see later.

Temperature dependence of Δ

According to BCS theory, the gap Δ at zero temperature is related to the superconductor's critical temperature:

$$\Delta(0) = 1.76 \ k_{\rm B}T_{\rm C} \ , \tag{2.6}$$

where $k_{\rm B}$ is the Boltzmann constant. The temperature dependence of the gap energy can be represented to a good approximation by

$$\frac{\Delta(T)}{\Delta(0)} = \sqrt{\cos(\frac{\pi}{2}\frac{T}{T_{\rm C}} \ ,)} \tag{2.7}$$

as shown in Fig. 2.2. Nb has a critical temperature of 9.2 K, corresponding to a gap voltage ($2\Delta \sim eV_{\rm gap}$) 3.0 mV and a gap frequency ($2\Delta \sim h\nu$) about 700 GHz.

Penetration depth and coherence length

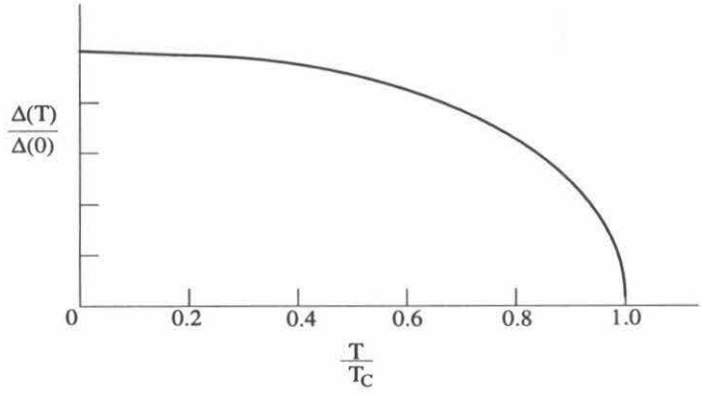

Figure 2.2: Superconducting energy gap as a function of temperature.

In 1933 Meissner found that the magnetic field is excluded from a superconductor. London (1935) gave a phenomenological description of the basic electrodynamic properties of a superconductor. He related the current density to the magnetic field by

$$\Delta \times \vec{J} = \frac{-1}{\mu_0 \lambda_L^2} \vec{B} \ , \tag{2.8}$$

which, along with Ampere's law, indicates that $\vec{B}$ falls off exponentially inside the superconductor. The penetration depth of the field is λ_L, referred to as the London penetration depth. λ_L for typical superconductors at $T = 0$ K lies in the region of 10 to 1000 nm. Its dependence on temperature is approximated by

$$\frac{\lambda_L(T)}{\lambda_L(0)} \approx \frac{1}{\sqrt{1 - (\frac{T}{T_C})^4}} \ . \tag{2.9}$$

Besides the London penetration depth, there is another important characteristic length, called the coherence length. This is the average separation distance between the two electrons forming a Cooper pair. At this distance the Coulomb repulsive force and the phonon-mediated attractive force are comparable. The coherence length can be estimated by an uncertainty-principle argument (Tinkham 1975): $\Delta x \gtrsim \hbar/\Delta p \approx$

$\hbar v_F / k_B T_C$, where v_F is the Fermi velocity. BCS microscopic theory shows that the intrinsic coherence length is given by

$$\xi_0 = 0.18 \frac{\hbar v_F}{k_B T_C} . \tag{2.10}$$

Pippard (Pippard 1953) deduced that the coherence length was reduced by the presence of impurities. He suggested an empirical relation for the reduced coherence length:

$$\frac{1}{\xi_{co}} = \frac{1}{\xi_0} + \frac{1}{l} , \tag{2.11}$$

where l is the electron mean free path. ξ_{co} is called the Pippard coherence length.

ξ_0 is typically 5 to 100 nm for conventional superconductors like Pb, Nb or NbN, and less than 1 nm for high-T_C materials like YBaCuO.

2.2 Semiconductor picture of SIS tunnel junctions

As mentioned in the last section, the quasiparticle excitation spectrum in a superconductor is highly analogous to the electronic density of states in a semiconductor, as shown in Fig 2.3. The ground state of the superconductor is like the ground state of a semiconductor, with a filled valence-like band and empty conduction-like band indicating the absence of quasiparticle excitations. The first excited state of the system is described by the promotion of an electron from the top of the valence band to the bottom of the conduction band by giving it an energy 2Δ. Two particles are created, a hole-like particle in the valence band and an electron-like particle in the conduction band. Since there are always equal numbers of electron-like and hole-like excitations, the superconductor is analogous to an intrinsic semiconductor, and the Fermi energy μ lies exactly centered in the 2Δ energy gap. The semiconductor picture is very successful in understanding most of the quasiparticle effects in superconductors, especially those which describe radiation detection by SIS junctions.

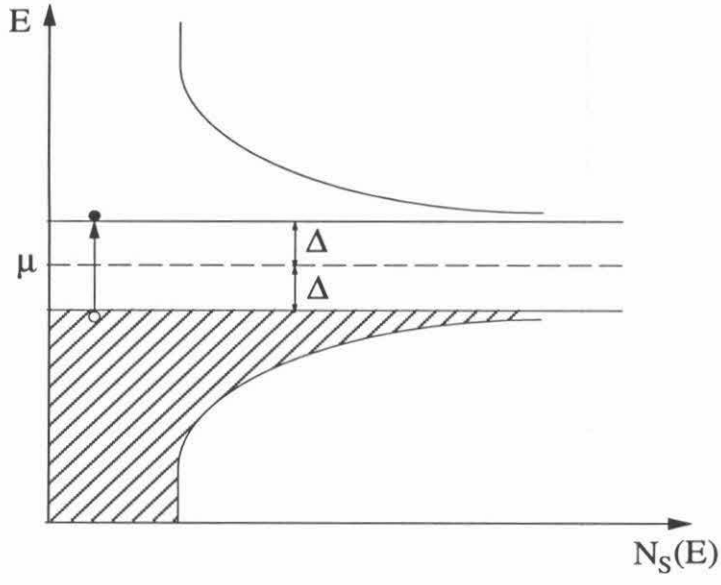

Figure 2.3: Semiconductor energy diagram for superconducting quasiparticles.

The dc *IV* characteristic of SIS junctions

In an SIS junction two superconductors are separated by an insulating layer. The two superconducting layers, in general, may be of different materials, but often they will be the same. The insulation is so thin, typically 10 to 20 Å, that the wavefunctions of electrons on either side have a significant overlap in the insulator. As a result, electrons and Cooper pairs can tunnel from one side of the barrier to the other. Because the insulators typically present a $\sim$0.5 eV barrier to the electrons, tunneling is the only significant current source at the bias voltages ($<$ 10 mV) and temperature ($<$ 5 K) at which the junctions are operated. The semiconductor energy level diagram for an SIS junction is presented in Fig. 2.4. If no bias voltage is applied to the junction, Fermi levels for electrons in the "left" and "right" superconductors, $\mu_{\rm L}$ and $\mu_{\rm R}$, are equal. If a bias voltage exists across the junction, the Fermi level for one side is shifted with respect to the other, $\mu_{\rm R} = \mu_{\rm L} + eV_0$, as shown in Fig. 2.4. We

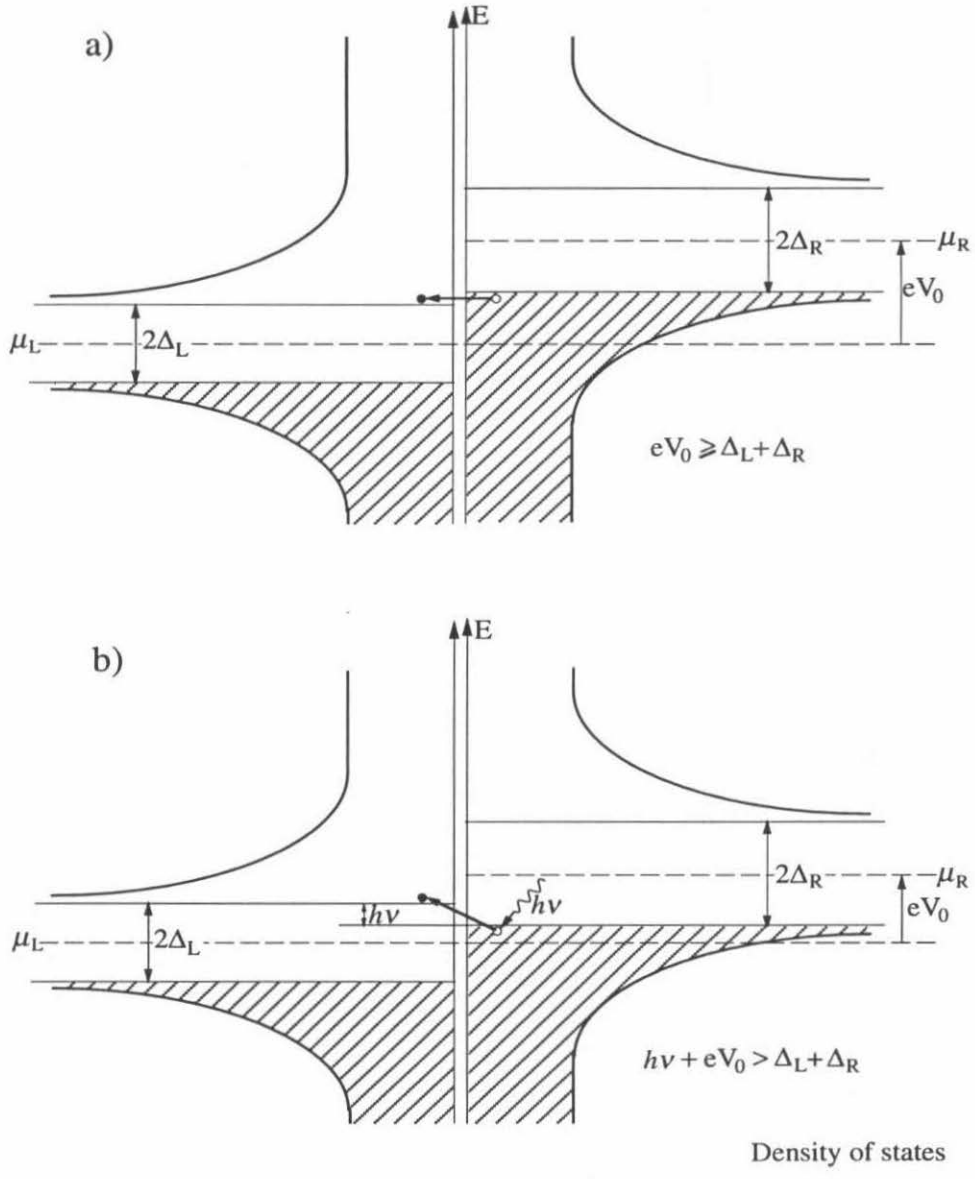

Figure 2.4: Semiconductor picture for an SIS tunneling junction. a) quasiparticle tunneling at the same energy level; b) photon assisted tunneling.

define the gap voltage $V_{\rm gap}$ as

$$V_{\rm gap} \equiv \frac{1}{e}(\Delta_{\rm L} + \Delta_{\rm R}) \ . \tag{2.12}$$

When there is no interaction with another particle (like a photon or phonon), the electron tunneling through the barrier must conserve energy. Thus an electron in one state can only tunnel to an empty state on the other side if the two states are at the same energy. At $T = 0$ K (*i.e.*, ignoring thermal excitations), if the bias voltage V_0 is smaller than $V_{\rm gap}$, there is no current through the junction. When V_0 is increased to be equal to $V_{\rm gap}$ (as shown in Fig 2.4a), there is a sudden onset and sharp increase of current. This sharp increase is due to the divergent density of states just below the gap for electron-like quasiparticles and above the gap for the hole-like quasiparticles. The direct current through the junction can be calculated as (Tinkham 1975)

$$I(V_0) = \text{const} \int_{-\infty}^{\infty} \frac{dN_{\rm S}(E)}{dE} \frac{dN_{\rm S}(E+eV_0)}{dE} \big[f(E+eV_0) - f(E)\big] dE \ , \tag{2.13}$$

where $N_{\rm S}$ is the density of states given by (2.5) and $f(E)$ is Fermi distribution given by (2.1). The dc IV curve calculated by (2.13) is presented in Fig. 2.5a.

Photon assisted tunneling in SIS junctions

In the presence of a radiation field, an electron-like quasiparticle can absorb a photon energy $h\nu$ and tunnel through the barrier, as shown schematically in Fig. 2.4b. Current will thus flow at a bias voltage lower than $V_{\rm gap}$. Tunneling is possible if $V_0 + nh\nu/e \geq V_{\rm gap}$, where n is an integer corresponding to the number of photons absorbed by a quasiparticle. The absorption probability decreases rapidly as the photon number increases. Current steps are expected in the dc IV curve at bias voltages $V_0 = V_{\rm gap} - nh\nu/e$, as shown in Fig. 2.5b. These steps are known as photon-assisted tunneling steps, and were first observed and explained by Dayem and Martin in 1962 (Dayem & Martin 1962). We can understand the photon steps below and above the gap voltage by considering first that only one photon is absorbed or emitted.

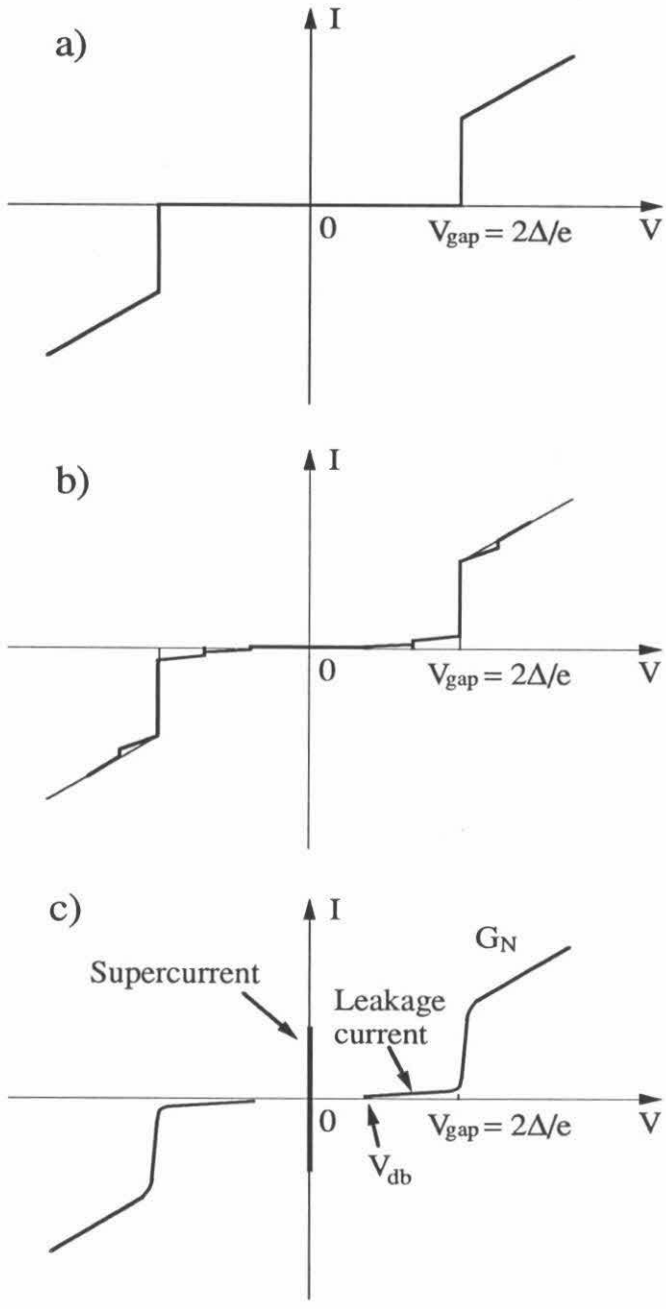

Figure 2.5: SIS IV characteristics. a) Ideal dc IV curve at 0 K, calculated from (2.13). b) Photon-assisted tunneling, the IV curve showing photon steps below and above the gap voltage. c) A more realistic model SIS IV curve, showing features such as the supercurrent, the dropback voltage, the smoothed gap voltage, and the leakage current below the gap.

When the bias voltage is increased from zero, the current remains zero up to $V_0 = V_{\rm gap} - h\nu/e$ where a sharp rise in current takes place due to electrons at the top of filled band which can now absorb a photon and tunnel into the empty states near the bottom of the empty band. The sharp rise is a result of the large density of states at the gap edges. The current will continue to rise until $V_0 = V_{\rm gap}$. For $V_0 > V_{\rm gap}$, the current is less than its corresponding value in the absence of the radiation field. Here an electron which absorbs a photon will make a transition to a higher energy level where the density of states is lower than that near the bottom of the band. However, when $V_0 > V_{\rm gap} + h\nu/e$, emission as well as absorption of a photon is possible. The current rises sharply at $V_0 = V_{\rm gap} + h\nu/e$ because now an electron from the top of the filled band can tunnel into a state near the bottom of the empty band after the emission of a photon.

For a bias voltage $V_0 < V_{\rm gap}$, the semiconductor picture of SIS indicates that only photons with energy $h\nu \geq eV_{\rm gap} - eV_0$ will induce tunneling current if multi-photon absorption is ignored. On the other hand, if the energy of the photon is so high, $h\nu \geq eV_{\rm gap} + eV_0$, that electrons on either side of the barrier can tunnel into the other side by absorbing a photon, the net current will be reduced. Therefore, one expects that an SIS junction biased at V_0 responds effectively only to radiation in the frequency range $e(V_{\rm gap} - V_0) < h\nu < e(V_{\rm gap} + V_0)$. When the junction is biased right below the gap voltage, the response has largest frequency range $0 < h\nu < 2V_{\rm gap}$.

Comments on Josephson pair tunneling

The semiconductor picture is very useful in explaining quasiparticle-related phenomena in SIS junctions, but it does not deal with Cooper pairs, which are also present in the tunneling current in an SIS. Fig. 2.5c shows a stylized version of a measured SIS IV curve when no magnetic field is applied to the SIS junction. Besides the smeared turn-on voltage and the subgap leakage current which are due to non-perfect barrier material or thermal excitations of quasiparticles, the different features of the IV are the current at zero bias voltage and the dropback voltage $V_{\rm db}$.

Below $V_{\rm db}$ no stable bias is available and the junction switches to zero voltage. Both the supercurrent and the dropback voltage are due to Cooper pair tunneling.

The phenomenon that supercurrent can flow through the junction at zero bias voltage was first predicted by Josephson in 1962 (Josephson 1962) and is known as dc Josephson effect. The Cooper pair tunneling current is described by equations

$$\begin{aligned} I &= I_{\rm C} \sin\phi \ , \\ \frac{d\phi}{dt} &= \frac{2eV}{h} \ , \end{aligned} \tag{2.14}$$

where ϕ is the difference in the macroscopic phase of the superconductor wavefunctions across the barrier. V is the voltage across the barrier. $I_{\rm C}$, called the critical current, is a constant determined by the barrier and junction area according to microscopic theory as

$$I_{\rm C} = \frac{1}{R_{\rm N}} \frac{\pi\Delta}{2e} \tanh \frac{\Delta}{2k_{\rm B}T} \approx \frac{\pi}{4} \frac{V_{\rm gap}}{R_{\rm N}} \ , \tag{2.15}$$

where $R_{\rm N}$ is the normal state resistance of the SIS junction.

At zero voltage, ϕ can take on any value, and the supercurrent can vary between $-I_{\rm C}$ and $+I_{\rm C}$. If the junction is biased at a voltage V_0, $\phi = \phi_0 + 2eV_0t/h$, and the current will oscillate at a frequency $\nu = 2eV_0/h$. This is referred to as the ac Josephson effect.

The dropback voltage is caused by the Josephson oscillations. At a small bias voltage, the voltage amplitude induced by the Josephson current oscillation might be larger than the bias voltage and the junction would switch to the zero-bias because the zero voltage state is a lower energy state than the finite voltage state. At larger bias voltages, the oscillations are at higher frequencies and will be shunted out by the junction capacitance; therefore, large bias voltages will be stable. In a mixer, if the local oscillator causes the ac bias to enter the unstable dropback region, the mixer will be very noisy.

Magnetic field is often used to suppress the undesired pair tunneling in an SIS quasiparticle mixer. This is done based on the fact that I_C is a function of the magnetic flux Φ threaded through the barrier region:

$$I_C = I_C(0)\left|\frac{\sin(\pi\Phi/\Phi_0)}{\pi\Phi/\Phi_0}\right| , \tag{2.16}$$

where $\Phi_0 = h/2e$ is the magnetic flux quantum. To fully suppress the Josephson effect, one quantum flux should be threaded through the barrier region. The magnetic field necessary is roughly $B = \Phi_0/t(d + 2\lambda)$, where t is the length of the junction size perpendicular to the direction of B, d is the barrier thickness and λ is the magnetic penetration depth. For a 1 μm $\times$ 1 μm junction with a penetration depth of 100 nm and a barrier that is 1 nm thick, the magnetic field needed is $\sim 10^2$ Gauss. For very small junctions, the magnetic field needed can be large enough to reduce the gap or even destroy the bulk superconductivity of the junction.

2.3 Heterodyne theory for SIS mixers

2.3.1 Current in an SIS junction

Tucker (Tucker 1979) derived the quasiparticle tunneling current in SIS using the transfer Hamiltonian introduced by Cohen *et al.* (Cohen *et al.* 1962). The interaction between the two electrodes across the barrier is described by the transfer Hamiltonian:

$$\begin{aligned} H_T &= \sum_{k,q} T_{kq} c_k^\dagger c_q + \sum_{k,q} T_{kq}^* c_q^\dagger c_k \\ &= H_T^+ + H_T^- \ . \end{aligned} \tag{2.17}$$

Here c_k and c_q are the annihilation operators representing Bloch states for electrons on the left and right sides of the junction, respectively. T_{kq} is the matrix element for tunneling from the q state on the right side to the k state on the left. H_T^+ contains terms which describe tunneling from right to left while the terms in H_T^- carry current in the opposite direction.

In the absence of direct voltage and ac signal, the Hamiltonians for the left and right electrodes are

$$\begin{aligned} H_{\mathrm{L}}^{0} &= \sum_{k} E_k c_k^{\dagger} c_k \ , \\ H_{\mathrm{R}}^{0} &= \sum_{q} E_q c_q^{\dagger} c_q \ . \end{aligned} \tag{2.18}$$

With a voltage $V(t)$ across the junction, the Fermi level for electrons in the right electrode is raised above that in the left electrode, so that now the Hamiltonian for the right side is

$$\begin{aligned} H_{\mathrm{R}} &= \sum_{q} \big(E_q + eV(t)\big) c_q^{\dagger} c_q \\ &= H_{\mathrm{R}}^{0} + eV(t) N_{\mathrm{R}} \ , \end{aligned} \tag{2.19}$$

where $N_{\mathrm{R}} = \sum_q c_q^{\dagger} c_q$ is the number operator for electrons in the right electrode. The total Hamiltonian for the system is then

$$H = H_{\mathrm{L}}^{0} + H_{\mathrm{R}}^{0} + eV(t) N_{\mathrm{R}} + H_{\mathrm{T}} \ . \tag{2.20}$$

The current is obtained by calculating the time derivative of the number operator:

$$\begin{aligned} I = e\frac{dN_{\mathrm{L}}}{dt} &= \frac{ie}{\hbar}\big[H_{\mathrm{T}}, N_{\mathrm{L}}\big] \\ &= \frac{ie}{\hbar}(H_{\mathrm{T}}^{+} - H_{\mathrm{T}}^{-}) \ . \end{aligned} \tag{2.21}$$

It is assumed that the potential term $eV(t)N_{\mathrm{R}}$ modulates the energy level of each electron on the right side sufficiently slowly that the only impact of the applied potential on the uncoupled system appears as a simple phase modulation of all right-side single particle operators through the phase factor $W(\omega)$, which is defined by:

$$\int_{-\infty}^{\infty} d\omega' W(\omega') e^{-i\omega' t} \equiv \exp\Big[-\frac{ie}{\hbar}\int^{t} dt' [V(t') - V_0]\Big] \ . \tag{2.22}$$

The expectation value for the total current is found to be

$$\langle I(t)\rangle = \mathrm{Im}\int_{-\infty}^{\infty} d\omega' d\omega'' W(\omega')W^*(\omega'')e^{-i(\omega'-\omega'')t} j(V_0+\hbar\omega'/e)\ . \tag{2.23}$$

This is the quasiparticle part of the whole current in a superconducting tunnel junction derived by Werthamer in 1966 (Werthamer 1966). $j(V)$ is a complex function, called the current response function. For the special case of a time-independent potential, we will have $W(\omega) = \delta(\omega)$, and the left side of (2.23) must be the dc IV, so

$$I_{\mathrm{dc}}(V_0) = \mathrm{Im}\ j(V_0)\ . \tag{2.24}$$

Thus $\mathrm{Im}j(V)$ may be directly measured. The real part of the response function $\mathrm{Re}j(V)$ characterizes the reactive portion of the tunneling current, and it can be related to the dissipative part $\mathrm{Im}j(V)$ through a Kramers-Kronig transform:

$$I_{\mathrm{KK}}(V) \equiv \mathrm{Re}\ j(V) = P\int_{-\infty}^{\infty}\frac{dx}{\pi}\frac{I_{\mathrm{dc}}(x)-x/R_{\mathrm{N}}}{x-V}\ . \tag{2.25}$$

Here R_{N} is the junction normal resistance and P indicates that Cauchy principal value is taken.

We can see that the ac response of an SIS junction is completely characterized by (2.22) - (2.25). We do not need to resort to microscopic theory for the determination of $\mathrm{Im}j(V)$ and $\mathrm{Re}j(V)$. The entire physical response for a particular junction is contained in its measured dc IV characteristic. In practice, once the measured I_{dc} is obtained, the reactive response I_{KK} can be calculated numerically.

We now derive the current expressions of SIS junctions under the imposition of a monochromatic radiation field with frequency ω. We assume that the only sinusoidal ac voltage that needs to be considered is the applied local oscillator (LO) at ω, and we ignore the complicated large-amplitude LO waveform problem which involves all harmonics of the LO (Tucker & Feldman 1985). This simplification is justified for most

SIS junctions since the large geometrical capacitance shorts out higher harmonics of the LO. The time-dependent voltage across the junction is thus

$$V(t) = V_0 + V_{\rm LO}\cos\omega t \ . \tag{2.26}$$

Solving (2.22) and (2.23), the induced tunneling current is found to be:

$$\begin{aligned} I_{\rm LO}(t) &= {\rm Im} \sum_{n,m=-\infty}^{\infty} J_n(\alpha) J_{n+m}(\alpha) e^{im\omega t} j(V_0 + n\hbar\omega/e) \\ &= a_0 + \sum_{m=1}^{\infty} (2a_m \cos m\omega t + 2b_m \sin m\omega t) \ , \end{aligned} \tag{2.27}$$

where J_n is the n-th Bessel function of the first kind and

$$\alpha = eV_{\rm LO}/\hbar\omega \ . \tag{2.28}$$

α is a measure of the LO pumping intensity. The current induced by the LO contains all components at various harmonics with amplitudes

$$\begin{aligned} 2a_m &= \sum_{n=-\infty}^{\infty} J_n(\alpha)[J_{n+m}(\alpha) + J_{n-m}(\alpha)] I_{\rm dc}(V_0 + n\hbar\omega/e) \ , \\ 2b_m &= \sum_{n=-\infty}^{\infty} J_n(\alpha)[J_{n+m}(\alpha) - J_{n-m}(\alpha)] I_{\rm KK}(V_0 + n\hbar\omega/e) \ . \end{aligned} \tag{2.29}$$

The pumped dc IV characteristic is given by a_0:

$$I_{\rm dc}(V_0, V_{\rm LO}) = a_0 = \sum_{n=-\infty}^{\infty} J_n^2(\alpha) I_{\rm dc}(V_0 + n\hbar\omega/e) \ . \tag{2.30}$$

The dissipative, in phase current $I'_{\rm LO}$ at the LO frequency ω is given by $2a_1$:

$$I'_{\rm LO} = 2a_1 = \sum_{n=-\infty}^{\infty} J_n(\alpha)[J_{n-1}(\alpha) + J_{n+1}(\alpha)] I_{\rm dc}(V_0 + n\hbar\omega/e) \ . \tag{2.31}$$

The reactive current component $I''_{\rm LO}$ is given by $2b_1$:

$$I''_{\rm LO} = 2b_1 = \sum_{n=-\infty}^{\infty} J_n(\alpha)[J_{n-1}(\alpha) - J_{n+1}(\alpha)]I_{\rm KK}(V_0 + n\hbar\omega/e) \ . \tag{2.32}$$

2.3.2 Heterodyne mixing in SIS junctions

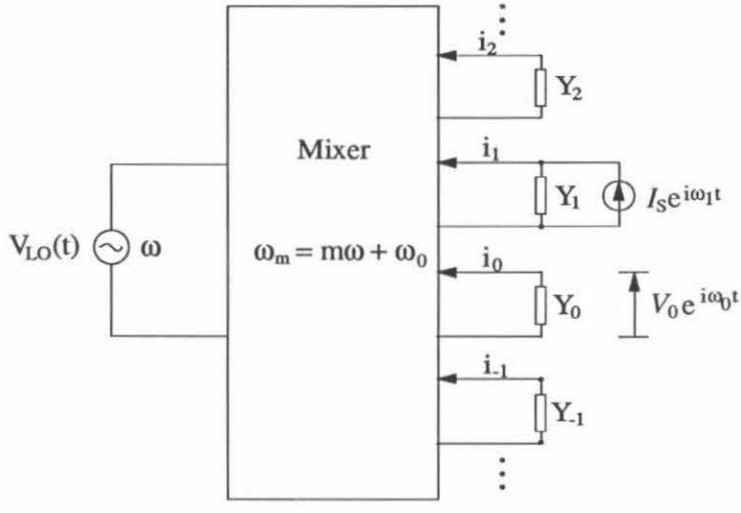

Figure 2.6: Schematic diagram of a heterodyne mixer, with applied LO frequency ω, signal frequency $\omega_S = \omega_1$, and IF output at ω_0. The equivalent embedding networks at all of the sideband frequencies $\omega_m = m\omega + \omega_0$ are indicated, with termination admittances Y_m.

A full mixer analysis including all the sidebands requires the Y-matrix formalism introduced by Torrey and Whitmer (Torrey & Whitmer 1948). Below we will first describe the compact explanation of this formalism presented by Tucker (Tucker 1979).

Fig. 2.6 shows a linear multi-port network representing a heterodyne mixer. Strong pumping at the LO frequency ω mixes the output IF frequency ω_0 with all sidebands,

$$\omega_m = m\omega + \omega_0, \qquad m = 0, \pm 1, \pm 2, ... \tag{2.33}$$

Each of these sidebands is represented in Fig. 2.6 by a mixer port with a termination admittance Y_m. The incoming signal at frequency $\omega_s = \omega_1$ is represented by a current generator $\mathcal{I}_s$ with a source admittance $Y_s = Y_1$. The function of the mixer is to convert this incoming signal power to the output frequency ω_0, and couple it into the load admittance $Y_L = Y_0$, *i.e.*, the input admittance of the IF amplifier.

The sideband current phasor i_m and voltage phasor v_m are linearly related for small signals by an admittance matrix

$$i_m = \sum_{m'} Y_{mm'} v_{m'} \ . \tag{2.34}$$

$Y_{mm'}$ is determined by the LO voltage waveform and the dc IV of the mixer. If an arbitrary set of current generators $\{\mathcal{I}_m\}$ are placed at each sideband port ω_m, then

$$\begin{aligned} \mathcal{I}_m &= i_m + Y_m v_m \\ &= \sum_{m'} (Y_{mm'} + Y_m \delta_{m,m'}) v_{m'} \ . \end{aligned} \tag{2.35}$$

Inverting these equations, the signal voltages produced by the current generators are obtained:

$$v_m = \sum_{m'} Z_{mm'} \mathcal{I}_{m'} \ , \tag{2.36}$$

where matrix $|Z_{mm'}|$ is the inverse of matrix $|Y_{mm'} + Y_m \delta_{mm'}|$. In particular, the output voltage at IF band ω_0 may be written in the form

$$v_0 = Z_{00} \sum_{m} \lambda_{0m} \mathcal{I}_m \ , \tag{2.37}$$

where $\lambda_{0m} = Z_{0m}/Z_{00}$ does not depend on the output load termination Y_0.

Now let's look at the conversion gain of a fundamental mixer. The available input power at the signal sideband ω_s is

$$P_{\text{in}} = \frac{|\mathcal{I}_s|^2}{8G_S} \ . \tag{2.38}$$

The output power delivered to the load at the IF sideband ω_0 is

$$P_{\text{out}} = \frac{1}{2}G_L|v_0|^2 = \frac{1}{2}G_L|Z_{01}|^2|\mathcal{I}_s|^2 \ . \tag{2.39}$$

The conversion gain is defined as the ratio of the two powers:

$$L^{-1} = \frac{P_{\text{out}}}{P_{\text{in}}} = 4G_S G_L|Z_{01}|^2 \ . \tag{2.40}$$

Here G_S and G_L represent the real parts of the source and load admittances Y_S and Y_L, respectively. The above expressions are for single sideband (SSB) mixers.

With this Y-matrix formalism laid out, what we need next is the small signal matrix $Y_{mm'}$ for an LO pumped SIS junction. The total voltage and current across the tunnel barrier in the presence of small signals can be written in the form

$$\begin{aligned} V(t) &= V_0 + V_{\text{LO}}(t) + \text{Re} \sum_{m=-\infty}^{\infty} v_m e^{+i\omega_m t} \ , \\ \langle I(t) \rangle &= I_{\text{LO}}(t) + \sum_{m=-\infty}^{\infty} i_m e^{+i\omega_m t} \ . \end{aligned} \tag{2.41}$$

The inclusion of $\sum v_m e^{+i\omega_m t}$ in the applied potential requires new terms in the phase factor $W(\omega)$. Retaining only terms to first order in v_m when solving $W(\omega)$ and the total current, the admittance matrix is found to be

$$Y_{mm'} = G_{mm'} + iB_{mm'} \ , \tag{2.42}$$

where

$$G_{mm'} = \frac{e}{2\hbar\omega_{m'}} \sum_{n,n'=-\infty}^{\infty} J_n(\alpha) J_{n'}(\alpha) \delta_{m-m',n'-n} \times \{[I_{\rm dc}(V_0 + n'\hbar\omega/e + \hbar\omega_{m'}/e) - I_{\rm dc}(V_0 + n'\hbar\omega/e)] + [I_{\rm dc}(V_0 + n\hbar\omega/e) - I_{\rm dc}(V_0 + n\hbar\omega/e - \hbar\omega_{m'}/e)]\} , \tag{2.43}$$

and

$$B_{mm'} = \frac{e}{2\hbar\omega_{m'}} \sum_{n,n'=-\infty}^{\infty} J_n(\alpha) J_{n'}(\alpha) \delta_{m-m',n'-n} \times \{[I_{\rm KK}(V_0 + n'\hbar\omega/e + \hbar\omega_{m'}/e) - I_{\rm KK}(V_0 + n'\hbar\omega/e)] - [I_{\rm KK}(V_0 + n\hbar\omega/e) - I_{\rm KK}(V_0 + n\hbar\omega/e - \hbar\omega_{m'}/e)]\} . \tag{2.44}$$

The admittance matrix elements separate into real and imaginary parts, which depend only upon the dissipative and reactive components, respectively, of the junction response. In other words, the conductance elements are determined by the dc IV characteristic and the susceptance elements by the Kramers-Kronig transform of dc IV. The matrix elements depend on the strength of the local oscillator through the parameter α.

The noise properties of a mixer can also be described using the multiport network. There are two noise sources, the image sideband terminations which have thermal noise and the LO pump current which gives rise to shot noise. Since the object of the heterodyne mixer is to overcome all the other noise sources with LO current, we will not consider thermal noise from terminations here. As seen in the last section, the combination of dc bias and LO waveform produce large tunneling current at frequency multiples $m\omega$ of the LO drive. Because this current results from the tunneling of individual quasiparticles, fluctuations about the average will produce shot noise currents at other frequencies; and some of this shot noise will be mixed into the output of the mixer. If a set of current noise source $\{\mathcal{I}_{Nm}\}$ can be found at each port to represent the noise caused by the tunneling current, then the noise

power coupled into the IF load is

$$\begin{aligned} P_{\text{noise}} &= G_{\text{L}}\langle v_0 v_0^* \rangle \\ &= G_{\text{L}} \sum_{m,m'} Z_{0m} Z_{0m'} \langle \mathcal{I}_{Nm} \mathcal{I}_{Nm'}^* \rangle \\ &= G_{\text{L}} \sum_{m,m'} Z_{0m} Z_{0m'} H_{mm'} \ . \end{aligned} \tag{2.45}$$

$H_{mm'}$ is called the current correlation matrix.

Tucker (Tucker 1979) derived the correlation matrix for SIS junction and found the mixer noise temperature $T_{\text{mix}}^{\text{LO}}$ in the form

$$k_{\text{B}} T_{\text{mix}}^{\text{LO}} = \frac{1}{4 G_{\text{S}} |\lambda_{01}|^2} \sum_{m,m'} \lambda_{0m} \lambda_{0m'}^* H_{mm'} \ , \tag{2.46}$$

where the current correlation matrix is expressed as

$$\begin{aligned} H_{mm'} =& e \sum_{n,n'=-\infty}^{\infty} J_n(\alpha) J_{n'}(\alpha) \delta_{m-m',n'-n} \\ & \times \{ \coth[(eV_0 + n'\hbar\omega + \hbar\omega_{m'})/2k_{\text{B}}T] I_{\text{dc}}(V_0 + n'\hbar\omega/e + \hbar\omega_{m'}/e) \\ & + \coth[(eV_0 + n\hbar\omega - \hbar\omega_{m'})/2k_{\text{B}}T] I_{\text{dc}}(V_0 + n\hbar\omega/e - \hbar\omega_{m'}/e) \} \ . \end{aligned} \tag{2.47}$$

This contribution $T_{\text{mix}}^{\text{LO}}$ to the total mixer noise is due to shot noise generated by the tunneling current. The thermal noise due to sideband resistive terminations is ignored. One additional noise source not included is the "quantum noise" due to uncertainty principle. The quantum noise sets a lower bound to the mixer noise temperature $T_{\text{mix}}^{\text{QM}} = \hbar\omega/k_{\text{B}}$ for a SSB mixer.

2.3.3 Three-port approximations

The matrix given in last section includes elements for all possible sidebands. In practice, since all the higher frequency sidebands are considered shorted (which is a good approximation for an SIS junction with large capacitance), the mixer will include only three ports: the signal, output, and image at frequencies ω_1, ω_0, and

$-\omega_{-1}$, respectively. Equation (2.34) thus becomes

$$\begin{pmatrix} i_1 \\ i_0 \\ i_{-1} \end{pmatrix} = \begin{pmatrix} Y_{11}+Y_1 & Y_{10} & Y_{1-1} \\ Y_{01} & Y_{00}+Y_0 & Y_{0-1} \\ Y_{-11} & Y_{-10} & Y_{-1-1}+Y_{-1} \end{pmatrix} \begin{pmatrix} v_1 \\ v_0 \\ v_{-1} \end{pmatrix}$$

where Y_1, Y_0 and Y_{-1} are the source admittance, the IF load admittance and image admittance, respectively. For a double-sideband mixer, the source and image have same admittance, so $Y_1 = Y_{-1}^* = Y_S = G_S + iB_S$, where Y_S is the source admittance. The conjugate on Y_{-1} is due to the fact that a negative frequency is defined for the image sideband.

In practice, the IF frequency ω_0 is much smaller compared to the LO frequency ω, such that we can make approximation $\omega_1 \approx -\omega_{-1} \approx \omega$ and assume $\hbar\omega_0/e$ is so small that the response of the tunnel barrier at the output frequency is essentially classical. Under this approximation, the nine matrix elements $Y_{mm'}$ and $H_{mm'}$ can be simplified to

$$\begin{aligned}
G_{00} &= \sum_{n=-\infty}^{\infty} J_n^2(\alpha) \frac{d}{dV_0} I_{dc}(V_0 + n\hbar\omega/e), \\
G_{10} = G_{-10} &= \frac{1}{2} \sum_{n=-\infty}^{\infty} J_n(\alpha)[J_{n-1}(\alpha) + J_{n+1}(\alpha)] \frac{d}{dV_0} I_{dc}(V_0 + n\hbar\omega/e), \\
G_{01} = G_{0-1} &= \frac{e}{\hbar\omega} \sum_{n=-\infty}^{\infty} J_n(\alpha)[J_{n-1}(\alpha) - J_{n+1}(\alpha)] I_{dc}(V_0 + n\hbar\omega/e), \\
G_{11} = G_{-1-1} &= \frac{e}{2\hbar\omega} \sum_{n=-\infty}^{\infty} [J_{n-1}^2(\alpha) - J_{n+1}^2(\alpha)] I_{dc}(V_0 + n\hbar\omega/e), \\
G_{1-1} = G_{-11} &= \frac{e}{2\hbar\omega} \sum_{n=-\infty}^{\infty} J_n(\alpha)[J_{n-2}(\alpha) - J_{n+2}(\alpha)] I_{dc}(V_0 + n\hbar\omega/e),
\end{aligned} \tag{2.48}$$

and

$$
\begin{aligned}
B_{00} &= B_{01} = B_{0-1} = 0, \\
B_{10} &= -B_{-10} = \frac{1}{2}\sum_{n=-\infty}^{\infty} J_n(\alpha)[J_{n-1}(\alpha) - J_{n+1}(\alpha)]\frac{d}{dV_0} I_{\mathrm{KK}}(V_0 + n\hbar\omega/e), \\
B_{11} &= -B_{-1-1} = \frac{e}{2\hbar\omega}\sum_{n=-\infty}^{\infty} [J_{n-1}^2(\alpha) - 2J_n^2(\alpha) + J_{n+1}^2(\alpha)] I_{\mathrm{KK}}(V_0 + n\hbar\omega/e), \\
B_{1-1} &= -B_{-11} = \frac{e}{2\hbar\omega}\sum_{n=-\infty}^{\infty} [J_{n-2}(\alpha)J_n(\alpha) - 2J_{n-1}(\alpha)J_{n+1}(\alpha) + J_n(\alpha)J_{n+2}(\alpha)] \\
&\qquad \times I_{\mathrm{KK}}(V_0 + n\hbar\omega/e),
\end{aligned}
\tag{2.49}
$$

and

$$
\begin{aligned}
H_{00} &= 2e\sum_{n=-\infty}^{\infty} J_n^2(\alpha)\coth[(eV_0 + n\hbar\omega)/2k_{\mathrm{B}}T] I_{\mathrm{dc}}(V_0 + n\hbar\omega/e), \\
H_{10} &= H_{-10} = H_{01} = H_{0-1} = e\sum_{n=-\infty}^{\infty} J_n(\alpha)[J_{n-1}(\alpha) + J_{n+1}(\alpha)] \\
&\qquad \times \coth[(eV_0 + n\hbar\omega)/2k_{\mathrm{B}}T] I_{\mathrm{dc}}(V_0 + n\hbar\omega/e), \\
H_{11} &= H_{-1-1} = e\sum_{n=-\infty}^{\infty} [J_{n-1}^2(\alpha) + J_{n+1}^2(\alpha)]\coth[(eV_0 + n\hbar\omega)/2k_{\mathrm{B}}T] \\
&\qquad \times I_{\mathrm{dc}}(V_0 + n\hbar\omega/e), \\
H_{1-1} &= H_{-11} = 2e\sum_{n=-\infty}^{\infty} [J_{n-1}(\alpha)J_{n+1}(\alpha)]\coth[(eV_0 + n\hbar\omega)/2k_{\mathrm{B}}T] I_{\mathrm{dc}}(V_0 + n\hbar\omega/e).
\end{aligned}
\tag{2.50}
$$

We employ these equations to estimate our double sideband mixer properties. First we obtain the unpumped and pumped dc IV curves, and deduce the parameter α, *i.e.*, the strength of LO pumping. Numerical analysis will then yield information on the mixer's gain and noise.

2.3.4 Comments on quantum effects

Having described the quantum theory for SIS mixers, we now look at some phenomena that are unique to quantum mixers. All these phenomena can be observed only in the

high-frequency quantum regime when the photon energy $\hbar\omega/e$ is large compared to the voltage width of the dc nonlinearity. Tucker has shown that the classical results will be resumed if $\hbar\omega/e$ is small compared to the voltage scale of the dc nonlinearity.

Mixer input admittance

An SIS mixer presents admittances to LO, signal and image sidebands. In a practical doube-sideband mixer, these admittances tend to have similar values. We define the input RF admittance as the admittance the mixer presents to the LO,

$$Y_{\rm RF} = \frac{I_{\rm LO}}{V_{\rm LO}} \ . \tag{2.51}$$

$Y_{\rm RF}$ is independent of sideband terminations and the IF load admittance. Since $I_{\rm LO}$ has dissipative and reactive components as pointed out by (2.31) and (2.32), the RF input admittance has non-zero susceptance, which is a quantum effect. When the LO voltage is smaller than the photon step, $V_{\rm LO} < \hbar\omega/e$, *i.e.*, $\alpha < 1$, $Y_{\rm RF}$ can be approximated from (2.31) and (2.32):

$$\begin{aligned} Y_{\rm RF} = & \ \frac{I_{\rm dc}(V_0 + \hbar\omega/e) - I_{\rm dc}(V_0 - \hbar\omega/e)}{2\hbar\omega/e} \\ & + i \ \frac{I_{\rm KK}(V_0 + \hbar\omega/e) - 2I_{\rm KK}(V_0) + I_{\rm KK}(V_0 - \hbar\omega/e)}{2\hbar\omega/e} \ . \end{aligned} \tag{2.52}$$

It can be seen that the real part of $Y_{\rm RF}$ will reduce to the classical conductance $dI_{\rm dc}/dV_0$ and the imaginary part will disappear when $\hbar\omega/e$ is smaller than the voltage scale of the dc nonlinearity.

Fig. 2.7 shows calculated RF input impedance as a function of dc bias voltage under various LO pumping strength. The dc IV used for this calculation is shown in Fig. 2.7a along with its Kramers-Kronig transform. The pumped dc IV curves under various LO voltage are calculated using (2.30) and given in Fig. 2.7b. The LO frequency is chosen to be 1/3 of the gap frequency. The conductance and susceptance are presented in Fig. 2.7c and Fig. 2.7d, respectively. For simplicity we assume here the pumping parameter $\alpha = eV_{\rm LO}/\hbar\omega$ is a constant. Strictly speaking, α is a function

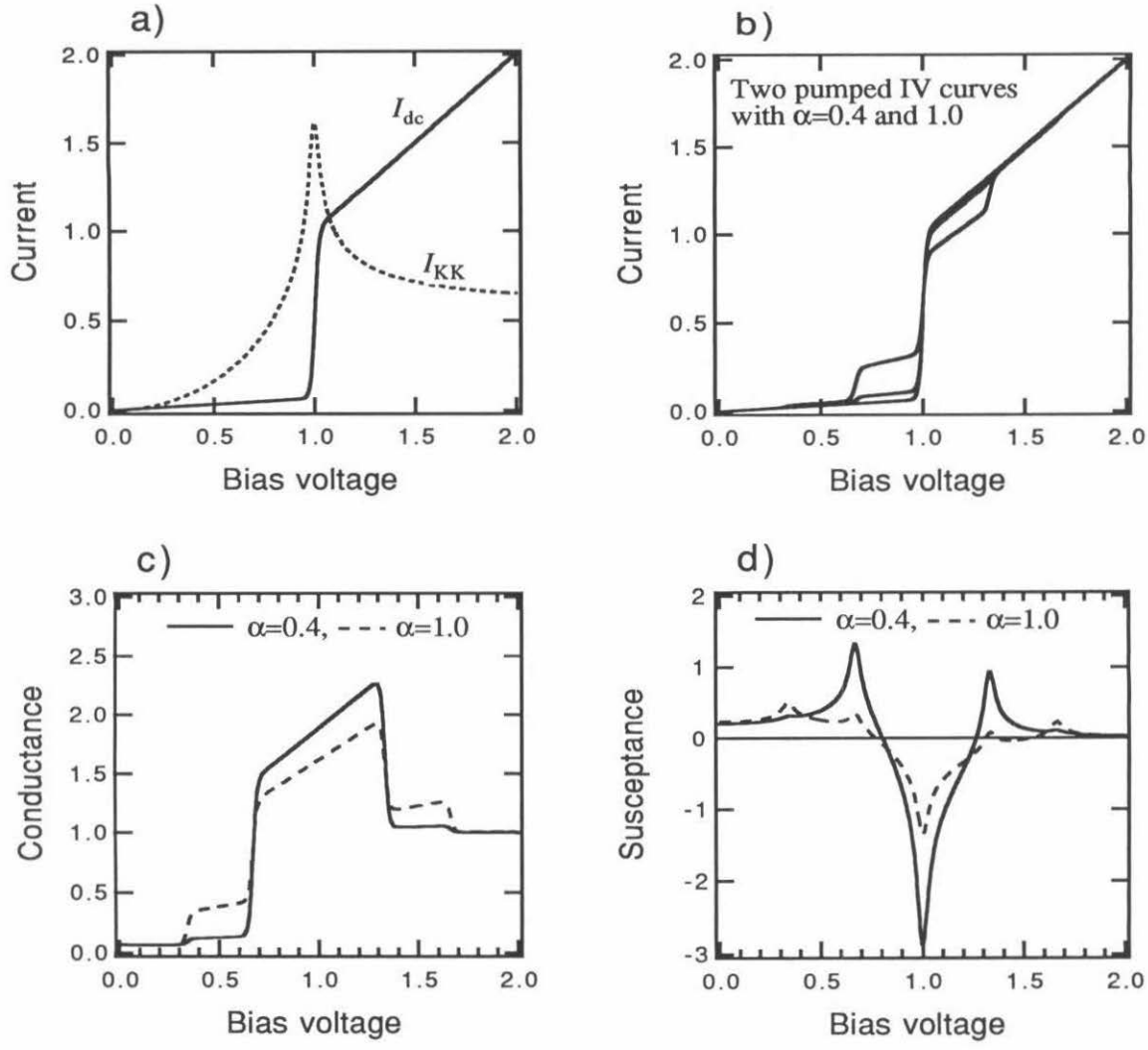

Figure 2.7: Quantum effects in SIS responses. a) Unpumped dc IV curve and its Kramers-Kronig transform. The voltage is normalized to the gap voltage and the impedance is normalized to the normal state resistance of the SIS junction. b) Pumped dc IV curves with LO strength of $\alpha = 0.4$ and $\alpha = 1.0$, respectively. The LO frequency is about 1/3 of the gap frequency. c) and d) RF input conductance and susceptance, respectively, calculated under the conditions of a) and b).

of bias voltage, due to the fact that the RF input impedance of the tunnel junction depends on bias voltage. However, the imperfectly matched RF circuits of a real SIS mixer tend to obscure this dependence and a constant α is often a fairly good assumption (de Lange (thesis) 1994).

Mixer output admittance and conversion gain

The mixer presents an output admittance $Y_{\rm IF}$ to the IF amplifier. If Z' denotes the Z matrix calculated with load admittance $Y_{\rm L} = Y_0 = 0$, it can be shown that (Shen 1981)

$$Y_{\rm IF} = \frac{1}{Z'_{00}} \, . \tag{2.53}$$

For a double sideband mixer, the output admittance is real due to the symmetry of the Y matrix, and can be written as

$$Y_{\rm IF} = G_{\rm IF} = \frac{1}{Z_{00}} - G_{\rm L} \, , \tag{2.54}$$

which is a quantity independent of the load conductance $G_{\rm L}$. $G_{\rm IF}$ is almost always the dynamic conductance of the SIS IV curve at its dc operating point with LO applied.

Tucker and Feldman (Tucker & Feldman 1985) argue that the output conductance of a classical mixer at the IF will always be positive and so regions of negative differential resistance can never be induced onto the dc IV curve by the LO drive. In the quantum regime, however, this is altered by the quantum nature of the photon-assisted tunneling. Under suitable experimental conditions, induced negative-resistance regions can occur on the measured dc IV curve, and indeed were observed first in 1981 (McGrath *et al.* 1981). This quantum effect has profound implications, one of which is that the SIS mixer can have conversion gain larger than unity, and theoretically infinite conversion gain is possible. As shown in section 2.3.2, the mixer gain is given by (2.40), and can be further written in terms of IF matching factor and

a matched gain (Shen 1981)

$$\begin{aligned} L^{-1} &= 4G_{\rm S}G_{\rm L}|Z_{01}|^2 \\ &= \Big(\frac{4G_{\rm IF}G_{\rm L}}{|Y_{\rm IF}+Y_{\rm L}|^2}\Big)\Big(\frac{G_{\rm S}}{G_{\rm IF}}|\lambda_{01}|^2\Big) \equiv \eta_{\rm IF}L_0^{-1} \ . \end{aligned} \tag{2.55}$$

The matched gain $L_0^{-1} = \frac{G_{\rm S}}{G_{\rm IF}}|\lambda_{01}|^2$ does not depend on the IF load admittance. For $G_{\rm L}$ and $G_{\rm IF}$ both greater than zero, the IF matching factor $\eta_{\rm IF}$ has a maximum of unity, which occurs when the IF load admittance is conjugately matched to the mixer, *i.e.*, $Y_{\rm L} = Y_{\rm IF}^*$. But when the output conductance is negative, $G_{\rm IF} < 0$, $\eta_{\rm IF}$ goes to infinity under a negative match condition $Y_{\rm L} = -Y_{\rm IF}$.

Conversion gain larger than unity is a non-classical effect. Torrey and Whitmer (Torrey & Whitmer 1948) prove that a classical double-sideband mixer is limited to $L^{-1} = 0.5$ and also find that the classical single-sideband mixer is theoretically limited to $L^{-1} = 1.0$. The prohibition of conversion gain arises solely from the assumption of instantaneous response of current to voltage for a classical mixer. At high enough frequency, in the quantum regime, the mixing element's response is not perfectly instantaneous as shown in section 2.3.1.

In practice large conversion gain is usually avoided because it tends to introduce instability and possible saturation of the mixer. It can be shown (Feldman 1982) that the reflection coefficient at the signal, image and every harmonic sideband port will tend to infinity when the mixer is negatively matched. This is clearly an unstable situation, which must be avoided. The saturation results from high voltage signal developed across an SIS junction which is delivering a large output power to a following IF amplifier. When this voltage is a significant fraction of a photon step voltage $\hbar\omega/e$, the actual gain will fall off as a result of the SIS sampling instantaneous bias voltages with lower gain (a saturation effect).

Chapter 3 Quasi-optical SIS Receivers

3.1 Introduction

The power collected by a submillimeter telescope is coupled into the SIS junction by a feed antenna. Traditionally the feed antenna is a machined waveguide feedhorn. The horn transforms the free space TEM waves into the guided modes of the waveguide mixer block. The junctions sit at the center of the waveguide, and coupled to the waveguide mode using a dipole-type antenna. The waveguide mixer mounts have the advantage of posessing well-defined clean beam, patterns and high efficiencies of coupling to the telescope beam, and adjustable backshorts can be tuned to match the highly capacitive SIS junctions. As frequency increases, the backshorts and waveguide suffer increasing losses which reduce the effectiveness of tuning. Over the past few years, integrated tuning circuits have been widely adopted with waveguide mount SIS mixers, relaxing the constraints placed on the backshorts. Waveguide SIS mixers have been built up to 1 THz (van de Stadt *et al.* 1996) and excellent performance has been achieved from 200 - 850 GHz (Blundell *et al.* 1995a; Blundell *et al.* 1995b; de Lange *et al.* 1994a; Honingh *et al.* 1995; Karpov *et al.* 1995; Kerr *et al.* 1992; Kooi *et al.* 1994a; Kooi *et al.* 1994b; Kooi *et al.* 1995a; Kooi *et al.* 1996; Tong *et al.* 1995a). However, waveguide mixers are difficult and expensive to construct at high frequencies ($>$ 500 GHz) because the critical dimensions scale with wavelength. The waveguide block becomes difficult to machine and the SIS devices are hard to fabricate because the substrate becomes extremely thin. Even mounting the SIS substrate in the waveguide block poses a challenge.

Quasi-optical technique provides an alternative to waveguide mixers. This approach has the advantage that two-dimensional microstructures are easily fabricated using conventional lithography. Quasi-optical mixers consist of SIS junctions monolithically integrated with a planar antenna on a thick dielectric substrate. This sub-

strate is then placed directly on the back of a substrate lens, usually a hyperhemisphere or ellipsoid, to increase the directivity of the planar antenna. A schematic of a hyperhemispherical substrate lens combined with an objective lens is shown in Fig. 3.1. The thick dielectric substrate simulates a semi-infinite dielectric half-space thus preventing the propagation of surface modes. Additionally, the planar antenna on the back of the substrate lens tends to radiate most of its power into the lens side. The ratio of the radiated power into the dielectric side and the air side is approximately $\epsilon_r^{3/2}$, for infinitesimal slot and dipole antennas, where ϵ_r is the relative dielectric constant of the substrate (Rutledge *et al.* 1983). To increase the directivity of the antenna, high dielectric constant substrates are preferred. However, the reflection at the lens/air interface increases with the dielectric constant, requiring anti-reflection coatings applied on the lens to reduce the reflection. Compared to waveguide mixers, quasi-optical mixers are much simpler to fabricate and install, and more suitable for focal-plane imaging array applications.

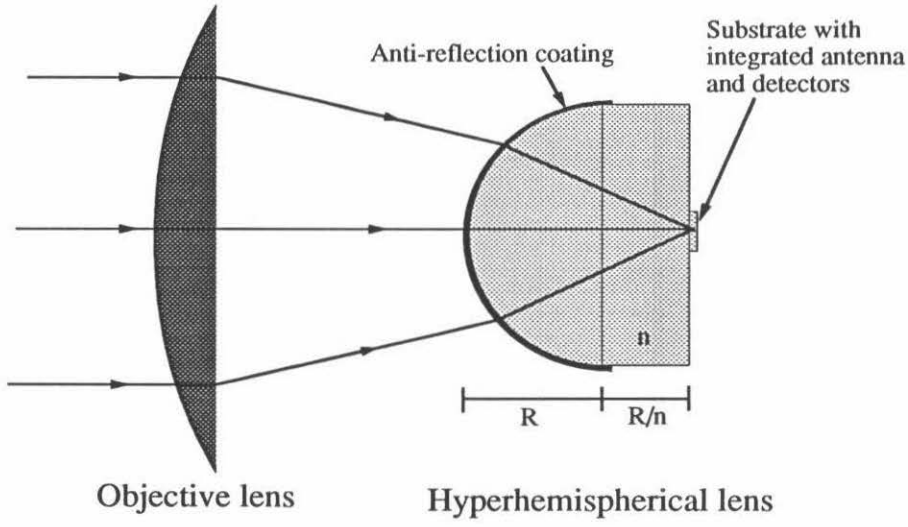

Figure 3.1: A hyperhemispherical lens combined with an objective lens.

One of the main challenges in constructing quasi-optical mixers is to obtain efficient radiation coupling. The antenna system should have low side-lobes, a symmetric main beam, low phase aberrations, and high coupling efficiency to a fundamental Gaussian beam. Most planar antennas, such as the bow-tie antenna (Compton *et*

al. 1987), the spiral antenna (Büttgenbach *et al.* 1988), and the twin-slot antenna (Zmuidzinas & LeDuc 1992; Zmuidzinas *et al.* 1995) have broad beam patterns and thus small f-numbers (typically $\sim f/1$). Here the f-number is defined as

$$f\text{number} \approx \frac{1}{2\tan\left(\theta_{\text{FWHP}}/2\right)} \ , \tag{3.1}$$

where θ_{FWHP} is the full width at half power of the beam. The substrate lens increases the f-number. Several substrate lenses have been investigated for this purpose. For example, a hyperhemispherical lens will reduce the beam width by n times, n being the refractive index of the lens (Kasilingam & Rutledge 1986). The hyperhemispherical lens uses the aplanatic focus of a sphere at a distance R/n from the center of the sphere where R is the radius of the sphere (Born & Wolf 1964). A hyperhemispherical lens usually requires an objective lens in front of it to couple to the narrow beams from the telescope. An elliptical lens is very efficient since any antenna placed on the back of the lens will result in a far-field pattern with a main-beam that is diffraction limited by the aperture of the elliptical lens. The elliptical lens is compatible with a large f-number imaging system due to the potential for achieving very narrow beam patterns (Filopovic 1995). However, the elliptical lens suffers somewhat from a larger effective reflection coefficient at the lens/air interface, due to a larger range of incidence angles. Another type of dielectric lens - the extended hemispherical lens - has been studied theoretically and experimentally (Büttgenbach *et al.* 1993; Filipovic *et al.* 1993a; Filipovic & Rebeiz 1993b). An extended hemispherical lens is a hemispherical lens with radius R and an attached extension length l. Note that the hyperhemispherical lens is a special case of the extended hemispherical lens when $l = R/n$. It is found that the directivity of this antenna is strongly dependent on the extension length (especially at high frequencies); and the Gaussian coupling efficiency is very high up to an intermediate position between the hyperhemispherical and synthesized elliptical length and then begins to drop gradually. A suitable compromise between the increase in directivity and the decrease in Gaussian-coupling efficiency is achieved at a position intermediate between the hyperhemispherical and synthesized

elliptical lengths. Filipovic has compared the performance of extended hemispherical lenses made out of quartz and silicon. He predicted a coupling efficiency around 90% for a twin-slot antenna on an anti-reflection coated silicon lens (Filipovic *et al.* 1993a).

The other challenge in constructing quasi-optical mixers arises from the fact that quasi-optical mixers lack an adjustable element equivalent to a waveguide backshort. Integrated tuning circuits are thus essential in order to achieve competitive performance. Over the last decade, microstrip transmission lines have been widely used as inductors to resonate out the SIS junction capacitance or as impedance transformers to match the impedance of the junction to that of the planar antenna. Quasi-optical SIS mixers with integrated tuning elements have achieved low noise performance equivalent to the best waveguide mixers above 500 GHz (Belitsky *et al.* 1995a; Bin *et al.* 1996; Gaidis *et al.* 1995b; Gaidis *et al.* 1996a; Rothermel *et al.* 1994). More detailed discussions on integrated tuning circuits will be provided in section 4.1.

3.2 A quasi-optical twin-slot antenna SIS receiver

In this section, the configuration of a quasi-optical receiver is illustrated using our laboratory test receiver setup with a twin-slot antenna double-junction SIS mixer. Fig. 3.2 shows the overall layout of the receiver. The dewar consists of two reservoirs, one for liquid helium to cool the work plate to 4.2 K, the other for liquid nitrogen keeping a radiation shield at 78 K. The signal and local oscillator (LO) are combined with a beamsplitter. The combined beam goes through the vacuum window and an infrared (IR) filter in the 78 K shield before it reaches the mixer block. The mixer block is the central part of the receiver. It includes a polyethelene lens, a hyperhemispherical lens, the mixer chip with an integrated twin-slot antenna and SIS junctions, and the supporting electronic circuits. The injection optics, the mixer block, the twin-slot antenna, and the mixer chip will now be described in more detail.

a) The signal/LO injection optics

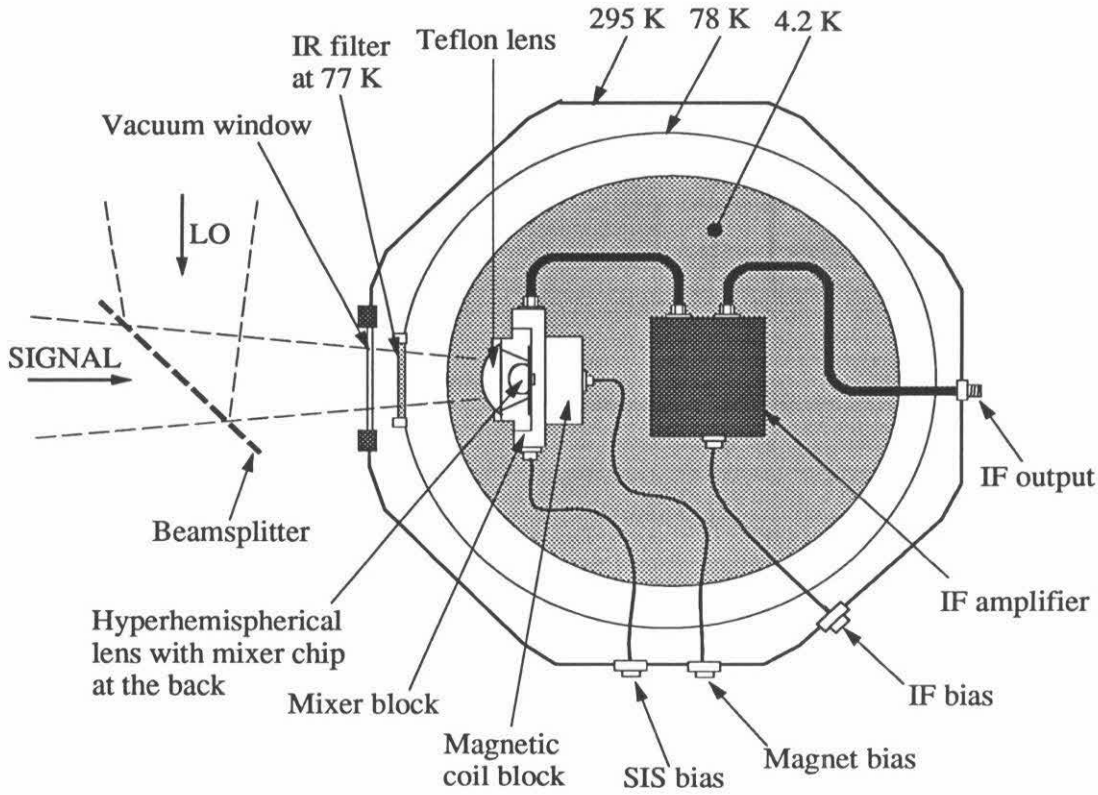

Figure 3.2: Layout of a quasi-optical receiver.

The sensitivity of the receiver is measured by the standard Y-factor method as discussed in section 1.2. The hot load (295 K) can be the room temperature background radiation. The cold load (78 K) is a convenient Eccosorb sheet immersed into liquid nitrogen. The LO source is usually a compact, solid-state, tunable Gunn oscillator with varactor multipliers (Carlstrom *et al.* 1985; Erickson & Tuovinen 1995; Zimmerman *et al.* 1995). The Gunn can provide microwave oscillation up to 145 GHz. Then the Gunn output is multiplied by a doubler ($\times 2$), a tripler ($\times 3$), or a cascades ($\times 2 \times 3$). Far-infrared lasers are also used for LO source when the frequency is high and the solid-state local oscillator can not provide enough power. For instance, a difluoromethane (CH_2F_2) far-infrared laser pumped by a $\lambda = 10\mu$m CO_2 laser can generate strong radiation at 1042 GHz ($\approx 288\mu$m).

The signal and LO inputs are combined with a beamsplitter. The beamsplitter is made of a thin Mylar sheet - 10 μm, 25 μm, or 51 μm thick beamsplitters are used. The LO (signal) coupling efficiency is equal to the reflectivity (transmissivity) of the beamsplitter, which is a function of frequency. Fig. 3.3 plots the reflectivity of the three beamsplitters in the submillimeter band. Two sets of values are shown for the cases when the polarization of the electric field is perpendicular or parallel to the incidence plane of the beam. Since our twin-slot antenna is installed with a vertical polarization, the set of values for the perpendicular polarization should be considered. The choice of thickness of the beamsplitter is determined by the requirements to maximize the signal, but to have adequate LO power at the same time. The lack of LO power at high frequencies often dictates the use of the thick beamsplitters. This can increase the receiver noise temperature significantly, as it replaces part of the signal with room-temperature thermal noise.

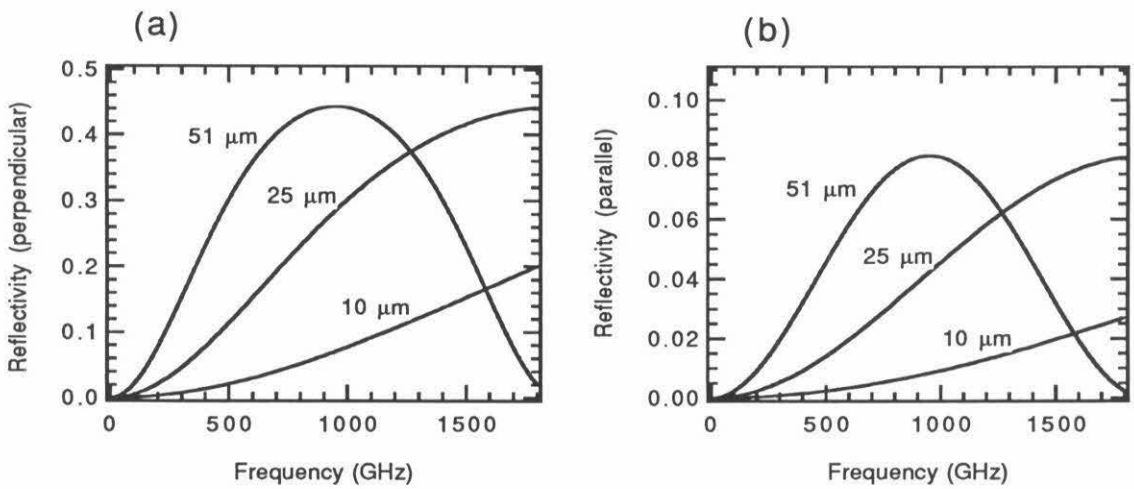

Figure 3.3: The reflectivity of the beamsplitter used as LO/signal combiner when the polarization of the electric field is (a) perpendicular or (b) parallel to the incidence plane.

The vacuum window at room-temperature is made of a 1 mil (25 μm) Mylar sheet or a z-cut crystal quartz disk. The quartz disk should have less absorption loss in the submillimeter range. The downside is that the quartz disk has a larger reflectance at

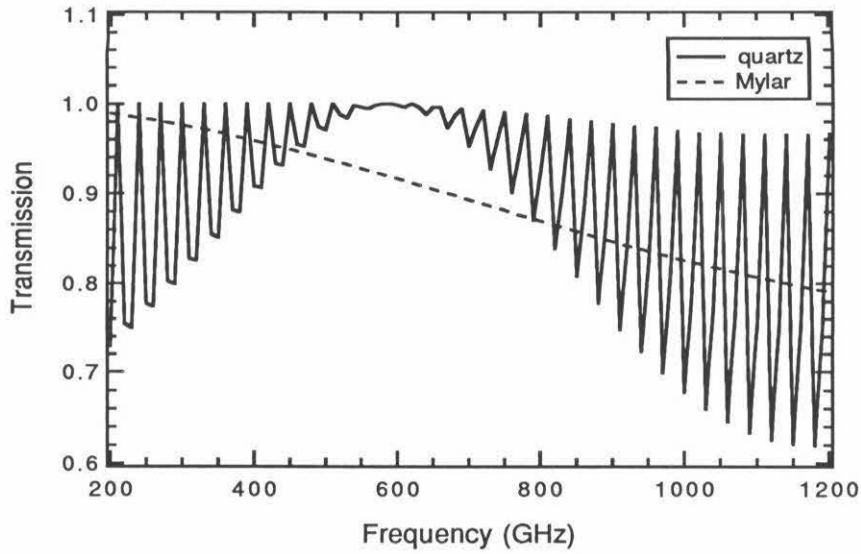

Figure 3.4: Calculated transmissions of a 25 μm Mylar sheet and a 2.5 mm AR-coated quartz disk as dewar windows. The quartz is coated with Teflon FEP for a center frequency of 590 GHz.

the air interface and it introduces fast resonance peaks (about 30 GHz apart if the plate is 2.2 mm thick) in the transmission due to the Fabry-Perot effect. To reduce this resonance, an anti-reflection (AR) coating is applied to both sides of the quartz disk. The AR coating utilizes several layers of clear Teflon FEP to build the coating up to the requisite quarter-wavelength thickness (Thermech Engineering Corp.). In Fig. 3.4 the calculated transmissions of 1 mil Mylar sheet and an AR-coated quartz disk are plotted against frequency. Since no absorption information is available for Mylar in the near submillimeter region, an ideal lossless Mylar with a refractive index of 1.73 is assumed for the calculation. The refractive index for quartz is 2.11 and the refractive index of Teflon FEP is 1.42, and again no absorption loss is considered.

The IR filter at 77 K is also an AR-coated z-cut crystal quartz disk. The AR coating utilizes an adhesion layer of black Xylan 1220 primer, mixed with Teflon FEP, and applied to a thickness of $\approx 10\mu$m. This is then covered by several layers of clear Teflon FEP to build the coating up to the requisite quarter-wavelength thickness (Thermech Engineering Corp.). A special Teflon film filled with air bubbles called Zitex has also been tried as an IR filter (Norton Performance Plastics). These IR

filters are quite durable and withstand repeated thermal cycling. The transmission of the quartz IR filter at 77 K has not been measured experimentally. A recent experiment (Gaidis 1996b) suggests that Zitex is an effective IR filter, with cutoff around 6 THz. A 10 mil thick Zitex G110 film has transmission $\sim$ 90% at 1 THz.

b) The mixer block[1]

The quasi-optical mixer consists of a polyethelyne lens, an AR-coated silicon hyperhemispherical lens, a mixer chip with an integrated planar antenna and the junctions and supporting electronic circuits. A detailed view of the mixer block used in our lab is presented in Fig. 3.5. The top of Fig. 3.5a shows the magnet housing. The magnet is used to suppress Josephson effects, and consists of approximately 3600 turns of superconducting NbTi wire on a #1018 cold-rolled steel core. The bottom of Fig. 3.5a shows the bias and IF circuitry and the mixer chip (at the center). As indicated in Fig. 3.5b, the SIS mixer chip and the silicon hyperhemisphere are glued to the opposite side of the silicon support disk using a UV-curing glue (Norland Optical Adhesive). The SIS devices are fabricated on a 0.25 mm thick 50 mm diameter, high-resistivity ($>$ 100 Ω-cm) silicon wafer, which is then diced into 1.2 mm $\times$ 1.5 mm individual chips. The high-resistivity ($>$ 100 Ω-cm) silicon support disk is 2.5 cm in diameter and 0.9 mm thick. The silicon hyperhemisphere consists of very high-resistivity silicon ($\sim$ 4000 Ω-cm) (Topsil U.S.), diamond-machined into a 6.35 mm radius hemisphere with a 0.7 mm extension (Janos Technology). Such high-resistivity silicon ensures low RF losses, but is likely not critical when operating at 4.2 K. The silicon lens is AR-coated with alumina-loaded epoxy to reduce reflection at the air interface (Zmuidzinas *et al.* 1995). The thicknesses of the hyperhemisphere extension, the support disk, and the chip substrate combine to place the device at the aplanatic focus of the hyperhemisphere.

The silicon disk is clamped in the mixer block by a printed circuit board, which itself is held in place by metal clamps and screws as shown in Fig. 3.5a. The circuit board is 0.6 mm thick TMM10i temperature stable microwave laminate (Rogers

[1]This section of the thesis is largely based on the work reported in the paper by Gaidis *et al.* (Gaidis *et al.* 1996a).

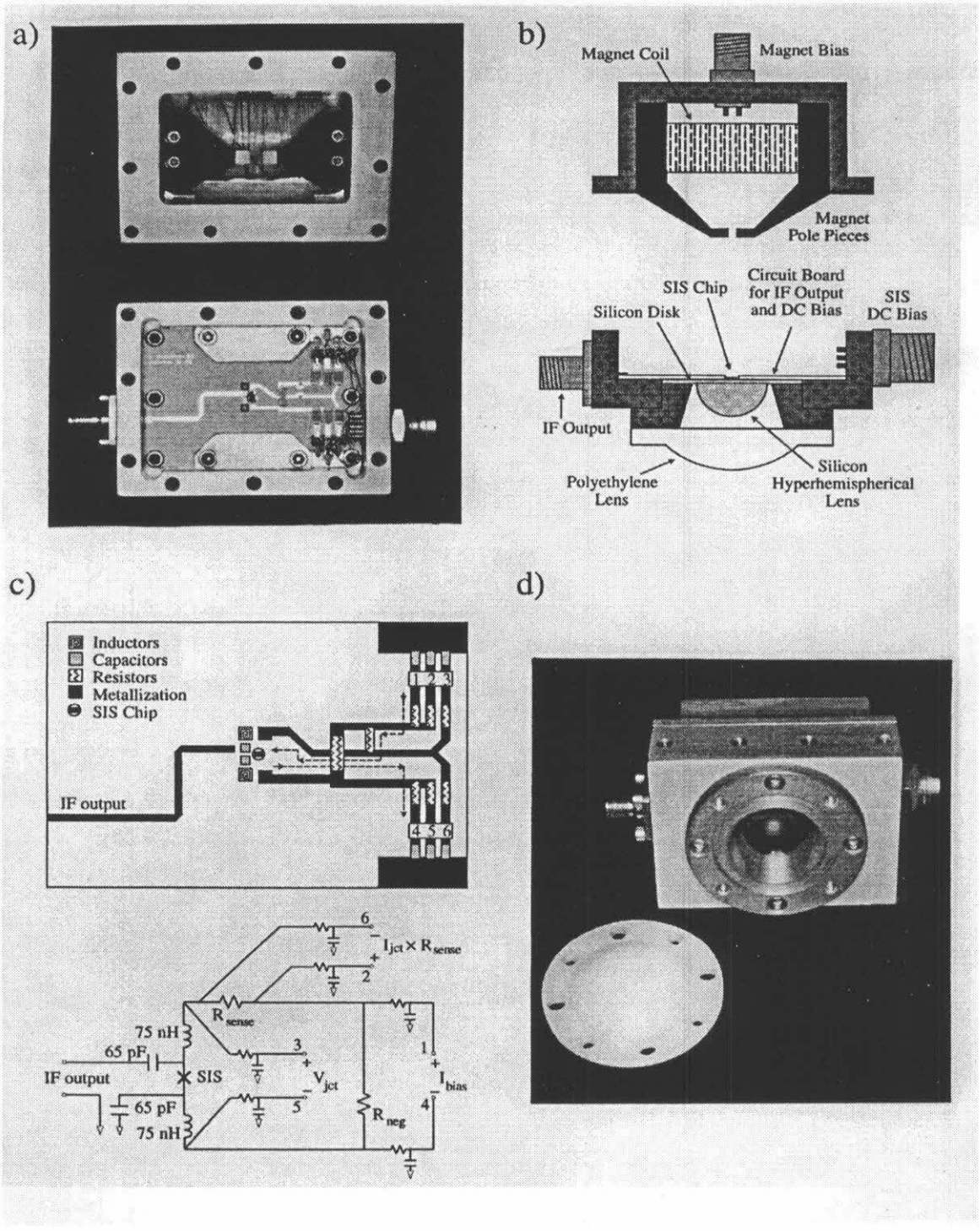

Figure 3.5: Actual and schematic views of the mixer block which houses the SIS mixer and associated circuitry.

Corp.), with room temperature dielectric constant 9.8 and room-temperature attenuation coefficient 0.001 48 Np/cm at 10 GHz. The board's thermal expansion is isotropic, and closely matched to the gold-plated copper metallization, allowing for reliable plated-through holes and low etch shrinkage.

DC bias supply and readout leads enter from the connector on the right, and the mixer IF output is carried on a microstrip line to a SMA connector on the left. The schematic in Fig. 3.5c details the circuitry on the printed circuit board. The dc bias source resistance is adjustable by feedback to present the mixer with either a current source or a voltage source. Resistor $R_{\rm neg}$ is chosen at approximately 100 Ω to prevent unstable biasing due to regions of negative dynamic resistance in the SIS IV curve. The current-sensing resistor $R_{\rm sense}$ is typically 10 Ω, and the IF-blocking inductors at 4.2 K add $<<$ 1 Ω series resistance. The upper 65 pF capacitor in Fig. 3.5c is attached to the IF output microstrip with silver-loaded epoxy. The lower 65 pF capacitor is attached to the ground plane via a plated-through hole with silver epoxy. The SIS mixer chip sits within a through hole at the center of the board, allowing straightforward wire-bonding of the mixer chip to the top electrodes of the two 65 pF capacitors. The chip inductors are wire-bonded to the top electrodes of the 65 pF capacitors and to the traces carrying the dc bias. The remaining chip resistors, chip capacitors, and connector pins are attached to the circuit board traces with either solder or silver-loaded epoxy.

The picture in Fig. 3.5d shows the assembled mixer block, with the polyethylene lens removed to reveal the silicon hyperhemispherical lens. A semi-rigid coaxial cable connects the SMA port on the left with a HEMT low noise IF amplifier (LNA). The LNA output is sent to room temperature amplifiers and a diode detector which measures the total power in a 500 MHz IF bandwidth.

c) The twin-slot antenna

A number of integrated planar antennas have been employed for SIS mixers, including bow-tie, spiral, log-periodic, and twin-slot antennas (Büttgenbach *et al.* 1988; Dierichs *et al.* 1992; Wengler *et al.* 1985; Zmuidzinas & LeDuc 1992). The first three

antennas belong to a family of frequency independent self-complementary antennas (Kraus 1988), for which characteristics like impedance, beam pattern, *etc.*, do not depend on frequency over several octaves. In air, the antenna impedance is half of the free space impedance ($Z_0 = 60\pi\ \Omega \approx 188\ \Omega$) and the beam is bidirectional broadside to the plane of the antenna. The radiation can be pulled forward in favor of one direction if the antenna is placed on a thick dielectric substrate, as mentioned in section 3.1. The antenna impedance is also changed by the dielectric substrate:

$$Z_{\rm ant} = \frac{Z_0}{\sqrt{(1+\epsilon_{\rm r})/2}}\ , \tag{3.2}$$

where $\epsilon_{\rm r}$ is the relative dielectric constant of the substrate. The first quasi-optical SIS receiver used a bow-tie antenna on a quartz hyperhemispherical lens (Wengler *et al.* 1985). However, bow-tie antennas have a complex large angle pattern, showing no single main beam in the desired direction perpendicular to the antenna-plane (Compton *et al.* 1987). The SIS receiver sensitivity was increased by a factor of ~ 2 by replacing the bow-tie with a spiral antenna (Büttgenbach *et al.* 1988), which has a much cleaner beam pattern. A beam pattern measurement of the spiral with hyperhemispherical lens resulted in side-lobe and pedestal structures at the -20 dB level. Experiments with planar log-periodic antennas on silicon hyperhemisphere also show that the antenna has a cross-polarization level of -5 to -15 dB, which varies periodically with frequency (Kormanyos *et al.* 1993).

Unlike the above-mentioned frequency independent antennas, the twin-slot is a resonant antenna. It has a number of desirable properties, including linear polarization, a symmetric beam with low sidelobes, a low antenna impedance, and an octave bandwidth (Zmuidzinas & LeDuc 1992). Once a design for one frequency band is made, it is easy to scale to different frequency bands, since the dimension scales inversely with frequency. The antenna impedance and radiation pattern can be calculated by a moment-method in the frequency domain (Kominami *et al.* 1985; Zmuidzinas & LeDuc 1992).

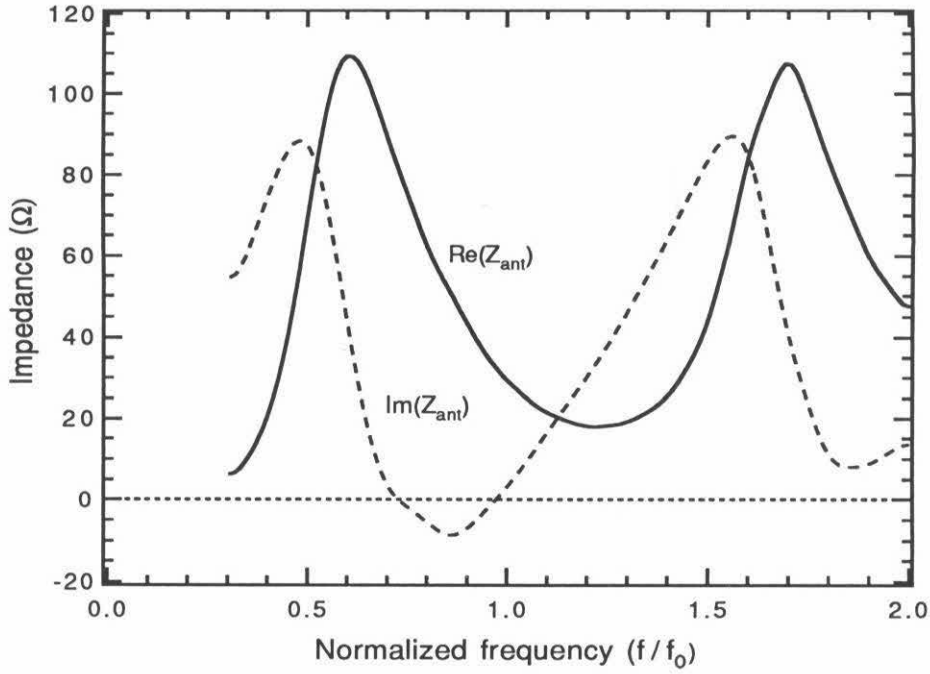

Figure 3.6: Calculated radiation impedance of a twin-slot antenna on a semi-infinite silicon substrate. The design parameters are given in the text.

Our mixer chip utilizes the twin-slot antennas designed previously in our group (Zmuidzinas *et al.* 1995). The antenna dimensions used for a silicon substrate are as follows: the slot length is $L = 0.33\lambda_0$, the separation between the two slots is $S = 0.17\lambda_0$, and the width to length ratio is $W/L = 0.05$. At the center frequency, the antenna impedance is real and has a value 33 Ω. Fig. 3.6 shows the twin-slot antenna impedance for this design on a silicon half-infinite substrate. Note that the real part of the impedance remains low for more than one octave bandwidth.

The beam pattern of this twin-slot, radiated into the dielectric, is calculated to be slightly asymmetric, with θ_{FWHP}=53° in the E-plane and θ_{FWHP}=46° in the H-plane (Zmuidzinas *et al.* 1995). The corresponding f-number is about 1.0. This small f-number is increased by the hyperhemispherical silicon lens and the polyethelene lens to as high as $f/17$ to match the beam of the Kuiper Airborne Observatory

telescope. The beam pattern of the whole quasi-optical system, which includes the twin-slot antenna, the hyperhemispherical silicon lens and the polyethelene lens, has been measured in our lab (Miller 1995). Fig. 3.7 presents the measured beam pattern of an SIS receiver at 508 GHz. The center frequency of the twin-slot antenna is 550 GHz. The FWHP angle of the beam is about 2.8°, corresponding to a f-number of 20.

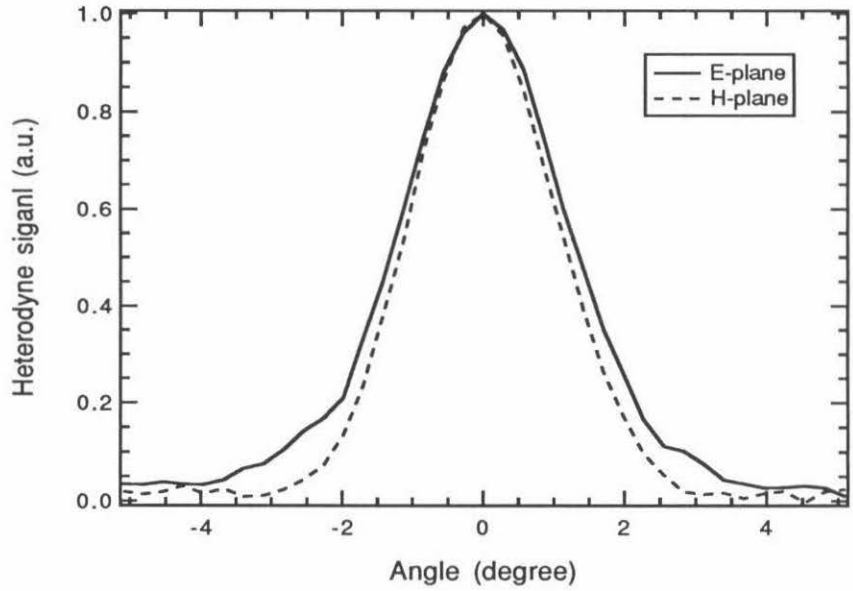

Figure 3.7: Measured beam pattern of a quasi-optical twin-slot SIS receiver at 508 GHz. Courtesy of David Miller.

d) The mixer chip

Fig. 3.8 displays the structure representative of our twin-slot double-junction anti-symmetrically driven mixers (Bin *et al.* 1996; Gaidis *et al.* 1996a; Zmuidzinas *et al.* 1995). The radiation received by the slot antennas is coupled into the SIS junctions with microstrip transmission lines. $\lambda/4$ microstrip radial stubs are used to effect the coupling to the slot antenna, by providing an RF short-circuit between the microstrip and one side of the slot antenna. This design simplifies the inductive tuning necessary to resonate the junction capacitance. The resonating inductance for each junction is simply one-half the total inductance joining the two junctions, as the anti-symmetric

feed creates a virtual ground at the midpoint between the two junctions (Zmuidzinas *et al.* 1994). One or two sections of microstrip transmission lines are used as impedance transformers to match the junction impedance ($\sim 10\Omega$) to that of the slot antenna ($\sim 30\Omega$). The IF signal is taken out by a two-section coplanar strip, which acts as an RF choke.

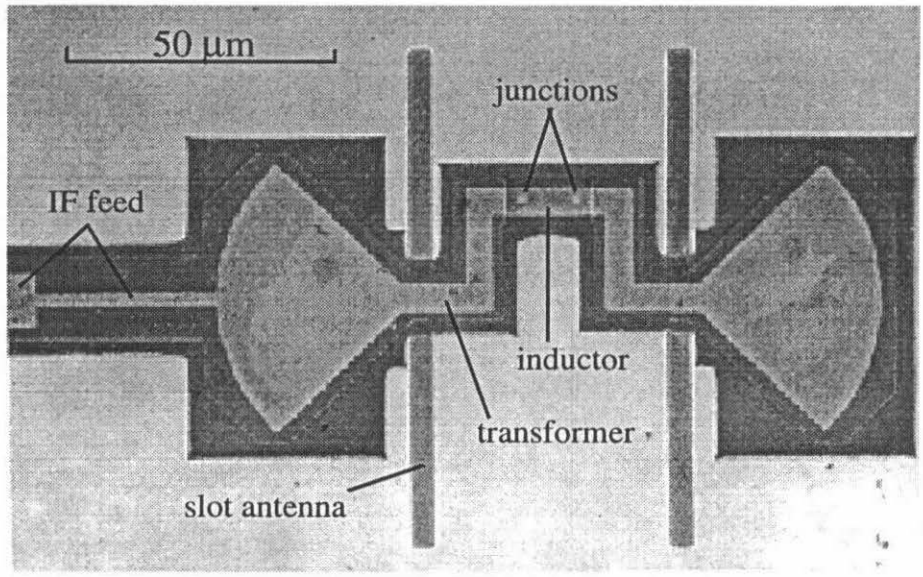

Figure 3.8: SEM of the twin-slot double junction SIS mixer.

The mixer design is optimized using an in-house developed program which will be described in chapter 4.

Chapter 4 Modeling of SIS Mixers with Integrated Tuning Circuits

It has become a common practice to utilize integrated tuning circuits among researchers working with either waveguide or quasi-optical SIS receivers. For waveguide receivers, the integrated tuning relaxes the dependence on backshorts, and fixed-tuned SIS receivers (no moving backshorts) can be obtained. For the quasi-optical SIS receivers, it is essential to have integrated tuning since they lack the adjustable tuning elements. The integrated tuning circuits are usually made of microstrip transmission lines, serving as inductors to resonate out the SIS junction's capacitance or as transformers to match the impedance of the junction to the driving antenna.

Nb/Al-oxide/Nb junctions with integrated Nb tuning circuits have achieved good performance up to 850 GHz (Gaidis *et al.* 1996a; Kooi *et al.* 1996), yet the noise temperature rises notably above 700 GHz, the niobium gap frequency. Below the gap frequency, the niobium has negligible rf loss as a superconductor. Above the gap frequency, niobium behaves like a normal metal since the rf photons have sufficient energy to break Cooper pairs. A large fraction of the radiation is thus lost in the tuning circuits. Since niobium is not a very good normal conductor, tuning circuits made out of good normal metals (Al, Ag, Au or Cu) should yield better performance above the gap frequency. Our work on Nb/Al-oxide/Nb with Al tuning circuits has obtained results comparable with all Nb mixers at 850 GHz and very good results at 1042 GHz (Bin *et al.* 1996).

Understanding the characteristics of microstrip transmission lines at high frequencies is critical for the design of SIS mixers. This chapter will describe the model we use for characterizing microstrip lines and also the methodology for optimizing mixer design.

4.1 Review of RF tuning circuits

Fig. 4.1 shows a simplified circuit model for an SIS mixer. The antenna is modeled as a current source with source admittance Y_S. The junction is modeled as an admittance Y_J in parallel with its geometric capacitance C. The tuning circuit is simplified as a shunt inductance L. Y_J is the RF admittance of the junction. It can be calculated from the junction's dc IV curve using (2.52). For simplicity, we can ignore the reactance at the moment, and assume the real part is given by the junction's normal state resistance, $Y_J = R_N^{-1}$.

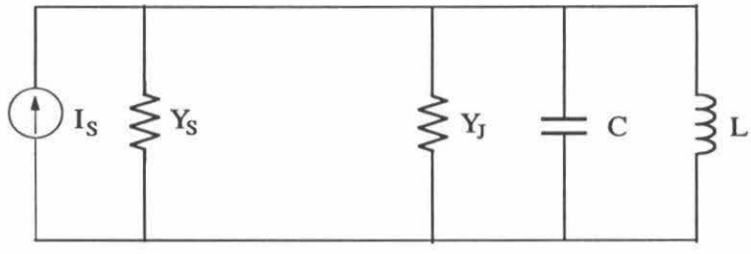

Figure 4.1: Equivalent circuit of an SIS mixer.

The RF coupling efficiency η_{RF} is defined as the ratio of absorbed power at the junction to the available power at the source. For our simplified model in Fig. 4.1,

$$\eta_{RF} = 1 - \left| \frac{Y - Y_S^*}{Y + Y_S} \right|^2 , \tag{4.1}$$

where

$$Y = R_N^{-1} + j\omega C + \frac{1}{j\omega L} . \tag{4.2}$$

Perfect coupling with $\eta_{RF} = 1$ is achieved when the resonant condition is satisfied, *i.e.*, $Y = Y_S^*$.

The standard measure of the parasitic effect of C is the junction $\omega R_N C$ product, the ratio of the junction's normal state resistance to its capacitance. When no tun-

ing circuits are used, the junction behaves like a low-pass RC circuit with a cut-off frequency $1/R_{\rm N}C$. If the source admittance is real, $Y_{\rm S} = R_{\rm S}^{-1}$, then the coupling efficiency of the tunerless mixer is

$$\eta_{\rm RF} = \frac{4R_{\rm S}/R_{\rm N}}{(1 + R_{\rm S}/R_{\rm N})^2 + (\omega R_{\rm N}C)^2} \ . \tag{4.3}$$

The best possible coupling can be achieved by making $R_{\rm S}$ the same as the absolute value of the junction's impedance:

$$R_{\rm S} = \frac{R_{\rm N}}{\sqrt{1 + (\omega R_{\rm N}C)^2}} \ . \tag{4.4}$$

The RF coupling is then given by

$$\eta_{\rm RF} = \frac{2}{\sqrt{1 + (\omega R_{\rm N}C)^2} + 1} \ . \tag{4.5}$$

For the tunerless mixers to work at high frequencies, the $R_{\rm N}C$ product must be small. Since $R_{\rm N}C$ is independent of the junction area, the junction tunnel barrier must be made thin, hence the critical current density is high for small $R_{\rm N}C$ junctions. However, the optimum value is found to be $\omega R_{\rm N}C \gtrsim 4$, not $\omega R_{\rm N}C \lesssim 1$ (Tucker & Feldman 1985). This is because the capacitance plays a constructive role in improving the mixer conversion efficiency by suppressing harmonic conversion effects (Richards & Shen 1980).

The ideal tuning circuit for an SIS junction would simply consist of a shunt lumped inductor L such that the junction's capacitance is resonated out at the signal frequency $\omega_0 = 1/\sqrt{LC}$. The quality factor of such a resonant circuit is given by

$$Q = \omega_0 R_{\rm N}C \ , \tag{4.6}$$

and the fractional bandwidth $\Delta\omega/omega_0$ defined by FWHP is

$$\frac{\Delta\omega}{\omega_0} = \frac{1}{Q} = \frac{1}{\omega_0 R_{\rm N}C} \ . \tag{4.7}$$

In practice the tuning inductance is often realized by a section of microstrip line, either in parallel or in series with the junction. For instance, the well-known "open-stub" tuner is a parallel shunt inductor made of $3/8\lambda$ open-circuited microstrip line, while $1/8\lambda$ microstrip is placed in parallel with the junction by using $1/4\lambda$ stub as an RF short circuit (Räisänen *et al.* 1985). In general, all the shunt inductance tuning circuits must have a blocking capacitance in series with the inductance to provide an RF short but an open dc circuit to allow dc bias to the junction. This may be implemented by a quarter-wavelength open-circuited microstrip line or a radial stub. In order to avoid reducing the bandwidth, the RF impedance of this dc blocking element must be kept small, $Z_{\rm b}(\omega) \ll 1/\omega C$. This constraint proves to be difficult to satisfy in practice for frequencies above 500 GHz (Zmuidzinas *et al.* 1994). The bandwidth of the open-stub is about 1/3 of the bandwidth of an ideal lumped-inductance tuning circuit (Büttgenbach *et al.* 1992). Even the radial stub, which is often used as a good RF short, reduces the bandwidth (Zmuidzinas *et al.* 1994). Both quarter-wave stub and radial stub tuning circuits have been used for 600 GHz waveguide receivers and yielded good mixer performance (Febvre *et al.* 1994; Salez *et al.* 1994).

Series inductance tuning (Büttgenbach *et al.* 1992) is commonly referred to as an "end-loaded" stub. The junction sits at the end of a microstrip line which serves as a series inductance. This circuit is an excellent choice for frequencies below 500 GHz, preserving the bandwidth, but it is less suitable for higher frequencies, because the serial inductance also acts as an impedance transformer, producing a real impedance on the order of $R_{\rm N}/(\omega_0 R_{\rm N} C)^2$. The resulting transformed impedance is too low for most planar antennas to drive directly, so multi-section microstrip quarter-wave transformers are needed to bring the impedance back up to match the antenna. The transformer will reduce the bandwidth and introduces loss at high frequencies. In addition, because of the very low impedance needed, the last section of the transformer becomes quite wide, and in fact the width can become comparable to the length. The traditional analysis based on the transmission line formula is inadequate to accurately characterize such a circuit (Zmuidzinas *et al.* 1994). Recent work on "end-loaded

stub" tuning demonstrates this aspect-ratio problem, though good receiver noise results are still obtained (Blundell *et al.* 1995b; Tong *et al.* 1995a).

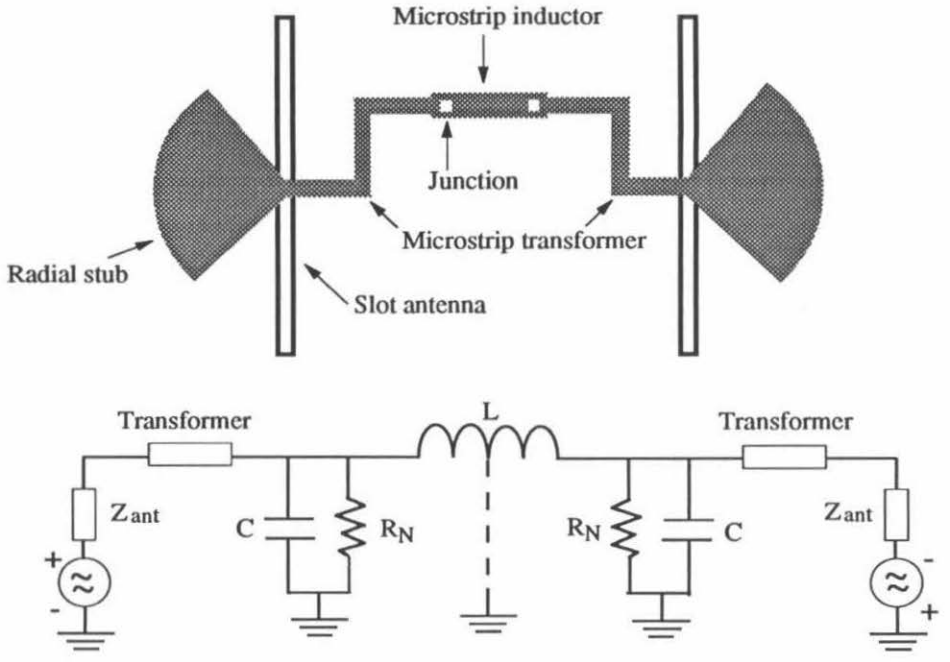

Figure 4.2: A twin-slot antenna, double junction mixer with antisymmetric feed.

Another way of tuning is to use a "double-junction transformer" (Belitsky *et al.* 1992). Two junctions are separated by a short section of transmission line, in such a way that the complex impedance of one junction, after transformed by the line, is equal to the complex conjugate of the other. This tuning circuit gives an impedance bandwidth equal to the ideal shunt-inductance circuit. These double-junction circuits do not use dc blocking capacitors, and the tuning inductance is precisely controlled by the separation of the two junctions. Since both junctions are defined in the same lithography step, the tuning inductance is nearly immune to registration errors between layers.

The tuning scheme used in this thesis is based on the "double-junction transformer," with the feed to the junction arranged in such a way that each junction is virtually tuned by a shunt inductance without an RF short needed (Zmuidzinas

et al. 1994; Zmuidzinas *et al.* 1995). Fig. 4.2 shows how this is realized. The two feed points of the twin-slot antenna are arranged so that the two signals are 180 degrees out of phase. This antisymmetric feed produces a virtual ground at the center of the tuning inductance L, so each junction is effectively shunted by an inductance of $L/2$. This tuning circuit will therefore approach the full possible bandwidth, $\Delta\omega/\omega_0 = 1/\omega_0 R_N C$, to the extent that the inductance and the junction behave as lumped elements. More analysis on this design is provided in section 4.5.

4.2 General characteristics of a transmission line

A transmission line can be thought of as a ladder of series impedances and shunt admittances, as shown in Fig. 4.3, where series resistance R, inductance L, shunt conductance G, and capacitance C are distributed quantities, measured per unit length (Ramo *et al.* 1984; Van Duzer & Turner 1981). Let $Z = R + j\omega L$ and $Y = G + j\omega C$, ω being the angular frequency. The transmission line equations are given by:

$$\frac{dV}{dz} = -ZI \ , \tag{4.8}$$

$$\frac{dI}{dz} = -YV \ , \tag{4.9}$$

where V and I are the voltage and current on the transmission line. The solutions for them are

$$V(z) = V(0)\exp\{-\gamma z\} \ , \tag{4.10}$$

$$I(z) = I(0)\exp\{-\gamma z\} \ . \tag{4.11}$$

The propagation constant $\gamma = \alpha + j\beta$ is determined by

$$\gamma = \sqrt{ZY} = \sqrt{(R + j\omega L)(G + j\omega C)} \,, \tag{4.12}$$

with α the attenuation constant and β the phase constant. The power transmitted on the line is

$$P(z) = Re[V(z)I(z)^*] = P(0)\exp\{-2\alpha z\} \,. \tag{4.13}$$

The power attenuation is hence given by 2α. Dispersion relations can be readily found out for the phase velocity $v_{ph} = \omega/\beta$ and group velocity $v_{\rm gr} = \partial\omega/\partial\beta$.

The characteristic impedance Z_0 of the transmission line, defined by the ratio of voltage to the current on the line, is

$$Z_0 = \sqrt{Z/Y} = \sqrt{(R + j\omega L)/(G + j\omega C)} \,. \tag{4.14}$$

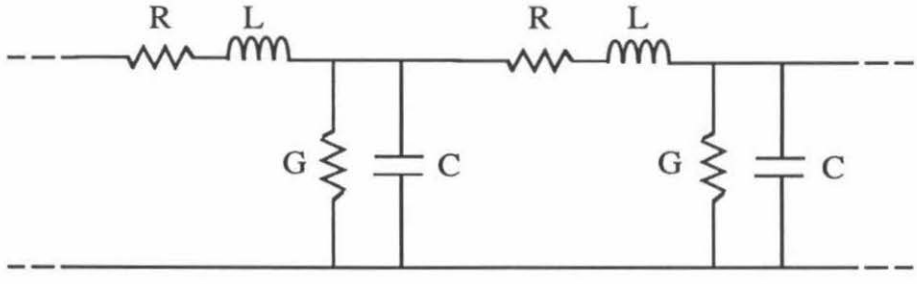

Figure 4.3: Equivalent circuit of a transmission line in the ladder representation.

The losses contributed by the conductors are represented by R, which is related to the surface impedance of the conductors. The losses in the dielectric are represented by G and are usually less important than the losses in the conductors. We will ignore the dielectric losses, *i.e.*, we assume $G = 0$. The series inductance L includes contributions from the surface impedance as well as that related to the magnetic flux in the space around the conductors.

To gain some insight on microstrip lines, let us now consider a parallel-plate line and find out how the characteristic impedance, phase velocity, and attenuation depend on geometrical factors and on the material properties of the dielectric and conductors. We assume the width w to be much greater than the spacing h so that fringing effects can be ignored. If the conductor is lossless ($R = 0$), we obtain (Jackson 1975)

$$L = \mu_0 \frac{h}{w} , \tag{4.15}$$

$$C = \epsilon_0 \epsilon_r \frac{w}{h} , \tag{4.16}$$

$$Z_0^{\text{lossless}} = \frac{\sqrt{\mu_0/\epsilon_0}}{\sqrt{\epsilon_r}} \frac{h}{w} = \frac{\eta_0}{\sqrt{\epsilon_r}} \frac{h}{w} , \tag{4.17}$$

$$\gamma^{\text{lossless}} = j\omega\sqrt{\mu_0\epsilon_0}\sqrt{\epsilon_r} = j\frac{\omega}{c}\sqrt{\epsilon_r} ; \tag{4.18}$$

here ϵ_r is the relative dielectric constant of the insulation layer. Note that $\eta_0 = \sqrt{\mu_0/\epsilon_0} = 377\ \Omega$ is the vacuum impedance and $c = 1/\sqrt{\mu_0\epsilon_0}$ is the speed of light in vacuum. The phase velocity is then

$$v_{\text{ph}} = \omega/\beta = \frac{c}{\sqrt{\epsilon_{\text{r}}}} . \tag{4.19}$$

Normal conductors will introduce RF losses due to the skin effect. The surface impedance Z_{S} of the two strips contributes to the series impedance of the transmission line, so now $Z = j\omega L + 2Z_{\text{S}}/w$ and Y is unchanged. For simplicity let us first consider the classical skin effect which gives:

$$Z_{\text{S}} = \frac{1}{\sigma\delta_{\text{c}}}(1 + j) , \tag{4.20}$$

in which δ_c is the classical skin depth:

$$\delta_c = \sqrt{\frac{2}{\mu_0 \omega \sigma}} , \tag{4.21}$$

with σ the electric conductivity of the conductor.

For a typical situation with resistivity of 0.5 $\mu\Omega$-cm (at 4 K), the penetration depth is calculated to be $\delta \approx 531$ Åat 500 GHz. Since the insulation layer is usually a few 10^3 Å, we have $\delta/h \ll 1$. Under such a condition Z_0 and γ can be approximated to the first order in δ/h as:

$$Z_0 = \sqrt{Z/Y} \approx Z_0^{\text{lossless}}(1 + \delta/2h) - jZ_0^{\text{lossless}}\delta/2h , \tag{4.22}$$

$$\gamma = \sqrt{ZY} \approx \frac{\omega}{c}\sqrt{\epsilon_r}\frac{\delta}{2h} + j\frac{\omega}{c}\sqrt{\epsilon_r}(1 + \frac{\delta}{2h}) . \tag{4.23}$$

We see that due to the skin effect, the real part of characteristic impedance is increased roughly by $\delta/2h$. The phase velocity is roughly reduced by $\delta/2h$. The attenuation constant is $(\omega/c)\sqrt{\epsilon_r}(\delta/2h)$. In one wavelength of travel the power will be attenuated by $\exp(-2\pi\delta/h)$. While the surface impedance introduces changes in characteristic impedance and phase velocity, it is the loss caused by the surface impedance that we are most concerned with. For instance, if $\delta/h \approx 0.2$, only 28.5% transmission is obtained after one wavelength travel. Here the wavelength refers to the propagation wavelength.

4.3 Design equations for microstrip lines

The geometry of a microstrip line is shown in Fig. 4.4. We calculate the characteristic impedance, phase velocity and loss of microstrip lines in the manner described by Zmuidzinas and LeDuc (1992). First the behavior of a microstrip line made from a perfect conductor ($\sigma = \infty$) is calculated using the design equations given by Hammerstad and Jensen (1980), which include the effects of the fringing fields. We also

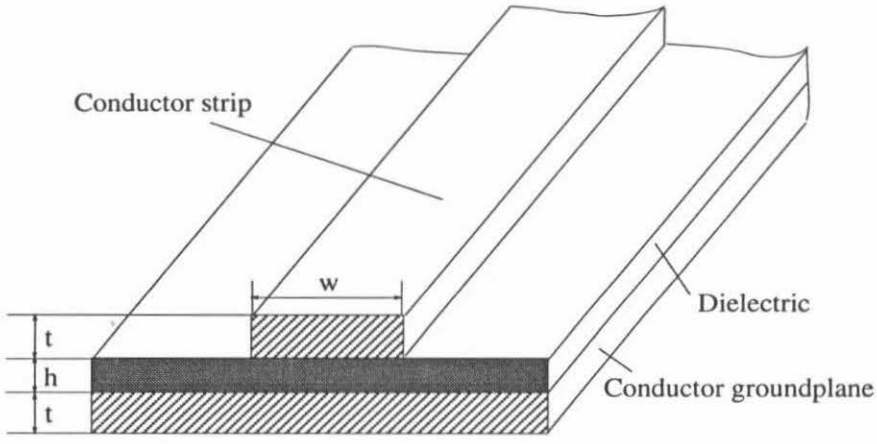

Figure 4.4: A layout of a microstrip line.

ignore dielectric losses, and only consider corrections for strip thickness and dispersion. The design equations start with an uncorrected characteristic impedance Z_{01} and effective dielectric constant ϵ_e:

$$Z_{01}(u) = \frac{\eta_0}{2\pi} \ln\left[\frac{f(u)}{u} + \sqrt{1 + (\frac{2}{u})^2}\right] , \tag{4.24}$$

$$f(u) = 6 + (2\pi - 6)\exp[-(\frac{30.666}{u})^{0.7528}] . \tag{4.25}$$

Here $\eta_0 = 376.73\ \Omega/\sqrt{\epsilon_r}$ is the wave impedance of the dielectric and $u = w/h$. The effective dielectric constant is:

$$\epsilon_e(u, \epsilon_r) = \frac{\epsilon_r + 1}{2} + \frac{\epsilon_r - 1}{2}(1 + \frac{10}{u})^{-a(u)\ b(\epsilon_r)} , \tag{4.26}$$

where

$$a(u) = 1 + \frac{1}{49}\ln\left[\frac{u^4 + (u/52)^2}{u^4 + 0.432}\right] + \frac{1}{18.7}\ln[1 + (\frac{u}{18.1})^3] , \tag{4.27}$$

and

$$b(\epsilon_r) = 0.564\ (\frac{\epsilon_r - 0.9}{\epsilon_r + 3})^{0.053}\ . \tag{4.28}$$

Including the correction for the strip thickness t, we have

$$Z_0(u, t, \epsilon_r) = Z_{01}(u_r)/\sqrt{\epsilon_e(u_r, \epsilon_r)}\ , \tag{4.29}$$

$$\epsilon_{eff}(u, t, \epsilon_r) = \epsilon_e(u_r, \epsilon_r)[Z_{01}(u_1)/Z_{01}(u_r)]^2\ , \tag{4.30}$$

with the corrected strip width u_1 and u_r given by:

$$u_1 = u + \frac{t/h}{\pi}\ \ln\left[1 + \frac{4\exp(1)}{(t/h)(\coth\sqrt{6.517u})^2}\right]\ , \tag{4.31}$$

$$u_r = u + \frac{1}{2}(1 + 1/\cosh\sqrt{\epsilon_r - 1})(u_1 - u)\ . \tag{4.32}$$

Correction for dispersion due to the non-ideal TEM mode introduces frequency dependence into the microstrip characteristic:

$$\epsilon_{eff}(f) = \epsilon_r - \frac{\epsilon_r - \epsilon_{eff}(0)}{1 + G(f/f_p)^2}\ , \tag{4.33}$$

$$Z_0(f) = Z_0(0)\sqrt{\frac{\epsilon_{eff}(0)}{\epsilon_{eff}(f)}}\frac{\epsilon_{eff}(f) - 1}{\epsilon_{eff}(0) - 1}\ , \tag{4.34}$$

where $f_p = Z_0/(2\mu_0 h)$ is an approximation to the first TE-mode cut-off frequency and G is an empirically determined factor:

$$G = \frac{\pi^2}{12}\frac{\epsilon_r - 1}{\epsilon_{eff}(0)}\sqrt{\frac{2\pi Z_0}{\eta_0}}\ . \tag{4.35}$$

Once Z_0 and ϵ_{eff} are known, the phase constant for a lossless microstrip is $\gamma = j2\pi\sqrt{\epsilon_{\text{eff}}}/\lambda_0$, and the series impedance Z and the shunt admittance Y per unit length can then be calculated from $Z = \gamma Z_0$, $Y = \gamma/Z_0$. Note that both Z and Y obtained here are purely imaginary.

Next the effect of replacing the perfect conductor by the real conductor is approximated by introducing an extra contribution to the series impedance of the line: $Z' = Z + gZ_{\text{S}}$, where Z_{S} is the surface impedance of the line and g is a geometrical factor. For finite strip width, the current distribution is non-uniform and g depends on the current distribution factor K (Pucel *et al.* 1968):

$$g = \frac{2}{w}K \ . \tag{4.36}$$

Hammerstad and Jensen found a good approximation to K:

$$K = \exp[-1.2(\frac{Z_{01}}{\eta_0})^{0.7}] \ . \tag{4.37}$$

This microstrip model is used to calculate both superconducting and normal-metal transmission lines. Now we need to find the surface impedance Z_{S}.

4.4 Surface impedance

Non-ideal conductors have a surface impedance Z_{S} which affects the characteristic of microstrip lines. For a thin conductor film of thickness d, the surface impedance is defined for a sinusoidal electric field $E_x(z,\omega)$ and current density $J_x(z,\omega)$ (Kautz 1979)

$$Z_{\text{S}}(\omega) = \frac{E_x(0,\omega)}{\int_0^d dz J_x(z,\omega)} \ . \tag{4.38}$$

The real part of Z_{S}, called the surface resistance, accounts for microstrip losses and the imaginary part, the surface reactance, contributes to the microstrip line inductance.

4.4.1 Normal-state conductors

When the electric field penetration depth is long compared to the electron mean free path, the local equation can be assumed for the relation between **J** and **E**:

$$\mathbf{J} = \sigma \mathbf{E} \ , \tag{4.39}$$

where σ is the complex conductivity. Solving Maxwell equations in the local theory for a film with finite thickness d, we obtain normal skin effect surface impedance (Matick 1969):

$$Z_S = (i\omega\mu_0/\sigma)^{1/2} \coth[(i\omega\mu_0\sigma)^{1/2} d] \ . \tag{4.40}$$

When the penetration depth is comparable with or smaller than the electron mean free path l, which is often true at high frequencies and cryogenic temperatures, a non-local form must be assumed for **J** and **E** (Kautz 1979; Pippard 1954):

$$\mathbf{J}(\mathbf{r_1}) = \frac{3\sigma}{4\pi l} \int d^3r \mathbf{r} (\mathbf{r} \cdot \mathbf{E}(\mathbf{r_1} + \mathbf{r})) r^4 e^{-r/l} \ , \tag{4.41}$$

where the relaxation time τ is assumed small compared to the inverse of the frequency ($\omega\tau \ll 1$), and the relaxation effect is not included in (4.41). This is true for microwave frequencies. In the submillimeter region and at low temperatures, $\omega\tau$ can be larger than unity. However, as discussed by Pippard, the appearance of relaxation in this region is governed not by the mean time between collisions, but by the time taken by an electron moving normal to the surface to traverse the skin depth, a much shorter time than τ since $\delta \ll l$. As a result the relaxation effect is assumed negligible in the submillimeter region.

Evaluation of the surface impedance also requires boundary conditions regarding the scattering of electrons from the conductor surface. Of the two simple limits, diffuse scattering and specular scattering, the former provides a good agreement with experiment and is used in the calculation (Kautz 1979). Following the arguments of

Pippard, the electric field in this case can be obtained by solving an integro-differential equation:

$$\frac{d^2E_x}{dz^2} = i\ al^{-3}\int_0^d dz' E_x(z')K((z'-z)/l)\ , \tag{4.42}$$

$$K(u) = \int_1^\infty dr[1/r - 1/r^3]e^{-|u|r}\ , \tag{4.43}$$

where $a = 3l^2/2\delta_c^2$. Here δ_c is the classical penetration depth given by (4.21).

The skin effect in the non-local regime is called the anomalous skin effect. A method to calculate Z_S for the anomalous skin effect is given by Kautz. A computer program was written to compute Z_S by solving (4.42) and (4.43). The formulas used are given in Appendix A.

Reuter and Sondheimer (1948) solved the integro-differential equation in the limit of infinite conductor thickness ($d \to \infty$) and obtained a simple expression for surface impedance for the extreme anomalous case ($a \gg 1$),

$$\begin{aligned} Z_S &= \frac{1}{3^{1/2}\pi^{1/3}}(1+\sqrt{3}i)\frac{a^{2/3}}{\sigma l} \\ &= \frac{3^{1/6}}{(16\pi)^{1/3}}(1+\sqrt{3}i)\mu_0{}^{2/3}\omega^{2/3}(l/\sigma)^{1/3}\ . \end{aligned} \tag{4.44}$$

As can be seen, at a certain frequency, the surface impedance in such limits depends only on σ/l, which is a constant of the material (independent of temperature).

For normal conductors the conductivity σ_n is a real constant if we ignore the time relaxation effect. For instance, the resistivity ρ of Al at room temperature is 2.45 $\mu\Omega$-cm, which corresponds to an electron mean free path l of 16 nm (Ashcroft & Mermin 1976). At lower temperatures, the resistivity can be much lower than this value. Since the product ρl is independent of temperature in bulk material (Ashcroft & Mermin 1976), and l is often limited by the conductor thickness in the case of a thin film, the amount of decrease in ρ for a thin film can be less than that for a bulk conductor. The resistivity ratio $\Re = \rho_{300K}/\rho_{4K}$ for an Al film, 200 nm thick, is

limited to 200 nm/16 nm $\approx$ 12. In practice we have measured a resistivity ratio of $\Re \approx 5$ at 4.2 K for a 200 nm thick Al film, which is equivalent to $\rho_{4K} \approx 0.5$ $\mu\Omega$-cm. The penetration depth at submillimeter frequencies and liquid helium temperature is a few tens of nanometers. Thus, the mean free path is larger than the penetration depth and is comparable to the film thickness, and we must apply the anomalous skin effect theory to calculate the surface impedance. An anomalous surface impedance result obtained by solving (4.42) and (4.43) is shown in Fig. 4.5 for an Al film of thickness 200 nm. For comparison, the results obtained with normal skin effect formula (4.40) and the extreme anomalous formula (4.44) are also presented in Fig. 4.5. It is worth noting that while the normal skin effect result is close to the anomalous one in the submillimeter region, the extreme anomalous result underestimates the surface resistance by almost 40%.

4.4.2 Superconductors

For superconductors the surface impedance should be computed by using the nonlocal Mattis-Bardeen theory (Mattis & Bardeen 1958) for a thin film as done by Pöpel (1989). This procedure can be simplified somewhat if the films are thick enough to use a bulk limit approximation. Actually, Pöpel found that if the thickness is more than three times the superconducting penetration depth, the bulk limit solution is a very good approximation to the exact solution. Pöpel carried out a numerical double integration to obtain the surface impedance, which is quite an involved procedure. Here we simplified further by using Mattis-Bardeen theory in the extreme anomalous limit, when the local approximation can be made. A complex conductivity $\sigma_s = \sigma_1 - i\sigma_2$ is conveniently introduced in this approximation. σ_s is a function of frequency and temperature, and can be calculated if the energy gap Δ and the normal state conductivity at the superconducting transition temperature σ_n are known:

$$\frac{\sigma_1}{\sigma_n} = \frac{2}{\hbar\omega}\int_{\Delta}^{\infty}[f(E) - f(E+\hbar\omega)]g(E)dE + \frac{1}{\hbar\omega}\int_{\Delta-\hbar\omega}^{-\Delta}[1 - 2f(E+\hbar\omega)]g(E)dE\ , \tag{4.45}$$

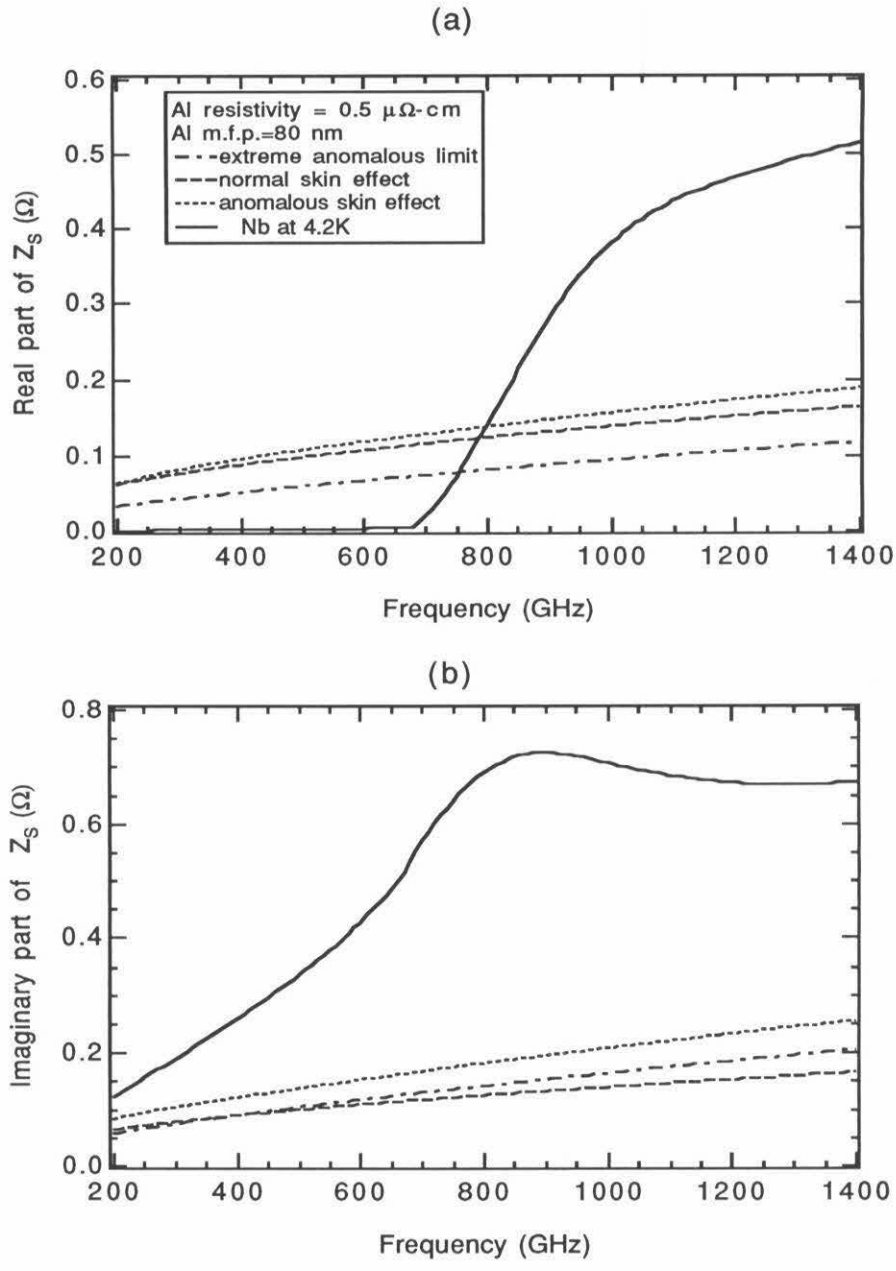

Figure 4.5: Calculated (a) real part and (b) imaginary part of surface impedance for Nb and normal-metal Al thin films at 4.2 K.

$$\frac{\sigma_2}{\sigma_n} = \frac{1}{\hbar\omega}\int_{\Delta-\hbar\omega,\ -\Delta}^{\Delta} \frac{[1-2f(E+\hbar\omega)][E^2+\Delta^2+\hbar\omega E]}{(\Delta^2-E^2)^{1/2}[(E+\hbar\omega)^2-\Delta^2]^{1/2}}dE\ , \tag{4.46}$$

where $f(E)$ is the Fermi function:

$$f(E) = \frac{1}{1+e^{E/k_BT}}\ , \tag{4.47}$$

and

$$g(E) = \frac{E^2+\Delta^2+\hbar\omega E}{(E^2-\Delta^2)^{1/2}[(E+\hbar\omega)^2-\Delta^2]^{1/2}}\ . \tag{4.48}$$

The first integral in (4.45) represents the conduction of thermally excited normal electrons, while the second integral accounts for the contribution of photon-excited quasi-particles and is zero for $\hbar\omega < 2\Delta$. σ_2 describes the effect of superconducting paired electrons. The lower limit on the integral for σ_2 becomes $-\Delta$ when $\hbar\omega > 2\Delta$.

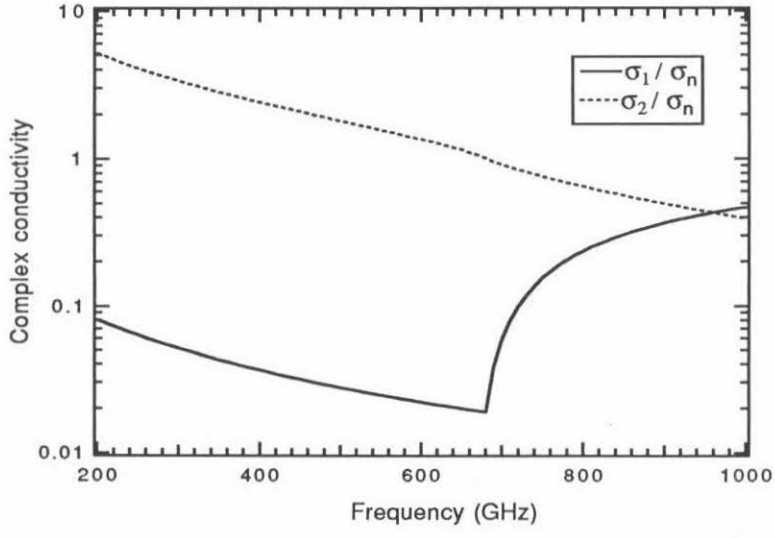

Figure 4.6: Calculated complex conductivity σ_s/σ_n for superconducting Nb at 4.2 K. The energy gap is 2.9 mV. The Nb normal-state conductivity σ_n at transition temperature 2.9 K is 5 $\mu\Omega$-cm.

The expression for σ_s is valid in the extreme anomalous limit, when the field penetration depth is small compared to the coherence length ($\lambda \ll \xi$). It is also valid in the extreme dirty limit, when the electron mean free path is smaller than the intrinsic coherence length ($l \ll \xi_0$) (Tinkham 1975). At 4.2 K, Nb has electron mean free path $l \approx$11 nm, penetration depth $\lambda \approx$86 nm and intrinsic coherence length $\xi_0 \approx$37 nm. These parameters satisfy the dirty limit condition and we can calculate the complex conductivity of superconducting Nb. For Nb, $T_C = 9.2$ K and $\sigma_n \approx 5$ $\mu\Omega$-cm. Calculated results of σ_1 and σ_2 for Nb at 4.2 K are shown in Fig. 4.6.

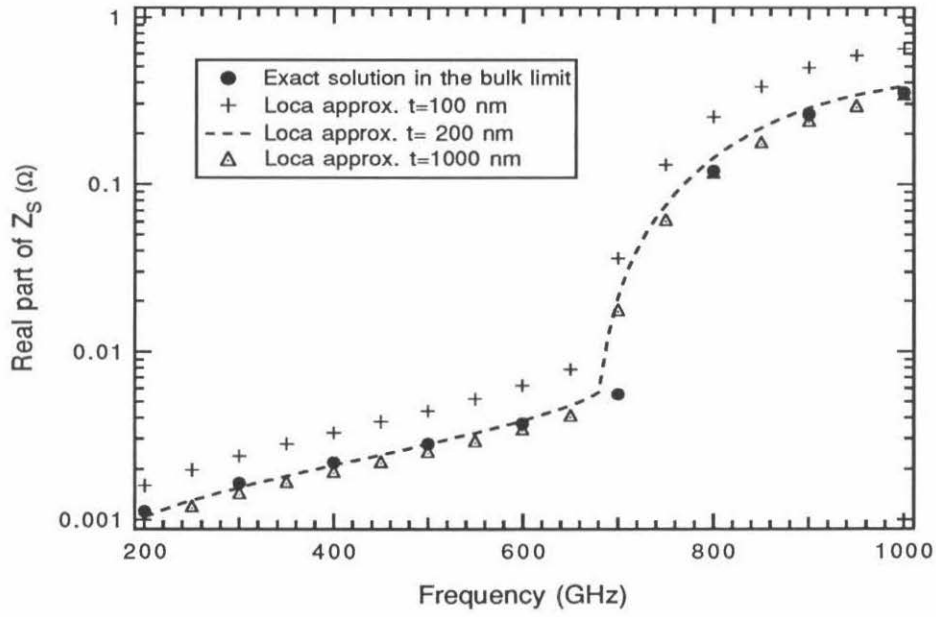

Figure 4.7: Surface impedance calculated for superconducting Nb film. Comparisons are made between exact solutions of Mattis-Bardeen theory in the bulk limit and the local approximation results.

The surface impedance is then calculated by placing this complex conductivity into the normal skin effect formula (4.40). We found good agreement between our approximate local-limit calculation and the complete non-local Mattis-Bardeen solutions for very thick films done by Pöpel. Fig. 4.7 compares our results with Pöpel's.

Back in Fig. 4.5, the real and imaginary parts of Z_S for superconducting Nb are plotted along with those for normal-metal Al. Note the real part of surface impedance of Nb increases sharply at the Nb gap frequency (700 GHz), and exceeds the value for Al at about 800 GHz. We can thus expect the RF losses in normal-metal Al lines would be less than those in Nb lines at frequencies higher than 800 GHz. Fig. 4.5b shows that the imaginary part of surface impedance of Nb is overall about three times higher than that of Al. This implies that microstrip lines made of Al would have larger phase velocity than those made of superconducting Nb.

4.4.3 Superconducting and normal-metal transmission lines

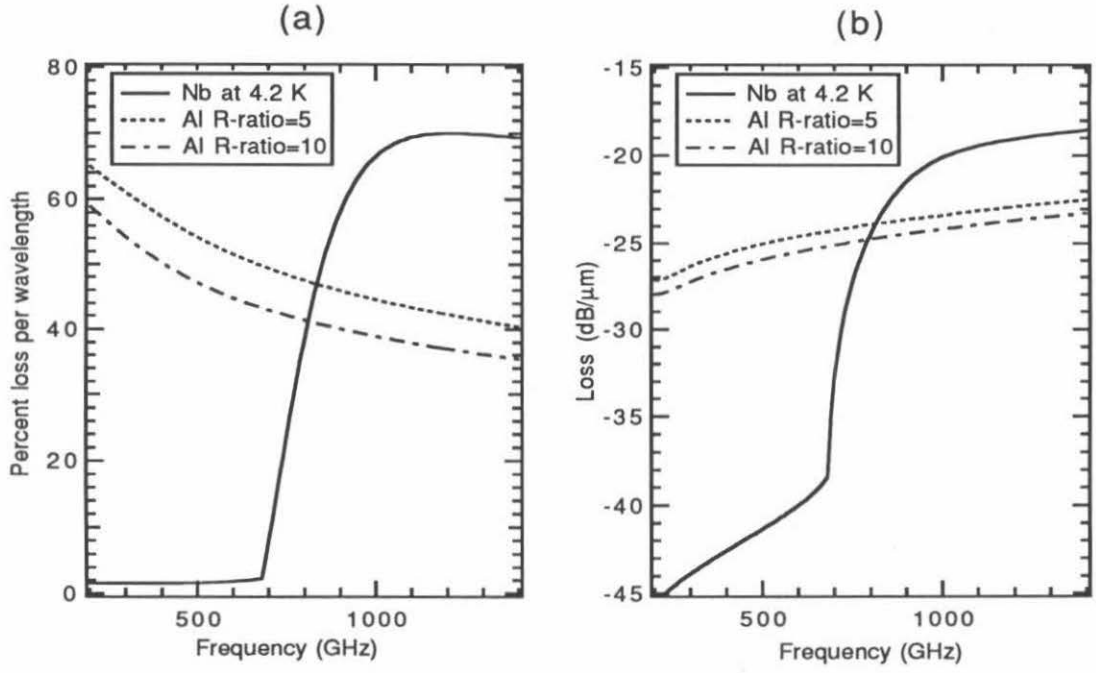

Figure 4.8: The calculated frequency dependence of (a) the power loss per wavelength and (b) the attenuation per unit length for 5 μm wide microstrip lines. The insulation layer is 400 nm SiO and the metal thickness is 200 nm. Calculations are made for temperature at 4.2 K. Two resistivity ratios ($\Re = \rho(300\text{ K})/\rho(4.2\text{ K})$) 5 and 10 are used for the Al film in the calculations; the room temperature resistivity is assumed to be 2.45 $\mu\Omega$-cm.

With Z_S calculated, the characteristics of microstrip lines can be obtained by the method described in section 4.3. For example, we have calculated the percent power loss per wavelength and the attenuation per unit length for a microstrip line. The microstrip line has a typical dimension used in the SIS tuning circuit: 5 μm width, 400 nm SiO insulation layer thickness, and 200 nm metal thickness. The results are shown in Fig. 4.8 for superconducting Nb and normal-metal Al microstrip lines. Note that the loss in the Nb line is negligible below gap frequency, but increases dramatically above 700 GHz and eventually has the same trend as a normal-metal line. Our calculation shows that the Al line is comparable in loss performance with Nb line at 830 GHz, but becomes a better choice at higher frequencies. The phase velocity of such a line made of either Al or Nb is also calculated and shown in Fig. 4.9. As pointed out earlier, since the imaginary part of surface impedance of Nb is higher than that of Al, the phase velocity of Nb microstrip line is smaller. Note that Nb microstrip line has large dispersion.

4.5 Optimization of the twin-slot double-junction SIS mixer

The goal in tuning circuit design is to achieve optimum RF coupling efficiency in the frequency band of interest. Often it is necessary to optimize the design using computer-aided programs. There are commercial software packages such as Touchstone (EEsof Inc.) for circuit simulation and optimization. However, these programs do not have the capability to deal with superconducting transmission line parameters. For normal-state microstrip lines, they calculate the conductor losses using the normal skin effect while we need to use the anomalous skin effect theory. In some cases, the superconducting line parameters had to be converted into pseudo normal-metal transmission lines to utilize the Touchstone optimization feature (Büttgenbach *et al.* 1992). To avoid this inconvenience, we have developed a design program, in which the superconducting and normal-state microstrip line models discussed in previous

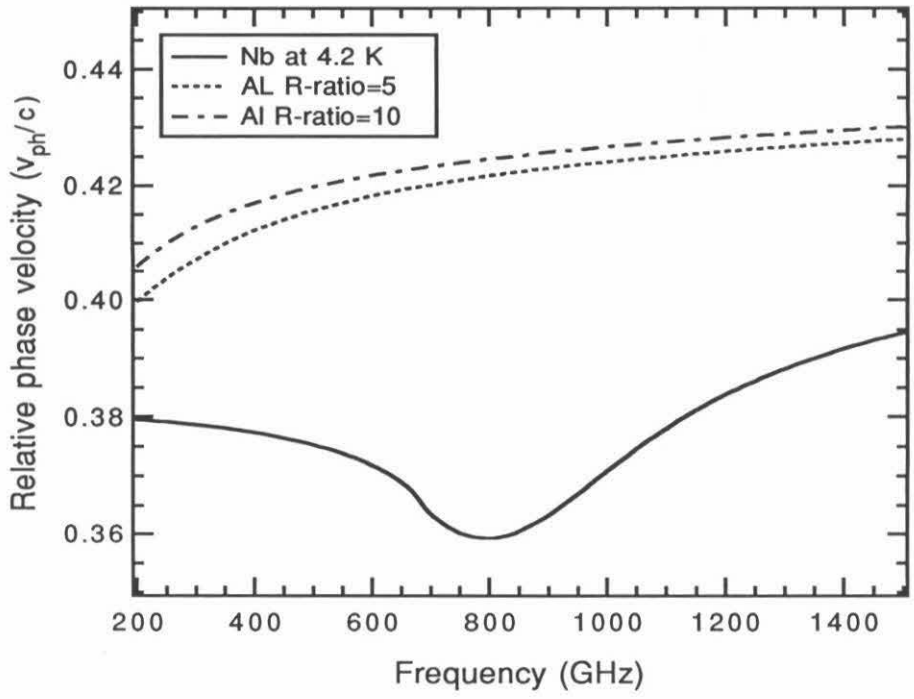

Figure 4.9: The calculated frequency dependence of phase velocity for 5 μm wide microstrip lines. The insulation layer is 400 nm SiO and the metal thickness is 200 nm. Calculations are made for temperature at 4.2 K. Two resistivity ratios ($\Re = \rho(300\text{ K})/\rho(4.2\text{ K})$) 5 and 10 are used for the Al film in the calculations; the room temperature resistivity is assumed to be 2.45 $\mu\Omega$-cm.

sections are incorporated. This program, called PCIRCUIT, was originally written by Zmuidzinas in FORTRAN 77 for the purpose of microwave circuit analysis. It is based on the microwave two-port network technique as briefly discussed in Appendix B.

As mentioned in section 4.1, a twin-slot double-junction mixer with an anti-symmetric feed (Zmuidzinas *et al.* 1994) is adopted in our design. This design has the advantage that no dc-blocking capacitance is needed in the tuning circuit. As shown in Fig. 4.2, the RF circuit design is symmetric about the center. The center microstrip connecting the two junctions serves as the tuning inductor L. The two transmission lines connecting the junctions to the slots are impedance transformers. The two radial stubs are the feed points of the twin-slot antenna and couple the radi-

ation into the transmission lines. Since the radial stubs sit at the opposite side of the slots, the two feeding signals are 180 degrees out of phase. This antisymmetric feed produces a virtual ground at the center of the tuning inductance L, so each junction is effectively shunted by an inductance of $L/2$. We can therefore look at half of the circuit for the study of the RF matching. Below we will describe how to model each circuit element using the program PCIRCUIT. The documentation for PCIRCUIT can be found in Appendix C.

Junction

The junction is modeled as an impedance shunted by its geometrical capacitance. The impedance is the RF impedance as a function of frequency calculated by (2.52) from the junction's dc IV curve. In the design stage when the exact dc IV curve is not available, the desired normal state resistance of junction can be used instead.

At high frequencies, even small junctions show the behavior of distributed elements. The two-dimensional current flow from the feeding transmission lines to the junction will cause a deviation from the simple junction model of an impedance in parallel with a capacitance. This effect has been studied for the special case of all-Nb SIS mixers at 750 GHz with junction areas of 1.5 μm $\times$ 1.5 μm and 2.5 μm $\times$ 2.5 μm, and microstrip line width of 5 μm (Naud & Zmuidzinas 1996). It is found that the deviation for 2.5 μm $\times$ 2.5 μm junction is significant while the deviation for 1.5 μm $\times$ 1.5 μm junction is negligible. We do not consider the distributed effect in PCIRCUIT.

Microstrip lines

To specify a microstrip line, we need geometrical information as well as dielectric and conductor parameters. Once these are defined, PCIRCUIT will calculate microstrip characteristics based on the models discussed in previous sections, and determine the scattering matrix. In particular, the tuning inductor is modeled as a short shunted stub and the transformers as series transmission lines.

PCIRCUIT does not consider the discontinuity effects associated with the step changes in microstrip width and the 90° bends of the microstrip lines.

Slot-antenna

The slot-antenna is a current source with a complex impedance as given in section 3.2. PCIRCUIT reads in the previously-calculated frequency-dependent impedance as a data file.

We ignore RF losses in the slot-antenna in our circuit modeling due to the lack of a simple and proved method to tackle the problem. The moment-method used to calculate the slot-antenna impedance does give the current distribution of the lossless and infinitely-thin antenna. But the singularity in the current distribution due to the infinitely thin ground plane assumed in the moment-method prevents us from integrating the current to obtain the RF power dissipation (Pregla 1980). However, we did estimate the RF dissipation in the antenna. The twin-slot antenna is approximated as a slot transmission line and the dissipative line resistance is estimated (Owyang & Wu 1958). This resistance is then included in PCIRCUIT, and we find its effect negligibly small. This result can be understood by noting that the slot width (~ 5 *mu*m) is much larger than the penetration depth of the metal.

Radial stub

An open-circuit radial stub is a good RF short and dc blocking component. For a lossy radial stub, the input impedance can be calculated using the formula given by March (March 1985). For the radial stub used in our mixer design, the real part of the impedance is typically less than 2 Ω for superconducting and normal metal stubs below 2 THz. The stub can be seen as a series impedance between the antenna and the transmission lines. Since this impedance is small compared to that of the antenna, the RF losses caused by it is also small. We can safely assume that the radial stub is a perfect short and ignore it in our mixer design.

As an example, we will show here the results by using PCIRCUIT to optimize two SIS mixers for the 1050 GHz frequency band. One mixer uses Nb tuning circuits and the other utilizes Al tuning circuits. Both mixers have the twin-slot double-junction configuration we just described. The junction is assumed to have a normal state resistance of 11.8 Ω. The thicknesses of the insulation layer and the electrodes are fixed, while the widths and lengths of the transmission lines are variables to be

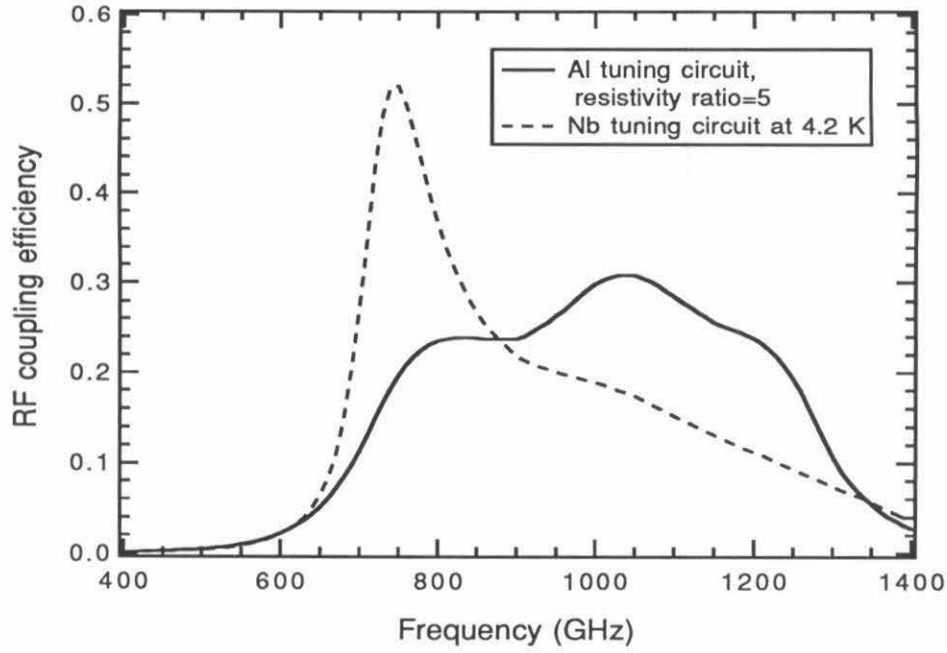

Figure 4.10: RF coupling comparison between all-Nb and Al-wiring SIS mixers. Both mixers are designed to have optimum RF coupling in the band of 1000 -1100 GHz. The Al microstrip line is calculated using the anomalous skin effect and a resistivity ratio of 5 is assumed.

optimized. The circuit program and the parameters used are given in Appendix D. The results for RF coupling efficiency are shown in Fig. 4.10.

Chapter 5 Fourier Transform Spectroscopic Study of SIS Detectors

To investigate an SIS receiver's frequency response, it is necessary to perform spectroscopic measurements over the whole submillimeter band. Fourier transform spectroscopy (FTS) has been proved to be such an ideal and powerful tool in SIS studies (Belitsky *et al.* 1995a; Bin *et al.* 1996; Büttgenbach *et al.* 1992; de Lange *et al.* 1995; Gaidis *et al.* 1996a; Hu *et al.* 1988). Large aperture and low focal ratio optics are also important to match the broad beams of most planar antennas used in quasi-optical SIS receivers. To meet the requirements needed for SIS studies, a special FTS was designed and built in our laboratory. Direct and heterodyne measurements of SIS detectors were carried out with the FTS to gain an improved understanding of the SIS frequency response. This chapter reports our efforts in using the FTS to help in SIS receiver design and calibration. A brief introduction to the FTS is provided in section 5.1. Section 5.2 describes the in-house-built FTS on which all the FTS data in this thesis were taken. Finally, some theoretical and experimental results from SIS direct and heterodyne measurements on the FTS are discussed in section 5.3.

5.1 Background on Fourier transform spectroscopy

A Fourier transform spectrometer (FTS) is basically a Michelson interferometer. It operates by separating the incoming radiation into two beams and then coherently recombining them to produce the output beam. Interference effects are produced by varying the relative length of optical paths traveled by the separated beams. This path difference is usually controlled by a moving mirror in one of the beam paths. The output beam intensity is modulated by the path difference δ. Let's assume the source has a spectrum intensity $S(\sigma)$, where σ is the wavenumber (inverse of wavelength λ).

The electric field intensity of the incoming radiation is correspondingly $E(\sigma)$. This radiation is split into two beams by a beamsplitter and the field intensities of each beam are $E(\sigma)e^{i2\pi\sigma x}$ and $E(\sigma)e^{i2\pi\sigma(x+\delta)}$ when they recombine at the output. The flux intensity at the output is then a linear superposition of the two beams:

$$\begin{aligned} B(\sigma,\delta) &= |E(\sigma)e^{i2\pi\sigma(x)} + E(\sigma)e^{i2\pi\sigma(x+\delta)}|^2 \\ &= S(\sigma)(1+\cos(2\pi\sigma\delta)) \ . \end{aligned} \tag{5.1}$$

The total power received by the detector is:

$$I(\delta) = \text{const} \int_0^\infty S(\sigma)(1+\cos\ (2\pi\sigma\delta))d\sigma \ . \tag{5.2}$$

When $\delta = 0$, all the waves add constructively and the power reaches maximum value:

$$I(0) = \text{const}\ 2\int_0^\infty S(\sigma)d\sigma \ . \tag{5.3}$$

When δ is very large, the cosine term oscillates fast and the average is zero in (5.1):

$$I(\infty) = \text{const} \int_0^\infty S(\sigma)d\sigma = \frac{1}{2}I(0) \ . \tag{5.4}$$

The relation $I(\infty) = \frac{1}{2}I(0)$ can be used in practice to align the optics in FTS system.

Rewriting (5.2), we obtain

$$I(\delta) - \frac{1}{2}I(0) = \int_0^\infty S(\sigma)\cos(2\pi\sigma\delta)d\sigma \ . \tag{5.5}$$

The inverse cosine transform reveals the spectral information:

$$S(\sigma) = \text{const} \int_{-\infty}^\infty [I(\delta) - \frac{1}{2}I(0)]\cos(2\pi\sigma\delta)d\delta \ . \tag{5.6}$$

Equation (5.6) can be generalized to complex Fourier transforms (Bell 1972):

$$S(\sigma) = \text{const} \int_{-\infty}^\infty [I(\delta) - \frac{1}{2}I(0)]e^{-i2\pi\sigma\delta}d\delta \ . \tag{5.7}$$

The intensity as a function of the path difference $I(\delta) - \frac{1}{2}I(0)$ or $I(\delta)$ is called an interferogram. The right side of (5.7) is an inverse Fourier transform of the interferogram and is called its spectrum.

In practice the interferogram $I(\delta)$ is sampled at discrete values of δ over a finite interval. The discrete interferogram is then inverse Fourier transformed by a computer to form a discrete spectrum. The problems encountered in discrete Fourier transforms for finite interferograms are nicely discussed by Brigham and Bell (Bell 1972; Brigham 1974).

The finite optical path difference sets the frequency resolution of the FTS and caused false sidelobes in the transformed spectra. This can be understood by examining the special case of a monochromatic source. The interferogram of a monochromatic source is an infinite cosine function of optical path displacement. Its spectrum is a δ-function at the source frequency. The truncated interferogram at a finite interval is equal to the product of the infinite interferogram and a rectangular function. Since the spectrum of a rectangular function is a sinc function ($\sin x/x$), according to the convolution theorem, the spectrum of the truncated interferogram is equal to the convolution of the δ-function and the sinc function, which is a sinc function. It is easy to derive that the full width at half maximum of this sinc function is $0.61/L$ where L is the maximum optical path difference. The resolution of the FTS is defined as

$$\Delta\sigma = \frac{0.61}{L} \,. \tag{5.8}$$

The sinc function has large negative sidelobes and these sidelobes often cause confusion in the spectrum interpretation. A corrective procedure for modifying the basic transform is to multiply the interferogram with an "apodization" function. The spectra of apodization functions have smaller sidelobes but larger half widths. Thus apodization reduces sidelobes at the cost of resolution. The often used apodization functions are given in Table 5.1, along with their properties.

Table 5.1: Apodization functions and their properties

Apodization function	Full width at half maximum peak	First sidelobe amplitude relative to maximum peak
No apodization	$0.6/L$	-22%
$\cos(\pi\delta/2L)$	$0.8/L$	-7.0%
$1-\lvert\delta\rvert/L$	$0.88/L$	+4.8%

The periodic sampling of an interferogram, in discrete Fourier transform theory, turns the spectrum into a periodic function with period $1/\Delta l$, where Δl is the optical path difference between sampling points. Only half of this period $1/\Delta l$ contains positive frequency spectrum. If the bandwidth of the physical spectrum is greater than $1/(2\Delta l)$, there will be frequency overlap in the computed spectrum. The distortion of the spectrum due to this frequency overlap is called aliasing. To avoid aliasing the maximum allowed spectral frequency σ_{max} is

$$\sigma_{max} \leq \frac{1}{2\Delta l} \,. \tag{5.9}$$

The sampled interferogram can be inverse Fourier transformed by the fast Fourier transform (FFT) algorithm on a computer (Brigham 1974). The FFT algorithm can be found in most computational packages. It requires that the number of sampled data points is equal to 2^n, n being an integer.

5.2 Construction of a laboratory FTS

5.2.1 FTS system description

An FTS with large throughput and high resolution was desired at the beginning of the 90's in our submillimeter group to study the properties of the SIS receivers properties at high frequencies ($\geq$ 500 GHz). Large throughput was needed to assure a good signal to noise ratio. A resolution much better than 1.5 GHz (the IF frequency) was desired to resolve the sidebands from the local oscillator in a heterodyne detection.

Since commercially available FTS systems were expensive and not very effective in the forementioned features, a custom-built FTS was proposed and constructed in our lab, with a large aperture size of 10 inches, a small focal ratio of $f/2.5$, and a high frequency resolution of 114 MHz. The FTS design is based on a shearing interferometer which was constructed to perform holographic measurements of the surface of the CSO dish (Serabyn *et al.* 1991). Fig. 5.1 depicts a schematic diagram of the FTS. The whole system is built on a 6 ft $\times$ 12 ft optical table. Below the FTS system is described in detail.

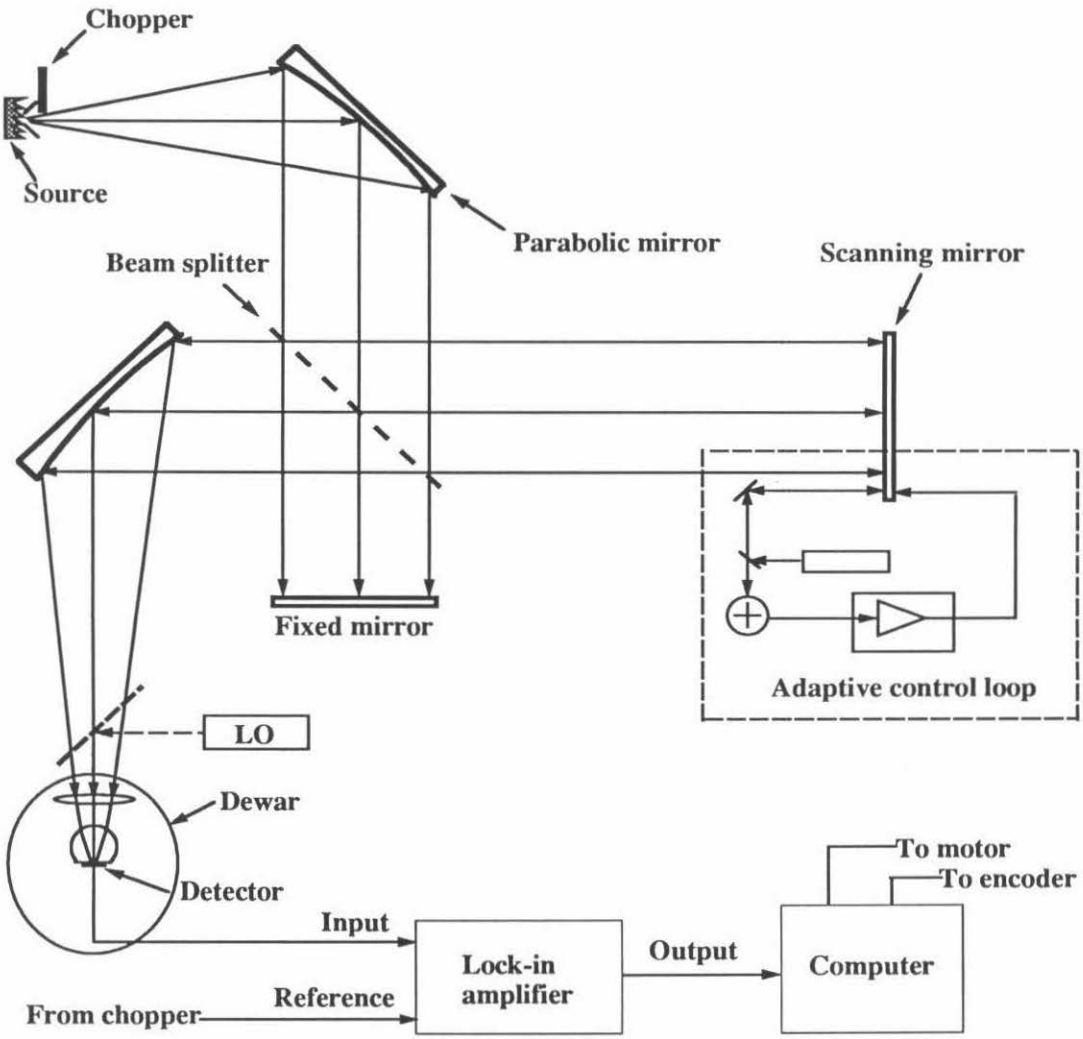

Figure 5.1: A block diagram of the FTS system.

The source

The radiation source consists of chopped hot and cold loads. The hot source is a low resistance coil of NiCr alloy in a ceramic housing (Perkin Elmer Corp.). When supplied with an ac voltage of 5 V and a current of 6 A, the temperature is roughly 1050 °C. The temperature can be varied by changing the current. The cold load is an Eccosorb sheet immersed in liquid nitrogen, serving as a 77 K blackbody. The source size is about 1 square inch.

The mirrors and beamsplitter

The optics is designed to have a large aperture size $\sim$ 10 inch. The fixed mirror and the moving mirror are 10 inch by 10 inch first surface mirrors. The entrance and exit collimation mirrors are 10 inch 12 inch 45° off-axis parabolas with focal ratios $f/2.5$ or $f/4.0$. The focal ratios are chosen small to match the broad beams of most planar antennas used in quasi-optical SIS detectors. The collimating mirrors were machined out of aluminum at the Caltech Central Plant with a numeral mill and gold-plated afterwards. The surface accuracy of the mirrors is about 3 μm.

The 14-inch-diameter beamsplitter is made of stretched sheet of Mylar. The holder of the beamsplitter is designed such that change of a different thickness beamsplitter is an easy procedure. The beamsplitter efficiency is a periodic function of the frequency (Chantry 1971) and can be calculated if the index of refraction, the thickness of the film and the beamsplitter angle are known. We use the beamsplitter in a 45° angle. Calculated efficiencies of the two beamsplitters (assuming the index of refraction of Mylar is 1.73) used on our FTS are plotted against frequency in Fig. 5.2. It is seen that a 2 mil (50.8 μm) thick Mylar beamsplitter is a good choice to cover the 300 - 1500 GHz range.

The throughput of the FTS is mainly determined by the beamsplitter efficiency. The effect of finite aperture size on throughput reduction comes in when the wavelength increases to about 1/10 of the aperture size. For our FTS, this sets a low frequency limit at $f \sim$ 12 GHz. This limit is far below the frequency region of interest.

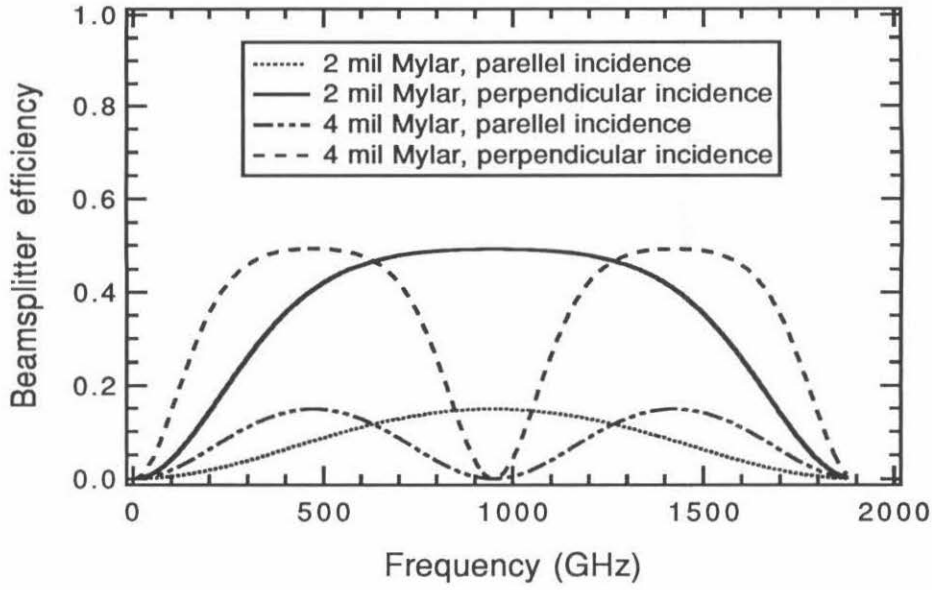

Figure 5.2: Calculation results of beamsplitter efficiency for 2 mil and 4 mil thick Mylar sheets.

The mirror positioning and frequency resolution

The moving mirror is controlled by a 2 meter long lead screw. A step motor with a linear microstepping driver moves the mirror continuously during a scan. The mirror position is read by a grating encoder and a bidirectional counter (Heidenhain Corp.). There is a TTL pulse given by the counter every 10 μm. This pulse is used to activate the data acquisition system such that samples are taken 20 μm apart. According to (5.9), this sampling interval sets the highest allowed frequency of the FTS:

$$f_{\max} = \frac{c}{2 \times (20\ \mu\text{m} \times 2)} = \frac{300\ \text{mmGHz}}{80\ \mu\text{m}} = 3750\ \text{GHz}\ . \tag{5.10}$$

The position of the fixed mirror can be adjusted so that two-sided or one-sided interferograms can be taken to the full length of the scanning mirror travel. Here a two-sided interferogram refers to a symmetric interferogram that the optical path difference is from $-\delta$ to $+\delta$. Only two-sided interferograms have been employed on this FTS. The advantage of taking two-sided interferograms is that there is no

Table 5.2: Available FTS frequency resolutions vs. scanning distances for two-sided interferograms

Scan length (mm)	5.12	10.24	20.48	40.96	81.92	163.84	···	1310.72
Resolution (GHz)	29.3	14.6	7.3	3.7	1.8	0.912	···	0.114

phase error distortions in the spectrum caused by missing a sample point at the true zero path difference. A second advantage is that it helps average out the effect of any experimental asymmetries of the interferogram due to lack of flatness or poor alignment of components (Richards 1967). The drawback of this method is that it takes twice the time for data-taking to achieve the same resolution. Also the track has to be twice the length. In order to utilize FFT algorithm, the number of data points should be 2^n, with n an integer. For our two-sided interferograms, the longest usable scan length is thus limited to $\sim$ 1.31 m. The highest frequency resolution, according to (5.8), is therefore

$$\Delta f = \frac{c}{2 \times 1.31} = 114 \text{ MHz} . \tag{5.11}$$

The available resolutions are listed in Table 5.2.

Electronic control and readout

The signal from the detector goes to the input of a lock-in amplifier. The integration time constant of the lock-in is determined by the user for a desirable signal to noise ratio. The speed of the scanning mirror is then set accordingly so that the step period of the mirror is twice the integration time constant.

A personal computer is dedicated to the FTS for system control and data acquisition. It reads in data and controls the mirror movement through the interfaces with the microstepping driver, the bidirection counter, and the lock-in amplifier. At present, a Macintosh power PC 9200 is serving as the computer for FTS and the FTS program is written in Labview, a graphic programming package from National Instrument Corp.

System purging with nitrogen

Table 5.3: Specifications of the FTS

Aperture and f-number	10 inch $\times$ 10 inch, $f/2.5$ or $f/4.0$
Frequency range	up to 3750 GHz
Frequency resolution	down to 114 MHz for two-sided interferogram
Beamsplitter	stretched sheet of 2 mil Mylar
Source	a hot coil of NiCr alloy vs. cold Eccosorb
Mirror drive	2 m translation stage with dc step motor
Position reading	grating encoder and a counter
Computer and programming	Power PC and Labview

Since water absorption is severe in the submillimeter, the optical path of the FTS should be clear of water vapor. We chose to purge the FTS system with nitrogen gas instead of evacuating it, because of the large volume of the system. The optical part of the FTS system is covered in a plastic box made of quarter-inch thick acrylic. Duct tape is adopted to seal the box for ease of use. The box is purged with dry nitrogen and held slightly over atmospheric pressure during FTS experiments to keep water from reentering. Liquid nitrogen from the standard 160 liter dewar is turned into room temperature vapor through a 10 feet long copper pipe wrapped with electric heater tape (about 400 Watts). The flow rate is controlled by a ball valve. A relative humidity of $\sim$ 5 - 10% is achievable after slow purging for one day.

The specifications of this FTS are summed up in Table 5.3.

5.2.2 FTS alignment

The flat and parabolic mirrors were first aligned with a He-Ne laser. All the mirrors can be tilted about two axes with an articulating support. This support consists of a cross which is bolted to the back of the mirror (or mirror holder). The cross has a machined recess at its center. A similarly machined conical recess is provided in the support stand, capturing a 3/4-inch-diameter ball. Four screws, one near each end of the cross, hold the cross to the support stand. By turning the screws in the appropriate directions, the angle of the mirror can be adjusted.

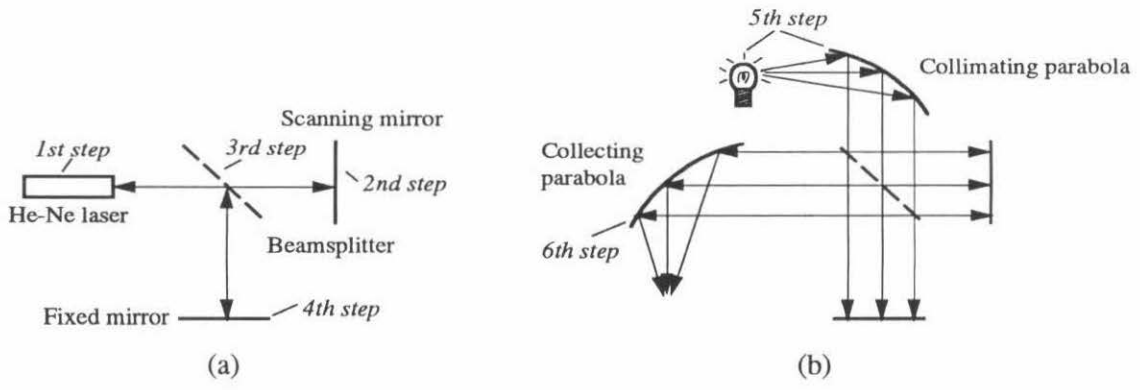

Figure 5.3: Steps in aligning the FTS system.

Fig. 5.3 shows the steps used in the He-Ne laser alignment. First the laser beam is adjusted so that it is 10 inches above the optical table and parallel to the lead screw shaft which moves the scanning mirror. This step ensures the laser beam is on the optical axis. Secondly, the moving mirror is adjusted so the reflected laser beam coincides with the outgoing beam at the laser output window. The beamsplitter is then put into position and adjusted so that the reflected laser beam from the beamsplitter is 10 inches above the optical table and is perpendicular to the transmitted beam. The fourth step is to align the fixed mirror to make sure the laser beam going to and the laser beam reflected back from the fixed mirror coincide at the beamsplitter. For the alignment of the parabola, an optical noncoherent point source is used. The source is placed at the focus of the collimating mirror, and the source and the mirror are adjusted together so that the images of the source reflected from the plane mirrors are back on the source. This assures that the beam from the source is collimated and is parallel to the optical axis established by the laser beam.

It is critical to have the moving mirror and fixed mirror each perpendicular to the incident radiation beams. Mirror tilt and lack of alignment of one mirror relative to the other can seriously affect the efficiency of the interferometer. The requirement for alignment is that at the exit port the wave fronts of the two beams must be parallel within a wavelength across the whole aperture. We can quantitatively describe this

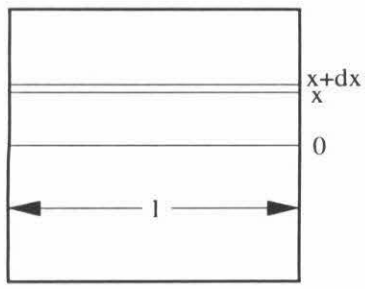

(a) Aperture of the flat mirror

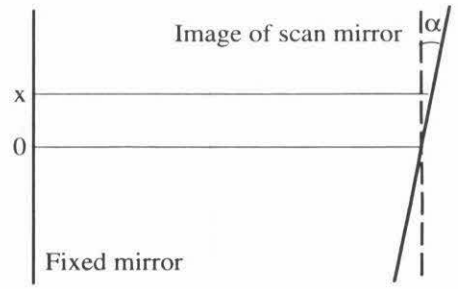

(b) Misalignment angle between two flat mirrors

Figure 5.4: Calculation of mirror misalignment

requirement by following arguments (Williams 1966). Fig. 5.4 shows the rectangular aperture of the mirror and the relative mirror positions. For a monochromatic source the power dP in the imaged interference pattern contributed by a small element of area $dA = ldx$ is

$$dP(\sigma, \delta) = 2I(\sigma)(1 + \cos 2\pi\sigma\delta)ldx \ , \tag{5.12}$$

as derived in section 5.1 if the two flat mirrors are perfectly aligned. When one mirror is tilted by a small angle α (in radians), the optical path difference becomes $\delta + 2\alpha x$, so

$$dP(\sigma, \delta) = 2I(\sigma)(1 + \cos 2\pi\sigma(\delta + 2\alpha x))ldx \ . \tag{5.13}$$

Integrating over the whole aperture, the total power becomes:

$$\begin{aligned} P(\sigma, \delta) &= 2I(\sigma) \int_{-\frac{l}{2}}^{\frac{l}{2}} (1 + \cos 2\pi\sigma(\delta + 2\alpha x))ldx \\ &= 2I(\sigma)l^2(1 + \frac{\sin(2\pi\sigma\alpha l)}{2\pi\sigma\alpha l}) \cos(2\pi\sigma\delta) \ . \end{aligned} \tag{5.14}$$

The interferogram is defined as in (5.5),

$$P(\sigma,\delta) - 1/2P(\sigma,0) = 2I(\sigma)l^2\text{sinc}(2\pi\sigma\alpha l)\cos(2\pi\sigma\delta) \ . \tag{5.15}$$

So the degradation in the interferogram is expressed as

$$B'(\sigma,\delta) = [\text{sinc}(2\pi\sigma\alpha l)]B(\sigma,\delta) \ . \tag{5.16}$$

Since the modification term in brackets is independent of path difference δ, it will appear as an amplitude distortion in the reconstructed spectrum:

$$I'(\sigma) = I(\sigma)[\text{sinc}(2\pi\sigma\alpha l)] \ . \tag{5.17}$$

The amplitude of spectrum at wavenumber σ will be reduced to zero when $\sigma\alpha l = 1/2$, *i.e.*, $\alpha = 0.5\lambda/l$. The amplitude will be 95% of its original value if $\alpha = 0.088\lambda/l$ and 50% if $\alpha = 0.30\lambda/l$. At higher frequencies, the alignment requirement on α is more stringent.

Unfortunately, during the alignment of the moving mirror, we found that its normal did not maintain a constant direction as the mirror moved along the translation stage. This is because the 2 meter lead screw is not straight and the thread pitch is not uniform. By shining an on-axis laser beam onto the mirror while it was moving and observing the movement of the reflected laser spot on a wall far away, we were able to estimate the angle change in the mirror's normal. Over the entire scanning distance the change in the normal was as large as 1.7 mrad. This was not tolerable for our frequency range of interest. To reduce this angle change, an adaptive optical control system was constructed.

Fig. 5.5 shows the block diagram of this adaptive control system. The idea is to use negative feed-back to stabilize the normal when the mirror is moving. A two-axis tilt positioner equipped with two piezo-translators (Physik Instrumente) holds the mirror from the back to the mirror support. When applying voltage to the two piezo-actuators, the mirror can be adjusted in horizontal or vertical directions. A He-Ne

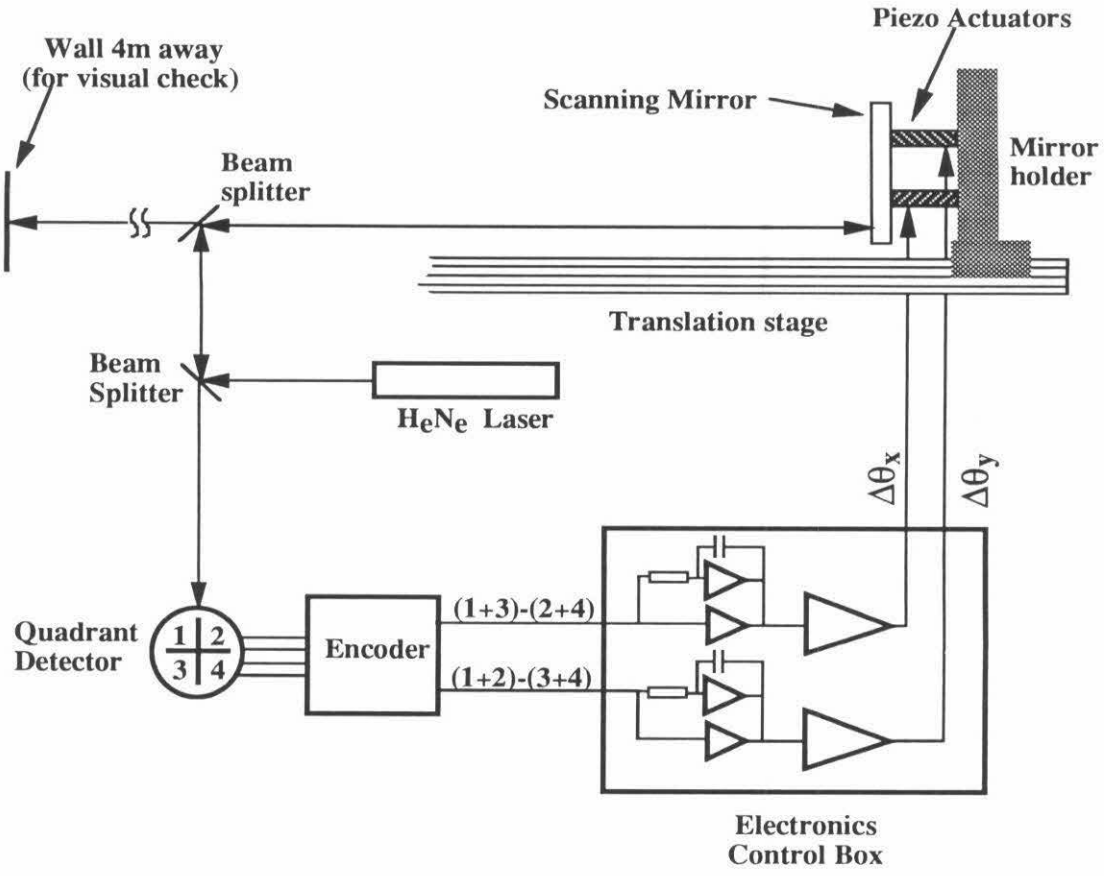

Figure 5.5: Block diagram of the optical control system for the moving mirror in the lab FTS system.

laser is devoted permanently to this system. The laser is adjusted so the incident beam to the mirror is parallel to the optical axis. The laser beam reflected back from the mirror is collected by a quadrant photon detector. The changes in the normal of the moving mirror in horizontal (x) or vertical (y) directions can then be turned into error signals by an electronic decoder. These electronic error signals are amplified by a proportional-integral (PI) power circuit and sent to drive the corresponding piezo-actuators. Since the piezo has a large capacitance (1.6 μF), care must be taken to avoid making the feed-back loop a positive one when the loop gain is larger than unity.

After the introduction of the optical control system, the angular swing of the moving mirror was reduced by more than 100 times. Now the swing is <1.7 mrad/100$\sim$ 17 μrad. As mentioned earlier, to preserve 95% of the original spectrum amplitude, the tilt angle should be smaller than $0.088\lambda/l$. At 2 THz, this corresponds to 52 μrad. Thus we conclude that with the control system we do not have to worry about the problem caused by the moving mirror misalignment.

5.3 Direct and heterodyne detection of SIS receivers with the FTS

5.3.1 Direct detection

Using an SIS junction as a direct detector on the FTS, we can obtain information about the SIS mixer's frequency response, and further gain knowledge of the tuning circuits.

Now we will derive the responsivity of the SIS direct detector based on the quantum tunneling current discussed in section 2.3.1. The direct tunneling current under RF irradiation was given by (2.30),

$$I_{\rm dc}(V_0, V_\omega) = \sum_{n=-\infty}^{\infty} J_n^2(eV_\omega/\hbar\omega) I_{\rm dc}(V_0 + n\hbar\omega/e) \ , \tag{5.18}$$

where $I_{\rm dc}(V_0)$ represents the unmodulated SIS dc IV characteristic, and V_ω is the applied RF voltage amplitude at frequency ω. For a direct detector, the incoming signal is small ($eV_\omega \ll \hbar\omega$) so that only single photon processes are important. Equation (5.18) reduces to the direct current increase (Tucker & Feldman 1985),

$$\Delta I_{\rm dc} = \frac{1}{4V_\omega^2} \frac{I_{\rm dc}(V_0 + \hbar\omega/e) - 2I_{\rm dc}(V_0) + I_{\rm dc}(V_0 - \hbar\omega/e)}{(\hbar\omega/e)^2} \ . \tag{5.19}$$

The dissipative current at the signal frequency is given by (2.31),

$$I_\omega(V_0, V_\omega) = \sum_{n=-\infty}^{\infty} J_n(eV_\omega/\hbar\omega)[J_{n+1}(eV_\omega/\hbar\omega) + J_{n-1}(eV_\omega/\hbar\omega)]I_{\rm dc}(V_0 + n\hbar\omega/e) \ . \tag{5.20}$$

In the limit of small ac amplitude, $I_\omega(V_0, V_\omega)$ can be reduced to

$$I_\omega = V_\omega \frac{I_{\rm dc}(V_0 + \hbar\omega/e) - I_{\rm dc}(V_0 - \hbar\omega/e)}{2(\hbar\omega/e)} \ . \tag{5.21}$$

The responsivity of a direct detector is defined as the induced change in direct current per unit ac signal power absorbed by the detecting element. The RF power absorbed by the junction is $P_{\rm RF} = V_\omega I_\omega/2$. So the responsivity is

$$\begin{aligned} R_i = \Delta I_{\rm dc}/P_{\rm RF} &= \frac{e}{\hbar\omega} \frac{I_{\rm dc}(V_0 + \hbar\omega/e) - 2I_{\rm dc}(V_0) + I_{\rm dc}(V_0 - \hbar\omega/e)}{I_{\rm dc}(V_0 + \hbar\omega/e) - I_{\rm dc}(V_0 - \hbar\omega/e)} \\ &\equiv \frac{e}{\hbar\omega}\,\eta_{\rm Q} \ . \end{aligned} \tag{5.22}$$

Here $\eta_{\rm Q}$ is the quantum efficiency of the junction in analogy to a photo-diode detector (Wengler & Woody 1987; Wengler 1992). For an ideal superconducting tunnel junction with no subgap leakage and no gap smearing, the responsivity becomes

$$R_i = \begin{cases} e/\hbar\omega, & \text{if } V_{\rm gap} - V_0 < \hbar\omega < V_{\rm gap} + V_0; \\ 0, & \text{otherwise.} \end{cases} \tag{5.23}$$

where V_0 is the dc bias voltage. Physically, each absorbed photon $\hbar\omega$ contributes one electron charge e to the tunneling current. The calculated responsivities for an ideal SIS junction and a real Nb tunnel junction are shown in Fig. 5.6. The junctions are supposed to have a gap voltage of 2.95 mV and a normal state resistance of 10 Ω. The bias voltage is 2.5 mV. Note that the two responsivity curves are nearly identical in the region $V_{\rm gap} - V_0 < \hbar\omega < V_{\rm gap} + V_0$, where the responsivity has a simple f^{-1} frequency dependence. This close identity is due to the sharp non-linearity and low dark current of the real device.

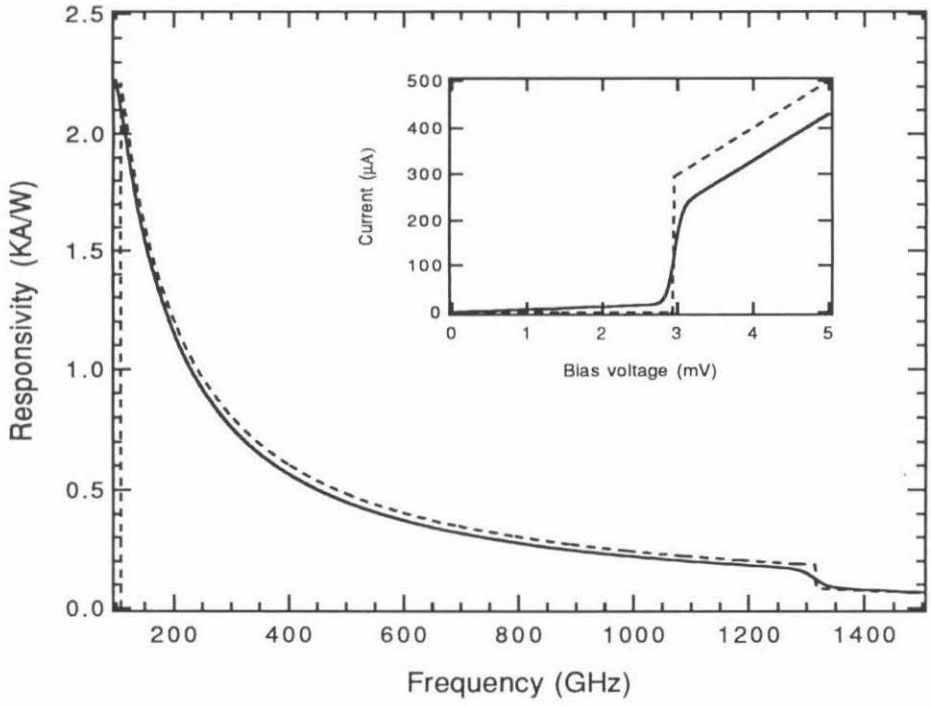

Figure 5.6: Calculated responsivity of SIS direct detector. The dashed line is for a theoretical SIS direct detector with a perfect sharp IV and zero sub-gap leakage current. The solid line is calculated using a real SIS IV curve. The IV curves are shown in the inset. Both IVs have normal-state resistance 10 Ω and gap voltage 2.95 mV. The bias voltage is 2.5 mV.

The change in direct current is measured as the signal from the FTS system. The spectrum obtained can be expressed as a product of several terms:

$$\Delta I_{\rm dc}(\omega) = R_i \; \eta_{rf} \; \eta_{opt} \; \eta_{FTS} \; P_S \; . \tag{5.24}$$

where R_i is the junction responsivity, η_{rf} is the RF coupling efficiency between the junction and the integrated antenna, η_{opt} is the optical coupling between the FTS and the detector, η_{FTS} is the FTS throughput, and P_S is the source spectrum. In the Rayleigh-Jeans limit ($h\nu \ll kT$), a single mode antenna, like the integrated antenna used in SIS detectors, receives power independent of frequency, $P_{\rm S} = k_{\rm B} T \Delta\nu$, from a blackbody of temperature T. η_{FTS} is mainly determined by the beamsplitter efficiency

as mentioned in section 5.2. η_{opt} is assumed to be a slow variation of frequency. This is not always true, as in the case of a thick quartz filter or window, which introduces fast Fabry-Perot resonances. From (5.24) it is obvious that by correcting the spectrum with beamsplitter efficiency and the detector's responsivity, we can obtain the RF coupling efficiency η_{rf}, and thus knowledge about the tuning circuits.

A typical interferogram using an SIS junction as a direct detector is shown in Fig. 5.7, along with the spectrum corrected for beamsplitter and detector responsivity. Since no absolute calibration is available for the FTS, we do not know the absolute value of the RF coupling efficiency. However, the FTS spectrum is still very useful in evaluating the tuning circuit design and the SIS mixer's performance by giving the shape and bandwidth of the frequency response.

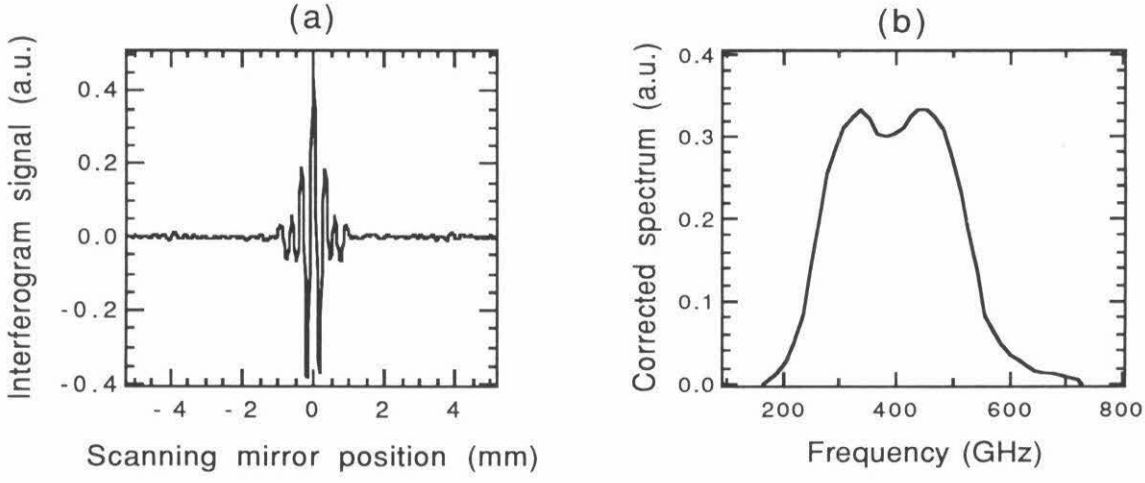

Figure 5.7: A typical interferogram (a) and its spectrum (b). The spectrum has been corrected for the beamsplitter efficiency and SIS responsivity. The resolution is 14 GHz. The data was obtained for a Nb SIS device with an Al tuning circuit designed to work in the 450 GHz band.

5.3.2 Heterodyne detection with the FTS

In the early days of SIS receiver development when the bandwidth was narrow, it was of importance to know if the responsivity of the two sidebands was the same. Even

today when broadband SIS mixers are available, it is still of interest to see that the two sidebands are equal in mixing. Heterodyne testing with the FTS provides a way to determine the sideband ratio.

The setup for a heterodyne test on the FTS is similar to a direct test on the FTS except 1) a local oscillator is introduced by a beamsplitter right in front of the dewar window; and 2) the signal is taken at the IF power output. The incoming radiation from the FTS is same as in direct detection mode. Below, a straightforward derivation is given to explain the heterodyne test results.

We simplify the problem by assuming that the conversion gain for the source and image are G_S and G_I, as can be calculated using Tucker's theory. The IF amplifier has a pass band centered at σ_{IF} with a bandwidth Δ_{IF}. This pass band can be described by a filtering function $F(\sigma - \sigma_0)$, as shown in Fig. 5.8(a). Suppose the radiation coming out of the FTS system has an intensity $B(\sigma, \delta)$ as described in section 5.1, the output IF power will be

$$P(\sigma, \delta) = G_S B(\sigma, \delta) F(\sigma - \sigma_S) + G_I B(\sigma, \delta) F(\sigma - \sigma_I) \ , \tag{5.25}$$

where $\sigma_S = \sigma_{LO} + \sigma_{IF}$ and $\sigma_I = \sigma_{LO} - \sigma_{IF}$ are the source and image wavenumbers. Using (5.1) for $B(\sigma, \delta)$,

$$B(\sigma, \delta) = S(\sigma)(1 + \cos(2\pi\sigma\delta)) \ , \tag{5.26}$$

we can obtain the interferogram by integrating over wavenumber σ:

$$\begin{aligned} P(\delta) &= \int_0^\infty P(\sigma, \delta) d\sigma \\ &= \int_0^\infty [G_S F(\sigma - \sigma_S) + G_I F(\sigma - \sigma_I)] S(\sigma)(1 + \cos(2\pi\sigma\delta)) d\sigma \ . \end{aligned} \tag{5.27}$$

Following the same steps in section 5.1, we obtain the spectrum after doing the inverse Fourier transform. The spectrum contains

$$[G_S F(\sigma - \sigma_S) + G_I F(\sigma - \sigma_I)]S(\sigma) \ . \tag{5.28}$$

This expression exactly provides the sideband information, as shown in Fig. 5.8(b). The heterodyne spectrum is equivalent to picking out the two sidebands and multiplying them by their corresponding conversion gains.

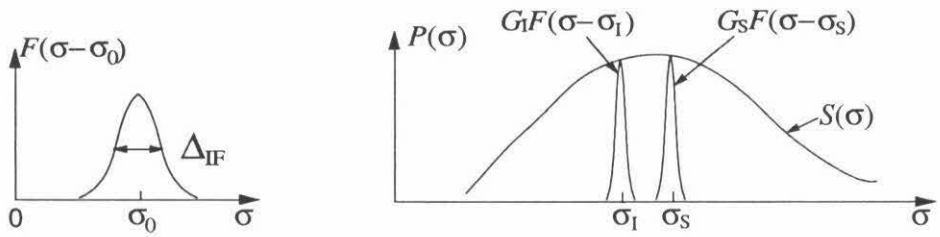

Figure 5.8: A spectroscopic view to show the heterodyne test process for an SIS detector with the Fourier transform spectrometer. (a) The filtering function represented by the IF amplifier circuit. (b) The heterodyne spectrum picks out two sidebands using the IF filtering function.

A heterodyne FTS interferogram and its spectrum are shown in Fig. 5.9 (Gaidis *et al.* 1996a). The device is an all-Nb SIS mixer which was designed to work at 750 GHz band. Since the IF amplifier is centered at 1.5 GHz with a bandwidth of 500 MHz, in order to separate the two sidebands a high frequency resolution of 114 MHz was used. The LO frequency for this test is 742 GHz. The spectrum (Fig. 5.9b) clearly shows significant response only near the LO frequency. The IF bandwidth and double-sideband operation are evident from the inset. The negative sidelobes are due to the finite interferogram and the chosen apodization procedure as discussed in section 5.1. Presumably the upper sideband peak is weaker than the lower sideband peak because of absorption near the 750 GHz water line. The FTS interferogram (Fig. 5.9a) shows the high frequency oscillations characteristic of the

742 GHz LO (see inset), modulated by the 3 GHz sideband separation and 500 MHz IF bandwidth.

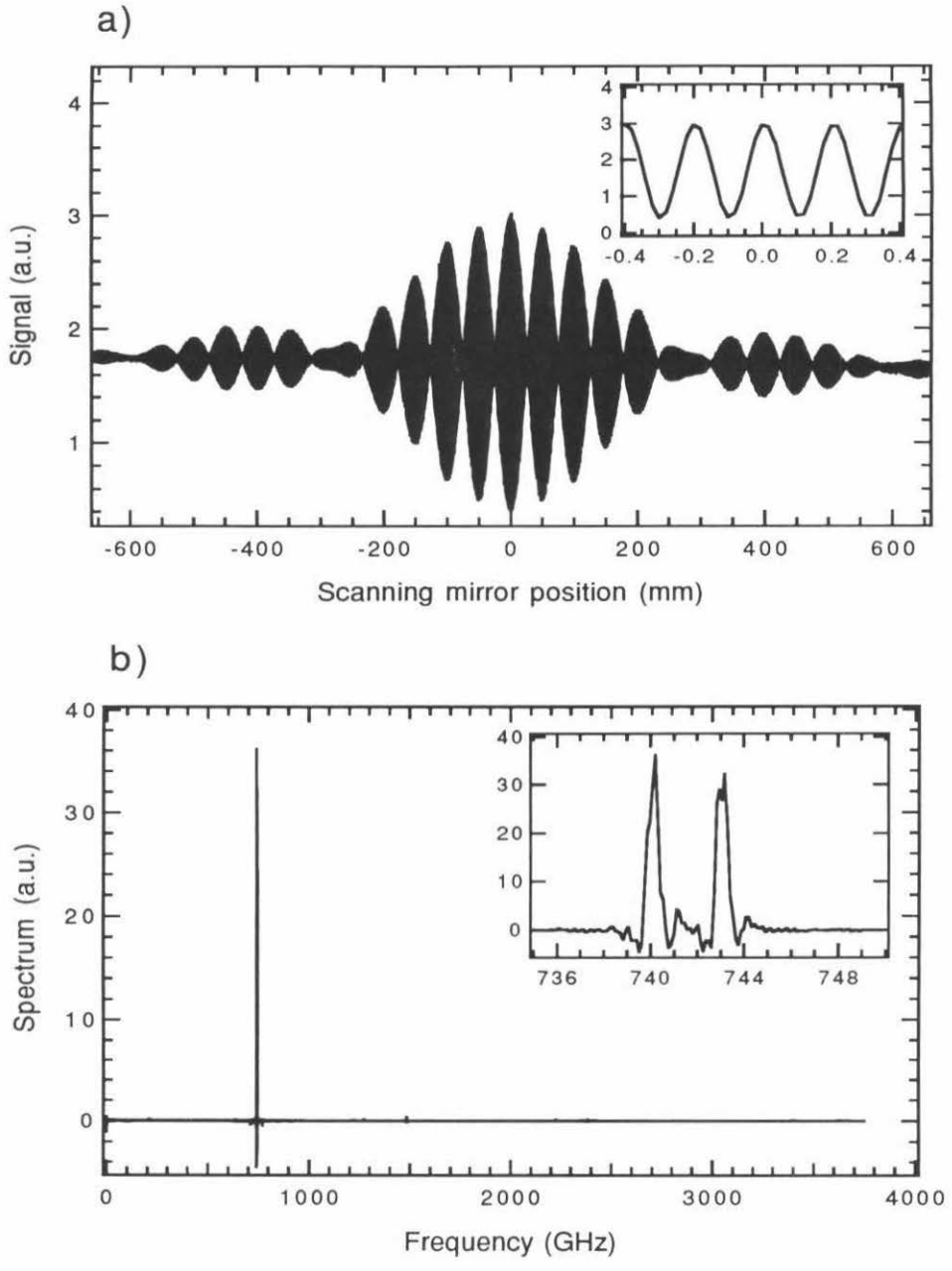

Figure 5.9: Heterodyne FTS interferogram (a) and the spectrum (b) showing two sidebands. The device under test is an all-Nb SIS mixer designed to work for the 750 GHz band. Courtesy of Mike Gaidis.

Chapter 6 All-Nb SIS Mixers for 400 - 850 GHz

This chapter describes the low-noise quasi-optical all-Nb SIS mixers recently constructed by the Caltech submillimeter group. These mixers are the result of an ongoing effort based on previous work (Zmuidzinas & LeDuc 1992; Zmuidzinas *et al.* 1994; Zmuidzinas *et al.* 1995). Improvements in receiver sensitivity have been made possible by concentrating on better optics and careful design of tuning circuits using our PCIRCUIT optimization program. The 400 - 850 GHz band is covered with four separate fixed-tuned mixers. Uncorrected double-sideband receiver noise temperatures around $5h\nu/k_B$ have been obtained to 700 GHz, and better than 540 K receiver temperature at 808 GHz.

Most of the work in this chapter has been published (Gaidis *et al.* 1996a).

6.1 Design and fabrication of all-Nb SIS mixers

The twin-slot double-junction antisymmetric-feed mixer configuration discussed in chapter 3 was employed for our new mixer designs. This configuration has several advantages previously mentioned, including low antenna driving impedance ($\sim 30\ \Omega$), a symmetric main beam, and no need for a dc blocking capacitance in the tuning circuits. Compared to the previous tuning circuit designs in the group (Zmuidzinas *et al.* 1995), right-angle bends in the transformer microstrip were introduced. These bends allowed better optimization of the impedance match between the slot-antenna and the tunnel junctions.

Critical current density $J_C \approx 10$ kA/cm^2 was the nominal design value for our Nb tunnel junctions. This current density corresponds to a junction normal-state resistance and area product $R_N A \approx 20\ \Omega$-μm^2, according to (2.15). The specific capacitance varies from approximately 65 fF/μm^2 to 85 fF/μm^2 for junctions with this critical current density. Since the relatively low antenna impedance promotes

good impedance matching to low-resistance tunnel junctions, large area junctions between 1.2 μm^2 ($R_N \sim 17\ \Omega$) and 2.3 μm^2 ($R_N \sim 9\ \Omega$) can be designed making use of JPL's all-optical-lithography junction fabrication process. Higher-resistance submicron junctions could be fabricated using electron-beam lithography, but the processing is more difficult, and the smaller devices can be more sensitive to static discharge. In addition, large-area devices are less susceptible to saturation from higher-intensity sources. One drawback of large junctions is the need for higher LO power, which scales directly with the total junction area. This can pose a problem at high frequencies, when strong LO power is not available, as will be shown later.

During the design stages, the most uncertain parameters are the junction specific capacitance and the junction area that will be achieved in a given fabrication run. To allow for parameter variation, three different nominal junction sizes were included for each tuning circuit design. The tuning circuit for each frequency band was designed for a junction area of 1.7 μm^2 and an assumed specific capacitance 85 fF/μm^2. The same tuning circuits were used on junctions with sizes of 1.2 μm^2 and 2.3 μm^2. So for the middle design, the junction would have a normal state resistance of 11.8 Ω and a capacitance of 140 fF.

A different tuning circuit was designed for each of the 450, 550, 650, and 750 GHz frequency bands. The design method optimized the rf coupling efficiency from the antenna to the tunnel junction resistance in the frequency range of interest, as discussed in chapter 4. For microstrip lines, the thickness of the Nb conductor films was assumed to be 200 nm. The insulation SiO layer had a nominal thickness of 200 nm for the center inductor but 400 nm for the transformer sections. The devices all utilized a 2.5 μm length of microstrip (with the width and thickness equal to those of the inductor) to connect the last transformer section with the inductor section. The insulation thickness around the junction was limited to about 200 nm because a thicker one would make the self-aligned lift-off technique difficult. The thicker insulation layer of the transformer sections helped to increase the characteristic impedance of the microstrip line. The width of the inductor was fixed at 5 μm. Optimiza-

Table 6.1: Assumed parameters in all-Nb mixer design

junction $R_N A$ product	20 Ω-μm^2
junction size	1.7 μm^2
junction specific capacitance	85 fF/μm^2
SiO thickness for the inductor	200 nm
SiO thickness for the transformer	400 nm
SiO dielectric constant	$\epsilon = 5.6\epsilon_0$
Nb film thickness	200 nm
Nb gap voltage V_{gap} at 0 K	2.9 mV
Nb critical temperature T_C	9.2 K
Nb normal state resistance at T_C	5 $\mu\Omega$-cm
physical temperature of the device	4.2 K

tion variables included the length of the inductor and the widths and lengths of the transformers. For all-Nb mixers, two sections of transformers were used.

The PCIRCUIT program was then used to optimize the tuning circuits in a frequency bandwidth of 100 GHz (*e.g.*, 400 - 500 GHz for the 450 GHz band). To summarize, the assumed parameters used in the design are given in Table 6.1, and the optimized microstrip widths and lengths are listed in Table 6.2. The calculated characteristic impedance and effective wavelength of the designed inductor and transformer microstrip lines at the center frequencies are presented in Table 6.3.

The mixer chips were fabricated at the JPL Center for Space Microelectronics Technology, using the standard Nb/Al-oxide/Nb trilayer process (LeDuc *et al.* 1987). First the trilayer was deposited *in situ* onto a 50 mm diameter, 0.25 mm thick high-resistivity silicon wafer. The ground plane and the slot antennas were defined with standard optical lithography and lift-off. Secondly a layer of 200 nm SiO film was deposited by thermal evaporation. The junctions were then defined by optical lithography and formed by reactive ion etching (RIE). Thirdly, an extra layer of 200 nm SiO was deposited on the appropriate area to produce a total SiO thickness of 400 nm for the impedance transformer. The transmission lines were then made out of a 0.2 μm thick Nb layer. Finally, the contact pads for the IF connectors and dc bias supply

Table 6.2: Designed parameters for the all-Nb SIS tuning circuits

microstrip parameters (width × length, μm^2)	**450 GHz device**	**550 GHz device**	**650 GHz device**	**750 GHz device**
Inductor (between jct. centers)	5.0 × 23.5	5.0 × 14.9	5.0 × 9.8	5.0 × 6.9
1st transformer section	2.0 × 51.9	2.0 × 45.9	2.0 × 37.7	5.8 × 15.0
2nd transformer section	4.6 × 62.3	4.7 × 50.7	4.5 × 41.1	3.3 × 15.0

Table 6.3: Characteristic impedance and effective wavelength of the designed microstrip lines given in Table 6.2 at the designed center frequency

characteristic impedance & effective wavelength	**device 450 GHz**	**device 550 GHz**	**device 650 GHz**	**device 750 GHz**
inductor Z_0	7.8 Ω	7.9 Ω	8.0 Ω	8.3 Ω
inductor λ_{eff}	216 μm	175 μm	145 μm	121 μm
1st transformer Z_0	27.2 Ω	27.4 Ω	27.8 Ω	11.7 Ω
1st transformer λ_{eff}	259 μm	210 μm	176 μm	148 μm
2nd transformer Z_0	13.8 Ω	13.6 Ω	14.3 Ω	19.1 Ω
2nd transformer λ_{eff}	252 μm	204 μm	171 μm	146 μm

were covered with gold for easy contacting. The whole wafer was diced into 1.2 mm × 1.5 mm individual mixer chips. A picture of a single mixer chip is shown in Fig. 6.1.

For this batch of mixer fabrication, it was found through the use of the test die on the device wafer that the undercut in the junction dimensions was ~ 0.2 μm. The junction specific capacitance was ~ 85 fF/μm^2 as determined by FTS tests discussed in next section.

6.2 Direct detection with the Fourier transform spectrometer

The mixer was installed in the test receiver dewar described in chapter 3, and receiver response as a function of frequency was measured with the FTS system described in chapter 5 by using the mixer as a direct detector. Usually the FTS (unheated) 300 K hot source chopped against 77 K cold source gave sufficient signal to allow scanning with 3.6 GHz resolution in less than 30 minutes.

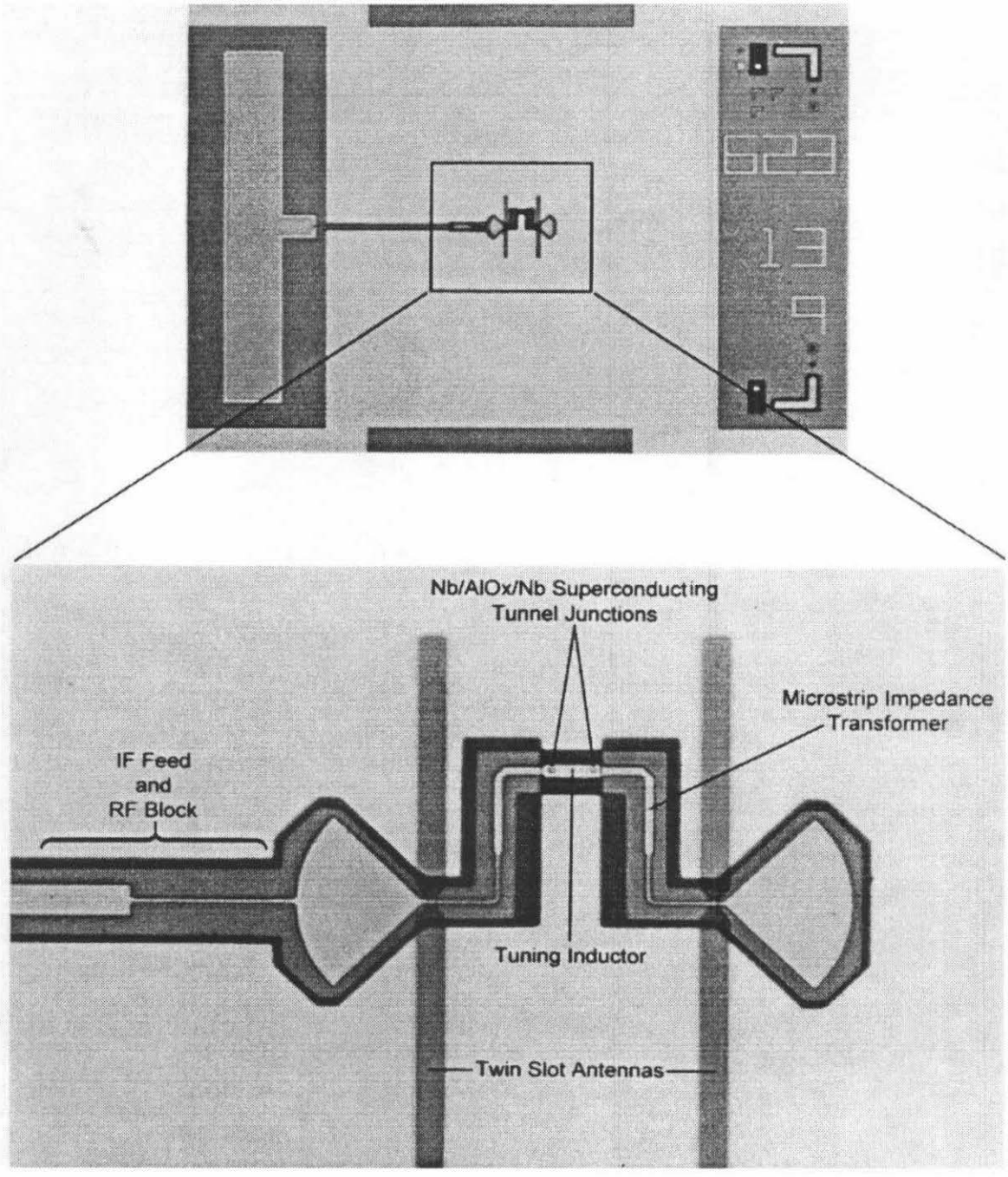

Figure 6.1: SEM picture of an all-Nb SIS mixer design. The upper portion of the figure shows the entire 1.2 mm × 1.5 mm mixer chip. Wire bonds make contact to the ground plane and to the large pad on the left. The lower portion of the figure details the device. The vertical slot antenna is sensitive to horizontal polarization. The 1.5 GHz IF is coupled out using a long section of coplanar waveguide that is attached to the RF choke on the left.

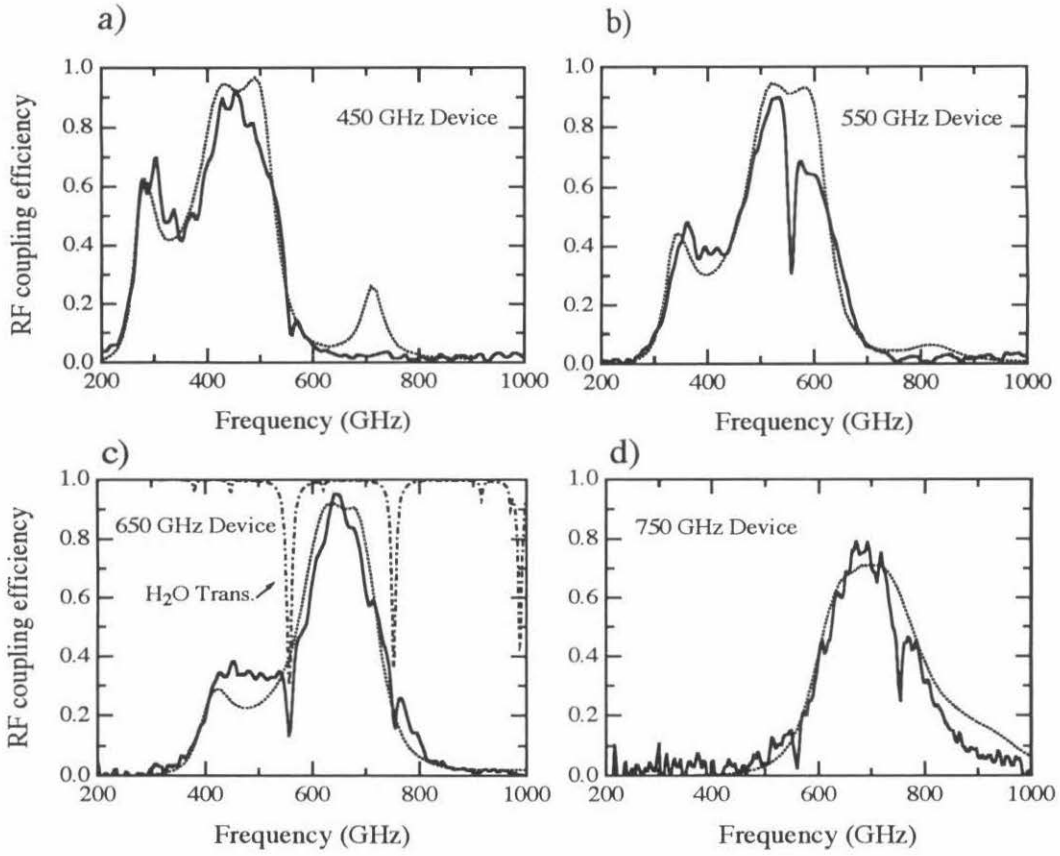

Figure 6.2: FTS measured response (solid lines) vs. mixer simulation (dashed lines) for the four devices spanning the 400 – 850 GHz band. Devices are labeled by the design center frequency. Graph (c) includes a curve representative of submillimeter transmission through the residual water vapor in the FTS.

Fig. 6.2 shows four measured FTS spectra taken with four devices for different design center frequencies. All the devices have a nominal designed junction area of 2.3 μm^2, but an actual area of approximately 1.7 μm^2 due to the undercut. In the figure, the theoretical simulations for RF coupling efficiency are also drawn for each device. Since no absolute calibration is available for the FTS system, the vertical scaling of the FTS data is adjusted to give the best match to the simulation. In the meantime, the best simulation is found by varying the junction specific capacitance to have the best bandwidth fit to the measured data.

In general, the agreement between simulation and experiment was quite good, given the nonidealities present in the measurement: strong water absorption lines at 557 and 752 GHz, and Fabry-Perot resonances from the quartz IR filter spaced approximately 30 GHz apart. These resonances are particularly noticeable in Fig. 6.2d, where the "bandpass" of the AR-coating on the quartz IR filter did not extend below about 700 GHz. Only two corrections were made to the FTS data: for the optical efficiency of the Mylar beamsplitter within the FTS, and for the quantum responsivity of the detector, which scales as $1/\nu$.

The most significant deviations from theory occur in the 450 GHz device near 700 GHz, in the 550 GHz device near 600 GHz, and in the 750 GHz device above 800 GHz. The reduced response apparent in the FTS data for the 450 GHz device near 700 GHz is due to a $\sim$ 91.5% decrease in the antenna main-beam efficiency, which was not incorporated into the simulation. No explanation has been found for the discrepancy in the 550 GHz device, but it is reproducible in similar devices from the same batch. The deviation in 750 GHz device above 800 GHz may be due to larger-than-expected surface loss in Nb above the gap frequency.

More than 20 different devices were tested (by Mike Gaidis) in this manner, and all agreed with the simulations to a degree represented by the graphs in Fig. 6.2, thus indicating that our simulation method is reasonably reliable. For a given fabrication run, the junction capacitance is the only significant variable parameter. When this is fixed by FTS data from one device, the FTS data from remaining devices on the same wafer will closely match the simulations with no fittable parameters (other than the arbitrary amplitude scaling). Recent device batches have consistently yielded specific capacitances of 85 $\pm$5 fF/μm^2. This is determined from FTS measurements of the device bandpass, as compared with simulations (below the Nb gap), and is adjusted for junction area variations through the use of test die on the device wafer. The uncertainty and variation in the junction areas limits the accuracy with which the junction specific capacitance can be determined. The (minor) observed variations in junction resistance have only a small effect on the overall bandwidth.

6.3 Heterodyne measurements

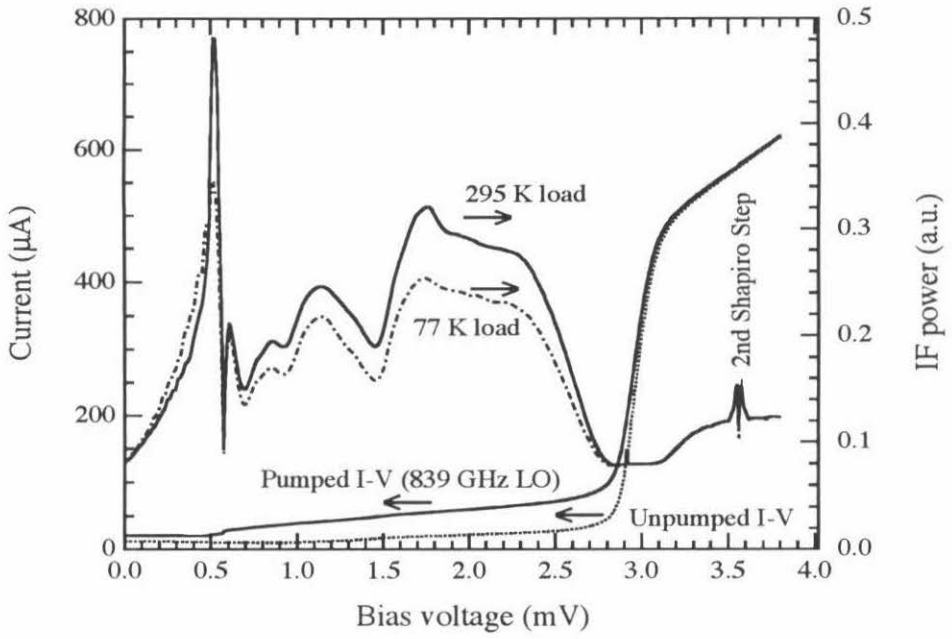

Figure 6.3: Current vs. voltage and IF power vs. voltage for 750 GHz device at 2.7 K. The LO frequency is 839 GHz, and the DSB receiver noise temperature is 722 K.

The noise temperatures of several devices, including those in Fig. 6.2, were measured using the Y-factor method. Our noise temperatures were referred to the input of the beamsplitter; unless otherwise noted, no corrections were made for beamsplitter or other optical losses. Fig. 6.3 shows the dc current-voltage characteristics of the 750 GHz device. The pumped (839 GHz) and unpumped IVs are shown for a bath temperature of 2.7 K. The second Shapiro step is visible at ~ 3.5 mV, and the photon step from the nonlinearity at $V = -2\Delta/e \approx -2.9$ mV appears at $V \approx +0.6$ mV, as expected from the 839 GHz LO input ($h\nu/e \approx 3.5$ mV). Also shown in Fig. 6.3 are the total IF output power in a 500 MHz bandwidth when room temperature and 77 K absorbers are placed at the receiver input. The curves are relatively smooth (particularly near the first Shapiro step), indicating good suppression of Josephson noise. With no mechanical tuning elements – simply adjustment of the junction dc bias,

magnetic field, and LO power – this device gives a DSB receiver noise temperature of 722 K at the 839 GHz LO frequency.

Fig. 6.4 displays receiver noise temperatures as a function of frequency for several of our best devices at a bath temperature of 4.2 K. The high-frequency (750 GHz) device was also tested at a pumped-LHe temperature of 2.7 K, with resulting noise temperatures displayed with open markers. Upon cooling to 2.7 K, the noise decreases by more than 100 K over most of the band of the 750 GHz device, in part due to the reduced dark current and its shot noise. (The dark current typically represents $\sim$ 40% of the total LO-pumped bias current at 4.2 K.)

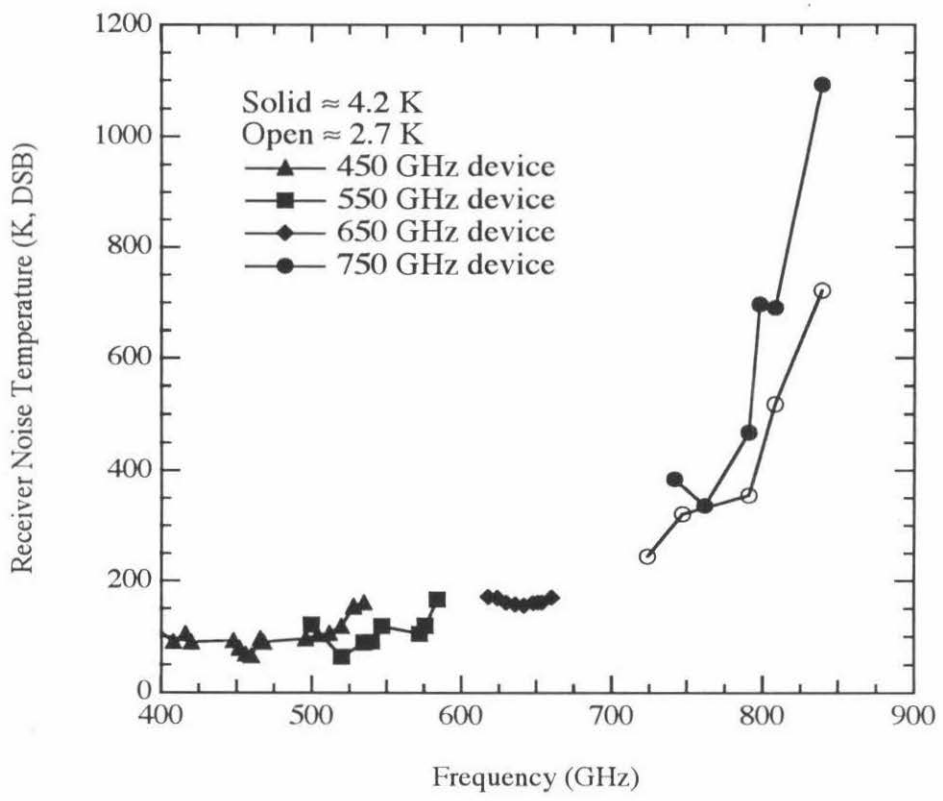

Figure 6.4: Uncorrected DSB noise temperatures of the devices described in Table 6.2. Note the superconducting gap $2\Delta/h$ is $\sim$ 700 GHz for our Nb films. Due to RF loss in the Nb, noise temperatures exhibit a sharp increase above this frequency.

Particularly at the higher frequencies, the receiver noise temperatures are adversely affected by the relatively low output power of our LO chains, and the situ-

ation is further degraded by our large junction areas. However, the use of thicker beamsplitters to couple in more LO power does not improve the receiver noise temperature, as a greater portion of the signal is reflected away from the mixer. The 750 GHz device would offer significantly lower noise temperatures if a stronger LO source and a thinner beamsplitter were employed. If we correct for beamsplitter losses, the 839 GHz, 4.2 K receiver noise temperature drops from 1100 K to $\sim$ 800 K. The anomalously low noise temperature of the 750 GHz device at 4.2 K and 761 GHz is the result of a more powerful LO. At this frequency, a far-infrared laser LO source was used, which produced a good deal more power than our standard LO chain. A thinner beamsplitter was employed ($\sim$ 6 μm Mylar) to improve the signal coupling efficiency.

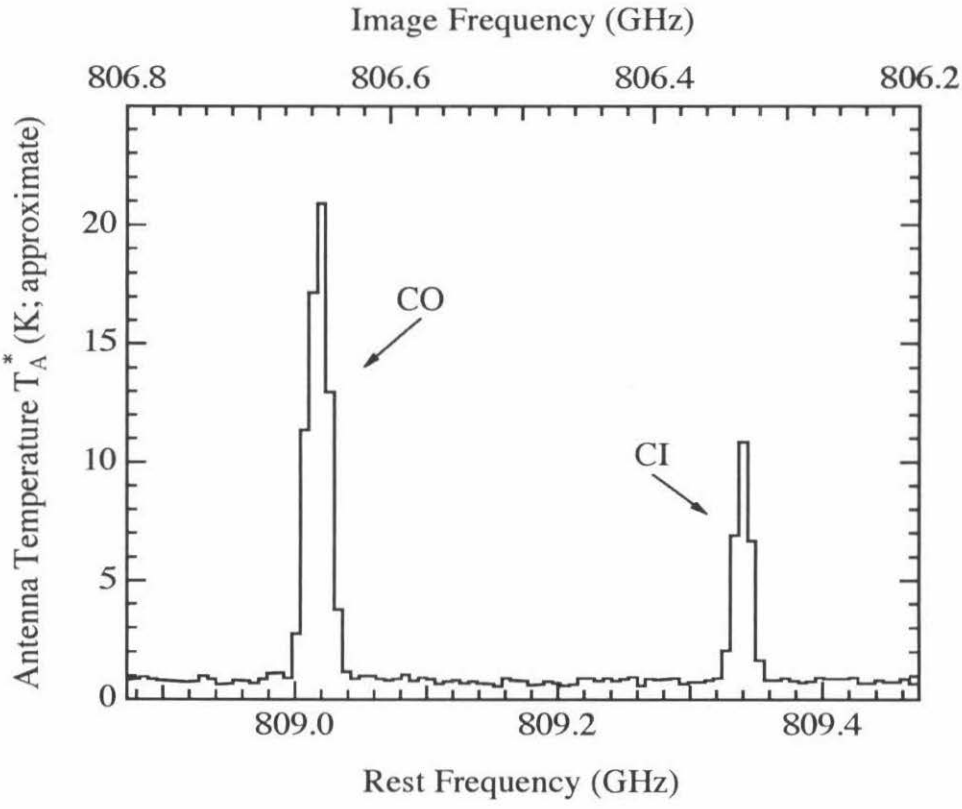

Figure 6.5: Observed emission from the CI ($^3P_2 \rightarrow {}^3P_1$) and CO (J = 7 $\rightarrow$ 6) transitions in M17.

To our knowledge, the (uncorrected) results presented in Fig. 6.4 are the best, or near the best for any broadband heterodyne receiver. At frequencies below the Nb gap, optical losses are likely to be the dominant contribution to the receiver noise temperature. Although the noise temperatures increase with frequency dramatically above the gap due to increased RF losses in the Nb, the 800 GHz results are particularly impressive if compared with the nearest competitor – GaAs Schottky corner-cube receivers at 1500 K (*after* correcting for the $\sim 50\%$ corner-reflector antenna efficiency) (Harris *et al.* 1989).

The low-noise 800 GHz receiver was used during observing runs aboard NASA's Kuiper Airborne Observatory (KAO) in June, 1995. The CI ($^3P_2 \rightarrow {}^3P_1$) and CO ($J = 7 \rightarrow 6$) transitions in the M17 HII region/molecular cloud complex were studied. Fig. 6.5 shows the data obtained with the double-sideband receiver, with an LO frequency of 807.8 GHz, and a 1 – 2 GHz IF band. The CI line lies in the upper sideband, at 809.3 GHz, while the CO line is found in the lower (image) sideband at 806.7 GHz. The nonzero baseline is indicative of dust continuum emission. A double-sideband system noise temperature (including telescope coupling, spillover, and atmospheric losses) of better than 2000 K was achieved.

6.4 Theoretical analysis for 839 GHz test results

In this section the theoretical mixer performance is calculated by using Tucker's theory for the case of the 750 GHz device working at 839 GHz. The calculated performance is then compared with experimental results. Reasonable agreement between theory and experiments has been found, showing the predictive power of Tucker's theory and the effectiveness of SIS junction mixers above the gap frequency.

6.4.1 Mixer performance calculation with 839 GHz LO

As discussed in section 2.3, if we know the unpumped dc IV curve, the LO pumping strength parameter α, and the embedding impedances at the RF source and IF load, we can calculate the mixer gain and noise temperature. For a double sideband mixer,

we can find out the necessary matrix elements according to (2.48) - (2.50), and then the mixer gain and noise from (2.40) and (2.46). Here we analyze the performance of our 750 GHz device at 839 GHz LO frequency based on our knowledge of the tuning circuits and the unpumped and pumped dc IVs shown in Fig. 6.3.

LO strength parameter α and RF embedding impedance

The RF embedding environment for the SIS mixer is set by the junction capacitance, the tuning circuits, and the twin slot-antenna. The RF embedding impedance can be calculated, along with the LO pumping strength parameter $\alpha = eV_{\rm LO}/\hbar\omega$, from the unpumped and pumped IVs in a way described by Skalare, the so-called "RF voltage matching method" (Skalare 1989). First α or $V_{\rm LO}$ as a function of bias voltage can be found in a straightforward way by using (2.30) and comparing the unpumped and pumped IVs. The large signal input admittance of the junction $Y_{\rm RF}$ as a function of bias voltage can be obtained by calculating (2.31), (2.32), and (2.51). The mixer model assumes that $Y_{\rm RF}$ is in parallel with the LO current source, consisting of $I_{\rm LO}$ and the RF embedding admittance $Y_{\rm emb}$. The LO voltage drop across the junction is then $V'_{\rm LO} = I_{\rm LO}/(Y_{\rm emb} + Y_{\rm RF})$. $I_{\rm LO}$ and $Y_{\rm emb}$ can be numerically found by minimizing the differences between the previously obtained $V_{\rm LO}$ and the newly calculated $V'_{\rm LO}$ at all selected bias voltage points.

Since α is usually a slow function of bias voltage in the first photon step when the LO pumping is not very strong ($\alpha < 1$), as in the examples given by de Lange (de Lange (thesis) 1994), we assume here α is a constant in the bias region of interest. With this assumption we deduce that $\alpha = 0.42$ from the IVs given in Fig. 6.3. The measured pumped IV and the calculated pumped IV (assuming $\alpha = 0.42$) are compared in Fig. 6.6a. Note that the current scale shown in Fig. 6.3 is the measured current with the double junction in parallel, while in Fig. 6.6a we plot the current for a single junction. For this device the normal state resistance of the junction at 2.7 K is 10.5 Ω.

Instead of searching for the RF embedding admittance by the so-called "RF voltage matching method," we calculate this admittance based on our knowledge of the

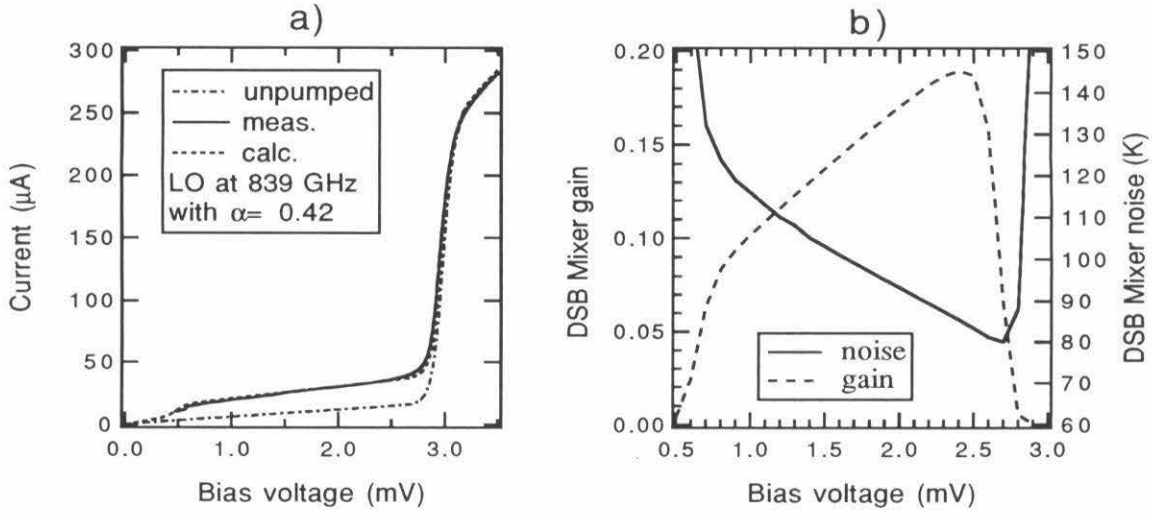

Figure 6.6: (a) Comparison between the measured and calculated IV with LO pumping at 839 GHz. The calculation for the pumped IV is carried out by assuming a constant LO voltage $\alpha = 0.42$. (b) The mixer performance calculated by using the IV curves in (a). In the calculation the RF embedding admittance is $2.24 + j2.34$ normalized to the normal state conductance, and the IF load impedance is 70 Ω.

antenna, the junction and the tuning circuits. We make use of our PCIRCUIT program and find that the RF embedding admittance at 839 GHz is approximately $2.24 + j2.34$, normalized to the normal state conductance of the junction $(10.5\ \Omega)^{-1}$. The circuit file used in the PCIRCUIT program and the calculated RF embedding impedance as a function of frequency are presented in Appendix D.2.

Calculation of mixer performance

Given the LO pumping strength α and the embedding admittance, we can use Tucker's 3-port approximation to calculate the mixer gain and noise temperature. The IF load impedance is 70 Ω as we chose a printed circuit board which transformed the 50 Ω input of the IF amplifier to 70 Ω, to match the junction's IF output resistance. The results obtained for a double sideband mixer are shown in Fig. 6.6b. Note we have included quantum noise in the calculation. The mixer noise temperature is $\sim$ 83 K at bias voltage 2.5 mV, about four times the quantum noise temperature

$h\nu/2k_B \sim 20$ K. At this bias, the mixer has a gain of ~ 0.17, corresponding to a conversion loss of ~ 7.7 dB.

Optimum pumping is not achieved with this LO drive ($\alpha = 0.42$) due to the lack of LO power at 839 GHz from the solid state LO chain. Using Tucker's 3-port theory we calculate that the optimum pumping would occur at $\alpha \approx 0.6$, with a mixer noise temperature of 75 K and a conversion loss of 6.6 dB at bias voltage 2.5 mV. Better LO pumping can be realized by using thicker beamsplitters, but this will not help with the overall receiver noise temperature since the RF signal loss is increased.

6.4.2 Comparison with experimental data

With the calculated mixer noise and gain in hand, we can further calculate the receiver performance and compare it with the experimental results. The output IF power $P_{\rm IF}$ can be written in the following form:

$$P_{\rm IF} = k_{\rm B}\left[(T_{\rm eff}({\rm mixer}) + {\rm T_{mix}}){\rm G_{mix}} + {\rm T_{IF}}\right]{\rm G_{IF}B}\ , \tag{6.1}$$

where $T_{\rm eff}$(mixer) is the effective input signal temperature right in front of the mixer; $T_{\rm mix}$, $G_{\rm mix}$, $T_{\rm IF}$ and $G_{\rm IF}$ are the noise temperature and gain of the mixer and of the IF amplifier, respectively, with noise referred to the input of each component. B is the bandwidth of the IF amplifier. Below we will describe how to find $T_{\rm IF}$ and $T_{\rm eff}$(mixer).

IF chain calibration using shot noise technique

The unpumped IV and IF power curves can be used to calibrate the IF amplifier's gain and noise temperature. The shot noise from the SIS junction biased above the gap voltage is used as a calibrated noise source (Rudner *et al.* 1981; Woody *et al.* 1985; Dubash *et al.* 1995). The noise current of an SIS junction without LO pumping is given by (Rogovin & Scalapino 1974):

$$\langle [I_0]^2 \rangle = 2eB\left[\coth(\frac{eV_0}{2k_BT})\right] I_{\rm dc}(V_0)\ , \tag{6.2}$$

where B is the bandwidth. For $eV_0 \ll 2k_BT$, $\langle[I_0]^2\rangle$ reduces to the Johnson noise formula $4k_BTB/R_0$, whereas for $eV_0 \gtrsim 2k_BT$, it reduces to the shot noise formula $2eI_{dc}B$. For SIS junctions biased above the gap voltage, the current noise takes the shot noise form. If we equate this noise to the thermal noise given by a resistance R_N at temperature T, $4k_BTB/R_N$, then the noise temperature of the junction is

$$\begin{aligned} T_{jct} &= \frac{e}{2k_B} I_{dc} R_N \\ &= (5.8\ \mathrm{K/mV})(V_{dc} - V_{offset}) \ . \end{aligned} \tag{6.3}$$

Here V_{offset} is the voltage where the linear portion of IV extrapolates to zero. The IF output power is then expressed as

$$P_{IF} = k_B \left[T_{jct}(1-\Gamma) + T_{isol}\Gamma + T_{IF}\right] G_{IF} \ . \tag{6.4}$$

Here T_{isol} is the noise contribution of the isolator connecting the junction with the IF amplifier. It is equal to the temperature of the terminating load, in our case 2.7 K. Γ is the reflection coefficient between the junction and the IF amplifier:

$$\Gamma = \left|\frac{R_{jct} - R_L}{R_{jct} + R_L}\right|^2 \ . \tag{6.5}$$

For our specific case, the dynamic resistance of the junction R_{jct} is equal to half of the normal state resistance $R_N/2 = 5.27\ \Omega$ (two junctions in parallel), and the IF load resistance $R_L = 70\ \Omega$, so $\Gamma \approx 0.74$. The linear portion of the IF power above the gap voltage allows us to obtain the amplifier noise T_{IF} and the gain G_{IF} through (6.3) and (6.4).

Unfortunately, the linear portion of the IF power curve was not recorded for this device, so we can not solve for T_{IF} and G_{IF} by using the shot noise technique. However, we know from other experimental data that $T_{IF} \sim 4$ K.

Effective RF signal and RF noise contribution

Table 6.4: Estimated contributions from the front end optics to receiver conversion loss and noise temperature

Components	Estimated transmission t	Temperature (K)		Noise (K)
		$T^{\rm amb}$	$T^{\rm amb}_{\rm eff}$	$T_{\rm n} = (1-t)T^{\rm amb}_{\rm eff}/t$
10 μm Mylar b.s.	0.94	295	275	17.6
25 μm Mylar window	0.86	295	275	44.8
IR quartz filter	0.96	77	58	2.4
Polyethelene lens	0.95	4.2	0.003	0.0
Silicon lens and antenna	0.85	4.2	0.003	0.0
Tuning circuit	0.20	4.2	0.003	0.0
Total RF optics gain $G_{\rm RF} = 0.125 = -9.0$ dB			Total contrib. noise $T_{\rm RF} = 68$ K	

The effective signal temperature in front of the mixer is calculated from the transmission and ambient temperature of all the components in the front end optics and RF tuning circuits. A lossy component in the path of a signal with signal temperature T, as we mentioned in section 1.2, will add noise temperature $(1-t)T^{\rm amb}_{\rm eff}$ to the transmitted signal tT, where t is the transmission of the component, and $T^{\rm amb}_{\rm eff}$ is the effective Planck temperature of the lossy component. The effective Planck temperature $T_{\rm eff}$ of a blackbody at temperature T is defined here so that $k_{\rm B}T_{\rm eff}$ is equal to the Planck radiation power (see section 1.2). If the signal goes through a series of lossy components, each with transmission t_n and ambient temperature $T^{\rm amb}_{\rm eff}(n)$, then the signal strength after the nth component will be

$$T(n) = t_n T(n-1) + (1-t_n)T^{\rm amb}_{\rm eff}(n) \ , \tag{6.6}$$

as schematically shown in Fig. 6.7. The receiver optics was described in chapter 3. Table 6.4 lists the the transmission and the ambient temperature of each component in the signal path of our receiver, along with the calculated effective Planck temperature, and the noise temperature referred to the input of each component.

The effective input signal temperature calculated for the position in front of each component in the signal path is given in Table 6.5. The hot load at 295 K and the cold load at 77 K have Planck temperature of 275 K and 58 K, respectively. The final results for $T_{\rm eff}$(mixer) are 43 K and 16 K for the hot and cold load, respectively. We

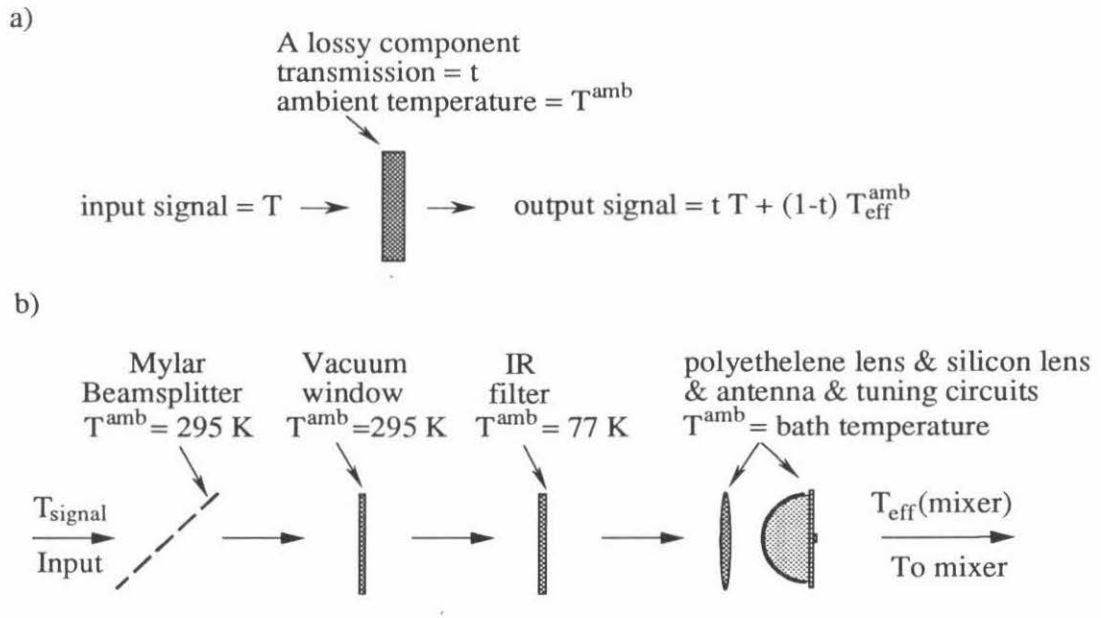

Figure 6.7: Schematic diagram showing (a) the effect of a lossy component on the signal throughput and noise contribution, (b) the front end optics of the receiver.

Table 6.5: Calculated hot and cold load effective signal temperatures before each component in the signal path

Effective load temperature	Before Mylar window	Before IR filter	Before the lens	Before the mixer
275 K	275 K	275 K	264 K	43 K
58 K	70 K	99 K	97 K	16 K

then calculate the Y-factor using (6.1). The calculated Y-factor as a function of bias voltage is compared with the experimental value in Fig. 6.8. The agreement is quite good except at the jump of the photon step about 0.5 mV, where the measured data has large noise, giving a falsely large Y-factor.

We now take a specific bias point 2.5 mV and calculate the receiver noise temperature based on our calculated mixer performance and the properties of optics and RF tuning circuits. The receiver noise temperature can be written as

$$T_{\rm rec} = T_{\rm RF} + \frac{T_{\rm mix}}{G_{\rm RF}} + \frac{T_{\rm IF}}{G_{\rm RF} G_{\rm mix}} , \qquad (6.7)$$

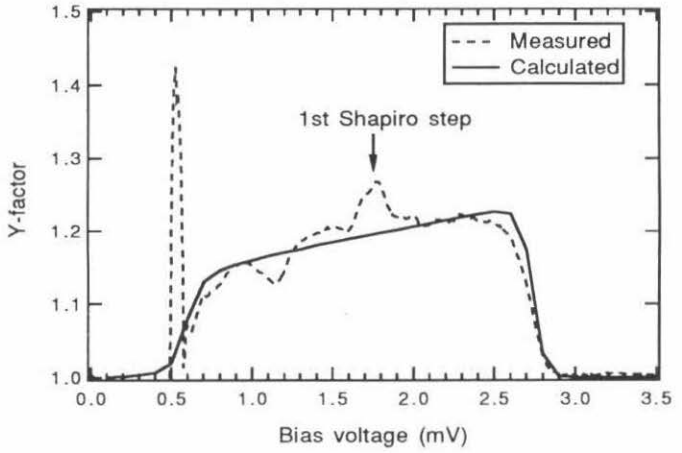

Figure 6.8: Measured and calculated Y-factors for the 750 GHz device at 839 GHz LO pumping.

Table 6.6: Breakdown of the receiver noise contributions for the 750 GHz device working at 839 GHz, biased at 2.5 mV

$T_{\rm RF} = 68$ K, $G_{\rm RF} = 0.125$	$T_{\rm RF} = 68$ K
$T_{\rm mix} = 83$ K, $G_{\rm mix} = 0.17$	$T_{\rm mix}/G_{\rm RF} = 664$ K
$T_{\rm IF} = 4$ K	$T_{\rm IF}/G_{\rm RF}G_{\rm mix} = 188$ K
Measured $T_{\rm rec} = 985$ K	Calculated $T_{\rm rec} = 920$ K

where $T_{\rm RF}$ is the noise contribution of the front end optics referred to the input of the receiver and $G_{\rm RF}$ is the total gain of the front end optics; their values are listed in Table 6.4. The breakdown of the total receiver noise into the contributions from the front end RF optics, the mixer and the IF amplifier is clearly demonstrated in Table 6.6. The calculated receiver noise temperature is 920 K, compared to the experimental value 985 K. We see that significant reduction in receiver noise temperature can be achieved if we can reduce the loss of the front end optics and the tuning circuit. From this also comes the observation that by using a thicker beamsplitter for a better mixer performance, when there is a lack of LO power, could adversely affect the receiver noise, because thicker beamsplitters introduce larger RF loss (smaller $G_{\rm RF}$) as well as more RF noise.

6.5 Chapter summary

We have demonstrated all-Nb low-noise SIS receivers with *predictable* performance at frequencies from 400 GHz to above 800 GHz. Our device simulation program can accurately predict the experimentally observed performance, giving us the ability to reliably design broadband, high sensitivity devices over our frequency range of interest. Fourier-transform spectroscopy has been used as a powerful tool for testing our predictions, and for selecting useful devices and optical configurations.

Our SIS receivers are the first to demonstrate substantially better performance than GaAs Schottky receivers for the astrophysically important CI and CO transitions near 810 GHz. Our quasi-optical devices are fully competitive with existing waveguide mixers at frequencies as low as 400 GHz. The simplicity and flexibility of the quasi-optical approach further increase the desirability of these devices at higher frequencies and for imaging arrays.

The large loss in the Nb tuning circuits above the gap frequency prompted us to minimize this problem through the use of lower-loss wiring materials such as Al and NbN. We will discuss the Al-wiring Nb-based SIS receivers in the next chapter.

Chapter 7 SIS Mixers with Normal-metal Al Wiring

This chapter describes the design and test of quasi-optical Nb-based SIS mixers with normal-metal Al wiring. The traditional Nb wiring in SIS mixers is replaced with Al wiring in the hope of achieving better receiver sensitivities at terahertz frequencies. As we saw earlier, the noise temperature of all-Nb SIS receivers increases significantly above the gap frequency ($\sim$ 700 GHz), because the rf photons have sufficient energy to break Cooper pairs, causing a large fraction of the incoming radiation to be dissipated in the superconducting wiring. In principle, tuning circuits fabricated using a high conductivity normal metal such as Al should offer better performance above $\sim$ 800 GHz, as we predicted in chapter 4. This approach has been demonstrated at $\sim$ 1 THz with waveguide receivers (van de Stadt *et al.* 1996) and quasi-optical receivers (Bin *et al.* 1996).

We have designed SIS mixers with Al wiring for frequency bands below and above the gap frequency, covering $\sim$ 300 – 1200 GHz, with emphasis on 1 THz devices. An uncorrected double-sideband receiver noise temperature of 840 K at 1042 GHz was obtained at a bath temperature of 2.5 K. This result is over a factor of four better than the best reported GaAs Schottky diode mixers at this frequency.

In this chapter we first describe the design issues and the FTS measurements. The heterodyne results are then presented and some detailed discussions are provided for various devices.

7.1 Design and FTS measurement of SIS mixers with Al wiring

The twin-slot double-junction antisymmetric-feed mixer configuration is adopted for our Al-wiring SIS mixer design. This configuration has been described in chapter 3 and also used for our all-Nb mixer designs as seen in chapter 6.

The design procedure is quite similar to that used in our all-Nb mixer design. Tuning circuits were designed for five frequency bands characterized by the center frequency: 450, 750, 850, 950 and 1050 GHz. We designed several devices for each band to allow for parameter variations, particularly in the junction area and specific capacitance. For each band, we optimized the tuning circuit for a single value of the junction area, 1.7 μm^2, but we used two different values of the specific capacitance, 65 fF/μm^2 and 85 fF/μm^2. For each tuning circuit design, we included three nominal junction areas (1.2 μm^2, 1.7 μm^2, and 2.3 μm^2) on the mask layout. Thus we had five bands, ten tuning circuits, and 30 different device designs. The structure of the tuning circuits is similar to that for the all-Nb mixers, except that one section of transformer was used instead of two sections of transformers. Our PCIRCUIT program was also used to optimize the tuning circuit design. The assumed parameters used in the design are given in Table 7.1, and the obtained microstrip widths and lengths are listed in Table 7.2.

The devices are labeled using three or four digit numbers that identify the device designs. The first one or two digits refers to the frequency band: 4, 7, 8, 9, 10 correspond to 450, 750, 850, 950, and 1050 GHz, respectively. The next digit gives the junction size, with 1, 2, 3 referring to 1.2 μm^2, 1.7 μm^2, and 2.3 μm^2. The last digit represents specific capacitance assumed for the design, with 6 and 8 indicating 65 fF/μm^2 and 85 fF/μm^2.

The Al-wiring mixer chips were fabricated by Henry LeDuc at the JPL Center for Space Microelectronics Technology, using a modified Nb/Al-oxide/Nb junction process. First, a 200 nm Al ground plane was deposited onto a 50 mm diameter, 0.25 mm thick high-resistivity silicon wafer, followed *in situ* by the Nb/Al-oxide/Nb

Table 7.1: Assumed parameters in Al-wiring mixer design

junction $R_N A$ product	20 Ω-μm^2
junction size	1.7 μm^2
junction specific capacitance	85 fF/μm^2 or 65 fF/μm^2
SiO thickness for the inductor	200 nm
SiO thickness for the transformer	400 nm
SiO dielectric constant	$\epsilon = 5.6\epsilon_0$
Al film thickness	200 nm
Al resistivity ratio	10 (anomalous skin effect)
physical temperature of the device	4.2 K

Table 7.2: Designed parameters for the Al-wiring SIS tuning circuits. Note the inductor length is the distance between the centers of the two junctions.

Microstrip parameters	**For $C_j = 85$ fF/μm^2**		**For $C_j = 65$ fF/μm^2**	
(width $\times$ length, μm^2)	**inductor**	**transformer**	**inductor**	**transformer**
For 450 GHz band	5.0 $\times$ 46.0	4.5 $\times$ 85.0	5.0 $\times$ 60.0	4.1 $\times$ 86.0
For 750 GHz band	5.0 $\times$ 15.2	5.0 $\times$ 51.0	5.0 $\times$ 20.6	4.6 $\times$ 52.5
For 850 GHz band	5.0 $\times$ 11.6	5.0 $\times$ 45.0	5.0 $\times$ 15.6	4.7 $\times$ 46.0
For 950 GHz band	5.0 $\times$ 9.2	5.0 $\times$ 40.0	5.0 $\times$ 12.4	4.7 $\times$ 41.2
For 1050 GHz band	5.0 $\times$ 7.4	5.1 $\times$ 36.0	5.0 $\times$ 10.0	4.8 $\times$ 37.0

trilayer. The ground plane and the slot antennas were patterned in this step using a lift-off technique. The junctions were defined with optical lithography and formed by reactive ion etching (RIE) of the Nb/Al-oxide/Nb trilayer. All of the unprotected Nb must be removed so that the Al ground plane was exposed for the microstrip lines. The junctions were isolated with a 200 nm SiO film patterned by self-aligned lift-off, and a second 200 nm SiO film was added on the appropriate area to produce a total SiO thickness of 400 nm for the impedance transformer. The 200 nm Al wiring layer was deposited as the last step. A picture of an Al-wiring mixer chip is shown in Fig. 3.8. For this batch of mixer fabrication, it was found through the use of the test die on the device wafer that the undercut in the junction dimensions was negligible. The junction specific capacitance was $\sim$ 85 fF/μm^2 as determined by FTS tests discussed later.

By comparing the measured frequency response of an SIS detector obtained on the FTS system with the theoretical simulation of RF coupling efficiency, we can deduce some of the junction parameters, such as the junction capacitance. Since no absolute calibration is available for our FTS system, we compare the experimental data with the theoretical simulation in such a way that the vertical scaling of the FTS data is adjusted to give the best amplitude match to the simulation, while the best simulation is achieved by varying some circuit parameters so as to have the best bandwidth match to the FTS data. It is then important to know how the circuit parameters affect the frequency response, especially the shape and position of the frequency bandwidth. We now examine some of the effects by looking at the simulated responses for mixers designed at 1050 GHz with assumed specific capacitance 85 fF/μm^2. In Fig. 7.1a, the predicted RF coupling efficiencies for device 1018, 1028 and 1038 are plotted. Since the three devices have the same tuning circuits, the differences in the RF coupling efficiencies should be caused by different junction capacitances (103 fF, 144 fF, and 191 fF, respectively), as well as the junction normal state resistances (16.5 Ω, 11.8 Ω, and 8.9 Ω, respectively). To pin down the effect of the junction resistance on the response, a simulation with junction capacitance equal to that of 1028 (144 fF),

but junction resistance equal to that of 1018 (16.5 Ω), is also plotted in Fig. 7.1a. The resulted efficiency has same shape and bandwidth as device 1028 does, and the only noticeable difference is the reduced amplitude. Therefore, we conclude that the junction resistance plays little role in the way we compare our FTS data with the simulation response. It is the junction total capacitance that determines the frequency response bandwidth.

In Fig. 7.1b we plot the RF coupling efficiencies for device 1028 calculated under different skin effect assumptions for the Al film in the microstrip lines. First we use the anomalous skin effect model and compare the results calculated with Al resistivity ratio of 5 and 10. The two responses differ mainly in the amplitude. To compare with normal skin effect model, we also plot the simulation calculated with normal skin effect for an Al resistivity ratio of 5. The response, compared to the anomalous skin effect case, shifts to higher frequencies by about 3%. This shift is measurable in FTS data. From these simulations, we see that the resistivity ratio of an Al film can not be easily deduced from the FTS data. If we know the junction capacitance, it is possible to tell whether the normal skin effect or the anomalous skin effect applies to the Al film better.

Fig. 7.2 shows some measured FTS spectra taken with five devices: 418, 428, 716, 816 and 1028. The simulated RF coupling efficiency for each device is also shown in the figure. For all the simulations, the junction specific capacitance is 85 fF/μm^2. The anomalous skin effect is used to calculate the Al microstrip lines and the Al resistivity ratio is 5. The measured dc IVs are used to calculate the RF impedance of the junctions. The rest of the circuit parameters used in the simulations are all nominal design values. In general, the agreement between simulation and experiment is quite good, given the nonidealities present in the measurement: strong water absorption lines at 557, 752, 986, 1094, 1114, 1163, 1211, and 1229 GHz, and Fabry-Perot resonances from the quartz IR filter spaced approximately 30 GHz apart. It seems that 85 fF/μm^2 is a good estimate for the junction specific capacitance, if the lithographic undercut of the junction area is negligible. The only big discrepancies occur in the data for devices 716 and 816. Since these two devices are next to

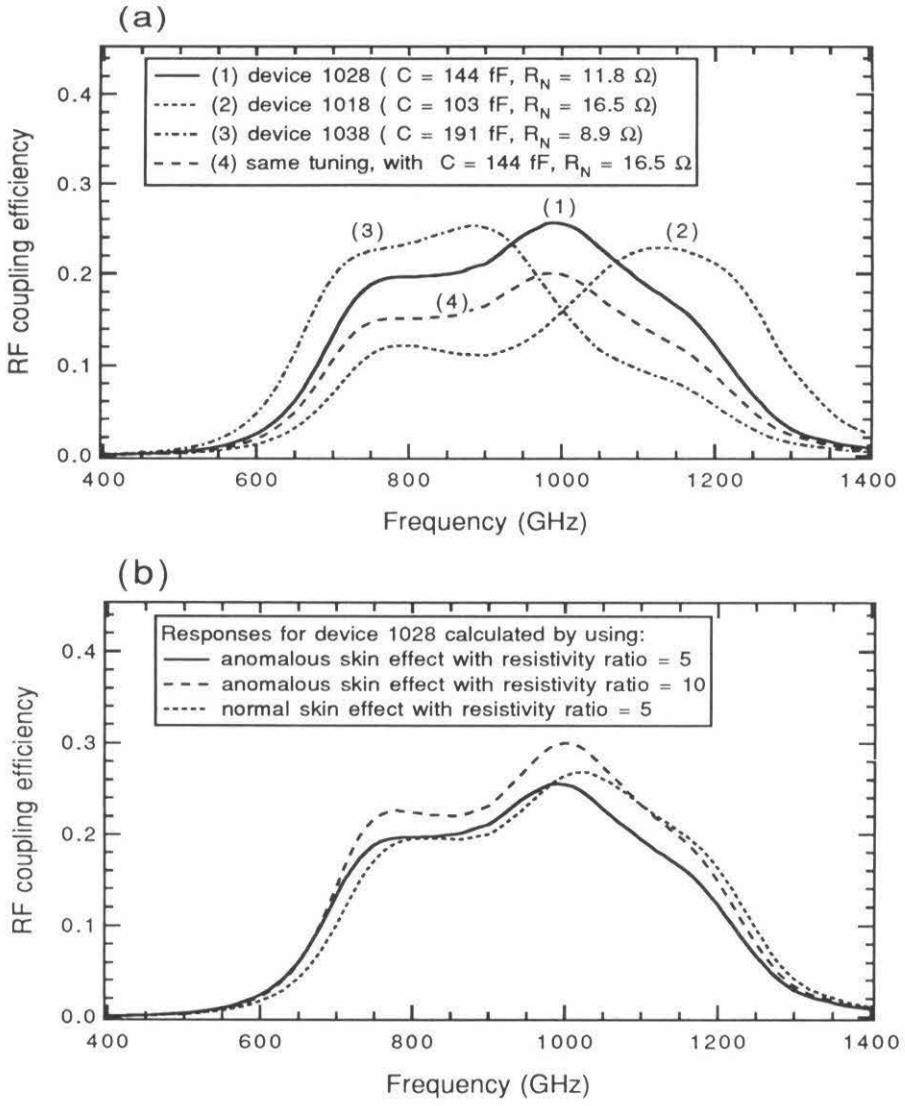

Figure 7.1: Simulated RF coupling efficiency for the Al-wiring mixer design at 1050 GHz and with an assumed specific capacitance 85 fF/μm^2. (a) Calculated RF coupling responses for mixers with same tuning circuits but different junction areas, showing the total junction capacitance determines the response bandwidth. (b) RF coupling efficiencies for the same mixer, but calculated with different Al film skin effect models and resistivity ratios, showing the bandwidths are similar for the same skin effect model, while different skin effect models may have different bandwidths.

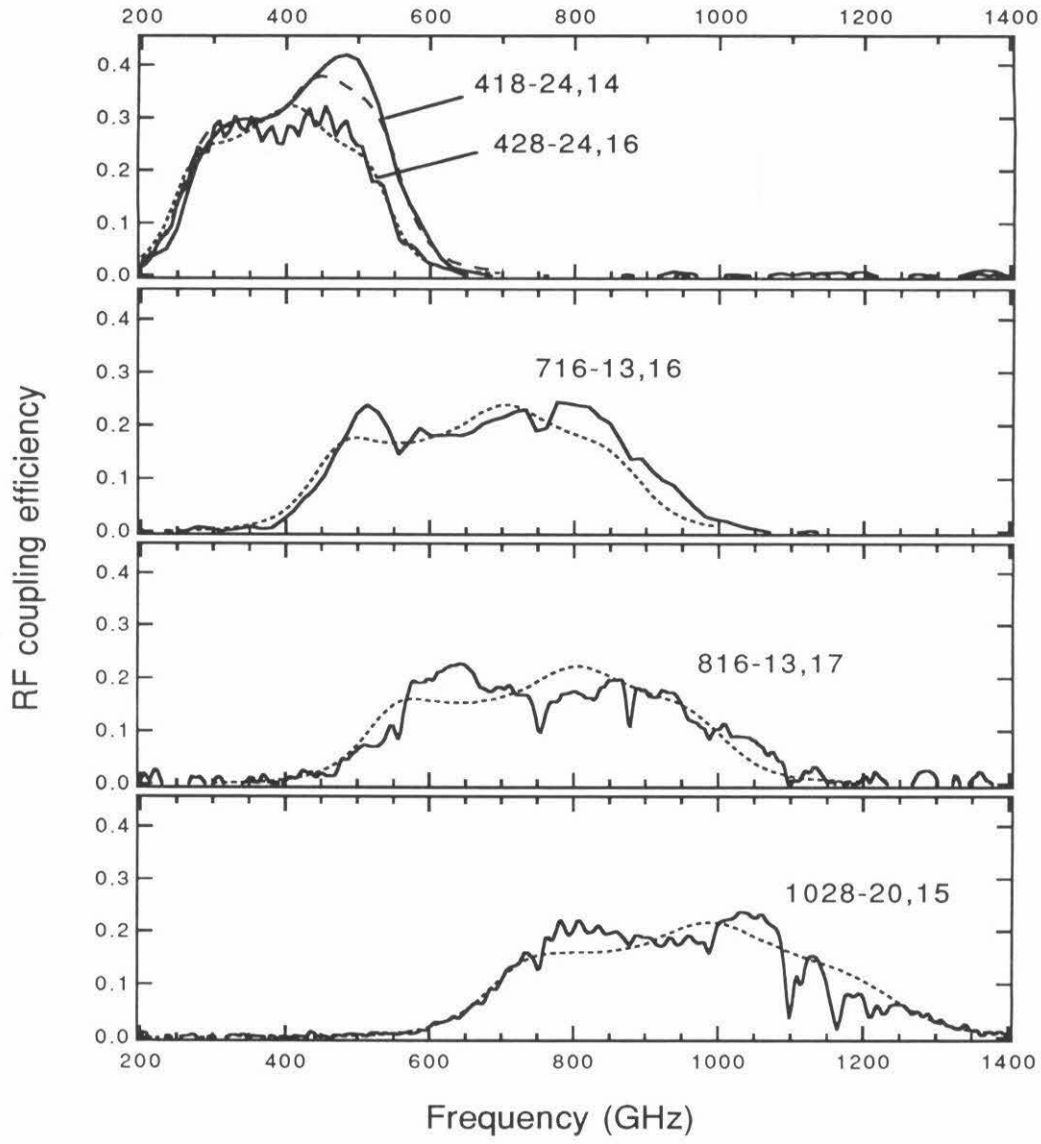

Figure 7.2: FTS measured response (solid lines) vs. RF coupling simulation (dashed lines) for five devices 418, 428, 716, 816, and 1028. These devices are from the same fabrication batch, their positions on the wafer indicated by the row and column number after the device name, like 24,16. All the simulations are calculated using a specific capacitance value of 85 fF/μm^2 and the nominal design values for the rest of the parameters. The anomalous skin effect is used to calculate the Al microstrip lines and the resistivity ratio for Al is 5.

each other on the wafer, it may be possible that they suffered a larger than average undercut (thus have smaller capacitance than assumed.)

The frequency responses of these Al-wiring devices are extremely wide, with bandwidths covering $\sim$ 300 – 500 GHz, as a result of the low Q resonant circuit. As we pointed out earlier, it is difficult, if ever possible, to exactly know the characteristic of the microstrip lines from these response measurement on the FTS. For instance, we can not determine the resistivity ratio of the Al film from the FTS data. The resistivity ratio is determined by the dc measurements, as we will discuss in section 7.2. To examine the microstrip performance, a simple resonance circuit with multiple resonance peaks and relatively narrow bandwidths, such as an open-ended stub, is preferred (de Lange *et al.* 1995; Hu *et al.* 1988). However, due to the large loss in Al microstrip lines, we were unable to design a resonant circuit for the SIS junction which promises measurable multiple resonant peaks. We did design and fabricate some SIS detectors consisting of junctions that were connected with one-section microstrip lines on broadband log-periodic antennas. As yet we have not investigated the frequency response of these detectors.

7.2 Heterodyne measurement results

The noise temperatures of several devices, including those in Fig. 7.2, were measured by using the Y-factor method (in the Rayleigh-Jeans limit, if not noted). Our noise temperatures were referred to the input of the beamsplitter; unless otherwise noted, no corrections were made for beamsplitter or other optical losses. The receiver optics has been described in chapter 3 and chapter 6, and may vary a little bit from receiver to receiver. Fig. 7.3 displays receiver noise temperature as a function of frequency for these devices at a bath temperature of 4.2 K.

Particularly at the higher frequencies, the receiver noise temperatures are adversely affected by the relatively low output power of our LO chains, and the situation is further degraded by our large junction areas. For better mixer performance, thicker beamsplitters were used to couple more LO power onto the junction in the case of

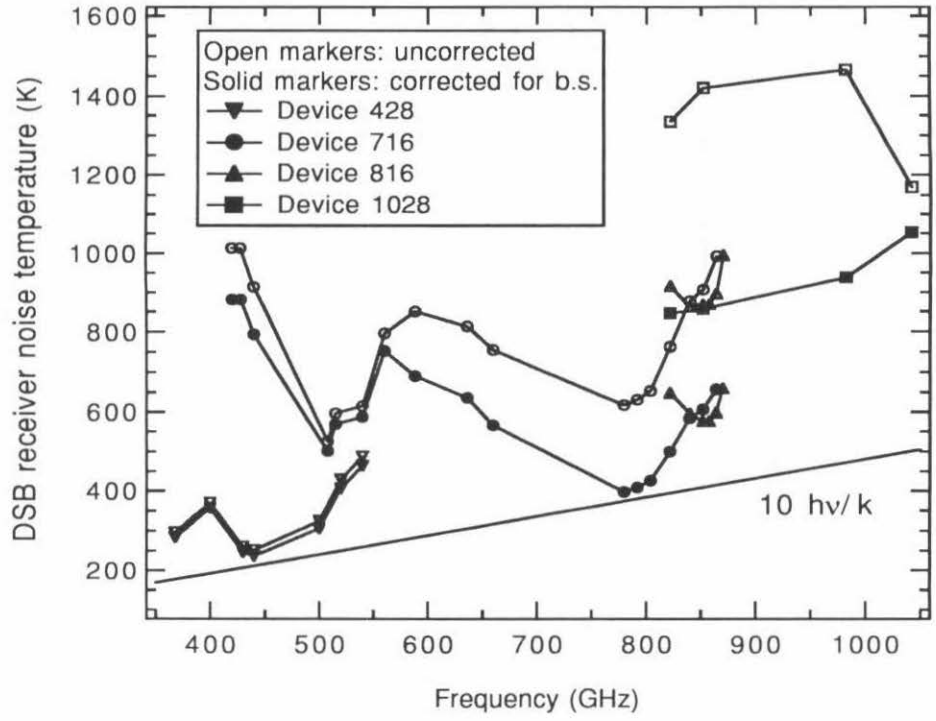

Figure 7.3: DSB noise temperatures of four Al-wiring SIS receivers measured at a bath temperature of 4.2 K. The open markers are uncorrected DSB receiver noise temperatures, while the corresponding solid markers are results corrected for the LO injection beamsplitters.

extreme LO starvation (we had three beamsplitter thicknesses: 10 μm, 25 μm, and 51 μm). However, thicker beamsplitters did not improve the receiver noise temperatures since they increased the optical losses. If we correct for beamsplitter losses, the receiver noise temperatures drop by a few hundred Kelvin at the high frequency end. For instance, the receiver noise temperature at 982 GHz drops from $\sim$ 1450 K to $\sim$ 950 K after correcting for the beamsplitter. The anomalously low uncorrected noise temperature at 1042 GHz is the result of a more powerful LO. At this frequency a far-infrared laser LO source was used, which produced a good deal more power than our standard LO chain. A thinner beamsplitter was employed ($\sim$ 10 μm instead of 51 μm thick Mylar) to improve the signal coupling efficiency.

The high-frequency devices were also tested at a pumped-LHe temperature of $\sim$ 2.5 K. Upon cooling to 2.5 K, the noise decreases by $\sim$ 100 K – 300 K over

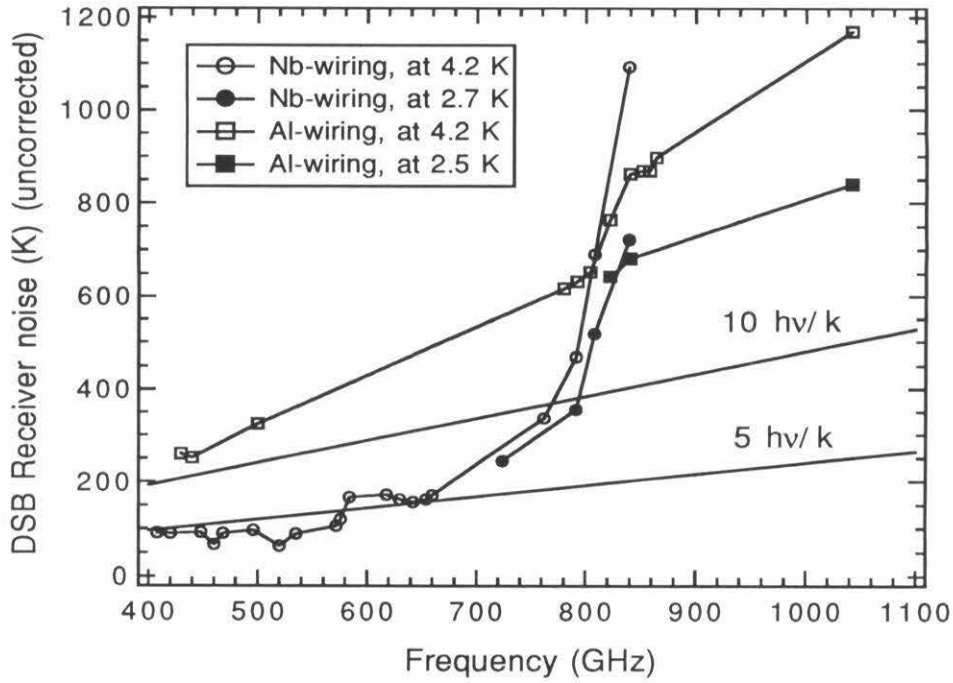

Figure 7.4: The best *uncorrected* receiver noise temperatures for quasi-optical Nb-wiring and Al-wiring SIS mixers developed at Caltech.

the band, in part due to the reduced dark current and its shot noise. The noise temperatures of the quasi-optical SIS receivers with Nb wiring or Al wiring developed in our group recently are summarized in Fig. 7.4. In the figure, the best uncorrected DSB receiver noise temperatures are shown, with data obtained at LHe 4.2 K and also at pumped LHe temperature. An uncorrected DSB receiver noise temperature of 840 K at 1042 GHz was obtained at a bath temperature of 2.5 K. This result is over four times better than the best reported GaAs Schottky diode mixers at this frequency. The comparison of our results with other groups' results can be found readily in Fig. 1.7.

In the next few sections, we will discuss these receiver performances in more detail. Before we do that, let's look at a measured IV curve.

Correction for bias voltage due to series resistance of the Al wiring

Fig. 7.5 shows a typical dc IV of the Al-wiring device at 4.2 K when no magnetic field is applied to suppress the supercurrent. The IV has a sloped supercurrent, which is the result of a resistance in series with the junction. This is caused by the resistive current path through the Al wiring. From the sloped IV curve, we can deduce the resistivity ratio of the Al film. For instance, the sloped supercurrent in Fig. 7.5 indicates a series resistance of 2.7 Ω. The dc current path, consisting of the IF feed, the radial stub and half of the tuning circuit, is $\sim$ 106 squares of 200 nm thick Al film. This gives a resistivity of 2.7 $\Omega/106 \times 200$ nm $= 0.51$ $\mu\Omega$-cm. The resistivity ratio is thus 4.8 (the room temperature resistivity for bulk Al is 2.45 $\mu\Omega$-cm).

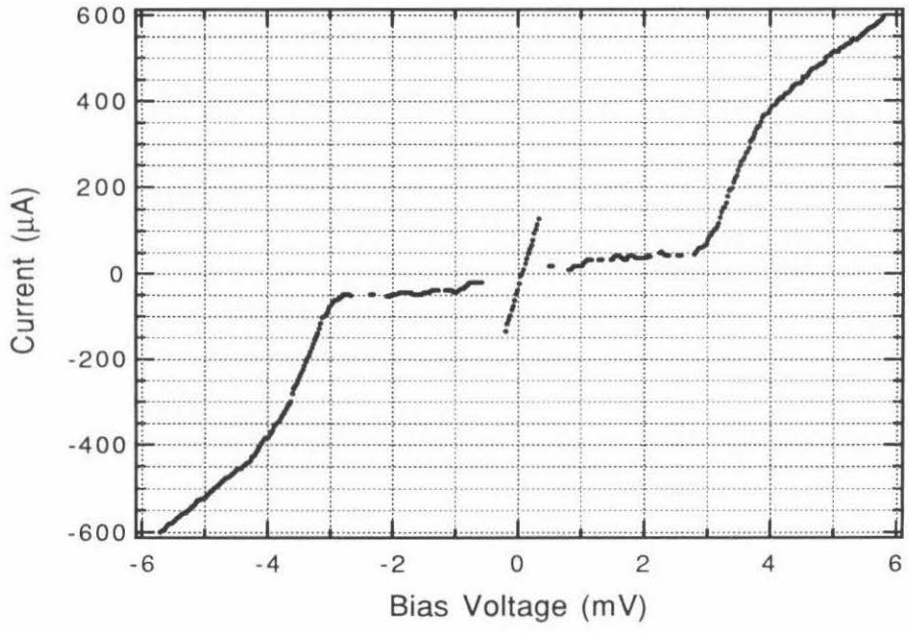

Figure 7.5: A typical dc IV measured without applied magnetic field for Al-wiring SIS mixer, showing the sloped supercurrent.

The bias voltage across the junction is obtained by subtracting the dc voltage across the series resistance from the measured voltage:

$$V_0 = V_{\text{meas}} - R_{\text{series}} \times I_{\text{meas}} \ . \tag{7.1}$$

We will use only the corrected dc bias voltage for the remainder of this chapter.

Apart from finding the series resistance from the sloped supercurrent, we can also determine the series resistance from the plot of IF power vs. bias voltage, as shown in Fig. 7.6. In this figure, the unpumped and pumped current and IF power are plotted against the corrected bias voltage for device 1028 at LO frequency 1042 GHz and bath temperature 4.2 K. If an appropriate series resistance is used in the voltage correction procedure through (7.1), the two dips in the IF power curve at the photon steps should be separated by twice the gap voltage. Of course this will not apply if the the superconducting energy gap decreases at biases well above the gap voltage due to quasiparticle injection by the junction. However, we find that our devices show little sign of these heating effects above the gap voltage, so this method of determining series resistance is practical.

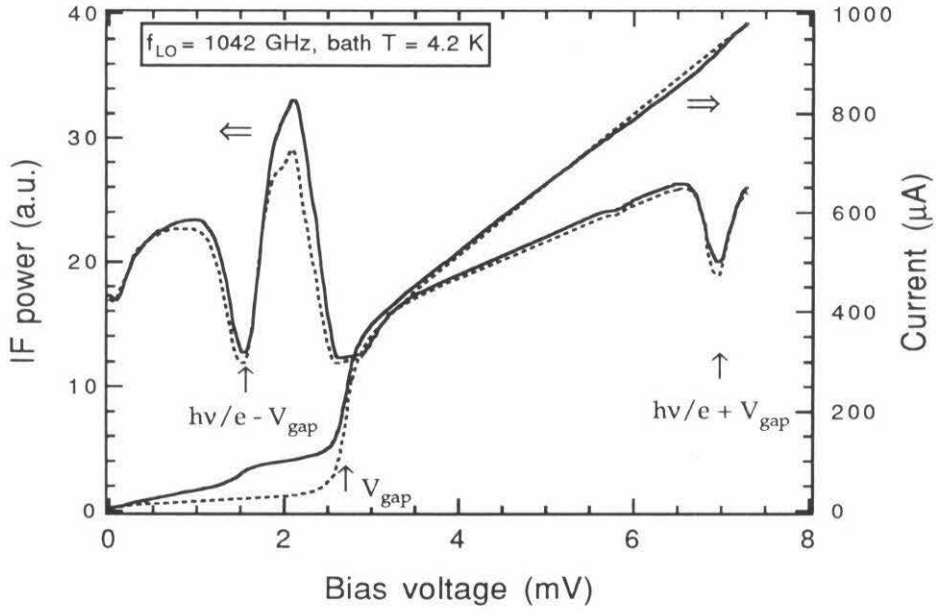

Figure 7.6: The current and IF power vs. corrected bias voltage for device 1028 at 1042 GHz LO and 4.2 K bath temperature. If the series resistance is chosen correctly, the two dips in the IF power curve at the photon steps should be separated by twice the gap voltage.

Table 7.3: Receiver noise temperature for device 1028

f_{LO} (GHz)	vacuum window & IR filter	uncorrected DSB receiver noise T_{rec}				corrected T_{rec}	
		51 μm b.s. at 4.2 K	25 μm b.s. at 4.2 K	51 μm b.s. at 2 K	25 μm b.s. at 2 K	at 4.2 K	at 2 K
822	qutz.; AR qutz.	1727 K	1334 K	1549 K	1207 K	846 K	756 K
852	qutz.; AR qutz.	1727 K	1420 K	1561 K	1207 K	857 K	757 K
982	qutz.; AR qutz.	–	1466 K	1587 K	1307 K	938 K	777 K
1042	Mylar; cl. qutz	1170 K, 10 μm b.s.		840 K, 10 μm b.s.		1050 K	752 K

7.3 Device 1028

The heterodyne performance of device 1028 was determined at LO frequencies 822, 852, 982, and 1042 GHz. Local oscillator power at 1042 GHz was generated using a difluoromethane (CH_2F_2) far-infrared laser, pumped by a $\lambda = 10$ μm CO_2 laser. Since this LO was very powerful, we used a 10 μm thick Mylar beamsplitter. The pressure window was 25 μm thick Mylar and the IR filter was a 2.2 mm thick clear quartz plate. The best uncorrected DSB receiver noise temperature at 1042 GHz was 1170 K at 4.2 K bath temperature, and 840 K when the device was cooled to $\approx$ 2.5 K. LO power at 982 GHz was obtained using a fixed-tuned solid-state Gunn/multiplier. An AR-coated 2.2 mm quartz pressure window and an AR-coated 2.2 mm quartz IR filter were used for the 982 GHz tests. Although the LO was said to produce $\approx$ 60 μW at 982 GHz, we could not obtain optimum pumping using a 25 μm thick Mylar beamsplitter. When a 51 μm thick Mylar beamsplitter was used, we got closer to the optimum pumping but the receiver noise temperature increased (as expected). The uncorrected DSB receiver noise temperature at 982 GHz is 1466 K with a 25 μm thick beamsplitter at 4.2 K bath temperature and 1307 K at 2.5 K bath temperature. LO power at 822 GHz and 852 GHz was provided by a tunable InP Gunn oscillator followed by a cascaded ($\times 2 \times 3$) GaAs Schottky varactor multiplier. We obtained just enough LO power with a 25 μm thick Mylar beamsplitter. The uncorrected DSB receiver noise temperature is 1420 K at 4.2 K bath temperature and 1207 K when the device was cooled to 2.5 K.

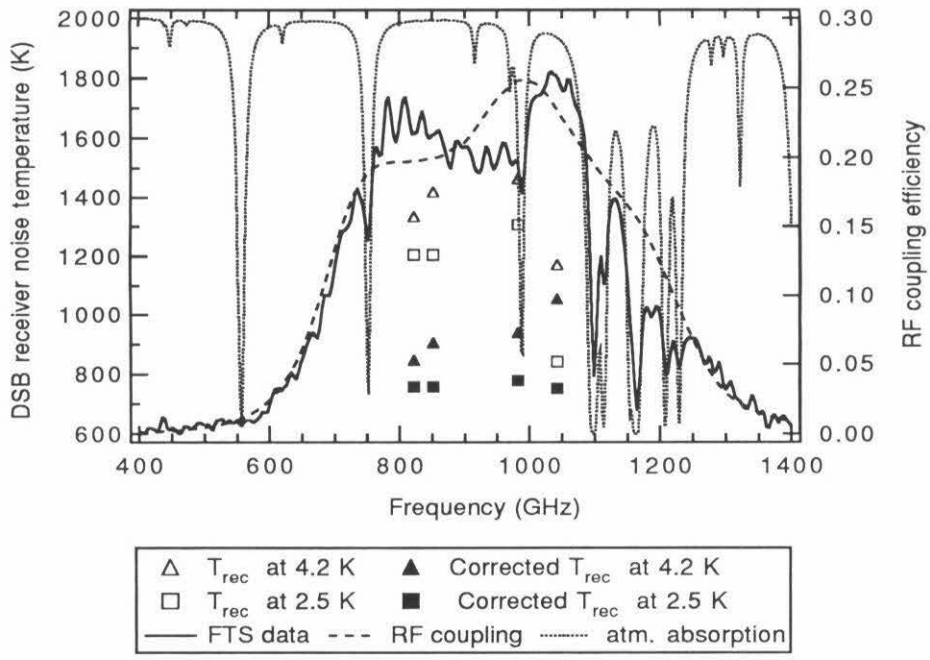

Figure 7.7: DSB noise temperatures of device 1028, shown with the background of measured FTS spectrum and simulated RF coupling efficiency. Uncorrected receiver noise temperatures as well as the noise after correction for beamsplitter are given both at bath temperature of 4.2 K and $\sim$ 2.5 K. Also shown in the figure is the calculated atmosphere transmission for the FTS, scaled from 0 to 1 over the vertical axis.

Table 7.3 summarizes the receiver noise temperatures for device 1028 under different testing conditions. At about 2.5 K this device gives low-noise performance in a wide band 822 – 1042 GHz with a DSB receiver noise (after correction for beamsplitter) $\sim$ 770 K. The results are also demonstrated in Fig. 7.7, along with the measured FTS data and simulated RF coupling efficiency for a better appreciation of the wide bandwidth available.

7.3.1 Device 1028 at 1042 GHz

Fig. 7.6 shows the heterodyne measurement at 1042 GHz and 4.2 K bath temperature. Shown in the figure are the pumped and unpumped IVs and total IF output power in a 500 MHz bandwidth with room temperature and 77 K absorbers placed at the

receiver input. The photon step from the nonlinearity at $V_{\rm gap} \approx -2.7$ mV appears at $V \approx +1.6$ mV, as expected from the 1042 GHz LO input ($h\nu/e \approx 4.3$ mV). The IF curve is quite smooth, indicating a good suppression of Josephson noise by the applied magnetic field.

The mixer performance for this set of heterodyne measurements is calculated using the 3-port approximation of Tucker's theory. We follow the discussion in section 6.4 to obtain the LO pumping strength parameter α through the unpumped and pumped dc IV curves, which yields $\alpha = 0.63$. This α value is equal to the optimum LO pumping predicted by the theory. The RF embedding admittance is calculated using the PCIRCUIT program and the value is found to be $3.5 + j2.1$, normalized to the normal state conductance $(13.2\ \Omega)^{-1}$. The IF load resistance is 70 Ω. The mixer gain and noise are then calculated in the same way as in section 6.4 for Nb-wiring device. At bias voltage 2.0 mV, the calculated mixer noise temperature is $\sim$ 131 K, about five times the quantum noise temperature ($h\nu/2k_{\rm B} \sim 25$ K). At this bias, the mixer has a gain of ~ 0.15, corresponding to a conversion loss of ~ 8.2 dB.

Given the calculated mixer noise and gain, we go further to calculate the receiver performance and compare with the experimental results. We calculate the IF output power using (6.1), written down again for convenience:

$$P_{\rm IF} = k_{\rm B}\left[(T_{\rm eff}({\rm mixer}) + {\rm T_{mix}}){\rm G_{mix}} + {\rm T_{IF}}\right]{\rm G_{IF}}. \tag{7.2}$$

First the unpumped IV and IF power curves are used to calibrate the IF amplifier's gain and noise temperature by using the shot noise technique discussed in section 6.4.2, which gives $T_{\rm IF} \approx 6$ K and $k_{\rm B}G_{\rm IF} \approx 0.968$. Secondly, the transmission and noise properties of the front end optics are estimated and given in Table 7.4. Thirdly, the effective signal temperature in front of the mixer for the hot load 295 K and cold load 77 K is calculated in the same manner as for Table 6.5. The final results of $T_{\rm eff}({\rm mixer})$ are 51.5 K and 21.4 K for the hot and cold load, respectively.

The measured and calculated pumped IVs are compared in Fig. 7.8a. The measured and calculated IF output powers are compared in Fig. 7.8b. It is remarkable

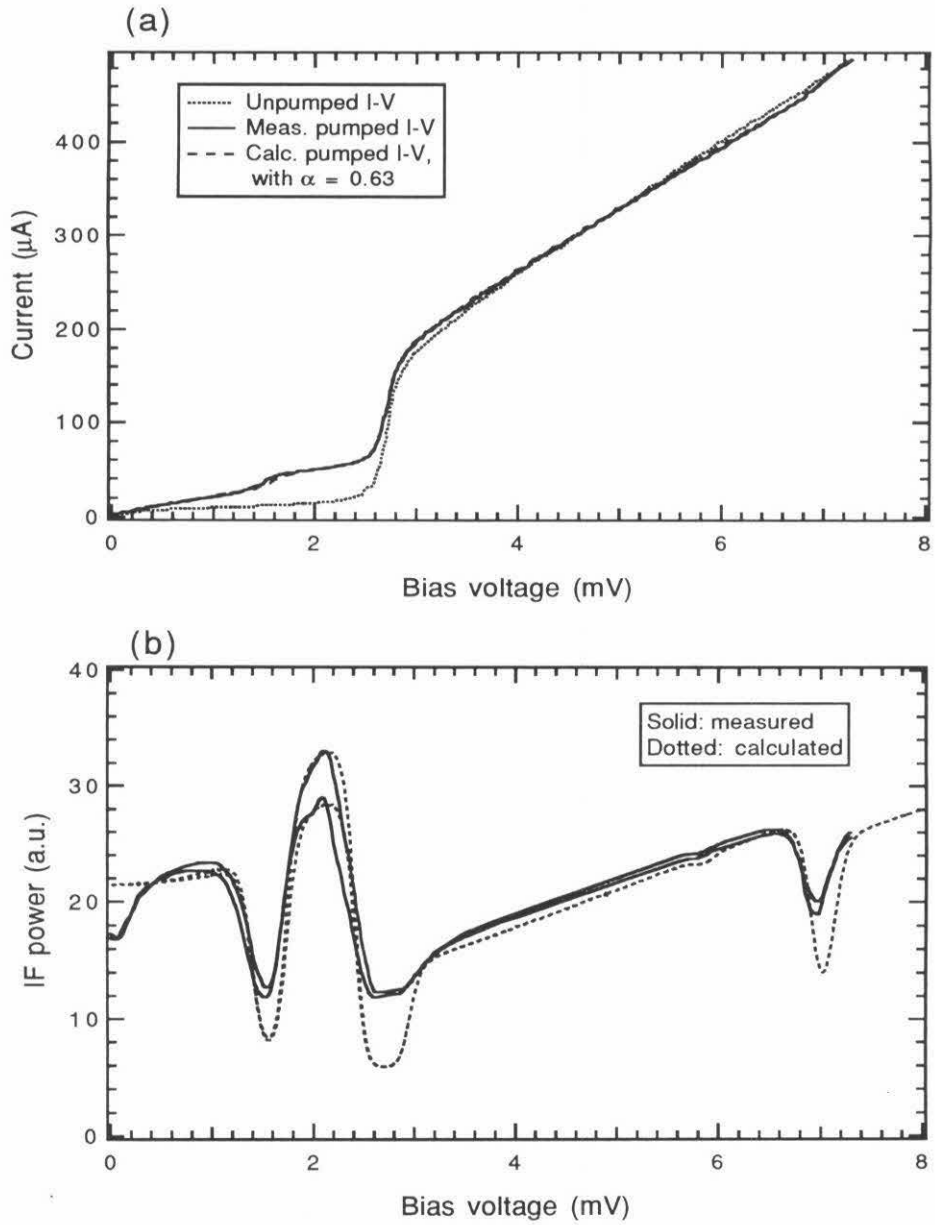

Figure 7.8: (a) Comparison between the measured and calculated IVs with LO pumping at 1042 GHz. The calculation for the pumped IV is carried out by assuming a constant LO voltage $\alpha = 0.63$. (b) The measured and calculated IF output powers. In the calculation the RF embedding admittance is $3.5 + j2.1$, normalized to the normal state conductance, and the IF load impedance is 70 Ω. The noise and gain of the IF amplifier is obtained using the shot noise technique.

Table 7.4: Estimated contributions from the front end optics to receiver conversion loss and noise temperature: device 1028 at 1042 GHz and 4.2 K

Components	Estimated transmission t	Temperature (K)		Noise (K)
		$T^{\rm amb}$	$T^{\rm amb}_{\rm eff}$	$T_{\rm n} = (1-t)T^{\rm amb}_{\rm eff}/t$
10 μm Mylar b.s.	0.91	295	275	27.2
25 μm Mylar window	0.82	295	275	60.4
IR clear quartz filter	0.97	77	58	1.8
Polyethelene lens	0.94	4.2	0.003	0.0
Silicon lens and antenna	0.85	4.2	0.003	0.0
Al tuning circuit	0.24	4.2	0.003	0.0
Total RF optics gain $G_{\rm RF} = 0.139 = -8.6$ dB			Total contrib. noise $T_{\rm RF} = 96$ K	

Table 7.5: Breakdown of the receiver loss and noise contributions for device 1028 working at 1042 GHz and 4.2 K, biased at 2.0 mV

	Noise	Loss	Breakdown of noise
RF optics	$T_{\rm RF} = 96$ K	$G^{-1}_{\rm RF} = 8.6$ dB	$T_{\rm RF} = 96$ K
Mixer	$T_{\rm mix} = 131$ K	$G^{-1}_{\rm mix} = 8.2$ dB	$T_{\rm mix}/G_{\rm RF} = 942$ K
IF chain	$T_{\rm IF} = 6$ K	–	$T_{\rm IF}/G_{\rm RF}G_{\rm mix} = 288$ K
Receiver (calculated)	1326 K	$L^{\rm calc}_{\rm rec} = 16.8$ dB	total $T_{\rm rec} = 1326$ K
Receiver (measured)	1201 K	$L^{\rm meas}_{\rm rec} = 16.2$ dB	

that only small deviations are observed of the calculated curves from the measured ones.

The measured receiver noise is obtained using the Y-factor method. By combining the knowledge of the IF amplifier chain obtained using the shot noise technique, we can also find the receiver conversion loss. The IF output powers for hot and cold load are expressed as

$$\begin{aligned} P^{\rm hot} &= k_{\rm B}G_{\rm IF}G_{\rm RF}G_{\rm mix}(T^{\rm hot}_{\rm signal} + T_{\rm rec}), \\ P^{\rm cold} &= k_{\rm B}G_{\rm IF}G_{\rm RF}G_{\rm mix}(T^{\rm cold}_{\rm signal} + T_{\rm rec}). \end{aligned} \tag{7.3}$$

The measured values of IF output power are 34 and 29 in arbitrary units for the hot and cold load, which have effective signal temperature of 275 K and 58 K. The IF gain $k_{\rm B}G_{\rm IF}$ is calibrated as 0.968 arbitrary units/K. Substituting these values into (7.3)

we get the measured receiver noise temperature 1201 K and the receiver conversion loss $L_{\rm rec} = (G_{\rm RF}G_{\rm mix})^{-1} = 16.2$ dB. The calculated receiver noise temperature at bias 2.0 mV is obtained using:

$$T_{\rm rec} = T_{\rm RF} + \frac{T_{\rm mix}}{G_{\rm RF}} + \frac{T_{\rm IF}}{G_{\rm RF}G_{\rm mix}} , \tag{7.4}$$

where $T_{\rm RF}$ is the noise contribution of the front end optics referred to the input of the receiver, and $G_{\rm RF}$ is the total gain of the front end optics, given in Table 7.4. The breakdown of the total receiver loss and noise into the contributions from the front end RF optics, the mixer and the IF amplifier is clearly demonstrated in Table 7.5. The calculated receiver noise temperature is 1326 K, about 10% higher than the experimental value of 1218 K. This discrepancy can be easily caused by any error in the estimate of gain and noise of the front end optics. We have calculated the front end optics losses in an extremely simplified manner: the transmission is mostly obtained by a simplified calculation or empirical estimation, and the physical temperature of a component is taken as its ambient temperature. In practice, it is difficult to calibrate the front end optics.

When the mixer was cooled to 2.5 K, the receiver noise temperature dropped from 1170 K to 840 K at 1042 GHz. The 40% improvement in the receiver noise temperature at the lower temperature can be largely explained by the reduction in the subgap leakage current and the increase in the gap voltage. The unpumped IVs at bath temperature of 4.2 K and 2.5 K are shown in Fig. 7.9. The dark current drops from 15 μA to 10 μA at 2 mV and the gap voltage increases from 2.7 mV to 2.9 mV. Tucker theory calculations based on these effects indicate a 20% drop in the mixer noise temperature and a 35% reduction in the conversion loss. Therefore, a 25%–35% reduction in the receiver noise temperature can be expected from these effects. The loss of microstrip lines at a lower temperature may also be smaller due to a lower Al resistivity. However, the series resistance due to the resistive current path only drops from 2.74 Ω to 2.65 Ω, indicating a 3% increase in Al resistivity ratio. The increase in RF coupling efficiency is negligible (0.4%) due to such a change in Al resistivity

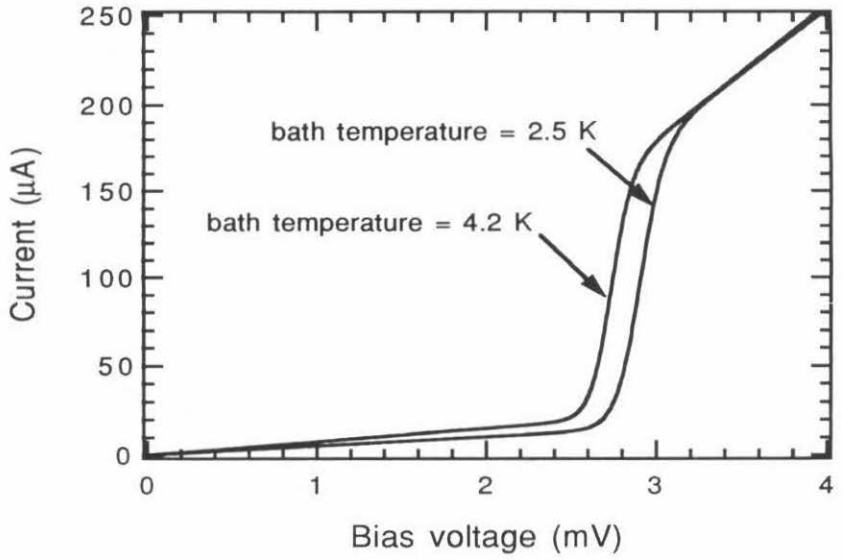

Figure 7.9: Unpumped dc IVs for device 1028 at a bath temperature of 4.2 K and 2.5 K. The reduction in the subgap leakage current and the increase in the gap voltage are largely responsible for the 40% receiver noise temperature drop from 4.2 K to 2.5 K.

ratio. Therefore, the reduction in microstrip loss is not a significant contributor to the drop of receiver noise temperature.

7.3.2 Device 1028 at 982 GHz

The analysis of receiver results at 1042 GHz shows us that the performance of Nb-based SIS mixers can be predicted quite well by Tucker's theory above the gap frequency. Now we will examine the experimental results at 982 GHz LO frequency and at 2.5 K bath temperature.

As we mentioned earlier, we were unable to obtain optimum pumping of the junction due to the lack of LO power at 982 GHz when using a 25 μm thick beamsplitter. The use of a 51 μm thick beamsplitter improved the pumping condition, and thus allowed a better mixer performance. However, the receiver noise temperature increased (as expected) because the thicker beamsplitter introduced more signal loss. The pumped IVs with these two beamsplitters were shown in Fig. 7.10. By assuming

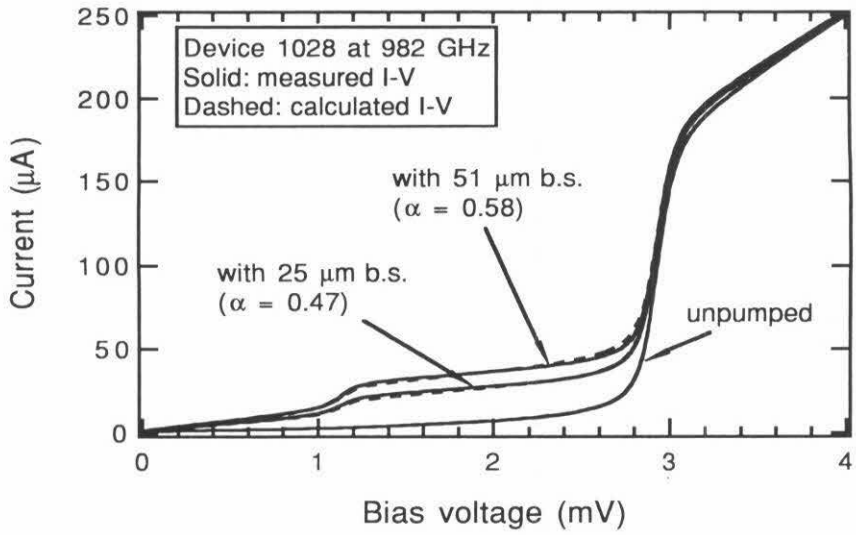

Figure 7.10: Unpumped and pumped dc IVs for device 1028 at 982 GHz and at a bath temperature of 2.5 K. The thicker beamsplitter (51 μm) couples more LO power onto the junction. Calculated IVs for the two pumping cases are also plotted.

constant LO voltage, we can calculate the pumped IV from the unpumped one. This allows us to find the LO voltage α of the pumping. With $\alpha = 0.47$ and $\alpha = 0.58$, the calculated IVs follow the measured ones very well as can be seen in Fig. 7.10. Tucker's mixer calculation can then be performed based on the pumping information and embedding environment. Using the PCIRCUIT program we find the RF embedding admittance to be $4.2 + j0.6$, normalized to the junction normal state conductance $(14\ \Omega)^{-1}$. The IF load resistance is 70 Ω. The theory predicts that the optimum pumping for the mixer would occur around $\alpha = 0.7$.

To calculate the receiver performance, the transmission and noise of the front end optics are estimated and listed in Table 7.6. Note the use of a 51 μm beamsplitter increased the RF loss by 1 dB and the RF noise by $\sim$ 100 K compared to the use of a 25 μm beamsplitter. We calibrated the IF chain using the shot noise technique. The calculated IF output powers for hot and cold load for the case of a 25 μm beamsplitter are shown in Fig. 7.11a, along with the measured IF output powers. The calculated power is $\sim$ 5.3% lower than the measured value in the subgap first photon step

Table 7.6: Estimated contributions from the front end optics to receiver conversion loss and noise temperature: device 1028 at 982 GHz and 2.5 K

Components	Estimated transmission t	Temperature (K)		Noise (K)
		$T^{\rm amb}$	$T^{\rm amb}_{\rm eff}$	$T_{\rm n} = (1-t)T^{\rm amb}_{\rm eff}/t$
25 μm b.s. / 51 μm b.s.	0.70 / 0.56	295	272	116.6 / 213.7
AR-coated qutz. window†	0.91	295	272	26.9
AR-coated qutz. filter†	0.96	77	55.8	2.3
Polyethelene lens	0.94	2.5	0.00	0.0
Silicon lens and antenna	0.87	2.5	0.00	0.0
Al tuning circuit	0.23	2.5	0.00	0.0
For 25 μm b.s.: RF gain $G_{\rm RF} = 0.12 = -9.2\ dB$, RF noise $T_{\rm RF} = 158.6\ K$				
For 51 μm b.s.: RF gain $G_{\rm RF} = 0.096 = -10.2\ dB$, RF noise $T_{\rm RF} = 266.2\ K$				

† The room temperature quartz window is AR-coated for center frequency of 714 GHz, with a calculated transmission of 94% at the center. The 77 K IR filter is AR-coated for center frequency of 814 GHz, with a peak transmission of 97%.

Table 7.7: Receiver performance of device 1028 at 982 GHz and 2.5 K. Comparisons between the use of two beamsplitters are made.

B.S.	$G_{\rm RF}$	$T_{\rm RF}$	$T_{\rm eff}$(mixer)		α	$T^{\rm calc}_{\rm mix}$	$G^{\rm calc}_{\rm mix}$	$T^{\rm calc}_{\rm rec}$	$T^{\rm meas}_{\rm rec}$
			hot	cold					
25 μm	-9.2 dB	158.6 K	51.7 K	25.8 K	0.47	87 K	-7.4 dB	1287 K	1339 K
51 μm	-10.2 dB	266.2 K	51.7 K	29.6 K	0.58	85 K	-6.8 dB	1594 K	1620 K

Note: all the temperature in this Table is the effective temperature of a blackbody, *i.e.*, $k_{\rm B}T$ is the radiated power received by an antenna.

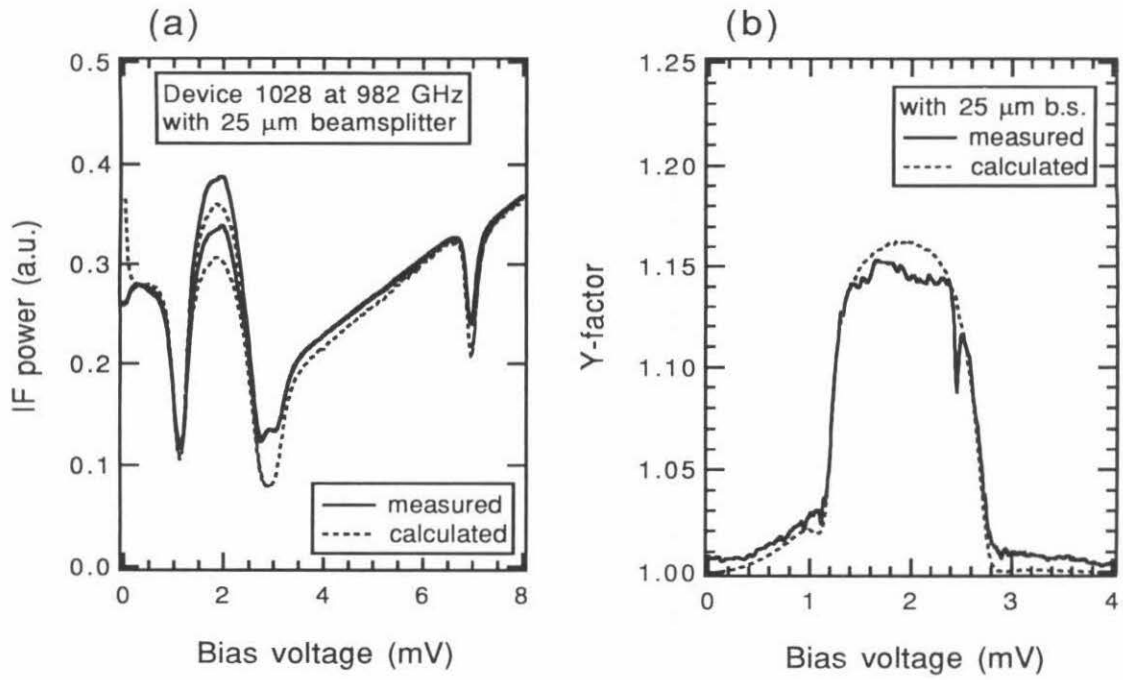

Figure 7.11: Measured and calculated IF output power (a) and Y-factor (b) for device 1028 at 982 GHz and 2.5 K bath temperature. The calculation assumes a LO pumping strength $\alpha = 0.47$ (see Fig. 7.10).

region. This can be a result of overestimated RF loss (giving smaller effective signal temperature), or small errors in the Tucker theory. Overall the simulation and the experimental data agree quite well. Fig. 7.11(b) shows the measured and calculated Y-factor.

The calculated mixer noise and gain and related values are listed in Table 7.7. Comparisons are made between the use of the two beamsplitters. Note that when a 51 μm beamsplitter is used, the mixer has a better performance (lower mixer noise and smaller mixer conversion loss), because the junction is better pumped. However, the receiver performance is adversely affected since the thicker beamsplitter has greater RF signal loss. If enough LO power is available and a 10 μm beamsplitter could be used, the uncorrected receiver noise is expected to be $\sim$ 850 K.

7.4 Device 716

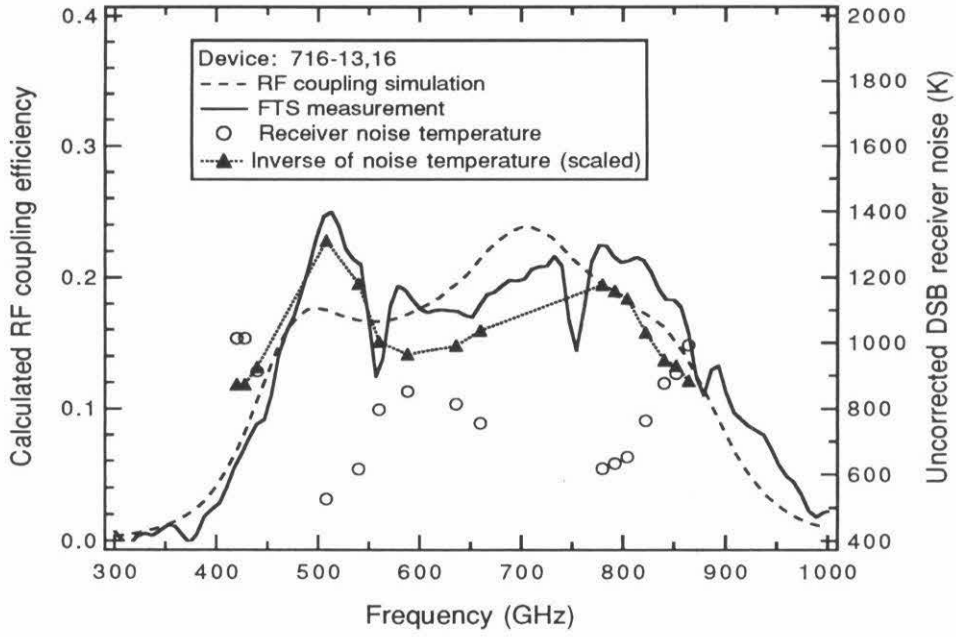

Figure 7.12: FTS spectrum and receiver performance for device 716. The measured and simulated RF coupling efficiencies are plotted vs. frequency. The measured receiver noise temperatures at a bath temperature of 4.2 K are also shown. The inverse of the receiver noise temperature is vertically scaled to demonstrate the relation between the FTS direct detection and the receiver heterodyne performance.

Device 716 is designed for center frequency of 750 GHz. The junction size is 1.2 μm^2. The tuning circuit is optimized for a junction area of 1.7 μm^2 assuming a specific capacitance of 65 fF/μm^2. Since the actual specific capacitance is approximately 85 fF/μm^2, device 716, instead of device 726, gives closer RF coupling response to the optimized simulation. The measured FTS spectrum and simulated RF coupling response are shown in Fig. 7.12. The response has wide 3 dB bandwidth from 450 GHz to 900 GHz. The two dips in the FTS spectrum at 557 GHz and 752 GHz are due to the absorption of residual water vapor in the FTS system.

The device is installed in a dewar which utilizes a 1 mil Mylar pressure window and a Zitex IR filter. The silicon hyperhemispherical lens is AR-coated for center

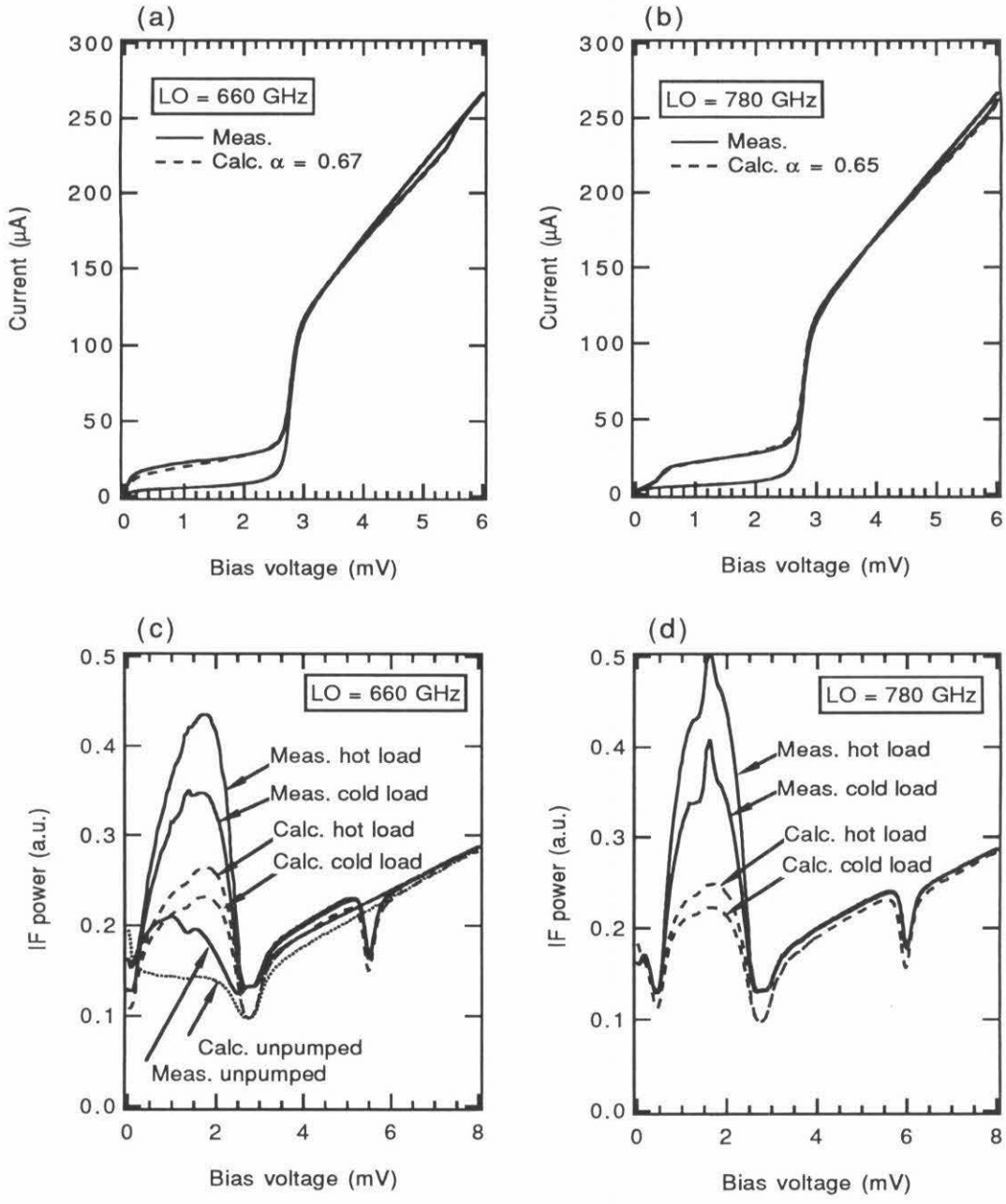

Figure 7.13: Calculated and measured receiver performance for device 716 at 660 GHz and 780 GHz LO frequencies and 4.2 K bath temperature. (a) and (b) show the measured and calculated pumped IVs. (d) and (c) present the measured and calculated IF output powers.

Table 7.8: Uncorrected DSB receiver noise temperatures of device 716 at bath temperatures of 4.2 K and 2.5 K.

Frequency (GHz)	T_{rec} at 4.2 K (K)	T_{rec} at 2.5 K (K)	Frequency (GHz)	T_{rec} at 4.2 K (K)	T_{rec} at 2.5 K (K)
392	1220	–	636	813	–
420	1013	–	660	755	–
428	1013	–	780	617	–
440	914	–	792	631	–
508	526	423	804	653	–
515	596	–	822	762	643
540	615	–	840	877	682
560	796	–	852	906	754
588	852	–	864	991	–

frequency of 750 GHz. We measured the receiver noise temperature from $\sim$ 400 GHz to 860 GHz. Several Gunn oscillators and multipliers are used to cover the frequency range. A 25 μm thick beamsplitter is used to combine the LO with the signal. The uncorrected DSB receiver noise temperatures are given in Table 7.8 and also shown in Fig. 7.12. To compare the direct detection response with the heterodyne detection result, the inverse of the receiver noise temperature is also plotted in Fig. 7.12. The inverse is vertically scaled to show an apparent correlation between the FTS measured response and the receiver noise performance. The figure shows that the receiver heterodyne frequency range can be predicted with FTS direct detection measurements. This correlation can be understood by examining the noise contributions to the receiver:

$$T_{rec} = T_{RF} + \frac{T_{mix}}{G_{RF}} + \frac{T_{IF}}{G_{RF}G_{mix}} .$$

The FTS measurement provides the frequency dependence of G_{RF}. T_{RF} is mostly determined by the front end optics (excluding the on-chip RF tuning circuits), and is a slow function of frequency. Under optimum bias and pumping conditions, the mixer gain G_{mix} and noise T_{mix} should also be slow functions of frequency. Hence the frequency dependence of the receiver noise is mainly inversely determined by the RF coupling efficiency G_{RF}.

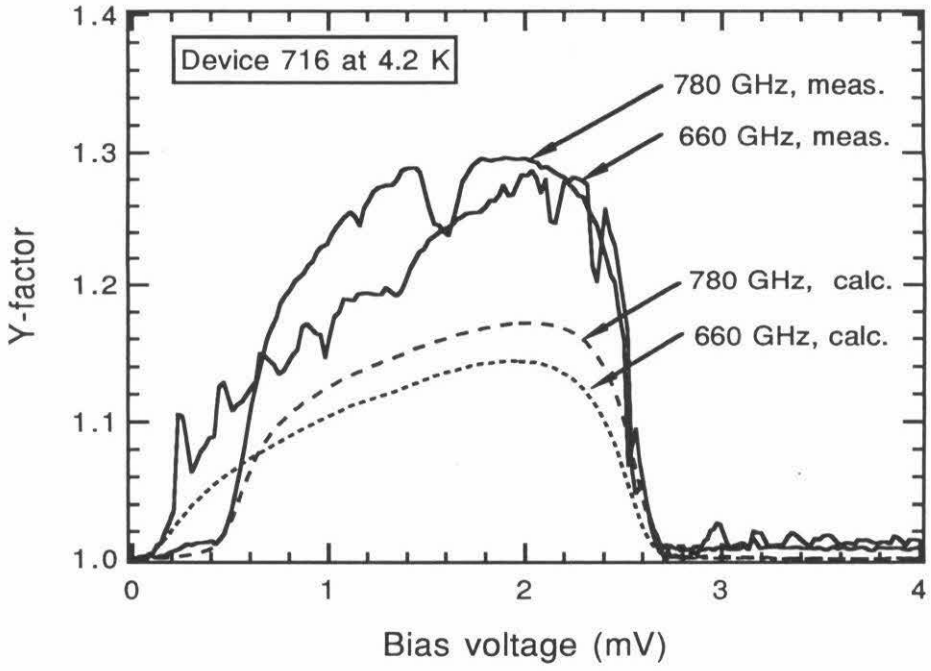

Figure 7.14: Calculated and measured Y-factors for device 716 at 660 GHz and 780 GHz LO frequencies and 4.2 K bath temperature.

We have tried to calculate the receiver performance of device 716 working at LO frequencies of 660 GHz and 780 GHz as we did for device 1028. We estimated the transmission and noise of the front end optics and RF tuning circuits; calculated the RF embedding admittance using the PCIRCUIT program; calibrated the IF chain properties using the shot noise technique; and found out the LO pumping strength α from the unpumped and pumped IVs. One thing to be pointed out here is that a different IF amplifier was used for device 716 than that for device 1028. For device 1028 we used a laboratory built IF amplifier (by Jacob Kooi) and the calibrated IF noise temperature is approximately 6 K. For device 716 a Berkshire IF amplifier with an isolator at the front was used and the calibrated noise temperature is approximately 16 K. The measured and calculated receiver performance results are shown in Fig. 7.13. The gap voltage is 2.75 mV, corresponding to a gap frequency of $\sim$ 660 GHz. From the pumped IVs we deduced the pumping strength $\alpha = 0.67$

for 660 GHz LO and $\alpha = 0.65$ for 780 GHz LO. The measured and calculated IVs are shown in Fig. 7.13a and b. The measured and calculated IF output powers are shown in Fig. 7.13c and d. Unlike the calculations for device 1028, here the discrepancies between the calculated and measured IF powers are large. The calculated IF powers are lower than the measured ones by approximately 40%. The Y-factors for the two cases are shown in Fig. 7.14. Again, the calculated and measured Y-factors differ by large amounts, with the calculated ones lower than the measured ones by approximately 12%. The discrepancies can not be explained by possible errors in the evaluation of the front end optics and RF tuning circuits. They are unlikely to be caused by excess mixer noise either since that would produce a lower measured Y-factor than the calculated one. It is possible that the IF embedding impedance is more complex than the assumed real value of 70 Ω, causing a different mixer gain in the subgap region. More careful studies need to be done before drawing conclusions.

7.5 Device 428

Device 428 is designed for the center frequency of 450 GHz. Since it works below the Nb gap frequency, the device is not designed to compete with the all-Nb junctions for the same frequency range. Rather it is used to check the RF tuning circuit design and modeling. In this section we describe the direct and heterodyne detection measurements for this device. Detailed analysis of receiver performance is made for a single frequency point at 430 GHz. We find that the mixer noise is at the quantum noise level and the high receiver noise is largely caused by the RF loss in the Al-tuning circuits.

The front end optics for the receiver consist of a 10 μm LO injection beamsplitter, an AR-coated quartz pressure window, a layer of Zitex IR filter at 77 K shield, a Teflon lens at 4.2 K, and an AR-coated silicon hyperhemispherical lens centered at 450 GHz. The FTS spectrum and the calculated RF coupling efficiency are shown in Fig. 7.15. The calculation is done using the PCIRCUIT program as before, with all the circuit parameters being the designed values. It can be seen that our circuit model predicts

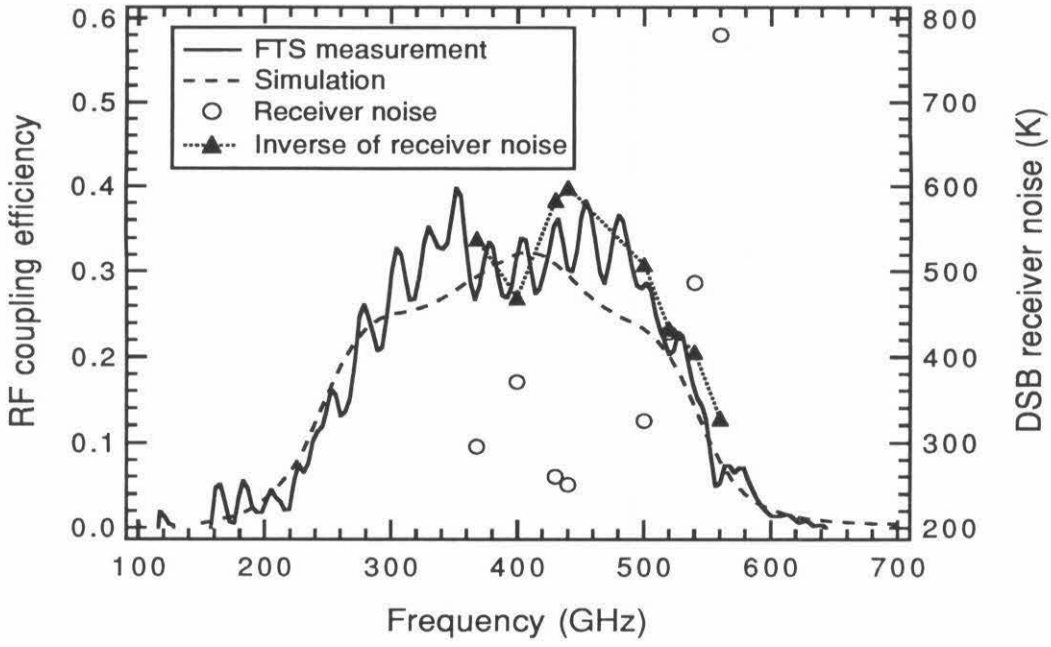

Figure 7.15: FTS spectrum and receiver performance for device 428. The measured and simulated RF coupling efficiencies are plotted vs. frequency. The measured receiver noise temperatures at a bath temperature of 4.2 K are also shown. The inverse of the receiver noise temperature is vertically scaled to demonstrate the relation between the FTS direct detection and the receiver heterodyne performance.

the RF coupling quite well. The heterodyne receiver performance is measured at several LO frequencies from 368 GHz to 560 GHz at a bath temperature of 4.2 K, with the lowest uncorrected DSB receiver noise temperature 250 K at 440 GHz. These receiver noise temperatures are given in Table 7.9 and also plotted in Fig. 7.15 to demonstrate the relation between the measured RF coupling efficiency and the heterodyne sensitivity. Again as in Fig. 7.12 for device 716, the (scaled) inverse of the receiver noise temperature follows the RF coupling response curve.

Table 7.9: Uncorrected DSB receiver noise temperatures of device 428 at a bath temperature of 4.2 K

Frequency	368	400	430	440	500	520	540	560
$T_{\rm rec}$	296	371	260	251	325	429	487	780

Table 7.10: Estimated contributions from the front end optics to receiver conversion loss and noise temperature: device 428 at 430 GHz and 4.2 K

Components	Estimated transmission t	Temperature (K)		Noise (K) $T_n = (1-t)T_{eff}^{amb}/t$
		T^{amb}	T_{eff}^{amb}	
10 μm beamsplitter	0.98	295	285	4.6
AR-coated qutz. window	0.97	295	285	15
Zitex 77 K IR filter	0.99	77	67	0.7
Polyethelene lens	0.96	4.2	0.15	0.01
Silicon lens and antenna	0.95	4.2	0.15	0.01
Al tuning circuit	0.35	4.2	0.15	0.35
Calculated from above values: RF gain $G_{RF} = 0.30 = -5.2$ dB, RF noise $T_{RF} = 21$ K				

Table 7.11: Breakdown of the receiver loss and noise contributions for device 428 working at 430 GHz and 4.2 K, biased at 2.1 mV

	Noise	Loss	Breakdown of noise
RF optics	$T_{RF} = 21$ K	$G_{RF}^{-1} = 4.0$ dB	$T_{RF} = 21$ K
Mixer	$T_{mix} = 32$ K	$G_{mix}^{-1} = 5.2$ dB	$T_{mix}/G_{RF} = 108$ K
IF chain	$T_{IF} = 16$ K	–	$T_{IF}/G_{RF}G_{mix} = 141$ K
Receiver (calculated)	271 K	$(G_{rec}^{calc})^{-1} = 9.2$ dB	total $T_{rec} = 271$ K
Receiver (measured)	278 K	$(G_{rec}^{meas})^{-1} = 7.6$ dB	

We now analyze the receiver performance at 430 GHz. First the IF chain is calibrated using the shot noise technique. The IF amplifier is a Berkshire amplifier with an isolator at the front, the same as we used for device 716. The calibrated IF amplifier noise is 16 K. The LO pumping strength $\alpha = 0.8$ is derived from the unpumped and pumped IVs, as shown in Fig. 7.16a. The RF embedding admittance is calculated using the PCIRCUIT program as $2.5 + j1.6$, normalized to the normal state conductance of the junction $(13.5\ \Omega)^{-1}$. The mixer performance is then calculated using Tucker's theory. The theory predicts that the lowest conversion loss occurs at a bias 2.1 mV and a LO pumping strength $\alpha = 0.8$, in agreement with the experimentally derived data. The DSB mixer conversion loss is 4.0 dB and the mixer noise is 32 K. The estimated transmission of the front end optics and the RF tuning circuits is given in Table 7.10. The total calculated conversion loss of the RF section G_{RF}^{-1} is 5.2 dB and the introduced noise T_{RF} is 21 K. The calculated receiver conversion

loss $G_{\rm rec}^{-1}$ is therefore 9.2 dB. Using (7.4) the calculated receiver noise temperature is found to be 271 K. Fig. 7.16b shows the calculated and measured IF output power for the hot load. Like device 716, the calculated IF output power is smaller than the measured one by a large amount $\sim 35\%$.

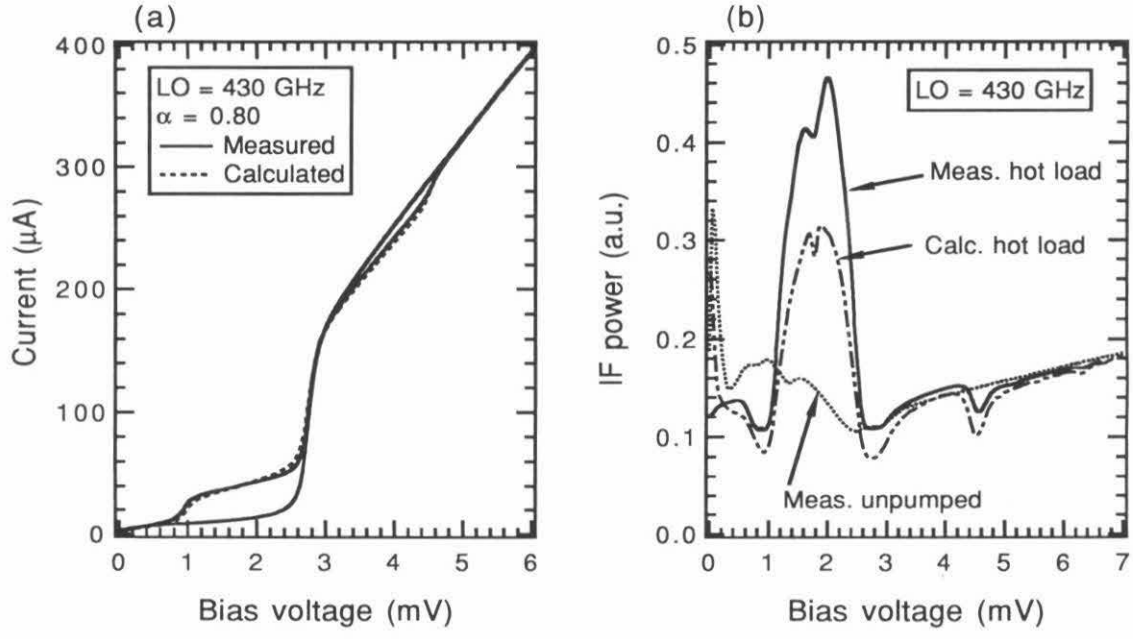

Figure 7.16: Analysis for device 428 at 430 GHz and 4.2 K bath temperature. (a) Comparison between the measured and calculated pumped IV. The calculation for the pumped IV is carried out by assuming a constant LO voltage $\alpha = 0.8$. (b) The measured and calculated IF output power for the hot load.

The experimental receiver performance is obtained using Y-factor method (7.3): measured receiver noise is 278 K and receiver conversion loss is 7.6 dB. The calculated and measured values are compared in Table 7.11, along with the breakdown of the noise contributions from different sections.

7.6 Chapter summary

Nb/Al-oxide/Nb SIS mixers employing normal-metal Al tuning structures have been demonstrated successfully as THz heterodyne detectors. Quasi-optical coupling is

used for ease of fabrication and operation at THz frequencies. More specifically, twin-slot antenna, double-junction, and anti-symmetric feed configuration is incorporated due to its advantages of good beam pattern, low driving impedance, and no dc blocking capacitance. The tuning structures consist of one section of transmission line connecting two junctions serving as a short shunted inductor, and another section of transmission line as impedance transformer. A device designed for 1050 GHz band covers a wide frequency bandwidth, from $\sim$ 700 GHz to 1200 GHz. The integrated RF tuning circuits have a coupling efficiency $\sim$ 25% at 1 THz. An uncorrected DSB receiver noise temperature of 840 K at 1042 GHz is obtained using this device.

Devices with normal-metal Al wiring have been designed for each of the frequency bands 450 GHz, 750 GHz, 850 GHz, 950 GHz, and 1050 GHz, for the purpose of checking design models. Fourier transform spectroscopy has been used to obtain the frequency response of the RF tuning circuits using the junction as a direct detector. Generally good agreement between the measurements and theoretical simulations is achieved, showing the successful design of the tuning circuits and verifying our circuit models discussed in chapter 4. The frequency response of heterodyne receiver performance is found to follow the response of the RF coupling very well, making FTS measurement a quick and reliable way to pre-sort mixer elements.

Mixer performance of several devices has been analysed using Tucker's theory. Calculated receiver performance based on the mixer analysis and the front end optics are compared with experimental results. Moderately good agreement was obtained for device 1028 at 982 GHz and 1042 GHz. However, large discrepancies in the receiver gain (about 2 dB) occurred for device 716 at 660 and 780 GHz, and for device 428 at 430 GHz. Apart from the errors introduced in the front end optics estimation, errors in the IF amplifier noise and gain calibration can be significant in the subgap region. More studies should be done before we can draw conclusions.

Our work demonstrates that Nb junctions can offer superior performance at THz frequencies when implemented with low-loss normal-metal Al tuning structures. The 200 nm thick Al film used in our mixers has a resistivity ratio of approximately 5 at $\sim 2-4$ K, compared to the room temperature bulk resistivity of 2.45 $\mu\Omega$-cm. Further

advances in THz SIS mixers may be possible using circuits fabricated with higher-gap superconductors such as NbN. However, this will require high-quality films with low RF surface resistance at THz frequencies.

Chapter 8 Summary

The goal of this thesis research is to find a way to extend the low noise performance of SIS mixers to frequencies above the gap. This was achieved by use of normal-metal Al rather that superconductor Nb microstrip lines in the tuning circuit. Performance of our quasi-optical Nb-based SIS receivers was measured in various ways including the use of a specially constructed FTS. In the previous chapters we have given detailed description of receiver systems and mixer designs, and analysis of the direct and heterodyne test results. Here we will summarize the thesis.

In chapter 1 and chapter 2 we covered some experimental and theoretical background of the SIS mixers. Tucker's SIS mixer theory was described. The three-port approximation of Tucker's theory laid down the basis for our mixer performance analysis.

We use quasi-optical coupling receivers for their intrinsic broadband nature and ease of fabrication and operation. Chapter 3 first gave a brief introduction to the substrate lens, the hyperhemispherical lens, used with the integrated micro-antennas. The front end optics and the mixer block circuitry of our receiver were then described in detail. Much attention was paid to the twin-slot antenna double-junction configuration incorporated in all of our mixers. The twin-slot antenna on a silicon substrate has a low driving impedance of about 30 Ω at the design frequency and a beamwidth around 50°, corresponding to a f-number of 2.5. This small f-number is further increased by the hyperhemispherical lens and an extra polyethelene lens.

The use of integrated tuning for SIS mixers has become a standard practice among SIS receiver builders to increase the bandwidth and the RF coupling efficiency. Chapter 4 first briefly reviewed the major RF tuning circuits to date, and the properties of microstrip transmission lines which serve as the tuning inductors and transformers. Microstrip design equations were then given to calculate the characteristic impedance,

phase velocity, and attenuation constant. In order to calculate the RF losses in the microstrip correctly, the surface impedance of superconductors and normal metals were studied theoretically. It was argued that the non-local anomalous skin effect has to be used for the normal metal films at low temperatures (approximately liquid helium temperature) and high frequencies (THz regime), because the film thickness (and presumably the electron mean free path) are much larger than the classical skin depth. For the case of normal-metal Al, the typical thickness $\sim$ 200 nm of the Al film used for the microstrip would limit the resistivity ratio to $\sim$ 10, due to the fact that the electron mean free path was limited to the film thickness. The resistivity ratio of the Al film in our mixers was found experimentally $\approx$ 5. The Mattis-Bardeen theory in the extreme anomalous limit was used to calculate the complex conductivity of superconducting Nb. The Nb surface impedance was calculated substituting the complex conductivity into the normal skin effect surface impedance formula. Good agreement between this approximate result and the strict solution of the Mattis-Bardeen equations was found. Although the resistivity ratio of Al was only 5, the resistivity of Al was still an order of magnitude smaller than the normal state resistivity of Nb at its critical temperature. We predicted that the RF coupling efficiencies of Al-wiring and Nb-wiring junctions were comparable around 830 GHz and the Al-wiring ones would become superior at higher frequencies.

In Chapter 4 we also described a circuit simulation program, PCIRCUIT. This program utilizes a two-port microwave technique to calculate circuit properties. Using PCIRCUIT we were able to simulate and optimize the mixer design in a quick and accurate way if we knew the antenna driving impedance, the junction IVs, and the geometrical and physical parameters of the tuning circuits.

Fourier transform spectroscopy is a powerful tool to quickly obtain the mixer frequency response. We have constructed a laboratory Fourier transform spectrometer (FTS) to study the frequency response of SIS mixers at submillimeter wavelengths. Chapter 5 described the FTS system and some related problem solving, such as the alignment of the optics and the purging of the system using N_2 gas. This FTS

features large aperture size (10 inch in linear dimension) and high frequency resolution (114 MHz). All the response spectra shown in this thesis were obtained on the FTS. The mechanism for testing SIS mixers in direct and heterodyne modes on the FTS were discussed based on the quantum theory of SIS mixers. Examples were given of the direct detection response and the heterodyne detection response. The FTS heterodyne spectrum had sufficiently high resolution to resolve the sidebands. It was the first heterodyne measurement done on a FTS system, verifying that our devices did in fact perform as mixers.

Using PCIRCUIT, we designed all Nb-wiring and Al-wiring Nb/Al-oxide/Nb SIS mixers. The all Nb-wiring mixers were designed for frequency bands from 450 GHz to 750 GHz whereas the Al-wiring mixers were designed for the bands from 450 GHz to 1050 GHz. Chapter 6 and chapter 7 are devoted to the description and analysis of these mixers. Below we will summarize the results presented in these two chapters.

The frequency responses of both Nb-wiring and Al-wiring devices were measured on the FTS and compared with the theoretical simulations. The agreement between experimental results and simulations are excellent given that all the parameters in the simulations are actual design values. This verifies our model for calculating lossy superconducting and normal-metal microstrip lines. It also proves the effectiveness of our circuit program PCIRCUIT. We compared the heterodyne response (receiver noise temperature vs. frequency) with the FTS measured RF coupling response for several devices and found close correlation between the two responses. FTS measurement hence serves not only as a check for the design ideas but also as a quick and reliable way of selecting mixer elements.

We used Tucker's theory to calculate the mixer performance of some devices. The mixer noise is usually a few times of the quantum-limited noise level no matter if the mixer has Nb-wiring or Al-wiring. The Nb-wiring mixer designed for center frequency 750 GHz had a DSB mixer noise of 83 K at 852 GHz ($h\nu \approx 41$ K) although the LO power was not sufficient. For Al-wiring mixers: device 1028 had a DSB mixer noise of 131 K at 1042 GHz ($h\nu \approx 50$ K) and 85 K at 982 GHz ($h\nu \approx 47$ K); device 428

has a mixer noise of 32 K at 430 GHz ($h\nu \approx 21$ K). It is clear that the Nb SIS mixers work very well high above the gap frequency into the THz regime. To achieve low noise receivers, it is important to have small RF loss, as it is the major cause of high receiver noise, especially for Al-wiring mixers and for Nb-wiring mixers above the gap frequency.

For our mixer design, the RF coupling (from the integrated antenna to the junction) of the Nb-wiring devices was around 90% (0.5 dB loss) below the gap frequency and 70% (1.5 dB loss) at 750 GHz. The Al-wiring device had RF coupling about 40% (4.0 dB loss) at 450 GHz and 25% (6.0 dB loss) at 750 GHz. Note that the design may not be the optimum since in the design stage we did not know the Al resistivity ratio and the actual junction IV curve. For instance, the current design of Al-wiring device 1028 has a RF coupling $\sim$ 25% at 1050 GHz. If we used the actual physical parameters and optimized the circuit again, a RF coupling of 30% could be obtained. At 1050 GHz, the RF coupling of the Al-wiring device was predicted to be 50% higher than that of the Nb-wiring one. The front end optics, from the LO injection beamsplitter to the integrated antenna, usually introduces a few dB loss at THz frequencies, depending on the thickness of the beamsplitter. The front end optics excluding the beamsplitter has 1.5 – 2.0 dB loss for most of the frequency range. The beamsplitter has loss of 0.4, 1.5 and 2.5 dB for a Mylar thickness of 10 μm, 25 μm and 51 μm, respectively. The lack of LO power at THz frequencies often dictates the use of thick beamsplitters, adversely increasing the receiver noise. The situation is further degraded by our relatively large junctions, since the LO power needed for optimum pumping scales directly with the total junction area. Smaller junction areas fabricated using the existing submicron junction technology would reduce the demand for LO power by a factor of six.

When cooling the bath temperature from 4.2 K to 2.5 K, the receiver noise temperature drops approximately 100 – 330 K. Analysis of Al-wiring device 1028 at 1042 GHz from a 4.2 K bath to a 2.5 K bath shows that the drop in receiver noise is largely explained by the reduction in the subgap leakage current and the increase in the gap voltage. Tucker's theory predicts a 20% drop in mixer noise temperature and

35% reduction in the mixer conversion loss, accounting for 25–35% of the measured 40% drop of the receiver noise temperature. The reduction in Al microstrip loss is negligible.

We calculated the IF output powers for Al-wiring mixers and compared them with measured ones. The mixer performance was calculated based on the unpumped and pumped IVs using Tucker's theory. The IF amplifier chain was calibrated using shot noise technique. For device 1028 at frequencies 1042 GHz and 982 GHz, the agreements between the calculations and the experiments are excellent, showing that the SIS mixer theory is valid high above the gap frequency. For device 716 at frequencies 660 GHz and 780 GHz, and device 428 at 430 GHz, the calculations qualitatively explained the experimental results. But there were large discrepancies, with the calculated IF powers smaller than the measured ones by $\sim 40\%$ in the first photon step below the gap voltage. The underestimate could not be explained by possible errors in the evaluation of the transmission and noise of the front end optics and RF tuning circuits. One difference in the measurement setup for these devices is that device 1028 used a laboratory built IF amplifier while device 716 and 428 used a commercial Berkshire IF amplifier. It is possible that the IF embedding environment was much more complex in the latter case, and the assumption of a real IF load impedance of 70 Ω did not apply. More careful studies are needed to obtain a good understanding on this point.

In conclusion, we list here the best receiver noise temperatures obtained for our quasi-optical twin-slot double-junction mixers with Nb- or Al-wiring. For Nb-wiring mixers, the 400 – 850 GHz frequency band was covered with four separate fixed-tuned mixers. The uncorrected DSB receiver noise temperatures are around $5h\nu/k_{\rm B}$ to 700 GHz, and better than 540 K at 808 GHz. These results are among the best reported to date for broadband heterodyne receivers. The THz Al-wiring mixer has an uncorrected DSB receiver noise of 1170 K at 1042 GHz and at 4.2 K bath temperature. The receiver noise drops to 840 K upon cooling the mixer to 2.5 K. This is the best receiver noise temperature at this frequency to date. We also tested this THz mixer at frequencies 822, 852, and 982 GHz, and obtained uncorrected receiver noise

temperatures 1207, 1207, and 1307 K, respectively, at 2.5 K bath temperature. These noise temperatures are higher than that at 1042 GHz because thicker beamsplitters were used. If the beamsplitter loss is corrected out, the receiver noise temperatures at frequencies 822, 852, 982, and 1042 GHz would become 756 K, 757 K, 777 K, and 752 K. Further advances in terahertz SIS mixers may be possible using circuits fabricated with higher-gap superconductors such as NbN. However, this will require high-quality films with low RF surface resistance at terahertz frequencies.

References

Ashcroft, N. W. and N. D. Mermin, *Solid State Physics*, Holt, Rinehart, and Winston, New York, 1976.

Bardeen, J., L. N. Cooper, and J. R. Schrieffer, "Theory of superconductivity," *Phys. Rev.*, vol. 108, pp. 1175-1204, 1957.

Bell, R. J., *Introductory Fourier Transform Spectroscopy*, Academic Press: New York and London, 1972.

Belitsky, V. Y., L. V. Filippenko, S. W. Jacobsson, and E. L. Kollberg, "Broad-band twin-junction tuning circuit for submillimeter SIS mixers," *Microwave and Opt. Tech. Lett.*, vol. 10, no. 2, pp. 74-78, 1995.

Belitsky, V. Y., S. W. Jacobsson, L. V. Filippenko, C. Holmstedt, V. P. Koshelets, and E. L. Kollberg, "Fourier transform spectrometer studies (300 -1000 GHz) of Nb-based quasi-optical SIS detectors," *IEEE Trans. Appl. Superconductivity*, vol. 5, no. 3, pp. 3445-3451, 1995.

Belitsky, V. Y., M. A. Tarasov, S. A. Kovtonjuk, L. V. Filippenko, and O. V. Kaplunenko, "Low-noise completely quasi-optical SIS receiver for radioastronomy at 115 GHz," *Int. J. IR and MM Waves*, vol. 13, pp 389-396, 1992.

Berkshire Technologies, Inc., 5427 Telegraph Ave., Suite B2, Oakland, CA 94609; model L-1.5-30HI.

Bin, M., M. C. Gaidis, J. Zmuidzinas, T. G. Phillips, and H. G. LeDuc, "Low-noise 1 terahertz niobium superconducting tunnel junction mixer with a normal metal tuning circuit," *Appl. Phys. Lett.*, vol. 68, no. 12, pp. 1714-1716, 1996.

Bin, M., M. C. Gaidis, J. Zmuidzinas, T. G. Phillips, and H. G. LeDuc, "THz SIS Mixers with Normal Metal Al Tuning Circuits," *Extended Abstracts 5th Intl. Superconductive Electronics Conference (ISEC'95)*, pp. 402-404, September 18-21, 1995, Nagoya, Japan.

Blundell, R., C.-Y.E. Tong, D. C. Papa, R. L. Leombruno, X. L. Zhang, S. Paine, J. A. Stern, H. G. LeDuc, and B. Bumble, "A wide-band fix-tuned SIS receiver for 200-GHz operation," *IEEE Trans. Microwave Theory Tech.*, vol. 43, pp. 933-937, 1995.

Blundell, R., C.-Y.E. Tong, J. W. Barrett, J. Kawamura, R. L. Leombruno, S. Paine, D. C. Papa, X. L. Zhang, J. A. Stern, H. G. LeDuc, and B. Bumble, "A fix-tuned SIS receiver for the 450 GHz frequency band," *Proc. Sixth Intl. Symp. Space Terahertz Tech.*, pp. 123-133, March 21-23, 1995, Pasadena, CA 91125.

Blundell, R. and C. -Y.E. Tong, "Submillimeter receivers for radio astronomy," *Proc. IEEE*, vol. 80, pp. 1702-1720, 1992.

Born, M. and E. Wolf, *Principles of Optics*, Pergamon: New York, 2nd ed., 1964.

Brigham, O. E., *The fast Fourier transform*, Englewood Cliffs, N. J., Prentice-Hall, 1974.

Büttgenbach, T. H., "An improved solution for integrated array optics in quasi-optical mm and submm receivers: the hybrid antenna," *IEEE Trans. Microwave Theory Tech.*, vol. 41, no. 10, pp. 1750-1761, 1993.

Büttgenbach, T. H., H. G. LeDuc, P. D. Maker, and T. G. Phillips, "A fixed tuned broadband matching structure for submillimeter SIS receivers," *IEEE Trans. Appl. Superconductivity*, vol. 2, no. 3, pp. 165-175, 1992.

Büttgenbach, T. H., R. E. Miller, M. J. Wengler, D. M. Watson, and T. G. Phillips, "A broadband low-noise SIS receiver for submillimeter astronomy," *IEEE Trans. Microwave Theory Tech.*, vol. 36, no. 12, pp. 1720-1726, 1988.

Carlstrom, J. E., R. L. Plambeck, and D. D. Thornton, "A Continuously Tunable 65 – 115 GHz Gunn Oscillator," *IEEE Trans. Microwave Theory Tech.*, vol. 33, pp. 610-619, 1985.

Carlstrom, J. E. and J. Zmuidzinas, "Millimeter and submillimeter techniques," *Reviews of Radio Science 1992 -1995*, ed. W. R. Stone, Oxford: The Oxford University Press, 1996.

Caves, C. M., "Quantum limits on noise in linear amplifiers," *Phys. Rev. D*, vol. 26, pp. 1817-1839, 1982.

Chantry, G. W., *Submillimetre spectroscopy; a guide to the theoretical and experimental physics of the far infrared*, Academic Press: London and New York, 1971.

Cohen, M. H., L. M. Falicov, and J. C. Phillips, "Superconductive tunneling," *Phys. Rev. Lett.*, vol. 8, no. 8, pp. 316-318, 1962.

Compton, R. C., R. C. McPhedran, Z. P. Popović, G. M. Rebeiz, P. P. Tong, and D. B. Rutledge, "Bow-tie antenna on a dielectric half-space: theory and experiment," *IEEE Trans. Antennas Propag.*, vol. 35, pp. 622, 1987.

D'addario, L. R., "An SIS mixer for 90-120 GHz with gain and wide bandwidth," *Int. J. IR and MM Waves*, vol. 5, no. 11, pp. 1419-1442, 1984.

Danchi, W. C. and E. C. Sutton, "Frequency Dependence of Quasiparticle Mixers," *J. Appl. Phys.*, vol. 60, pp. 3967-3977, 1986.

Dayem, A. H. and R. J. Martin, "Quantum interaction of microwave radiation with tunneling between superconductors," *Phys. Rev. Lett.*, vol. 8, no. 6, pp. 246-248, 1962.

de Lange, G., J. J. Kuipers, T. M. Klapwijk, R. A. Panhuyzen, H. van de Stadt, and M. W. M. de Graauw, "Superconducting resonator circuits at frequencies above the gap frequency," *J. Appl. Phys.*, vol. 77, no. 4, pp. 1795-1804, 1995.

de Lange, G., "Quantum limited heterodyne detection of 400-840 GHz radiation with superconducting Nb tunnel junctions," *Ph.D. Dissertation*, University of Groningen, the Netherland.

de Lange, G., C. E. Honingh, J. J. Kuipers, H. H. A. Schaeffer, R. A. Panhuyzen, T. M. Klapwijk, H. Van de Stadt, and M. M. W. M. de Graauw, "Heterodyne Mixing with Nb Tunnel Junctions Above the Gap Frequency," *Appl. Phys. Lett.*, vol. 64, pp. 3039-3041, 1994.

de Lange, G., C. E. Honingh, M. M. T. M. Dierichs, H. H. A. Schaeffer, R. A. Panhuyzen, T. M. Klapwijk, H. Van de Stadt, and M. M. W. M. de Graauw, "Quantum limited responsivity of a $Nb/Al_2O_3/Nb$ SIS waveguide mixer at 460 GHz," *Physica B*, vol. 194, pp. 93-94, 1994.

Dierichs, M. M. T. M., C. E. Honingh, R. A. Panhuyzen, B. J. Feenstra, A. Skalare, J. J. Wijnbergen, H. van d. Stadt, and T. H. de Graauw, "Evaluation of integrated elements with SIS devices," *Proc. Third Intl. Symp. Space Terahertz Tech.*, pp. 522-537, March 24-26, 1992, The Univ. of Michigan, Ann Arbor, Michigan.

Dolan, G. J., T. G. Phillips and D. P. Woody, "Low-noise 115 GHz mixing in superconducting oxide-barrier tunnel junctions," *Appl. Phys. Lett.*, vol. 34, pp. 347-349, 1979.

Dubash, N. B., M. J. Wengler, and J. Zmuidzinas, "Shot noise and photon-induced correlations in 500 GHz SIS detectors," *IEEE Trans. Appl. Superconductivity*, vol. 5, no. 2, pp. 3308-3311, 1995.

Erickson E. F. and J. A. Davidson, "SOFIA: The future of air-borne astronomy," *Air-borne Astronomy Symposium on the Galactic Ecsystem: From Gas to Stars to Dust, ASP Conference Series*, M. R. Haas, J. A. Davidson and E. F. Erickson eds., vol. 73, 1995.

Erickson N. R. and J. Tuovinen, "A Waveguide Tripler for 800 – 900 GHz," to appear in *Proc. Sixth Intl. Symp. Space Terahertz Tech.,* March 21-23, 1995, Caltech, Pasadena, CA 91125.

European Space Agency (ESA), "FIRST: Far Infrared and Submillimeter Space Telescope," SCI(93)6, September, 1993.

Febvre, P.,W. R. McGrath, P. Batelaan, B. Bumble, H. G. LeDuc, S. George, and P. Feautrier, "A low-noise SIS receiver measured from 480 GHz to 650 GHz using Nb junctions with integrated RF tuning circuits," *Int. J. IR and MM Waves*, vol. 15, no. 6, pp. 943-965, 1994.

Feldman, M. J., "Some analytical and intuitive results in the quantum-theory of mixing," *J. Appl. Phys.*, vol. 53, no. 1, pp. 584-592, 1982.

Feldman, M. J., S.-K. Pan, A. R. Kerr, and A. Davidson, "SIS mixer analysis using a scale model," *IEEE Trans. Magn.*, vol. 19, pp. 494-497, 1983.

Filipovic, Daniel. F., "Analysis and design of dielectric-lens antennas and planar multiplier circuits for millimeter-wave applications," Ph.D. thesis, The University of Michigan, Ann Arbor, Michigan 48109, 1995.

Filipovic, D. F., S. S. Gearhart, and G. M. Rebeiz, "Double slot antenna on extended hemispherical and elliptical silicon dielectric lenses," *IEEE Trans. Microwave Theory Tech.*, vol. 41, pp. 1738-1749, 1993.

Filipovic, D. F., and G. M. Rebeiz, "Double slot antenna on extended hemispherical and elliptical quartz dielectric lenses," *Int. J. IR and MM Waves*, vol. 14, pp. 1905-1924, 1993.

Gaidis, M. C., private communications.

Gaidis, M. C., M. Bin, D. Miller, J. Zmuidzinas, H. G. LeDuc, and J. A. Stern, "Design and characterization of two-junction tuning circuits for submillimeter SIS mixers," *Proc. Sixth Intl. Symp. Space Terahertz Tech.*, pp. 305-313, March 21-23, 1995, Caltech, Pasadena, CA 91125.

Gaidis, M. C., M. Bin, D. Miller, J. Zmuidzinas, H. G. LeDuc, and J. A. Stern, "Characterization of quasi-optical twin-slot double-junction submillimeter SIS mixers," *Extended Abstracts 5th Intl. Superconductive Electronics Conference (ISEC'95)*, September 18-21, 1995, Nagoya, Japan.

Gaidis, M. C., H. G. LeDuc, M. Bin, D. Miller, J. A. Stern, and J. Zmuidzinas, "Characterization of low-noise quasi-optical SIS mixers for the submillimeter band," *IEEE Trans. Microwave Theory Tech.*, vol. 44, no. 7, pp. 1130-1139, 1996.

Groesbeck, T., *Doctoral Dissertation*, California Institute of Technology, 1994.

Gurvitch, M., M. A. Washington, and H. A. Huggins, "High-quality refractory Josephson tunnel-junctions utilizing thin aluminum layers," *Appl. Phys. Lett.*, vol. 42, no. 5. pp. 472-474, 1983.

Ha, T. T., *Solid-State Microwave Amplifier Design*, John Wiley & Sons, New York, 1981.

Hammerstad, E., and O. Jensen, "Accurate models for microstrip computer-aided design," *IEEE MTT-S Int. Microwave Symp. Dig.*, pp. 407-409, 1980.

Harris, A. I., J. Stutzki, U. U. Graf, and R. Genzel, "Measured Mixer Noise Temperature and Conversion Loss of a Cryogenic Schottky Diode Mixer Near 800 GHz," *Int. J. Infrared and Millimeter Waves*, vol. 10, pp. 1371-1376, 1989.

Heidenhain Corp., 115 Commerce Drive, Schaumburg, IL 60173.

Honingh, C. E., K. Jacobs, S. Hass, D. Hottenroth, and J. Stutzki, "Niobium SIS mixers at 490 GHz, 690 GHz, and 810 GHz," *IEEE Trans. Appl. Superconductivity*, vol. 5, pp. 2216-2219, 1995.

Hu, Q., C. A. Mears, and P. L. Richards, "Measurements of integrated tuning elements for SIS mixers with a Fourier transform spectrometer," *Int. J. IR and MM Waves*, vol. 9, no. 4, pp. 303-320, 1988.

Jackson, J. D., *Classical Electrodynamics*, chapter 8, p. 386, 2nd ed. New York: Wiley, 1975.

Jacobs, K., U. Müller, U. Schwenk, D. Diehl, C. E. Honingh, and S. Haas, "SIS receivers with large instantaneous bandwidths for radio astronomy," *Proc. Fifth Intl. Symp. Space Terahertz Tech.*, pp. 60-72, May 10-12, 1994, U. of Michigan, Ann Arbor, MI.

Janos Technology, Inc., HCR #33, Box 25, Route 35, Townshend, VT 05353-7702.

Josephson, B. D., "Possible new effects in superconductive tunneling," *Phys. lett.*, vol. 1, no. 7, pp. 251-253, 1962.

Karpov, A., J. Blondel, M. Voss, and K. H. Gundlach, "Four photon sensitivity heterodyne detection of submillimeter radiation with superconducting tunnel junctions," *IEEE Trans. Appl. Superconductivity*, Vol. 5, pp. 3304-07, 1995.

Kasilingam D., and D. B. Rutledge, "Focusing properties of small lenses," *Int. J. IR and MM Waves*, vol. 7, no. 10, pp. 1631-1647, 1986.

Kautz, R. L., "Miniaturization of normal-state and superconducting striplines," *J. Res. Natl. Bureau Std.*, vol. 84, no. 3, pp. 247-259, 1979.

Kerr, A. R., S.-K. Pan, and M. J. Feldman, "Integrated tuning elements for SIS mixers," *Int. J. IR and MM Waves*, vol. 9, pp. 203-212, 1988.

Kerr, A. R., S.-K. Pan, A. W. Lichtenberger, and D. M. Lea, "Progress on tunerless SIS mixers for the 200-300 GHz band," *IEEE Microwave and Guided Wave Lett.*, vol. 2, pp. 454-456, 1992.

Kohjiro, S., S. Kiryu, and A. Shoji, "Surface resistance of epitaxial and polycrystalline NbCN films in the submillimeter wave region," *IEEE Trans. Appl. Superconductivity*, vol. 3, pp. 1765-1767, 1993.

Kominami, M., D. M. Pozar, and D. H. Schaubert, "Dipole and slot elements and arrays on semi-infinite substrates," *IEEE Trans. Antenna Propagat.*, vol. 33, pp. 600-607, 1985.

Kooi, J. W., M. S. Chan, P. Shaffer, B. Bumble, H. G. LeDuc, C. K. Walker, T. G. Phillips, "An 850 GHz waveguide receiver using a tuned Nb SIS tunnel junction fabricated on a 1 μm Si_3N_4 membrane," *Proc. Seventh Intl. Symp. Space Terahertz Tech.*, Univ. of Virginia, Charlottesville, VA 22903, March 12-14, 1996.

Kooi, J. W., M. S. Chan, M. Bin, B. Bumble, and H. G. LeDuc, "The development of an 850 GHz waveguide receiver using tuned SIS junctions on 1 μm Si_3N_4 membranes," *Int. J. IR and MM Waves*, vol. 16, pp. 349-362, 1995.

Kooi, J. W., M. S. Chan, C. K. Walker, B. Bumble, H. G. LeDuc, P. L. Schaffer, and T. G. Phillips, "180-425 GHz low-noise SIS waveguide receivers employing tuned Nb/Al-O_x/Nb tunnel junctions," *Int. J. IR and MM Waves*, vol. 15, pp. 783-805, 1994.

Kooi, J. W., C. K. Walker, H. G. LeDuc, P. L. Schaffer, T. R. Hunter, D. J. Benford, and T. G. Phillips, "A low-noise 665 GHz SIS quasi-particle waveguide receiver," *Int. J. IR and MM Waves*, vol. 15, pp. 477-492, 1994.

Kormanyos, B. K., P. H. Ostdiek, W. L. Bishop, T. W. Crowe, and G. M. Rebeiz, "A planar wideband 80-200 GHz subharmonic receiver," *IEEE Trans. Microwave Theory Tech.*, vol. 41, no. 10, pp. 1730-1737, 1993.

Kraus John, D., *Antennas*, 2nd Ed., McGraw-Hill: New York, 1988.

LeDuc, H. G., J. A. Stern, S. Thakoor, and S. Khanna, "All refractory NbN/MgO/NbN SIS tunnel junctions," *IEEE Trans. Magn.*, vol. 23, pp. 863-865, 1987.

March, S. L., "Analyzing lossy radial-line stubs," *IEEE Trans. Microwave Theory Tech.*, vol. 33, no. 3, pp. 269-271, 1985.

Matick, R. E., *Transmission Lines for Digital and Communication Networks*, New York: McGraw-Hill, 1969.

Mattis, D. C. and J. Bardeen, "Theory of the anomalous skin effect in normal and superconducting materials," *Phys. Rev.* vol. 111, no. 2, pp. 412-417, 1958.

McGrath, W. R., P. L. Richards, A. D. Smith, H. van Kempen, and R. A. Batchelor, "Large gain, negative resistance, and oscillations in superconducting quasiparticle heterodyne mixers," *Appl. Phys. Lett.*, vol. 39, pp. 655-658, 1981.

Miller, D., private communications, 1995.

Naud, J., and J. Zmuidzinas, "Two-dimensional calculation of an SIS junction in a microstrip transmission line," submitted to *IEEE Trans. Microwave Theory Tech.*.

Norland Optical Adhesive #61, Norland Products Inc., New Brunswick, NJ.

Norton Performance Plastics, 150 Dey Rd., Wayne, NJ 07470.

Owyang, G. H. and T. T. Wu, "The approximate parameters of slot lines and their complement," *IRE Trans. Antennas and Propagation*, pp. 49-55, 1958.

Perkin-Elmer Corp., 761 Main Ave., Norwalk, CT 06859-0001.

Phillips, T. G. and J. G. Dolan, "SIS mixers," *Physica*, vol. 109 & 110B, pp. 2010-2019, 1982.

Phillips, T. G. and J. Keene, "Submillimeter astronomy," *Proc. IEEE*, vol. 80, no. 11, pp. 1662-1678, 1992.

Physik Instrumente, Main U.S. office, 3001 Redhill Ave. Bldg. 5-102, Costa Mesa, CA 92626.

Pippard, A. B., "An experimental and theoretical study of the relation between magnetic field and current in a superconductor," *Proc. Roy. Soc. (London)*, vol. A216, pp. 547-568, 1953.

Pippard, A. B., "Metallic conduction at high frequencies and low temperatures," in *Advances in Electronics and Electron Physics*, vol. VI, pp. 1-45, L. Marton Ed., New York: Academic Press, 1954.

Pöpel, R., "Electromagnetic Properties of Superconductors," pp. 44-78 in V. Kose, ed., *Superconducting Quantum Electronics*, Springer-Verlag: Berlin, 1989.

Pregla, R., "Determination of conductor losses in planar waveguide structures (A comment to some published results for microstrips and microslots)," *IEEE Trans. Microwave Theory Tech.*, vol. 28, no. 4, pp. 433-434, 1980.

Pucel, R. A., D. J. Massé, and C. P. Hartwig, "Losses in microstrip," *IEEE Trans. Microwave Theory Tech.*, vol. 16, no. 6, pp. 342-350, 1968.

Räisänen, A. V., W. R. McGrath, P. L. Richards, and F. L. Lloyd, "Broadband RF match to a millimeter-wave SIS quasi-particle mixer," *IEEE Trans. Microwave Theory Tech.*, vol. 33, no. 12, pp. 1495-1500, 1985.

Ramo, S., J. R. Whinnery, T. Van Duzer, *Fields and Waves in Communication Electronics*, 2nd ed. New York: Willey, 1984.

Reuter G. E. H. and E. H. Sondheimer, "The theory of the anomalous skin effect in metals," *Proc. Roy. Soc.*, (London), vol. A195, pp. 336-364, 1948.

Richards, P. L., "Fourier transform spectroscopy," in *Spectroscopic Techniques for Far-infrared, Submillimeter, and Millimeter Waves*, ed. by D. H. Martin, North-Holland Pub. Co., New York Wiley: Armsterdam, 1967.

Richards, P. L., T. M. Shen, R. E. Harris, and F. L. Lloyd, "Quasiparticle heterodyne mixing in SIS tunnel junctions," *Appl. Phys. Lett.*, vol. 34, pp. 345-346, 1979.

Richards P. L. and T.-M. Shen, "Superconducting devices for millimeter wave detection, mixing and amplification," *IEEE Trans. Electron Devices*, vol. 27, pp. 1909-, 1980.

Rogers Corporation, Microwave Circuit Materials Division, 100 S. Roosevelt Ave., Chandler, AZ 85226.

Rogovin, D., and D. J. Scalapino, "Fluctuation phenomena in tunnel junctions," *Annals of Physics*, vol. 86, no. 1, pp. 1-90, 1974.

Rothermel, H., K. H. Gundlach, and M. Voss, "A 350 to 700 GHz open structure SIS receiver for submillimeter astronomy," *Journal de Physique IV*, vol. 4, pp. C6-267 - C6-272, 1994.

Rudner, S. and T. Claeson, "Arrays of superconducting tunnel junctions as low-noise 10 GHz mixers," *Appl. Phys. Lett.*, vol. 34, no. 2, pp. 711-713, 1979.

Rudner, S., M. J. Feldman, E. Kollberg, and T. Claeson, "Superconductor-insulator-superconductor mixing with arrays at millimeter-wave frequencies," *J. Appl. Phys.*, vol. 52, p. 6366, 1981.

Rutledge, D. B., D. P. Neikirk, and D. P. Kasilingam, "Integrated circuit antenna," in *Infrared and Millimeter Waves*, vol. 10, pp. 1-90, K. J. Button, Ed., Academic Press: New York, 1983.

Salez, M., P. Febvre, W. R. McGrath, B. Bumble, H. G. LeDuc, "An SIS waveguide heterodyne receiver for 600-635 GHz," *Int. J. IR and MM Waves*, vol. 15, no. 2, pp. 349-368, 1994.

Schoelkopf, R. J., "Studies of noise in Josephson-effect mixers and their potential for submillimeter heterodyne detection," Ph.D. Dissertation, 1995, California Institute of Technology, Pasadena, CA 91125.

Schuster, K. F., A. I. Harris, and K. H. Gundlach, "A 691 GHz SIS receiver for radio astronomy," *Int. J. IR and MM Waves*, vol. 14, pp. 1867-1887, 1993.

Serabyn, E., T. G. Phillips, C. R. Masson, "Surface figure measurements of radio telescopes with a shearing interferometer," *Appl. Optics*, vol. 30, no. 10, pp. 1227-1241, 1991.

Shen, T. M., "Conversion gain in millimeter wave quasi-particle heterodyne mixers," *IEEE J. Quantum Electronics*, vol. 17, no. 7, pp. 1151-1165, 1981.

Shitov, S. V., A. M. Baryshev, V. P. Koshelets, J. R. Gao, W. Luinge, H. van de Stadt, and Th. de Graauw, "Wide-band quasi-optical SIS mixers for integrated receivers up to 1200 GHz," *Proc. Seventh Intl. Symp. Space Terahertz Tech.*, Univ. of Virginia, Charlottesville, VA 22903, March 12-14, 1996.

Skalare, A., "Determining embedding circuit parameters from dc measurements on quasiparticle mixers," *Int. J. IR and MM Waves*, vol. 10, no. 11, pp. 1339-1353, 1989.

Skalare, A., M. M. T. M. Dierichs, J. Mees, H. van de Stadt, R. A. Panhuyzen, Th. de Graauw, and T. M. Klapwijk, "SIS mixers using endfire and broadside double dipole antennas at 435 and 480 GHz," *Proc. Fourth Intl. Symp. Space Terahertz Tech.*, UCLA, Los Angeles, CA 90024, March 30 - April 1, 1993.

Thermech Engineering Corp., 1773 W. Lincoln Ave., Bldg. K, Anaheim, CA 92801.

Tinkham, M., *Introduction to Superconductivity*, New York: McGraw-Hill, 1975.

Tong, C.-Y. E., R. Blundell, B. Bumble, J. A. Stern, and H. G. LeDuc, "Quantum-limited heterodyne detection in superconducting nonlinear transmission lines at submillimeter wavelengths," *Appl. Phys. Lett.*, vol. 67, no. 9, pp. 1304-1306, 1995.

Tong, C.-Y. E., R. Blundell, D.C. Papa, J.W. Barnett, S. Paine, X. Zhang, J.A. Stern, and H. G. LeDuc, "A fixed tuned low noise SIS receiver for the 600 GHz frequency band," *Proc. Sixth Intl. Symp. Space Terahertz Tech.*, pp. 295-304, March 21-23, 1995, Caltech, Pasadena, CA 91125.

Topsil U.S., 25 Burlington Mall Rd., Suite 300, Burlington, MA 01803.

Torrey, H. C. and C. A. Whitmer, *Crystal Rectifiers*, MTT Rad. Lab. Series, vol. 15, New York: McGraw Hill, 1948.

Touchstone CAD Software, EEsof, Inc., 5795 Lindero Canyon Road, Westlake Village, CA 91362.

Tucker, J. R., "Quantum limited detection in tunnel junction mixers," *IEEE J. Quantum Electron.*, vol. 15, no. 11, pp. 1234-1258, 1979.

Tucker, J. R. and M. J. Feldman, "Quantum detection at millimeter wavelengths," *Rev. Mod. Phys.*, vol. 57, no. 4, pp. 1055-1113, 1985.

van de Stadt, H., A. Baryshev, J. R. Gao, H. Golstein, Th. de Graauw, W. Hulshoff, S. Kovtonyuk, H. Schaeffer, and N. Whyborn, "A sensitive 1 THz waveguide mixer," *Proc. Seventh Intl. Symp. Space Terahertz Tech.*, Univ. of Virginia, Charlottesville, VA 22903, March 12-14, 1996.

van de Stadt, H., A. Baryshev, P. Dieleman, Th. de Graauw, T. M. Klapwijk, S. Kovtonyuk, G. de Lange, I. Lapitskaya, J. Mees, R. Panhuyzen, G. Pokopenko, and H. Schaeffer, "A 1 THz Nb SIS heterodyne mixer with normal metal tuning structures," *Proc. Sixth Intl. Symp. Space Terahertz Tech.*, March 21-23, 1995, Caltech, Pasadena, CA 91125.

van de Stadt, H. *et al.*, "Nb and NbN SIS junctions in mixers up to 1.06 THz," presented at *Third Intl. Workshop on Terahertz Electronics*, August 31 - September 1, 1995, Zermatt, Switzerland.

Van Duzer, T. and C. W. Turner, *Principles of Superconductive Devices and Circuits*, New York: Elsevier, 1981.

Wang, Z., A. Kawakami, Y. Uzawa, and B. Komiyama, "High critical-current density NbN/AlN/NbN tunnel junctions fabricated on ambient-temperature MgO substrate," *Appl. Phys. Lett.*, vol. 64, pp. 2034-2036, 1994.

Wengler, M. J., "Submillimeter wave detection with superconducting tunnel diodes," *Proc. IEEE*, vol. 80, no. 11, pp. 1811-1826, 1992.

Wengler, M. J. and D. P. Woody, "Quantum Noise in Heterodyne Detection," *IEEE J. Quantum Electronics*, vol. 23, pp. 613-622, 1987.

Wengler, M. J., D. P. Woody, R. E. Miller, and T. G. Phillips, "A low-noise receiver for millimeter and submillimeter wavelength," *Int. J. IR and MM Waves*, vol. 6, pp. 697-706, 1985.

Werthamer, N. R., "Nonlinear self-coupling of Josephson radiation in superconducting tunnel junctions," *Phys. Rev.*, vol. 147, no. 1, pp. 255-263, 1966.

Williams Charles, S., "Mirror misalignment in Fourier spectroscopy using a Michelson interferometer with circular aperture," *Appl. Optics*, vol. 5, no. 6, pp. 1084-85, 1966.

Winkler, D. and T. Claeson, "High Frequency Limits of Superconducting Tunnel Junction Mixers," *J. Appl. Phys.*, vol. 62, pp. 4482-4498, 1987.

Woody, D. P., R. E. Miller, and M. J. Wengler, "85 - 115 GHz receivers for radio astronomy," *IEEE Trans. Microwave Theory Tech.*, vol. 33, no. 2, pp. 90-95, 1985.

Zimmerman, R., T. Rose, T. W. Crowe, and T. W. Grein, "An all Solid-State 1 THz Radiometer for Space Applications," *Proc. Sixth Intl. Symp. Space Terahertz Tech.,* March 21-23, 1995, Caltech, Pasadena, CA 91125.

Zmuidzinas, J., PCIRCUIT CAD Software, Caltech 320-47, Pasadena, CA 91125.

Zmuidzinas, J., N. G. Ugras, D. Miller, M. Gaidis, H. G. LeDuc, and J. A. Stern, "Low-Noise Slot Antenna SIS Mixers," *IEEE Trans. Appl. Superconductivity*, vol. 5, pp. 3053-3056, 1995.

Zmuidzinas, J., H. G. LeDuc, J. A. Stern, and S. R. Cypher, "Two-Junction Tuning Circuits for Submillimeter SIS Mixers," *IEEE Trans. Microwave Theory Tech.*, vol. 42, pp. 698-706, 1994.

Zmuidzinas, J. and H. G. LeDuc, "Quasi-Optical Slot Antenna SIS Mixers," *IEEE Trans. Microwave Theory Tech.*, vol. 40, pp. 1797-1804, 1992.

Appendix A Numerical Solution for the Anomalous Skin Effect

The numerical solution of (4.42) and calculation of the surface impedance for general l, δ_c, and d were obtained following the method presented by Kautz (Kautz 1979). First the integration of (4.42) by parts yields

$$\begin{aligned} E_x(z) &= E_x(d) + i\frac{\alpha}{l}\int_0^d dz' E_x(z') G_1((z'-d)/l, (z'-z)/l), \\ G_1(u,v) &= \int_u^v dr \int_1^\infty ds (v-r)\left(\frac{1}{s} - \frac{1}{s^3}\right) e^{-|r|s}, \end{aligned} \tag{A.1}$$

where the kernel G_1 can be evaluated in terms of E_1, the exponential integral

$$E_1(x) = \int_x^\infty \frac{e^{-x}}{x} dx. \tag{A.2}$$

Over the domain of interest ($u \le 0, v \ge u$),

$$\begin{aligned} G_1(u,v) = &\frac{1}{24}[(u^3 + u^2 - 10u - 6)e^u + (u^4 - 12u^2)E_1(|u|)] \\ &+ \frac{1}{24}[(|v|^3 - v^2 - 10|v| + 6)e^{-|v|} - (v^4 - 12v^2)E_1(|v|)] \\ &+ \frac{1}{6}(v-u)[(u^2 + u - 4)e^u + (u^3 - 6u)E_1(|u|)] \\ &+ \frac{2}{3}(|v| + v). \end{aligned} \tag{A.3}$$

Note there was a sign error in the second term in the above equation in Kautz paper. Equation (A.1 is a Fredholm equation of the second kind. A numerical solution results when the integral is approximated by a sum consisting of N terms in which the integrand is evaluated at the points $z' = z_1, z_2, \cdots, z_N$. By choosing z to be each of these z_i in succession, one obtains a set of N linear equations which can be solved

for the unknown $E_x(z_i)$. Computerized program for this procedure is available in *Numerical Recipes.*[1]

Once $E_x(z)$ is known, the integral over current density required for the surface impedance is obtained from

$$\begin{aligned} \int_0^d dz J_x(z) &= \frac{3}{4}\sigma \int_0^d dz E_x(z) G_2((z-d)/l, z/l), \\ G_2(u,v) &= \int_u^v dr \int_1^\infty ds \left(\frac{1}{s} - \frac{1}{s^3}\right) e^{-|r|s}, \end{aligned} \tag{A.4}$$

where for the domain of interest ($u \leq 0,\ v \geq 0$),

$$\begin{aligned} G_2(u,v) = \frac{3}{4} &+ \frac{1}{6}[(u^2+u-4)e^u + (u^3-6u)E_1(|u|)] \\ &+ \frac{1}{6}[(v^2-v-4)e^{-v} - (v^3-6v)E_1(v)]. \end{aligned} \tag{A.5}$$

[1]We use SUBROUTINE fred2 and FUNCTION fredin in Chapter 18, *Numerical Recipes in FORTRAN*, 2nd ed., Cambridge Univ. Press, 1992.

Appendix B Matrix Representation of Two-port Networks

A microwave circuit can be described as a collection of two-port networks that are connected in various ways.

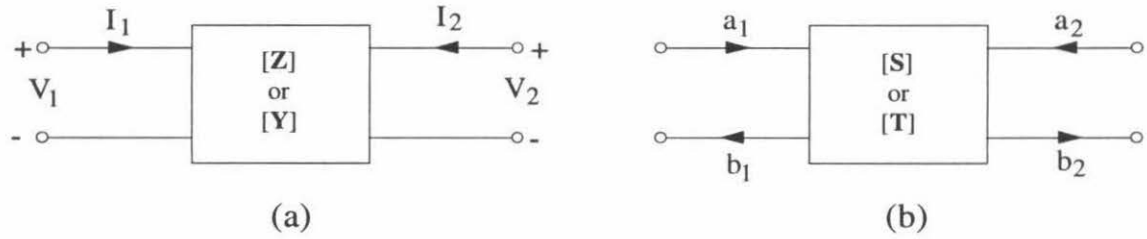

Figure B.1: A two-port network with (a) voltage and current shown at each port, and (b) voltage wave amplitude shown at each port.

Given in Fig. B.1 is a two-port network with voltage and current at each port denoted by V_1, I_1, V_2 and I_2, respectively. If the voltage vector $\mathbf{V} = \binom{V_1}{V_2}$ can be related to the current vector $\mathbf{I} = \binom{I_1}{I_2}$ through

$$\mathbf{V} = \mathbf{Z}\,\mathbf{I}\,, \tag{B.1}$$

then the 2×2 matrix $\mathbf{Z}$ is called the impedance matrix of the two-port network. Vice versa, if

$$\mathbf{I} = \mathbf{Y}\,\mathbf{V}\,, \tag{B.2}$$

we say the two-port has an admittance matrix $\mathbf{Y}$. When both $\mathbf{Z}$ and $\mathbf{Y}$ are well defined, it is clear that

$$\mathbf{Y} = \mathbf{Z}^{-1} \ . \tag{B.3}$$

A very important description of networks, especially in the microwave frequency range, is the scattering matrix $\mathbf{S}$. Consider the two-port network in Fig. B.1, and define an incident voltage wave $\mathbf{a}$ and scattered voltage wave $\mathbf{b}$ as

$$\mathbf{a} = \frac{1}{2\sqrt{Z_0}}(\mathbf{V} + Z_0\mathbf{I}) \ , \qquad \mathbf{b} = \frac{1}{2\sqrt{Z_0}}(\mathbf{V} - Z_0\mathbf{I}) \ . \tag{B.4}$$

Here Z_0 is the normalization impedance. The scattered wave and incident wave are connected by the scattering matrix:

$$\mathbf{b} = \mathbf{S}\ \mathbf{a} \ . \tag{B.5}$$

The power absorbed by the network is $P = |\mathbf{a}|^2 - |\mathbf{b}|^2$.

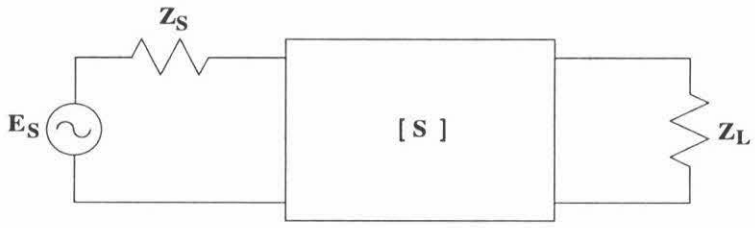

Figure B.2: A two-port network terminated with a source and a load. The transducer power gain is determined by the scattering matrix of the two-port and the source and load impedances.

Consider a system shown in Fig. B.2. The load $Z_{\rm L}$ is connected to the source through a two-port network which is characterized by its scattering matrix $\mathbf{S}$. The source has a source impedance $Z_{\rm S}$. It can be shown (Ha 1981) that the transducer power gain, defined as the ratio of the power absorbed by the load to the available

power of the generator, is given by

$$G = |S_{21}|^2 \frac{(1-|\Gamma_S|^2)(1-|\Gamma_L|^2)}{|(1-\Gamma_S S_{11})(1-\Gamma_L S_{22}) - \Gamma_S \Gamma_L S_{12} S_{21}|^2} , \tag{B.6}$$

where $\Gamma_S = (Z_S - Z_0)/(Z_S + Z_0)$ and $\Gamma_L = (Z_L - Z_0)/(Z_L + Z_0)$ are the source and load reflection coefficients with respect to Z_0.

Another matrix is very useful when interconnecting various two-ports. We define the chain scattering matrix $\mathbf{T}$ as:

$$\begin{pmatrix} a_1 \\ b_1 \end{pmatrix} = \mathbf{T} \begin{pmatrix} b_2 \\ a_2 \end{pmatrix} . \tag{B.7}$$

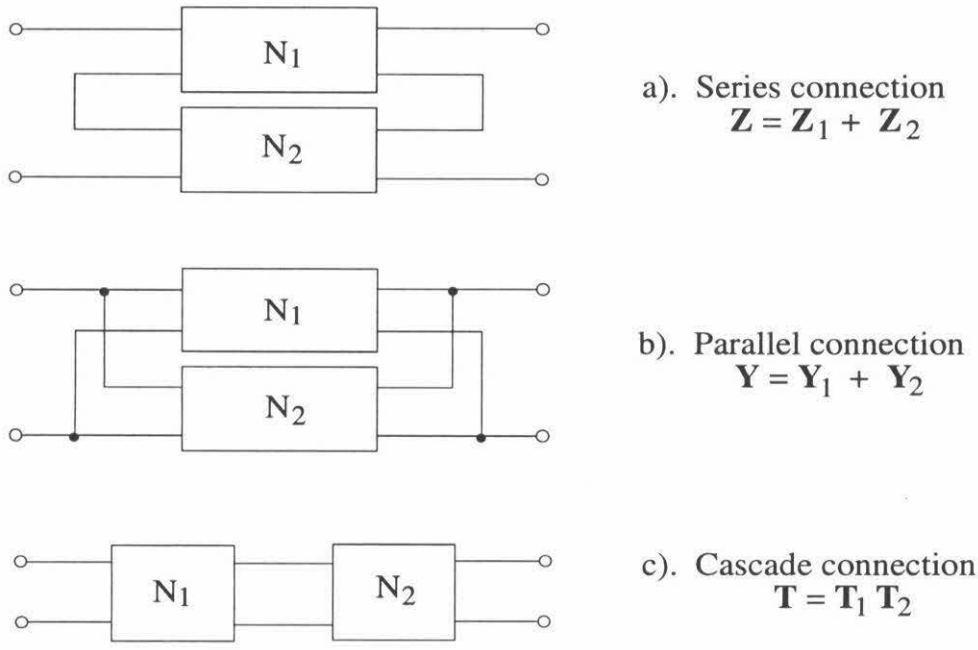

Figure B.3: Interconnections of two-port networks.

The basic interconnections between two-port networks are the series, the parallel, and the cascade connections as shown in Fig. B.3. For two networks N_1 and N_2 in series, the current leaving port 1 (2) of network N_1 is equal to the current entering port 1 (2) of network N_2. Since the port currents are equal and port voltages add,

the series connection has an impedance matrix

$$\mathbf{Z} = \mathbf{Z_1} + \mathbf{Z_2} \ . \tag{B.8}$$

For parallel connection, port 1 (2) of N_1 is connected in parallel with port 1 (2) of N_2. Since the port voltages are identical and the port currents add, the parallel connection has an admittance matrix

$$\mathbf{Y} = \mathbf{Y_1} + \mathbf{Y_2} \ . \tag{B.9}$$

When two networks are cascaded, a_2 and b_2 of N_1 become b_1 and a_1 of N_2, so the cascade connection has a chain scattering matrix

$$\mathbf{T} = \mathbf{T_1}\mathbf{T_2} \ . \tag{B.10}$$

A number of two-port networks connected together can be reduced to a single two-port network with a scattering matrix **S**. The relations between various matrices are listed below:

$$\mathbf{S} = (\mathbf{Z} + Z_0\mathbf{I})^{-1}(\mathbf{Z} - Z_0\mathbf{I}) \ , \tag{B.11}$$

$$\mathbf{S} = (\frac{1}{Z_0}\mathbf{I} + \mathbf{Y})^{-1}(\frac{1}{Z_0}\mathbf{I} - \mathbf{Y}) \ , \tag{B.12}$$

$$\mathbf{Z} = Z_0(\mathbf{I} + \mathbf{S})(\mathbf{I} - \mathbf{S})^{-1} \ , \tag{B.13}$$

$$\mathbf{Y} = \frac{1}{Z_0}(\mathbf{I} - \mathbf{S})(\mathbf{I} + \mathbf{S})^{-1} \ , \tag{B.14}$$

$$\mathbf{T} = \begin{pmatrix} \frac{1}{S_{21}} & -\frac{S_{22}}{S_{21}} \\ \frac{S_{11}}{S_{21}} & \frac{S_{12}S_{21}-S_{11}S_{22}}{S_{21}} \end{pmatrix} , \tag{B.15}$$

$$\mathbf{S} = \begin{pmatrix} \frac{T_{21}}{T_{11}} & \frac{T_{11}T_{22}-T_{12}T_{21}}{T_{11}} \\ \frac{1}{T_{11}} & -\frac{T_{12}}{T_{11}} \end{pmatrix} . \tag{B.16}$$

Each circuit element used in our SIS mixers can be modeled as a two-port, and its matrices can be obtained accordingly. For example, a series transmission line has a scattering matrix

$$\mathbf{S} = \begin{pmatrix} 0 & \mathrm{e}^{-\gamma l} \\ \mathrm{e}^{-\gamma l} & 0 \end{pmatrix} . \tag{B.17}$$

Here $\mathbf{S}$ is normalized to the transmission line's characteristic impedance. γ is the propagation constant and l is the length of the transmission line. By analyzing the tuning circuit as a network, the RF coupling efficiency of the mixer can be obtained using (B.6).

Appendix C PCIRCUIT Documentation

PCIRCUIT

Program Documentation

J. Zmuidzinas and M. Bin

I. Introduction

PCIRCUIT is a simple program for the analysis of microwave circuits. PCIRCUIT includes a full noise analysis capability, which commercial software (i.e., Touchstone) often lacks. This includes the ability to specify the physical temperatures of lossy (and therefore noisy) passive elements. PCIRCUIT also has a basic optimization capability. In comparison to commercial programs, PCIRCUIT has a rather sparse element library, but does include most of the basics. The circuit is described in an ASCII file, in a format similar to that used by the commercial simulator COMPACT. Basically, the circuit is described as a collection of two-port networks that are connected in various ways: in cascade, in series, in parallel, etc. PCIRCUIT is written in FORTRAN-77, and has been compiled and run on a wide variety of machines, including VAX/VMS, UNIX, PC's, and Macs. The user interface is strictly character-based; it is very useful to have a plotting program to graphically display the results.

II. Units

PCIRCUIT uses a fixed set of units. Either of the following can be used, as long as one is consistent within a data file:

FREQUENCY	CAPACITANCE	INDUCTANCE	TIME	TEMPERATURE
MHz	pF	nH	ns	K
GHz	fF	pH	ps	K

III. Circuit Element Library

The following section describes the circuit elements available in PCIRCUIT, as of 04/95. The basic format of a line in the circuit file describing a two-port circuit element in the circuit file is as follows:

```
DEV PP OP arg1 arg2 ...  argn.
```

Here `DEV` is a three-character code for the type of circuit element; e.g., `RES` for a resistor, `CAP` for a capacitor, etc. This element is given a two-letter name, here denoted by `PP`. These can be any two ASCII characters, although it is customary to stick with repeated characters, i.e., `AA, BB, CC,` ..., in simple circuits. Often, several options are available for a given circuit element, and these are specified by the two-letter option code `OP`. For instance, a two-port resistor `RES` can be a series resistor, in which case the option code would be `SE`, or it can be a parallel resistor, in which case it would be `PA`. A series resistor would have an *admittance* matrix

$$Y = \frac{1}{R}\begin{pmatrix} 1 & -1 \\ -1 & 1 \end{pmatrix}$$

whereas a parallel resistor would have an *impedance* matrix

$$Z = R \begin{pmatrix} 1 & 1 \\ 1 & 1 \end{pmatrix}$$

Finally, each circuit element has several arguments, `arg1 arg2 ... argn`, that specify component values, etc. For instance, a resistor `RES` takes two arguments, the resistance in Ohms (Ω) and the physical temperature in Kelvin (K). This second argument is optional; if it is not given, the general ambient temperature of the circuit as a whole is assumed (this is specified at run time). The noise of all lossy elements is included in the calculation.

LUMPED ELEMENTS

`RES AA OP R T`

A resistor. `OP` can either be `SE`, for a series connected resistor, or `PA` for a parallel connected resistor. `R` gives the resistance, and `T` gives the physical temperature (the temperature is optional; if it is not given, ambient temperature will be assumed).

`IND AA OP L`

An inductor. `OP` can either be `SE` or `PA`. `L` gives the inductance. Temperature is not needed since purely reactive components have no loss or noise.

`CAP AA OP C`

A capacitor. `OP` can either be `SE` or `PA`. `C` gives the capacitance.

`SRL AA OP R L T`

A resistor in series with an inductor. `OP` can either be `SE` or `PA`. The parameters have the same meanings as above.

`PRL AA OP R L T`

A resistor in parallel with an inductor. `OP` can either be `SE` or `PA`.

`SRC AA OP R C T`

A resistor in series with a capacitor. `OP` can either be `SE` or `PA`.

`PRC AA OP R C T`

A resistor in parallel with a capacitor. `OP` can either be `SE` or `PA`.

`SLC AA OP L C`

An inductor in series with a capacitor. `OP` can either be `SE` or `PA`.

`PLC AA OP L C`

An inductor in parallel with a capacitor. `OP` can either be `SE` or `PA`.

`SRX AA OP R L C T`

A resistor, inductor, and capacitor all in series. `OP` can either be `SE` or `PA`.

`PRX AA OP R L C T`

A resistor, inductor, and capacitor all in parallel. `OP` can either be `SE` or `PA`.

NUMERICALLY SPECIFIED ELEMENTS

`TWO AA S1 Znorm`

This specifies a two-port whose scattering parameters and noise parameters are specified numerically in the circuit file (see circuit file section for format). PCIRCUIT does not interpolate between data points; hence, data must be given at each frequency that the circuit is to be simulated. The only valid option is `S1`, meaning that the four scattering parameters, s_{11}, s_{21}, s_{12}, and s_{22} will be given in magnitude-phase format. The noise parameters are specified using minimum noise figure NF_{min}, magnitude and phase of the optimum input reflection coefficient, $|\Gamma_{opt}|$ and $\arg\Gamma_{opt}$, and the normalized noise resistance R_n. All scattering parameters, reflection coefficients, and R_n are taken to be normalized to the impedance `Znorm` specified as an argument.

`TWF AA S1 filename`

This specifies a two-port whose scattering parameters and noise parameters are specified numerically in a data file. PCIRCUIT interpolates between data points; hence, data need not be given at each frequency that the circuit is to be simulated. The only valid option is `S1`, meaning that the four scattering parameters, s_{11}, s_{21}, s_{12}, and s_{22} will be given in magnitude-phase format. The noise parameters are specified using minimum noise figure NF_{min}, magnitude and phase of the optimum input reflection coefficient, $|\Gamma_{opt}|$ and $\arg\Gamma_{opt}$, and the normalized noise resistance R_n. All scattering parameters, reflection coefficients, and R_n are taken to be normalized to the impedance `Znorm` specified as an argument.

The data file format for `TWF`:

ZNORM
Z_{norm}
END
SCATT
f s_{11} s_{21} s_{12} s_{22}
...
END
NOISE
f NF_{min} $|\Gamma|$ $arg\Gamma$ R_n
...
END

`ONE AA IR Znorm`

This specifies a two-port which consists of an impedance placed in parallel across the two ports, and which is specified numerically in the circuit file. The only valid option is `IR`. The impedance data must be given at each frequency to be simulated, in terms of a reflection coefficient Γ normalized to `Znorm`. The noise of this impedance must also be specified in terms of an equivalent temperature.

`ONF AA IR filename`

This specifies a two-port which consists of an impedance placed in parallel across the two ports, and which is specified numerically in a data file. (To specify a data file for a series impedance, combine

ONF and PTS. See PTS in section IV.) The only valid option is IR. The impedance data can be given in terms of a reflection coefficient Γ normalized to Znorm or in terms of the real and imaginary parts of the impedance. The noise of this impedance can be specified in terms of an equivalent temperature.

Data file format for ONF:

ZNORM (optional)
Z_{norm}
END
REFLE (need ZNORM)
f $|\Gamma|$ $arg\Gamma$
...
END
IMPED (doesn't need ZNORM)
f Z_{real} Z_{img}
...
END
NOISE (optional, otherwise assume $T_{physical}$)
f T_{equiv}
...
END

`SIF AA SE filename`

This pseudo two-port specifies surface impedance (both real and imaginary parts) vs. frequency for a conductor. The conductor's thickness is also specified. SIF is used to define the strip line or ground plane properties for a microstrip line MSL or MSJ. The only valid option is SE.

Data file format for SIF:

ZSURF
f Z_{real} Z_{img}
...
END
THICK
t
END

TRANSMISSION-LINE ELEMENTS

`TRL AA SE Z0 θ Freq Loss T`

An ideal lossy transmission line with characteristic impedance Z0 and phase length θ (in degrees) at frequency Freq. Loss and T are optional; if specified, Loss is the *percent power loss per wavelength at frequency* Freq. This means that $0 \leq$ Loss < 100. This loss is assumed to be due to a frequency-independent series resistance or shunt conductance per unit length; hence, the loss per unit of PHYSICAL length is independent of frequency. Note that this means that the dB power loss per wavelength scales as 1/frequency. If specified, T gives the temperature for noise calculations; otherwise, ambient is assumed. There are three options available, SE, SL and PL, depending on

how the loss originates in the transmission line. SE will keep characteristic impedance real. SL will calculate complex characteristic impedance assuming that all of the loss is due to series resistance. PL will calculate complex characteristic impedance assuming that all of the loss is due to shunt conductance.

SSI AA SE t_m ρ_n V_{gap} T

A pseudo two-port. SSI defines a superconducting strip or ground plane for a microstrip transmission line MSL or MSJ. It provides parameters of a superconductor for calculating its surface impedance. t_m $[\mu m]$ is superconducting film thickness. The superconductor has a gap voltage V_g $[mV]$ at $0°K$ and its normal resistivity at critical temperature is ρ_n $[\mu\Omega - cm]$. T is optional; if missing, environmental temperature is assumed. The only valid option is SE. See MSL and MSJ

SIF AA SE *filename*

A pseudo two-port. SIF allows one to specify the surface impedance of conductors in a data file. It can define strip line or ground plane properties for microstrip line MSL or MSJ. For data file format please refer to numerically specified elements. See MSL and MSJ

NSI AA SE t_m ρ_n R_{ratio}

A pseudo two-port. NSI is used to define a normal metal strip or ground plane for a microstrip transmission line MSL or MSJ. It calculates the metal's surface impedance in the normal skin effect regime. t_m $[\mu m]$ is the conductor film thickness. ρ_n $[\mu\Omega - cm]$ is resistivity at room temperature. R_{ratio} is the residual resistivity ratio, which is defined as the ratio of room temperature bulk resistivity to the metal film resistivity at working temperature. The only valid option is SE. See MSL and MSJ

ASI AA SE t_m ρ_n l R_{ratio}

A pseudo two-port. ASI defines a normal metal strip or ground plane for a microstrip transmission line MSL or MSJ. It calculates the metal's surface impedance in the anomalous skin effect regime. t_m $[\mu m]$ is the conductor film thickness. ρ_n $[\mu\Omega - cm]$ is resistivity at room temperature. l $[\mu m]$ is mean free path at room temperature. R_{ratio} is the residual resistivity ratio,which is defined as the ratio of room temperature bulk resistivity to the metal film resistivity at working temperature. The only valid option is SE. See MSL and MSJ

SUB AA SE ϵ_1 $tan\delta_1$ ϵ_2 $tan\delta_2$ h

A pseudo two-port. SUB is needed for MSL and MSJ. It provides substrate information for a microstrip line. Superstrate and substrate dielectric constants are given by ϵ_1 (relative) $tan\delta_1$ ϵ_2 (relative) and $tan\delta_2$. h $[\mu m]$ is the height of substrate. The only valid option is SE. See MSL and MSJ

MSL AA SS GG SB w L

A general microstrip transmission line. w $[\mu m]$ and L $[\mu m]$ are microstrip line's width and length. The strip line is described by a pseudo two-port SS which is defined by SIF, SSI, NSI or ASI. The ground plane is described by GG similarly. Substrate is given by SB which is defined via SUB. The definitions of SS GG and SB must precede MSL in the circuit file. Please refer to SIF SSI NSI ASI and SUB.

MSJ AA SS GG SB R_nA w L

A general microstrip junction. R_nA [$\Omega - \mu m^2$] is normal resistance-area product of the junction. w [μm] and L [μm] are microstrip junction's width and length. The strip line junction is described by a pseudo two-port SS which is defined via SIF, SSI, NSI or ASI. The ground plane is described by GG similarly. Substrate is given by SB which is defined via SUB. The definitions of SS GG and SB must precede MSJ in the circuit file. Please refer to SIF SSI NSI ASI and SUB.

OST AA PA Z0 θ Freq

An ideal lossless open-circuited transmission line stub. Note that a lossy stub can be synthesized with TRL and PBR. Only the PA option is valid.

SST AA PA Z0 θ Freq

An ideal lossless short-circuited transmission line stub. Note that a lossy stub can be synthesized with TRL and PBR. Only the PA option is valid.

ELEMENTS FOR MODELING

TCO AA SG gm τ_1 τ_2

An ideal transconductance. This element has an open-circuit input, and an ideal current generator at its output. Its behavior is specified by

$$I_2 = \pm g_m e^{j\omega\tau_1} \frac{1}{1 + j\omega\tau_2} V_1$$

where V_1 is the voltage at the first (input) port, and I_2 is the current flowing into the second (output) port. The sign of the current I_2 is given by the option code SG: PO means +, and NE means −. The time constants τ_1 and τ_2 are optional; these will be set to zero if not specified. This element is useful for FET or HEMT models.

XFM AA SE Z1 Z2

An ideal transformer from impedance Z1 to impedance Z2. The impedance ratio Z1/Z2 is all that matters, but for convenience the input (Z1) and output (Z2) impedances can be specified separately. The only allowed option is SE. Ideal transformers are noiseless.

XIN AA BB Rterm Rin

This element can be used to construct an ideal transformer, which has a fixed real input impedance given by Rin, but whose output impedance is an arbitrary complex function of frequency. The output impedance is specified via the two-port BB which also appears on the XIN line. The output impedance of the transformer AA is taken to be the *input* impedance of BB, *when the output port of* BB *is terminated with* Rterm. By using a numerically specified BB, i.e., by using a statement of the form ONE BB IR ... or ONF BB IR ..., one can obtain any transformation that one wishes. This element is particularly useful when designing circuits which must match a given frequency-dependent impedance: one cascades the XIN transformer with the matching circuit, and optimizes the gain of this cascade. Ideal transformers are noiseless.

XOU AA BB Rterm Rout

This element is entirely analogous to XIN, except the roles of the input and output ports are reversed.

XOU can be used to construct an ideal transformer, which has a fixed real *output* impedance given by Rout, but whose *input* impedance is an arbitrary complex function of frequency. Again, the input impedance of the transformer AA is taken to be the *input* impedance of BB, *when the output port of* BB *is terminated with* Rterm.

ATN AA SE L Z1 T

An ideal attenuator, with loss L in dB, matched to a characteristic impedance Z1, at temperature T (optional). The only allowed option is SE.

ISO AA SE Z1 T

An ideal isolator, matched to a characteristic impedance Z1, at temperature T (optional). It is assumed that the transmission is from port 1 to port 2, i.e., from input to output. The only allowed option is SE.

IV. Circuit Connections

The circuit element library allows you to define various two-ports. These can be interconnected in various ways to obtain a useful circuit. The following connections are available:

CAS AA BB

Cascades two-ports AA and BB, with the resulting two-port now contained in AA. Cascading means connecting the output of AA to the input of BB.

PAR AA BB

Places two-ports AA and BB in parallel, with the resulting two-port now contained in AA. This means that the input and output ports are wired in parallel; mathematically, one adds the *admittance* matrices:

$$Y = Y_{AA} + Y_{BB} \ .$$

SER AA BB

Places two-ports AA and BB in series, with the resulting two-port now contained in AA. This means that the input and output ports are wired in series; mathematically, one adds the *impedance* matrices:

$$Z = Z_{AA} + Z_{BB} \ .$$

EQU AA BB

This is not really a connection at all. This simply creates a duplicate two-port AA from the two-port BB. This will, of course, overwrite any previous definition of AA. This is handy if a circuit element appears many times, e.g., a HEMT or FET in a multistage amplifier.

PBR AA BB Zterm

This creates a parallel branch circuit from the two-port BB and saves it in AA. What this means is: the output of BB is terminated with impedance Zterm, creating a one-port with some impedance Z and equivalent noise temperature T_n. This impedance is then placed in parallel across the two ports of AA. This is analogous to the element RES AA PA R...

```
PST AA BB
```

This converts a parallel impedance into a series impedance. It's useful with `ONF` since `ONF` only specifies data file for a parallel impedance.

V. Printing Results

To print out the results for a two-port circuit, the circuit file must include a statement of the form

```
PRI AA S1 Rnorm
```

This will output the four scattering parameters, the gain in dB, and the stability factor K. The optimum noise figure, temperature, reflection coefficient and impedance, and actual noise temperature will also be printed. All scattering parameters, etc., will be normalized to `Rnorm`. These results are also saved in several files: `circuit.prt` contains all of this data, with column headings, in a nice format for printouts. `circuit.spar` and `circuit.npar` contain the scattering and noise parameters, respectively, in a simple ASCII column format suitable as input for plotting programs. Please note that these files are created ONLY when you choose the "Analyze" option from the PCIRCUIT prompt. The "Optimize" option does not create any files, whereas the "Map" option creates only the `circuit.prt` file.

To print out one-port results, the circuit file must include a statement of the form

```
PRI AA IR Rnorm Rterm
```

The output of the two-port `AA` will be terminated with resistance `Rterm`, and the input impedance and noise-equivalent temperature will be calculated. The input reflection coefficient (normalized to `Rterm`) will be printed, along with the input impedance and equivalent noise temperature. These will be saved in `circuit.prt` for printing, and `circuit.spar` for plotting.

One last but very important point: the `PRI` statement is responsible for evaluating the error function during an optimization run. The choice of a two-port or one-port `PRI` statement affects the definition of the error function. In general, you should have one and only one `PRI` statement in your circuit file, especially when performing an optimization, since PCIRCUIT will sum the error functions obtained for each `PRI` statement and attempt to minimize this total.

VI. File Format

The circuit file is split up into several sections, which are separated by `END` statements. The general order of these sections is the circuit definition, frequency data, two-port data (optional), one-port data (optional), and optimization weights (optional).

COMMENTS

! COMMENT statements can be placed anywhere in the circuit file. These begin with the exclamation mark (!) in the first column of the line.

CIRCUIT DEFINITION

This consists of element definitions, interconnections, and (usually) a single `PRI` statement, followed by an `END` statement.

FREQUENCY DATA

Frequency data is required. This consists of several lines, each of which defines a frequency "band" to be simulated. The importance of splitting up the frequencies into bands is that the optimization weights can be specified separately for each band. For instance, a bandpass filter might have a low-pass "reject" band, a pass band, and a high-pass "reject" band. The bands are specified in one of two ways. Either the start and stop frequencies, and the frequency step can be given:

`f1 f2` Δf

or the frequencies can simply be listed:

`f1 f2 f3 ... fn`

The frequency data is followed by an `END` statement.

TWO-PORT DATA (Optional)

This is where you put the numerical data if you use the element `TWO`. If you do not use the `TWO` element, you ignore these sections, and you don't need to add any extra `END` statements.

The two-port data is split up into two sections, with each terminated by its own `END` statement. You first give the noise parameters, with one line of data for each frequency:

`junk` `NF`$_{min}$ $|\Gamma_{opt}|$ $\arg\Gamma_{opt}$ R_n/Z_0

The first number, "`junk`", is ignored, but is needed to keep compatibility with COMPACT (!). After the noise parameters for all frequencies are given, you need an `END` statement, followed by the s-parameter data. Again, one line of data for each frequency:

$|s_{11}|$ $\arg s_{11}$ $|s_{21}|$ $\arg s_{21}$ $|s_{12}|$ $\arg s_{12}$ $|s_{22}|$ $\arg s_{22}$

and you follow these with an `END` statement. If you use several `TWO` statements, you need to put all of the noise data for the first element, followed by all of the noise data for the second element, etc., in the first section. Do NOT separate these by `END` statements - there is only one `END` statement after ALL of the noise data has been given. The second section then has all of the s-parameters for the first element, and then the second element, etc. Again, only one `END` statement is needed after this section.

ONE-PORT DATA (Optional)

This is where you put the numerical data if you use the element `ONE`. If you do not use the `ONE` element, you ignore this section, and you don't need to add an extra `END` statement.

Both impedance and noise data for `ONE` elements are placed in a single section, in contrast to the situation for `TWO` elements. The single section is terminated by an `END` statement, and consists of one line for each frequency with the following data:

$|\Gamma|$ $\arg\Gamma$ T_{noise}

If you use several `ONE` statements, give all of the data for the first element, followed by all of the data for the second element, etc. Only one `END` statement is needed, after all of the data has been given for all elements.

OPTIMIZATION DATA (Optional)

PCIRCUIT is also capable of optimizing the performance of your circuit. To use this feature, you must first decide which elements in your circuit will be varied during the course of the optimization. Almost any variable appearing as an argument to a line in the circuit file can be used as an optimization variable. You can flag variables to be optimized by assigning them NEGATIVE values in the circuit file. PCIRCUIT will ignore the negative sign in assigning the initial value, but will note that parameter as being adjustable. Example:

```
TRL AA SE -40.  -80.  5500.
```

creates a two-port `AA` which is a transmission line with $Z_0 = 40\Omega$ and $\theta = 80°$ at $f = 5500$ MHz. The values of Z_0 and θ will be allowed to vary in the optimization. One can also place lower and upper limits on variables:

```
TRL AA SE -40.  (20.  100.)  -80.  (30.  150.)  5500.
```

will constrain the optimization to obey $20 < Z_0 < 100$ and $30 < \theta < 150$.

The optimization attempts to minimize the value of the error function, which is defined by the data given in this section of the circuit file. The format of this data is as follows: `(Target error function value)`

w_1 w_2 w_3 w_4 w_5 w_6 `(one line of data for each frequency band)` followed by an `END` statement.

The target error function value specifies at which point the optimization procedure should stop. This can normally be set to zero, since the number of iterations can also be given to PCIRCUIT at the prompt. The weights w_i give the definition of the error function, which depends on the `PRI` statement is being used. If it is a two-port statement, i.e., `PRI AA S1 50.`, the definition is as follows:

$$\textit{Error function} = \sum_{freq} \left[w_1 |s_{11}|^2 + w_2 |s_{22}|^2 + w_3 (G(dB) - w_4)^2 + w_5 (T_n(K) - w_6)^2 \right]$$

where the sum extends over all frequencies in all bands. Note that the weights w_i can change values from band to band. Here $G(dB)$ is the gain of the two-port in dB, and $T_n(K)$ is the noise temperature in K. Therefore, w_4 can be considered as the target gain, and w_6 is the target noise temperature.

If a one-port `PRI` statement is used, i.e., `PRI AA IR 50.  50.`, then the definition is

$$\texttt{Error function} = \sum_{freq} \left[w_1 |\Gamma|^2 + w_2 (T_{equiv}(K) - w_3)^2 \right]$$

Appendix D PCIRCUIT Program Examples

D.1 Mixer design

This is the circuit file for the PCIRCUIT program to optimize the Al-wiring or Nb-wiring SIS mixer design for the frequency band of 1050 GHz. The mixer configuration is described in chapter 4, and the results of the calculated RF coupling efficiencies are also given in that chapter.

```
!
!RF coupling optimization for twin-slot two-junction
!SIS mixer with Al-wring at 1050 GHz frequency band.
!
!Al film electrical and geometrical parameters:
!
ASI YY SE 0.20000 2.4500 0.016000 5.0000
!
!Dielectrical and geometrical parameters for the SiO insulators:
!
SUB S1 SE 1.0 0 5.6 0 0.4
SUB S2 SE 1.0 0 5.6 0 0.2
!
!The antenna impedance is stored in data file "Zslot.1050":
!
ONF AA IR Zslot.1050
!
!Normalized to a 50 Ω resistance:
!
XIN BB AA 100000000 50.0
!
!The microstrip section serving as the impedance transformer:
!both width and length are to be optimized.
!
MSL DD YY YY S1 -4.9762 (3.0 10.0 ) -33.679 (10.0 50.0 )
!
!The spacer next to the junction:
!
MSL EE YY YY S2 5.0 2.5
!
!Junction capacitance:
!
```

```
CAP FF PA 110.
!
!The microstrip section serving as the tuning inductor: the width is fixed
!5.0 μm, the length is a variable to be optimized:
!
MSL GG YY YY S2 5.0 -4.3129 (3.0 10.0 )
PBR HH GG 0.0000000001
!
!The junction RF impedance is stored in data file "jctimp":
!
ONF II IR jctimp
XOU JJ II 100000000 50.000
!
!Connections:
!
CAS BB DD
CAS BB EE
CAS BB FF
CAS BB HH
CAS BB JJ
PRI BB S1 50.0
END
!
!Sweep the circuit from 400 to 1400 GHz, in three bands:
!
400 990 10
1000 1100 10
1110 1400 10
END
!
!Optimize for maximum RF coupling in the second band (1000–1100 GHz):
!Target error function = 0.
!
0
0 0 0 0 0 0
0 0 1 0 0 0
0 0 0 0 0 0
END
```

The circuit file for the Nb-wiring mixer is given below without any comments. Instead of using one section of impedance transformer as for the Al-wring design, the Nb-wiring mixer utilizes two sections of impedance transformers.

```
!Circuit file for Nb-wiring mixer design at 1050 GHz band:
```

```
SSI XX SE 0.2 5.0 2.9 4.2
SUB S1 SE 1.0 0 5.6 0 0.2
SUB S2 SE 1.0 0 5.6 0 0.4
ONF ZZ IR Zslot.1050
XIN YY ZZ 1000000 50.0
MSL AA XX XX S2 -7.3517 (2.0 10.0 ) -11.649 (10.0 100.0 )
MSL EE XX XX S2 -6.0218 (3.0 15.0 ) -13.152 (10.0 100.0 )
MSL BB XX XX S1 5.0 2.5
MSL HH XX XX S1 5.0 -3.0 (3.0 20.0 )
PBR JJ HH 0.000000001
CAP CC PA 110.
ONF GG IR jctimp
XOU DD GG 1000000 50.0
CAS YY AA
CAS YY EE
CAS YY BB
CAS YY CC
CAS YY JJ
CAS YY DD
PRI YY S1 50.0
END
400 990 10
1000 1100 10
1110 1400 10
END
0
0 0 0 0 0 0
0 0 1 0 0 0
0 0 0 0 0 0
END
```

D.2 RF embedding impedance calculation

Here a circuit example is given of the device 73 in section 6.4 for the calculation of the RF embedding impedance seen by the junction using the PCIRCUIT program.

```
!
!This calculates the RF embedding impedance seen by the junction for a
!Nb-wiring mixer design at the 750 GHz band. The embedding includes the
!twin-slot antena, the junction capacitance, and all the microstrip lines
!as inductor and impedance transformer.
!
```

```
!Nb film electrical and geometrical parameters:
!
SSI ZZ SE 0.2 5.0 2.9 4.3
!
!SiO insulator parameters:
!
SUB YY SE 1.0 0.0 5.6 0.0 0.4
SUB XX SE 1.0 0.0 5.6 0.0 0.2
!
!The antenna impedance is stored in data file "Zslot.750":
!
ONF AA IR Zslot.750
!
!Two sections of microstrip lines as impedance transformer:
!
MSL CC ZZ ZZ YY 5.8086 15.0
MSL DD ZZ ZZ YY 3.2656 15.0
!
!Spacer:
!
MSL EE ZZ ZZ XX 5.0 2.5
!
!Junction capacitance = 85 fF/μm² × (1.3 × 1.3) μm²:
!
CAP FF PA 144.00
!
!The microstrip line as tuning inductor:
!
MSL GG ZZ ZZ XX 5.0 3.4611
PBR HH GG 0.00000001
!
!Circuit connection:
!
CAS FF HH
CAS FF EE
CAS FF DD
CAS FF CC
CAS FF AA
!
!To calculate the input impedance of a two-port using IR option in PRI code:
!
PRI FF IR 50 100000000
END
```

```
!
!Sweep from 250 to 1500 GHz:
!
250 1500 10
END
```

Fig. D.1 shows the calculated RF embedding impedance as a function of frequency.

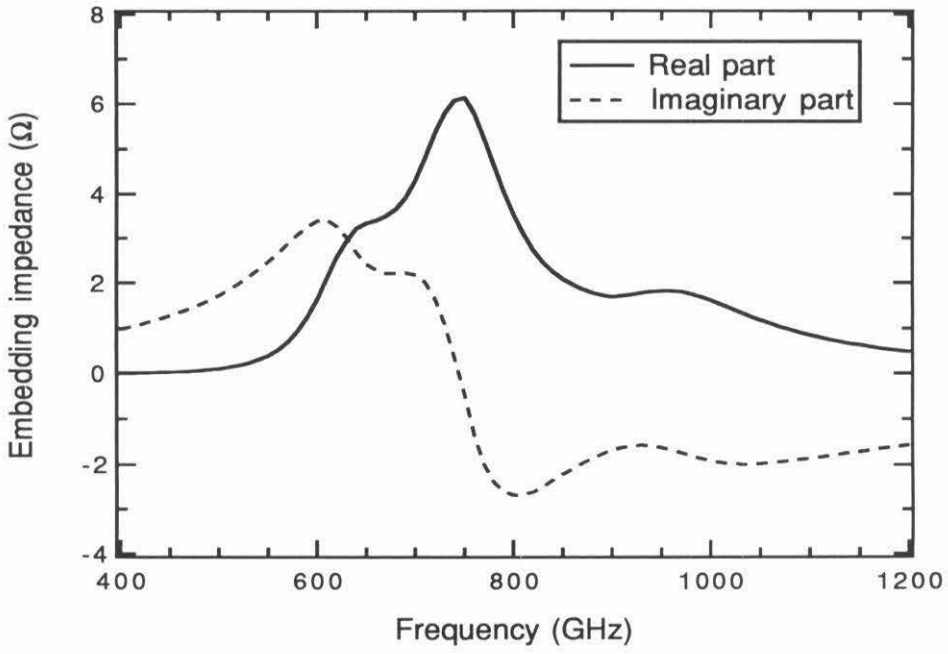

Figure D.1: Calculated RF embedding impedance of a Nb-wiring mixer, device 73. The mixer is designed for center frequency 750 GHz.